EPFL

Thèse n° 8958

Understanding Thermomechanical Treatments Induced by Laser Powder Bed Fusion Process

Présentée le 1er octobre 2021

Faculté des sciences et techniques de l'ingénieur
Laboratoire de métallurgie thermomécanique - Chaire PX Group
Programme doctoral en manufacturing

pour l'obtention du grade de Docteur ès Sciences

par

Hossein GHASEMI TABASI

Acceptée sur proposition du jury

Prof. C. Moser, président du jury
Prof. R. Logé, Dr J. Jhabvala, directeurs de thèse
Prof. M. Attallah, rapporteur
Dr U. E. Klotz, rapporteur
Dr J.-M. Drezet, rapporteur

École polytechnique fédérale de Lausanne

2021

Acknowledgements

My acknowledgements first go to Prof. Roland Logé and Dr. Jamasp Jhabvala, my thesis director and co-director. I thank you Roland and Jamasp for your kind and caring supervision and invaluable guidance during my studies. I am thankful also to all the members of my thesis jury: Prof. Moataz Attallah, Dr. Ulrich E. Klotz, Dr. Jean-Marie Drezet and Prof. Christophe Moser, for their time and their valuable comments.

I would like to thank Competence Center for Materials Science and Technology (CCMX) and the Swiss industrial consortium for supporting my project. I am particularly thankful to Dr. Eric Boillat for his help in numerical simulation of my project. Thank you Eric for teaching me the complex physics behind your calculations and for encouraging and supporting me during these four years. I would like to thank Dr. Cyril Cayron and Dr. Steven Van Petegem for their availability and kindness in helping me and answering all of my questions.

A large part of this thesis was done in collaboration with Empa and I would like to thank Dr. Christian Leinenbach and Dr. Seth Griffiths for sharing their knowledge with me. I would also like to thank Dr. Václav PEJCHAL and Dr. Sébastien Lani at CSEM and Cyril Dénéréaz at EPFL (LMM) for allowing me to work with their equipment, for mechanical testing, and their support over the years. I would like to thank Siddartha Berns and the staff of the HEIG-VD in Ste-Croix for their kind help and support provided for my experiments.

I was lucky also to have kind and friendly colleagues at LMTM. Since the day I joined, your continued support is the one thing I can always count on. You showed me patience, guided and motivated me whenever the situation arose. Therefore, I would like to thank all LMTM lab members: Navid & Mahtab, Céline, Rita, Margaux, Baptiste, Joëlle, Nikola, Charlotte, Toni, Lucas, Milad, Reza, and Claire. A special thanks also to Priscille and Mathijs, who actively participated in my experiments, for their technical help, suggestions and ideas. It goes without saying that I cannot thank enough my friends in Neuchâtel for making the daily life more enjoyable: Pieter, Gözden, Kevin, Julien, Julie, Ulas, Duygu, Arun, Enrico, Ruben, Saood, Samuel, Olivier, Bastien, Maxime, Lena, Annika, Aari, Arnout, Babak, Ryan, Eric, Sajjad, Arash, Sorour, Milad, Mohammad, Tavoos, Dayan, Elham, Leila, Abbas, Saeed, Alaleh, Fereshteh, Armin, Soroush, and Ali.

Finally, I am profoundly thankful to my family, for their continued support, not only during my PhD work, but since the very beginning. I would especially like to thank Shima, my best friend, my beloved wife who has always been supportive of me during these stressful times, and the person with whom I share all the joys life has to offer.

Neuchâtel, 29.08.2021

Abstract

Additive Manufacturing (AM) is referred to technologies that produce directly 3D parts in a layer-by-layer fashion. Laser Powder Bed Fusion (L-PBF) is one of the most important AM processes, enabling production of very complex metallic objects from a computer-aided design (CAD) model. In this research, the L-PBF process has been studied at different scales, going from laser/matter interaction to the identification of thermomechanical conditions undergone by the material, to optimization of process parameters, and identification of cracking mechanisms. The studied alloys were bronze, red gold, 316L stainless steel and the CM247LC Ni-based superalloy.

The first part of the thesis deals with the optimization of L-PBF parameters of one alloy, red gold, taking advantage of known optimized parameters for bronze. Printing gold samples by laser melting processes is usually difficult because of their high reflectivity and thermal conductivity. It is, therefore, proposed to use an alternative material, CuSn8 (bronze), as a test material before printing gold alloys, which is cheaper and has physical properties such as melting point and absorptivity close to the gold alloy. In addition, an experimental L-PBF station capable of working with small amounts of precious powder has been developed. The processing of 18-Carat gold alloy was optimized in two steps. The first step consisted in finding the best parameters for printing bronze samples with the highest density. Relative densities as high as 99.8% were obtained. In a second step, gold alloy samples were printed by scaling the bronze best parameters. The concept of normalized enthalpy was used to take into account the differences in thermal and optical properties among the different materials. A translation rule was derived for the prediction of optimal processing conditions, based on the ones found for the test material. One important input for this translation rule is the powder absorptivity, which was measured at the appropriate laser wavelength and at room temperature. This approach eventually leads to the highest reported density for an additive manufactured 18-carat gold alloy (99.81% relative density). Finite element (FEM) simulations justify the translation rule formulation by showing the importance of the laser/powder interactions during the L-PBF process, leading to a finite penetration depth of the laser in the powder bed due to multiple reflections. The translation rule was further validated by considering 316L steel instead of red gold.

The second part of the thesis looks at laser/matter interaction and process parameters effects on the melt pool formation. Numerical finite element simulations identified precise thermal histories, which were used to understand phenomena such as phase transformation in red gold, or cracking in CM247LC.
CM247LC is susceptible to cracking during manufacturing by L-PBF process. In order to unveil the mechanisms of crack formation, both Gleeble testing of LPBF samples, and high-speed synchrotron X-ray imaging in combination with a miniaturized L-PBF set-up that reproduces real processing conditions have

been employed. Hot cracking could be differentiated from liquation. Reduction in crack density could be obtained by 3D laser shock peening (LSP), process optimization, and chemical composition modification. The impact of the disordered/ordered phase transformation on the microstructure of additively manufactured red-gold alloy has been studied. 3D printed red-gold samples with different post processing treatments were subsequently heat treated at 250 ºC, and characterized by Electron backscatter diffraction (EBSD). Textures after heat-treatment were shown to strongly depend on the stress state in the early stages of the phase transformation, during the manufacturing process. This stress state depends itself on the process parameters used to print the samples. Final textures relate to stress-induced variant selection during the early stages of the disorder-order transformation, and are not affected by a stress change or stress relaxation occurring after the early stages of the phase transformation.

Keywords
Additive Manufacturing, Laser-Powder Bed Fusion, absorptivity, gold-alloy, Ni-base superalloys, cracking

Résumé

La fabrication additive (AM) fait référence aux technologies qui produisent directement des pièces en 3D, couche par couche. La fusion laser sur lit de poudre (L-PBF) est l'un des procédés de fabrication additive les plus importants, permettant la production d'objets métalliques très complexes à partir d'un modèle de conception assistée par ordinateur (CAO). Dans cette recherche, nous avons étudié le procédé L-PBF à différentes échelles, allant de l'interaction laser/matière à l'identification des conditions thermomécaniques subies par le matériau, à l'optimisation des paramètres du procédé, et à l'identification des mécanismes de fissuration. Les alliages étudiés sont le bronze, l'or rouge, l'acier inoxydable 316L et le superalliage à base de nickel CM247LC.

La première partie de la thèse traite de l'optimisation des paramètres L-PBF d'un alliage, l'or rouge, en partant des paramètres optimisés connus pour le bronze. L'impression d'échantillons d'or par des procédés de fusion laser est généralement difficile en raison de leur forte réflectivité et conductivité thermique. Il est donc proposé d'utiliser un matériau alternatif, le CuSn8 (bronze), comme matériau test ; il est moins cher et possède des propriétés physiques telles que le point de fusion et l'absorptivité qui sont proches de l'alliage d'or. En outre, une station expérimentale de L-PBF capable de travailler avec de petites quantités de poudre précieuse a été développée. Le traitement de l'alliage d'or 18 carats a été optimisé en deux étapes. La première étape a consisté à trouver les meilleurs paramètres pour imprimer des échantillons de bronze avec la densité la plus élevée. Des densités relatives aussi élevées que 99,8 % ont été atteintes. Dans un deuxième temps, des échantillons d'alliage d'or ont été imprimés en adaptant les paramètres optimaux trouvés pour le bronze. Le concept d'enthalpie normalisée a été utilisé pour prendre en compte les différences de propriétés thermiques et optiques entre les différents matériaux. Une règle de transfert a été dérivée pour la prédiction des paramètres de procédé optimales, sur la base de celles trouvées pour le matériau test. Une donnée importante pour cette règle de transfert est l'absorptivité de la poudre, mesurée à la longueur d'onde appropriée et à température ambiante. Cette approche conduit finalement en la densité la plus élevée rapportée pour un alliage d'or 18 carats fabriqué de manière additive (densité relative de 99,81 %). Des simulations par éléments finis (FEM) justifient la formulation de la règle de transfert en montrant l'importance des interactions laser/poudre au cours du processus L-PBF, qui conduisent à une profondeur de pénétration finie du laser dans le lit de poudre en raison des réflexions multiples. La règle de transfert a été validée en considérant l'acier 316L en plus de l'or rouge.

La deuxième partie de la thèse s'intéresse à l'interaction laser/matière et aux effets des paramètres du procédé sur la formation du bain liquide. Des simulations numériques par éléments finis ont permis d’identifier des

histoires thermiques précises, qui ont été utilisées pour comprendre des phénomènes tels que la transformation de phase dans l'or rouge, ou la fissuration dans le CM247LC.

Lors du procédé L-PBF, le CM247LC est susceptible de se fissurer pendant la fabrication . Afin de dévoiler les mécanismes de formation des fissures, il a été utilisé à la fois des tests Gleeble sur des échantillons de LPBF, et de l'imagerie à grande vitesse par rayons X synchrotron en combinaison avec un montage L-PBF miniaturisé reproduisant les conditions réelles de traitement. La fissuration à chaud a pu être différenciée de la liquéfaction. La réduction de la densité de fissures a pu être obtenue par martelage par choc laser (Laser Shock Peening, LSP) en 3D, optimisation du procédé et modification de la composition chimique.

L'impact de la transformation de phase désordre-ordre sur la microstructure de l'alliage d'or rouge fabriqué de manière additive a été étudié. Des échantillons d'or rouge imprimés en 3D avec différents post-traitements ont ensuite été traités thermiquement à 250 ºC, et caractérisés par diffraction d'électrons rétrodiffusés (EBSD). Il a été démontré que les textures après traitement thermique dépendent fortement de l'état de contrainte acquis pendant les premiers stades de la transformation de phase, lors du processus de fabrication. Cet état de contrainte dépend lui-même des paramètres du procédé utilisés pour imprimer les échantillons. Les textures finales sont liées à la sélection de variants induite par l'état des contraintes au cours des premières étapes de la transformation désordre-ordre, et ne sont pas affectées par un changement ou une relaxation de contraintes après les premiers stades de la transformation de phase.

Mots clés

Fabrication additive, fusion laser sur lit de poudre, absorptivité, alliage d'or, superalliage à base de nickel, fissuration.

Contents

Chapter 1: Introduction

1.1. Additive Manufacturing

Additive manufacturing (AM), also referred to as 3-D printing, refers to the numbers of technologies, which allow a sample to be built up layer by layer. In contrast, conventional manufacturing processes such as machining, involves removing material from stock until the final part geometry. In addition to the benefit of less waste, AM enables complex internal and external geometries previously unattainable by conventional manufacturing. These can be achieved with short production times and minimal custom tooling [1,2] .

During recent years, different industries have been trying to follow a new model and paradigm to increase the performance and efficiency of their products such as medical, energy, aerospace, jewelry, and automotive applications. For the whole market, more than 25 % compound annual growth rate (CAGR) is expected (Figure 1). AM fabricated parts offer the same or even better functional qualities than the specimens produced with traditional techniques while reducing the waste material, final weight, and finally the cost [3,4]. Combining these advantages with the possibility to produce parts with complex geometries and advanced design, makes AM processes ideal for high-value, low-volume production of complex parts in different industries. As an example, in aerospace parts, which contain complex geometries, assembly of different parts was necessary in conventional methods, whereas using AM technologies results in lightweight-engineered structures and as a result, a significant cost saving. Patient-matched devices made a considerable improvement in medical industry; with AM technologies, people can use their own medical imaging data to produce implants and devices.

Figure 1. Metal additive manufacturing market 2019- Supplier vs buyer forecast 2024 in Euro billions[5].

Metal AM is one of the technologies with intense growth and its expanding development centers are revealing new discoveries[6]. So far, more than 30 different AM processes have been classified for manufacturing of the metallic components (Figure 2).

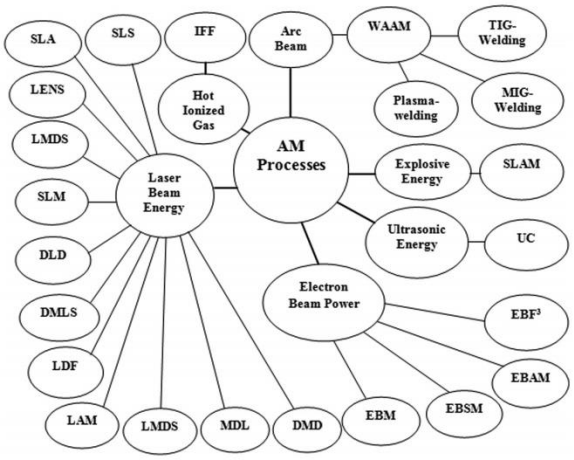

Figure 2. Different AM processes classification[7].

Directed Energy Deposition (DED, also known as DMD, Direct Metal Deposition) and Powder Bed Fusion (PBF) are the two main categories defined for AM of metallic components, based on ASTM Standard F2792. Considering the main heat source applied in each process, another distinction step exists for electron beam (EB), laser (L), gas metal arc (GMA), and plasma arc (PA).

Among different AM techniques, the Laser Powder Bed Fusion (L-PBF, also called Selective Laser Melting (SLM)) process has received the most focus. L-PBF is a layer-by-layer process: at each step, a layer of powder (20-90 μm) is deposited on a substrate, and the laser selectively melts powders according to a CAD file which slices the desired part into different planar layers, indicating a scan path upon pre-specified parameters for the materials and machine configuration [8,9]. The density of energy received by the powder is usually defined by the layer thickness, the effective laser power, the movement speed of the laser, the hatching distance and the absorptivity of the powder [10]. Producing AM parts using the L-PBF technique requires a significant number of trials and errors cycles to optimize the process parameters, in relation with the metallic powder and its physical and chemical properties [11–13].

The main steps of L-PBF process are as follows (see Figure 3):

- The powder container is raised up bringing a small amount of powder particles in front of the coater

- The coater system moves the powder particles across the build plate

- A laser (or in some case multiple lasers) selectively melts the powder particles according to a CAD file

- The build plate moves down by the thickness of a single layer.

- This process is repeated until the part is completely printed.

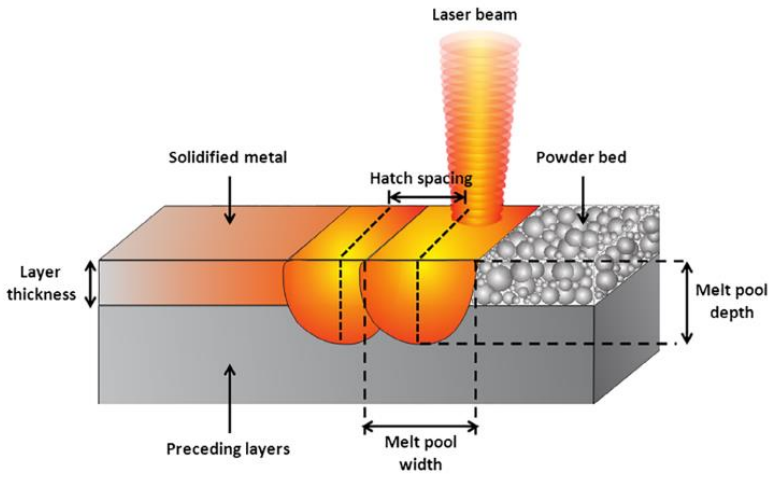

Figure 3. Schematic of L-PBF and its process parameters [14].

The provided powder particles for the L-PBF process have a size in the range of 20 μm–50 μm. Each new layer of powder particles deposited on top of the substrate or previously printed layers has a given *layer thickness*. The separation between two adjacent laser beams is defined as *hatching distance* (or hatch spacing, i.e. the distance from the center of one laser track to the center of the next track as shown in Figure 3). The hatching distance is an important parameter which is chosen such as to have enough overlap between laser tracks. The final quality of the printed samples is greatly dependent on a proper optimization of the process parameters [15].

On a given layer, the L-PBF process consists in locally heating the powder particles, which melt and solidify rapidly. When the laser light hits the deposited powder particles, a part of the input energy is reflected from the powder bed and a part of it is absorbed. There are different parameters which can affect the amount of absorbed heat by the powder particles, such as chemical composition, packing density, and average particles size. The absorbed light heats the powder particles. The heat transfer in the first stage of the process consists of heat convection between the powder particles and the environment, and heat conduction inside the deposited powder layer, and between the powder particles bed and previous layers/substrate [16]. A high power density laser is used to melt the powder particles and form a stable melt pool which moves with the heat source. The maximum temperature in the melt pool can be significantly higher than the liquidus

temperature of the alloy. Depending on the process parameters, the melt pool shape has two main operational regimes: *conduction and keyhole mode*. When the applied energy density is lower than a critical value, the conduction mode is dominant, and the melt pool has a shape close to semicircular [17].

On the other hand, higher energy densities lead to deep vapor cavity formation inside the melt pool and complex liquid flow in which instabilities and collisions of the melt pool walls may result in porosities. In addition, due to the highly localized heat, evaporation of metallic elements becomes significant, and thermo-capillary convection (also known as Marangoni convection) is the dominant mode of heat transfer[18,19]. This is called the keyhole regime. The name comes from the fact that the Marangoni flow makes the top part of the melt pool much wider than its bottom which resembles the shape of a keyhole[20]. In addition, at high energy densities, the melt pool and adjacent powder particles experience significant recoil pressure due to the local evaporation. As a result, metallic powders and the molten droplets from the melt pool may be ejected and form spatters in the printed samples. As mentioned earlier, laser/powder interaction, heat transfer mechanisms and melt pool formation are complex phenomena and change with the physical and chemical properties of each metallic powder. Thus, printing defect free samples requires a significant number of trials and errors cycles to optimize the process parameters.

The thermal history due to the deposition of many layers plays an important role on the final microstructure and the state of stress of the printed parts. Precipitation and crack formation in the HAZ of Ni-based superalloys, or phase transformations in Ti alloys, are examples of microstructure evolution mechanisms related to the thermal cycles induced by the L-PBF process (heating and cooling rates in particular). Considering the typical size of the melt pool and the typical heating and cooling rates, L-PBF should be studied at multiple scales. The first one is a “macro scale” (a few mm), where our objective is to study microstructures and thermal stresses. To understand the origin of these stresses and microstructures, a “meso scale” study is relevant, i.e. typically a few hundreds of microns. This lower scale is focused on the melt pool and its stability according to laser-matter interactions. The process parameters leading to various laser dwelling times and temperature distributions in the part will affect the amount of liquid and the melt pool steady state shape, which in turn will influence porosity/crack formation. Finally, a “micro scale” (a few tenth of microns) becomes relevant, such as to get access to parameters like absorptivity and thermal conductivity in the powder bed and in the liquid, or thermodynamic quantities like the enthalpy of the material. To summarize, tailoring the thermal cycles in L-PBF samples along with the formation of the melt pool can lead to a thorough understanding of microstructure evolution phenomena in L-PBF parts such as phase transformation, precipitation, recrystallization and porosity/cracks formation.

1.2. Different scales in L-PBF process

1.2.1. Macro Scale: Residual stresses, Microstructure

A result of the deposition of liquid material on a solid substrate with lower temperature or previous solidified layers is the existence of high temperature gradients and generation of residual stresses [21,22]. Layers delamination during the process, part distortion, and decrease in fatigue life are among the consequences of these residual stresses[23,24]. Spatial thermal gradients due to localized heating and cooling, and associated local thermal expansion and contraction are at the origin of residual stresses in L-PBF parts. During the deposition of a new layer the material below the melt pool in the HAZ is rapidly heated to high temperatures. This temperature gradient causes expansion that creates compressive yielding (Figure 4A). During the melting, stresses cannot be sustained by the melt pool itself. However, the already solidified parts of the material just behind the melt pool accumulate high tensile stresses. Restricted thermal shrinkage is the main reason for tensile residual stresses in this zone (Figure 4B)[25–27]. Finally, stress redistribution makes a tensile stresses distribution along the outer surfaces, and compressive stresses within the printed samples[28]
.

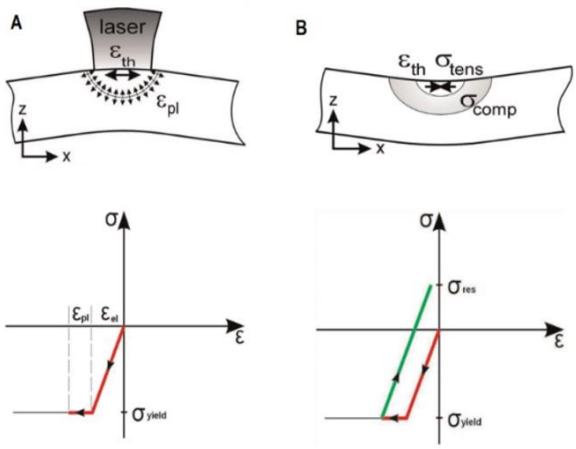

Figure 4. A) Induced stresses and deformation because of laser heating, and B) cooling in the L-PBF process[29].

In the L-PBF process, there is a downward heat flow during the solidification which is opposite to the build direction. The size and morphology of the microstructure in the additive manufactured samples is affected by different parameters [30]. The cooling rate is one of the most important factors, defining the final grain size: increased cooling rates lead to finer grain sizes [31]. Changing the parameters of the L-PBF process could modify the texture of the printed sample, e.g. power, layer thickness and scanning speed, because these parameters directly define the geometry of the HAZ and the amount of previously solidified material which will undergo remelting. After the melt pool has solidified, it can still undergo solid-state

transformations upon cooling. Moreover, additions of new layers reheat the already solidified parts and these thermal cycles can further promote solid-state transformations, and change the distribution of the residual stresses [32]. The final microstructure or grain size distribution of the L-PBF parts can be modified by changing different processing parameters [33]. As an example, formation of cracks in Ni-based superalloys is influenced by the cooling rate from the melt and by the associated chemical segregations. Figure 5 indicates extensive cracking in CM247LC as built L-PBF samples[34].

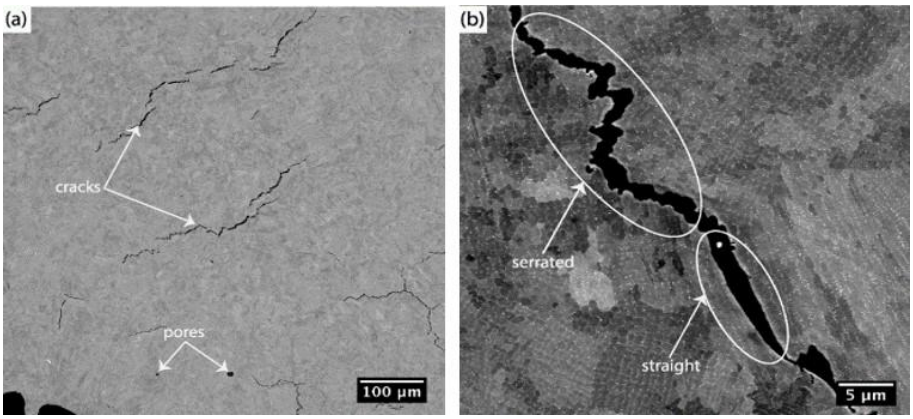

Figure 5. SEM micrographs of L-PBF samples indicate a) the presence of cracks in a transverse section of CM247LC alloy; b) preferential propagation of the cracks along the cell boundary at higher magnification [34].

In the literature, several mechanisms are reported to be responsible for cracking during the manufacturing of Ni-based superalloys. Solidification cracking, liquation cracking and ductility dip cracking (DDC) are the main mechanisms that have been suggested [34–39].

Solidification cracking occurs in the last stages of solidification, due to a combination of solute-rich liquid entrapment between solid interfaces and tensile residual stresses that pull the interfaces apart [34–36]. Liquation cracking results from the micro-segregation that takes place during fast solidification, which locally lowers the solidus point. When an adjacent line scan or additional layer is processed, localized melting and associated cracking occur in the HAZ [34–36]. Finally, ductility reduction in a [0.5 $T_{solidus}$ – $T_{solidus}$] temperature range has been reported in Ni-based superalloys. As is the case for solidification and liquation cracking, the presence of residual stress within this temperature range results in the so-called "ductility dip cracking" (DDC) [37–39].

1.2.2. Meso scale : Melt pool

L-PBF involves melting and solidification under the influence of a high power laser source. The laser power and scan speed have a direct influence on the melt pool size [40,41]. When the laser power is low and/or the

scan speed is high, the formation of melt pool is difficult to observe since the melt pool size is small and most of the molten powders instantaneously transform to consolidated particles. Increasing laser power and decreasing scanning speed increase the melt pool area [42]. Figure 6 indicates the effect of the laser power and speed variation on the melt pool depth of tool steel.

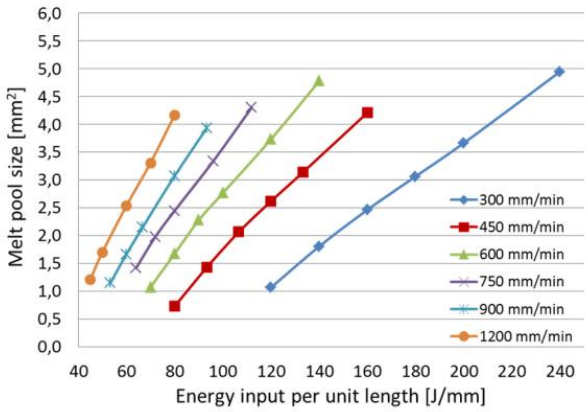

Figure 6. Melt pool size(Y-Z plane) in dependence of energy input during the laser deposition (DED) of 32CrMoV steel on X38CrMoV tool steel process [41].

When an excessive increase of laser power leads to significant evaporation from the melt pool, the recoil pressure increases and a deep surface depression forms inside of the melt pool, leading to keyhole. Light multiple reflections at steep angles inside the keyhole walls increase the heat accumulation, which lead to higher penetration depth of the melt pool [43].

Porosities and lack of fusion voids are general defects in L-PBF parts that need to be minimized or excluded due to their detrimental effects on final mechanical properties. Three main mechanisms have been suggested for formation of these defects (see Figure 7). First, high power density produces keyholes during the melting/solidification process [44]. Instability of keyhole melting, leaves entrapped vapor inside the deposit[44,45]. Second, the entrapped gases inside the powders during the atomization process result in spherical gas pores. There are also other sources for gas pores such as entrapment of the shielding gas during AM or alloy vaporization inside the melt pool[46].

A third category is the lack of fusion defect which is the result of insufficient melt pool penetration of the upper layer into the solid substrate or the last deposited layer [47,48].

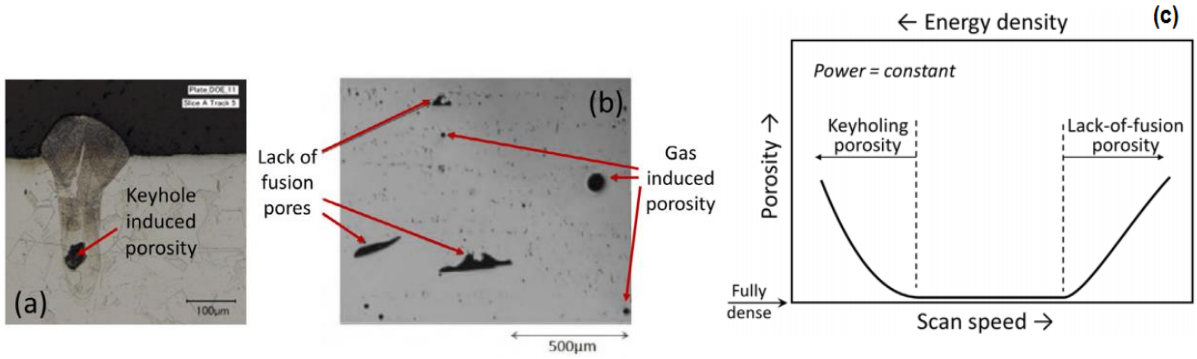

Figure 7. (a) Keyhole, (b) lack of fusion and gas induced porosity , and (c) effect of energy density and scan speed on type of the porosities [49].

1.2.3. Micro scale: Laser-Powder interaction

When a high power laser irradiates the surface of the material, a part of the beam energy is absorbed by the material, possibly leading to melting and even vaporizing. Applications include cutting, drilling and welding [50]. The geometry of the melt pool depends on the material optical properties, laser beam characteristics, and material thermo-physical properties [51]. However, laser absorption by a powder is increased compared to a bulk material. Multiple scattering and effects of the powder geometry are the most important characteristics which should be considered when studying optical properties of the powder. Such studies have been done both empirically and by simulation, to investigate the absorption mechanisms in different metals.

The experimental study of absorption evaluation by temperature is not easy since absorptivity depends on different factors such as laser intensity, angle of incidence, wavelength, temperature, surface chemistry (oxidation) surface roughness, and contamination [52]. During melting, there is a non-stationary interaction between the melt pool and the laser, which directly affects the absorption. Even the powder distribution fluctuation would change the absorption during the AM process [53].

This work will address different scales mentioned earlier, investigating challenges in the parameters optimization of the L-PBF process, by looking at laser/matter interaction. The resulting models will be used to analyze the effects of the temporal and spatial temperature distributions, inherent to AM, on metallurgical phenomena such as phase transformations and crack formation.

Chapter 2: State of the Art

This chapter presents selected fundamental topics related to the multiscale nature of the L-PBF process, and a literature review on the AM fabrication of the materials covered in this work.

2.1. Laser/matter interaction

The percentage of light energy absorbed by a material depends on different parameters such as composition, laser wavelength, roughness, oxide layer and temperature. Most of the metallic components surfaces in real life have some degree of roughness (or texture). Regardless of the chemical composition of a material, pits and valleys on the surface of the metallic materials (Figure 8) affect the optical properties, and a fraction of the light can be trapped due to the surface features, resulting in increased absorption [54,55].

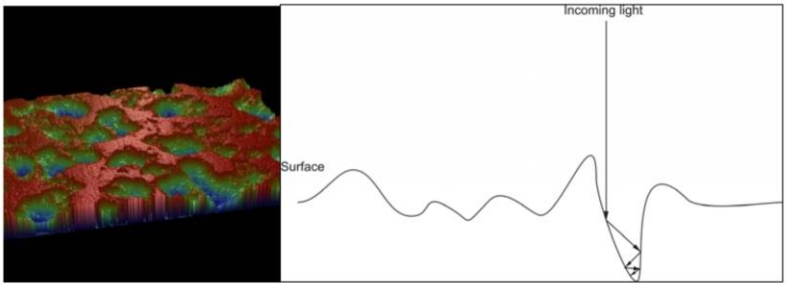

Figure 8: Left) Profilometry scan of a rough metal surface. Right) The texture of a surface may "trap" some of the light and enhance absorption[56].

Both chemical and optical properties of oxide layers are different from the properties of the metal itself. For most metals, the presence of an oxide layer on the surface increases light absorption.

In most laser processing technologies such as laser cutting, laser welding, and laser drilling, at the beginning of the process, the laser light hits a bulk metallic surface. The optical properties of metallic surfaces are associated with high reflectivity and low transmission. However, due to the high energy density of these processing methods, melting occurs fast, and as a result, almost instantaneously a part of the laser beam interacts with a liquid phase. As mentioned in the introduction, several studies have used ellipsometer to investigate the optical properties of liquid metals [57–61]. However, measuring optical properties of a liquid

phase is very difficult. Controlling composition (avoid oxidation and element evaporation at high temperatures), temperature, and roughness is crucial to have an accurate measurement.

As an example, for gold, various models for absorption have been considered, depending on the conditions [57,62–64]. Gold in solid state is known to be very reflective in nature [65]. While other metals like iron, palladium, aluminum, and platinum show a relatively lower reflectivity of 60-70% at the infrared wavelength, copper, silver and gold show nearly total reflectivity. Therefore, a surface reflects most of the laser energy; thus, melting these metals by laser is difficult despite their low melting temperature [66]. Different models have attempted to describe the reflectivity in the liquid state (Figure 9) [62,63,67]. Since data on the temperature-dependent optical properties of materials is scarce, simple approximations are proposed to estimate the amount of the absorbed light. Equation 1 represents the absorptivity for a specific material:

$$A = 1 - R = \frac{(1-n)^2+k^2}{(1+n)^2+k^2} \tag{1}$$

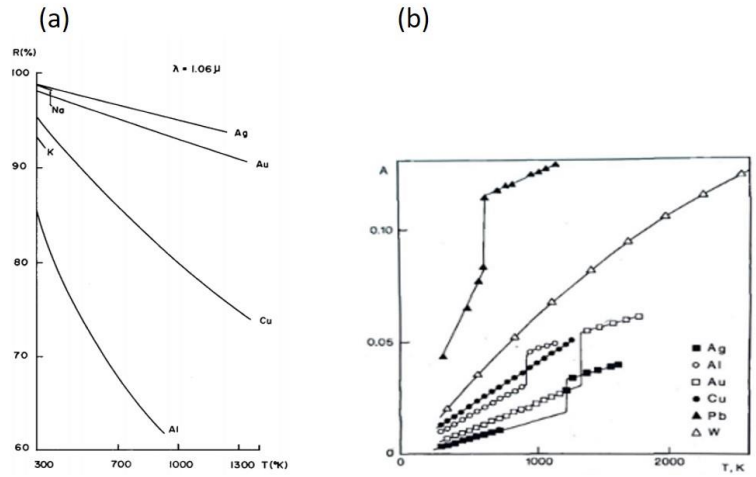

Figure 9. (a) Reflectivity [67], and (b) absorptivity [62] evaluation of different bulk metals by temperature.

where A is the absorption, R is the reflectivity, and n and k are the index of refraction and absorption coefficient, respectively. Figure 10 indicate the refractive index (**n)** and the absorption coefficient (**k)** of gold as a function of temperature, respectively. There graphs show there is a discrete jump at the melting point for n and k.

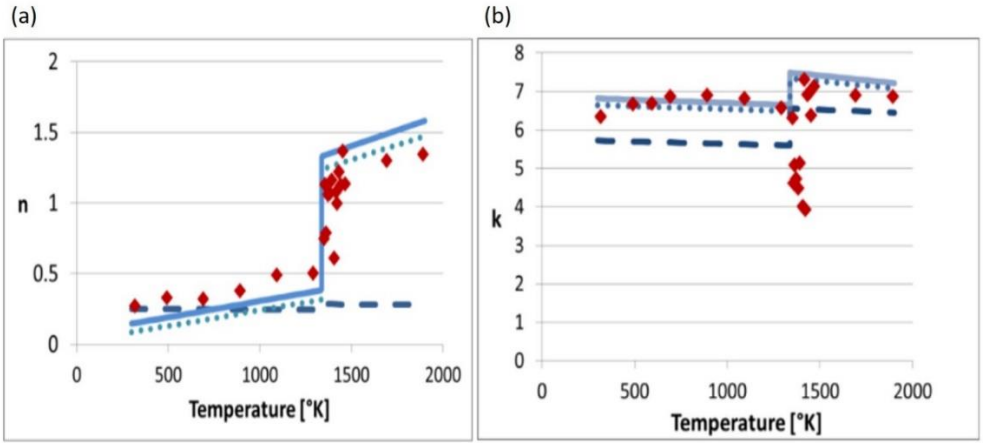

Figure 10. a) Refractive index n and b) absorption coefficient k of gold as a function of the temperature; comparing measurement (red diamonds) with three sets of calculated values from three models, presented in blue dotted line, blue dashed line, and blue straight line [57].

In most metals, a stable melt pool in the conduction mode has a flat surface which reflects most of the incident beam[68]. Figure 11 indicates the evolution of pure gold reflectivity with temperature, based on equation 1. Although R decreases in the liquid compared to the solid, it remains very high. For comparison, pure gold powder reflectivity is reported as 0.85 (with mean particle size of 24μm) in [69].

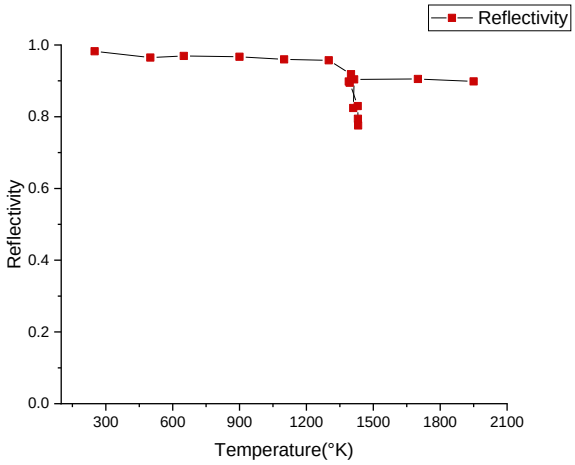

Figure 11. Reflectivity of surface polished pure gold as a function of temperature [57].

In laser processes, high energy density heat sources usually increase the temperature significantly beyond the melting point of metallic parts, with possible vaporization from the melt pool. At even higher energy densities, escaping vapor form the melt pool exerts a recoil force and; therefore, the laser would interact with a vapor plume. The vapor plume corresponds to a mixture of different hot gases which. Finally, due to

the interaction of the laser with this plume, laser induced plasma (LIP) can be formed due to the ionization of the vapor plume at higher temperatures.

The effect of the plasma on the total absorptivity of the laser depends on the characteristic of the formed plasma layer. At the first stage, when the LIP detaches from the melt pool, has a strong shielding effect and reduces the laser energy coming on the surface, due to laser beam defocusing [70]. Kawahito et al. [71] observed a decrease in total weld penetration due to the attenuation of the laser beam by plasma formation. At much higher laser intensities used for deep laser welding (108 W/cm^2), the plasma layer absorbs even more energy and acts like a black body [70]. For typical laser powder bed fusion parameters when the melt pool is in the conduction mode, the intensity of the laser is only a few MW/cm^2 and scanning speeds are faster than the ones used for welding processes, therefore, laser plasma absorption or interaction with vapor plumes do not play a significant role in total absorption of the beam [72,73]. However, for laser beams with higher energy densities, keyholes form and multiple reflections occur in the keyhole cavity: a metal liquid surface with a high reflectivity can then absorb most of the incident beam energy (see Figure 12) [19].

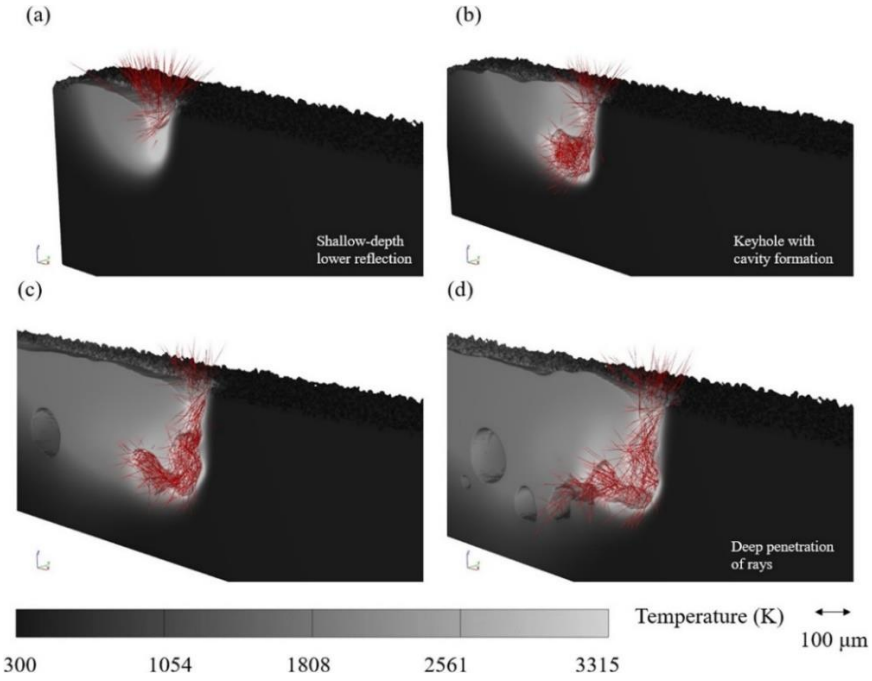

Figure 12. Temperature contours along with the reflected laser ray trajectories departing the free surface of the metallic phase: (a) t = 0.6 ms, (b) t = 1 ms, (c) t = 2 ms and (d) t = 3 ms. A significant number of rays are trapped due to complex keyhole shapes in (b)–(d). [74]

Ye et al. [72] studied the correlation between the melt pool depth and total absorptivity of the beam during laser processing of 316L samples using direct calorimetric measurements. Their results indicate that when

a keyhole is formed, by increasing the laser power, total absorptivity increases. The above mentioned results has been also confirmed by numerical simulation of the laser/keyhole interaction in different studies[74–77].

L-PBF shares some characteristics with other laser processing techniques such as laser welding. However, in the L-PBF process, the laser interacts with powders which have completely different responses from bulk solid materials in welding. Laser/powder interaction is also a function of the powder size distribution and layer thickness. In processes such as laser cutting, drilling, and welding, when a high power laser irradiates the surface of the material, a part of the beam energy is transferred to the piece by heat conduction. When dealing with powders, multiple scattering, and powder geometry effects play a major role in determining the effective optical properties [53]. These aspects have been studied both empirically and by numerical simulation. In primary studies, to simplify the situation, it has been assumed that powder is a homogeneous continuum body [51,79,80]. With a fine-scale model, Khairallah et al [53] consider the powder bed as a set of randomly distributed particles. Using a ray-tracing method, they indicate that the powder absorption is much larger than the value measured for a flat metal surface, because of multiple scattering. A real powder bed has a distribution of particle sizes and is not densely packed, which also has an influence on the total absorption. These aspects were taken into account in the rain-packing algorithm [81]. Simulations reveal that a flat surface or an isolated sphere has less absorptivity than a set of powder particles, which confirms the importance of multiple scattering effects (Figure 13).

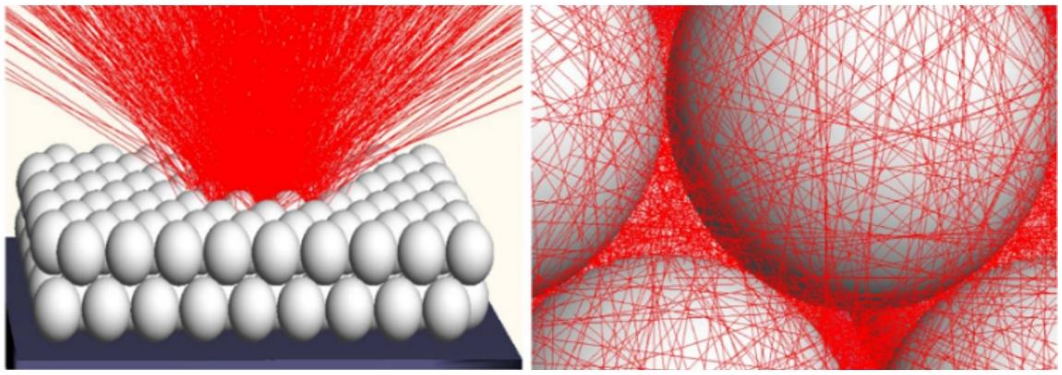

Figure 13. Multi-Scattering of a laser beam by powder particles[53].

When the beam undergoes multiple reflections inside the powder bed, the absorption coefficient is larger than that of a liquid surface[79]. Figure 13 shows the absorption value for stainless steel powders along a 1 mm laser path. Figure 14 indicates that the minimum absorption occurs when the beam strikes bigger particles, as these will reflect most of the light. Reversely, the maximum absorption happens when the laser

strikes the small powder particles. In other words, higher ratios of beam vs particle size increase the chance for multiple reflections, and therefore increase laser absorption [53].

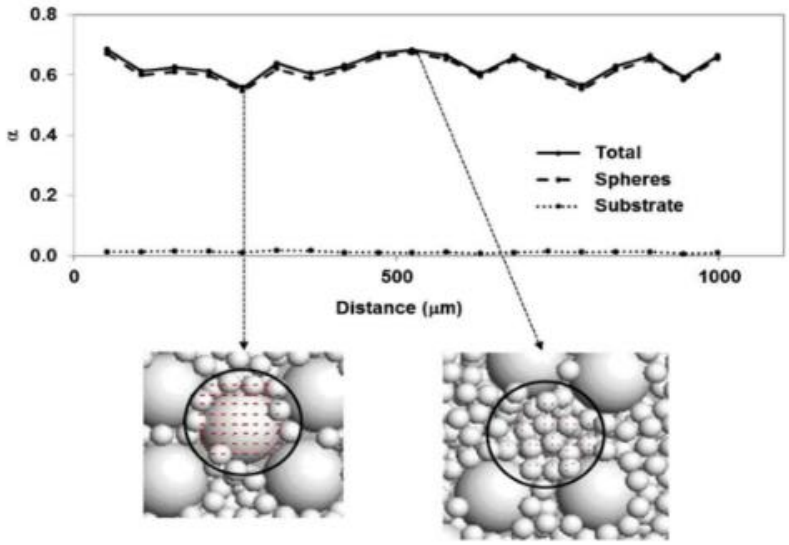

Figure 14. Absorption for a bimodal powder size distribution of 316L[53].

The effect of multiple reflections in the powder bed is more remarkable for materials with high reflectivity, like gold. For these materials, a penetration depth has to be taken into account inside the powder bed, effectively increasing the laser absorption compared to the bulk solid state[53,69]. An issue of metallic powders is the difficulty in dealing with reproducible shape, size, and geometry, as these tend to vary from one powder batch to another. These variations result in changing laser material interactions [82]. The importance of powder particles absorptivity has been highlighted mainly for highly reflective materials such as copper and gold alloy samples. Different attempts to increase the amount of absorbed light during laser manufacturing of copper powder can be mentioned: oxidizing copper powder surface[83], coating powders with other materials with higher absorptivity[84], and mixing them with carbon nanoparticles [85] . Klotz et al. [86,87] studied L-PBF of yellow gold alloys and analyzed the total porosity distributions in the samples. Alloying additions (Fe and Ge) and thermal heat treatments have been used to modify the optical reflectivity and, as a result, printability of the powders. The average porosity using untreated powder particles was in the order of 3% to 4%. With the use of thermal heat treatment and alloying, the final porosity could be decreased to 0.7% and 0.1–0.3%, respectively. Addition of Ge to yellow gold helped to lower the solidus temperature, which provided easier conditions to melt the material. Moreover, the addition of Fe increased the oxidation of the powder particles and, as a result, decreased their reflectivity.

2.2. Melt pool formation

One important issue in L-PBF is the time-consuming identification of a process window leading to quasi fully dense parts (> 99.8%), often based on trials and errors. This step usually needs to be repeated when working with a new material or a new machine. Thus, one of the main challenge in AM techniques, is finding ways to adjust optimized process parameters from one machine to another, or from one material to another. Different approaches are used to compare different process parameters. The Volume Energy Density (VED) is the most used method to compare the L-PBF process parameters between different materials and machines. The volume energy density is given by:

$$\mathrm{VED} = \frac{\alpha \,.\, \mathrm{P}}{\mathrm{V.h.L}} \tag{2}$$

where α is the material absorptivity, P the laser power (W), V the laser speed (m/s), h the hatching distance (m), and L the layer thickness (m).

Ciurana et al [88] used the VED to compare the quality of printed CoCrMo single tracks in their study and noticed that, in order to have a continuous and defect free single track, the value of the VED should be higher than 151 J/mm3. Similarly, Gong et al. [89] used the VED to find the optimal process parameters to print Ti-6Al-4V samples with high relative densities. Their results show that being in a precise and well chosen process parameter window leads to printing samples with low porosity content. In other words, at low VED values, they observed poor melting conditions in the samples and high number of large (Lack of Fusion) pores. On the other hand, at higher energy densities, they observed keyhole porosities in the printed samples.

Bertoli et al. [90] in their research on L-PBF of 316L samples showed that it is possible to get very different melt pool geometries for the same VED value. Indeed the VED does not consider all essential quantities, and it is well known that different sets of parameters in Equation (2) may lead to the same VED but different melt pool depths, which in turn leads to different part qualities (see Figure 15). In other words, there are not enough material related parameters in the VED equation, to use this quantity to scale process parameters from one material to another, or from one L-PBF machine to another [91].

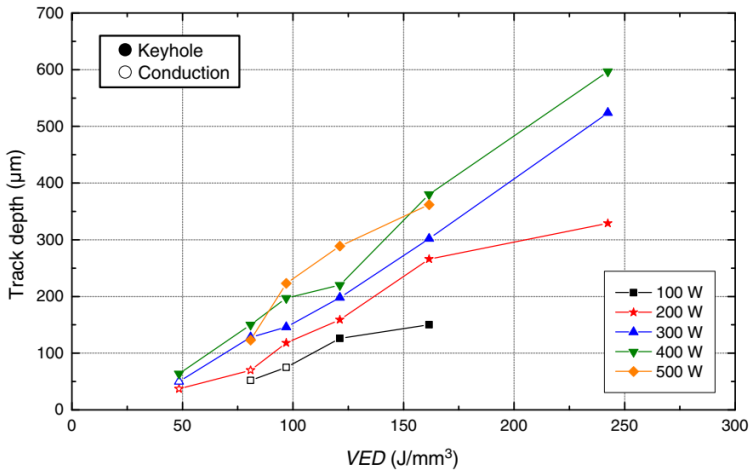

Figure 15. Melt pool depth against volume energy density values for printed 316L samples [90].

Using dimensionless numbers, Ion et al [17] developed diagrams for laser processing of different materials. q^* and V^* are the dimensionless power and speed numbers defined as :

$$q^* = \frac{\alpha P}{K\omega(T_m - T_0)} \tag{3}$$

$$V^* = \frac{V\omega}{D} \tag{4}$$

Where K is the thermal conductivity (W/m.K), ω the laser beam radius (m), and D the thermal diffusivity (m^2/s). Normalized experimental data have been plotted to define practical operating regions for different laser processes (heating, welding, surface treatments etc.).

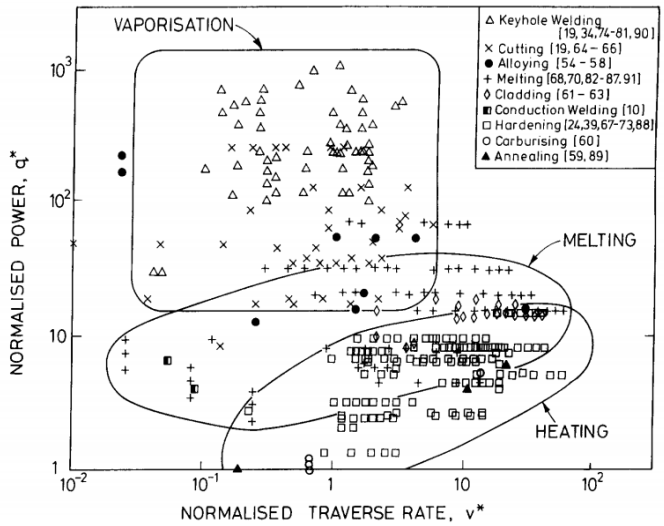

Figure 16. Group of data for different materials and processes plotted on dimensionless maps [17].

Sketched boundaries in Figure 16 enclose zones for each process group. These dimensionless maps are somehow independent of the materials and could be used to define process parameters that provide acceptable quality.

Thomas et al. [92] extended the approach proposed by Ion et al. and developed another dimensionless diagrams for AM processes. L-PBF introduces new parameters compared to other processes (welding, heat treatment, polishing, cutting, etc.), such as the layer thickness (l) and the hatch spacing (h). Equations 5 and 6 represents dimensionless laser beam power (q^*) and dimensionless hatch distance ($1/h^*$), respectively.

$$q^* = \left[\frac{Aq}{2vlr_B}\right]\left[\frac{1}{\rho C_p (T_m - T_0)}\right] \tag{5}$$

$$1/h^* = \frac{r_B}{h} \tag{6}$$

where A is the surface absorptivity, q is the laser power, v is the scanning speed, l is the layer thickness, r_B is the beam radius, ρ is the density, T_m and T_0 are the respective melting and initial temperatures of the material, and h is the hatch spacing.

Similarly to the previous map, different zones with special features are positioned based on dimensionless numbers (figure 17).

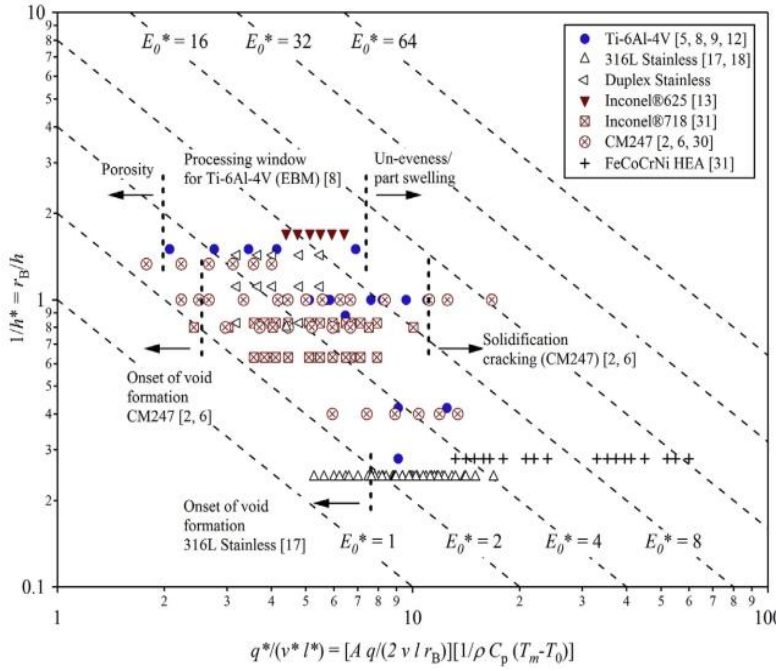

Figure 17. Normalized processing map (dimension less hatch distance vs dimensionless laser beam power) for additive manufacturing of different alloys. Process parameters are extracted from literature [92].

These types of graphs are useful tools to quantify different regimes in different laser processes such as welding, heating, cutting, and cladding. However, most of them fail to provide a solution for scaling optimized process parameters from one material to another.

The keyhole formation threshold has been suggested in different studies as a fundamental approach to find optimum processing conditions [93–99]. Hann et al. [96] introduced dimensionless normalized enthalpy/melt pool graphs to locate the transition zone between the conduction mode and the keyhole mode in laser welding. Equations 7 and 8 represent the normalized enthalpy and normalized melt pool depth.

$$\overline{\Delta H} = \frac{\Delta H}{\Delta h} = \frac{\alpha P}{\rho(C\Delta T + L_m)\sqrt{\pi\omega^3 VD}} \tag{7}$$

$$\bar{d} = \frac{d}{\omega} \tag{8}$$

In these equations, ρ is the density($\frac{kg}{m^3}$), C the specific heat($\frac{J}{kg.K}$), ΔT the difference between the melting and initial temperature (K), L_m the latent heat of melting($\frac{kJ}{kg}$), and d the melt pool depth (m). The normalized enthalpy considers an energy balance between the input energy and the dissipated energy during laser processing. By plotting the normalized melt pool depth as a function of the normalized enthalpy , Hann et al. [96] observed similar behaviors for different materials (see Figure 18). In the conduction mode, the slope of the curve is moderate. At higher energy densities, due to keyhole formation, the slope dramatically increases. Optimal conditions therefore lie in a transition zone between the two modes, while at lower energy densities incomplete melting of powders leads to lack of fusion porosities. Figure 19 indicates that the dimensionless weld depths $\bar{d}$ (here denoted δ) are consistent for 304 steel welds which have been produced with similar normalized enthalpy values $\Delta H/\Delta h$ (here denoted $\Delta H/h_s$).

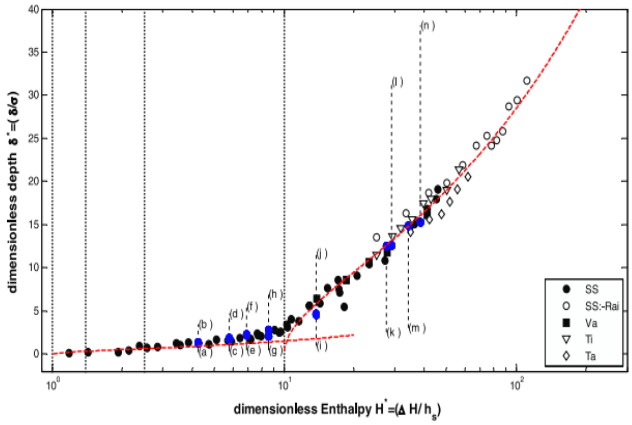

Figure 18. Dimensionless graph indicating the normalized melt pool depth $\bar{d}$ as a function of the normalized enthalpy ΔH/Δh for the laser welding process, and considering different metals and alloys[96].

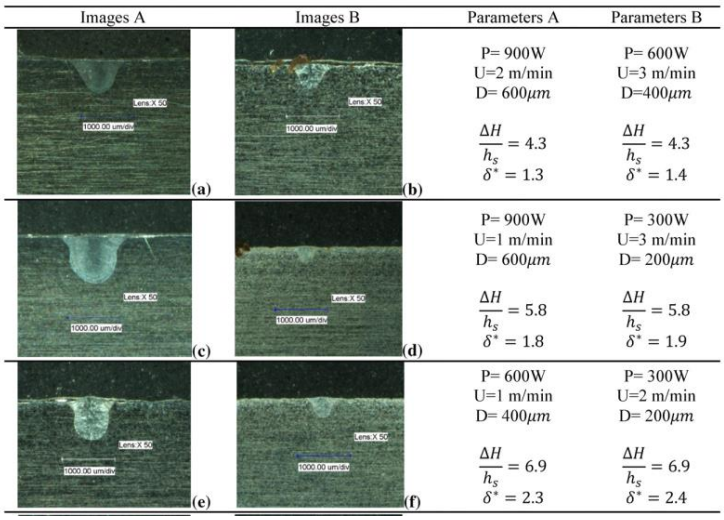

Figure 19. Sample images of 304 steel laser welds conducted with different parameters (laser powder, scan speed, and laser beam size) but the same normalized enthalpy value ΔH/hs (=ΔH/Δh). The results indicate also comparable normalized melt pool depth values δ^* (=$\bar{d}$) [96].

These efforts are devoted to prevent defects formation in the printed samples, and for most of them, the initial concept usually comes from the welding science. But whereas in welding we are usually dealing with single tracks and simple geometries, in AM technologies, the number of tracks and complexity of the printing geometries is much higher, which makes difficult to manufacture samples that meet qualification standards. Process parameters need to be optimized for different sample sizes and geometries with different pathways for heat transfer. Figure 20 indicates some defects that lead to dimensional inaccuracy of the

printed samples. The microstructure and mechanical properties of the printed samples are also affected by size and geometry. J. Yu et al. [100] observed size dependence in the yield strength of additively manufactured 316L samples. As the width of printed tensile samples decreases, the yield strength continuously increases. In smaller samples, the effect of the contour tracks become increasingly important. Contour scanning is usually essential when high dimensional accuracy is required. In the contour scanning, the laser remelts already solidified layers; therefore, solidification rates are faster in the second melting compared to the first one, which leads to grain refinement.

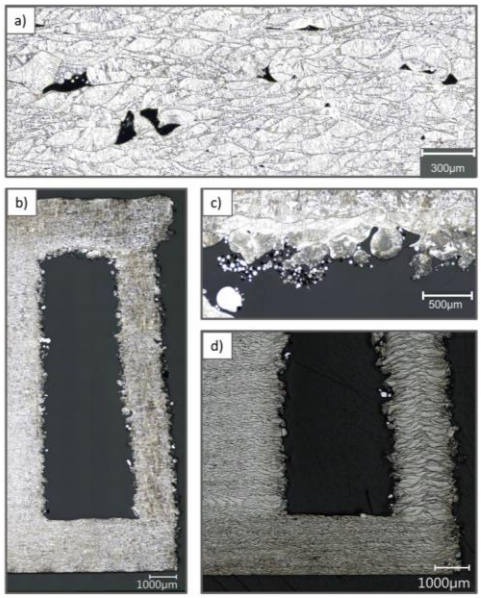

Figure 20. Examples of defects in printed samples, such as a) porosities in the bulk region, b) warping of a thin wall, c) balling defects at flat overhang, and d) enlarged melt pool depth in a thin wall region [101].

Numerical simulations could be an option to determine the optimal process parameters before printing parts with different sizes. However, full scale numerical simulations of the manufacturing process is time consuming. Druzgalski et al. [101] developed an algorithm which identifies the geometry of the sample in 2D and 3D and adjusts the process parameters (mainly the laser power) in the different zones (Figure 21). The main objective is to reach a consistent layer-to-layer average surface temperature.

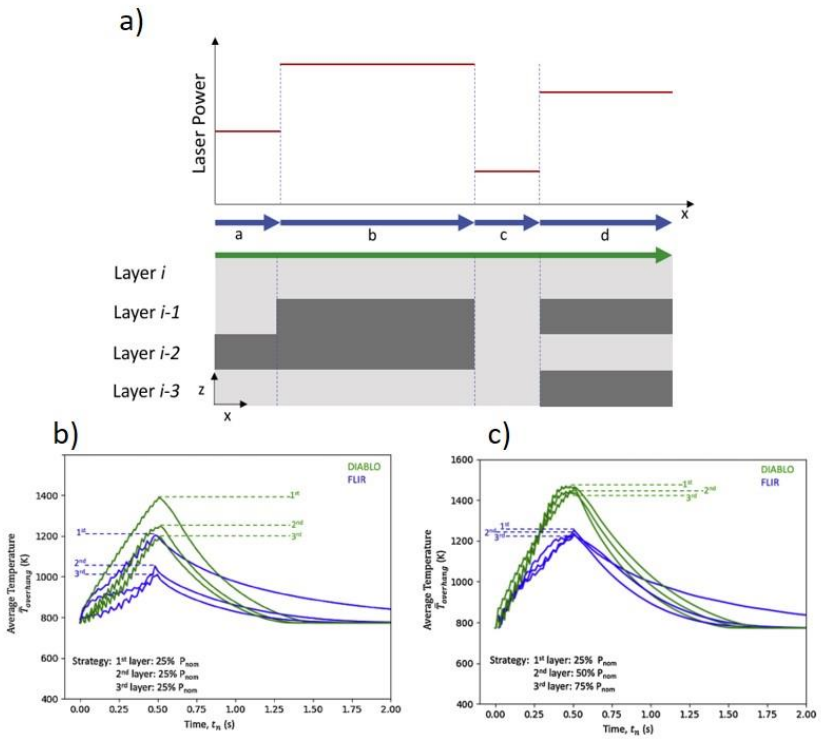

Figure 21. a) The laser power is adjusted throughout a weld line to accommodate different local thermal conditions. Average surface temperature of 1st, 2nd, and 3rd layers are predicted from thermal simulations (green lines) and measured experimentally with an in situ FLIR camera (blue lines), and plotted in b) and c). (b) Without the control strategy, the average surface temperature decreases with subsequent layers. (c) With the control strategy the objective of maintaining a consistent layer-to-layer average temperature is achieved[101].

Stathatos et al. [102] regulated the temperature by adapting the laser power during scanning of a complex linear geometry. Using a constant laser power, different shapes of the laser path can cause instabilities on the maximum temperature. In their study, they used finite element simulations to train an artificial neural network to predict the maximum temperature, and gradually modify the laser power (Figure 22).

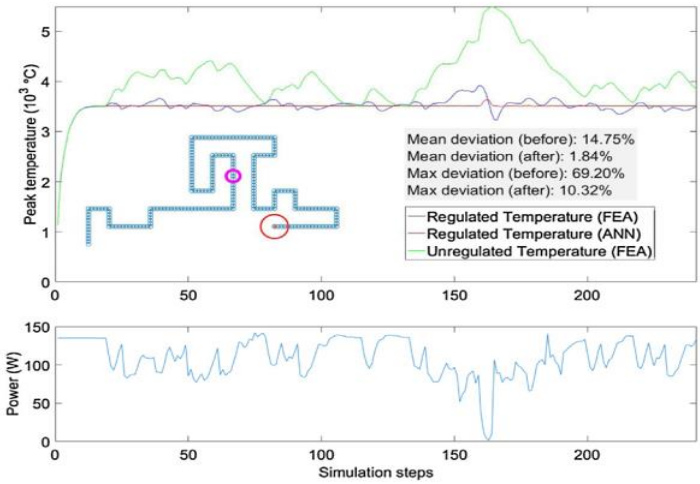

Figure 22. Temperature regulation based on the peak temperature using ANN (Artificial neural network) FEA (Finite element model) [102].

2.3. Residual stresses and phase transformations

The total porosity content in parts built by L-PBF is an important criterion to achieve an acceptable quality standard. The formation of defects such as porosities and cracks can significantly decrease the final mechanical properties, and should therefore be minimized. From the metallurgical point of view, L-PBF is a very complex process, in which melting and solidification rates are high, leading to large thermal gradients. Complex thermal cycles result from scans on hundreds of layers, involving consolidation phenomena, remelting of the previous layer(s), and reheating of the already solidified layers. The combination of thermal gradients and large degree of shrinkage occurring during liquid - solid transformations creates high residual stresses and non-uniform microstructures in the printed samples, which may favor crack formation [103–105].

Most of the Ni-based superalloys are susceptible to cracking during additive manufacturing (AM), which hampers their widespread industrial adoption. Different studies have been conducted on the additively manufactured precipitation strengthened Ni-based superalloys [34–39]. Carter et al. [37] observed columnar grain structures along the building direction of the printed CM247LC samples. The DDC mechanism has been diagnosed as the main cracking mechanism, with most of the observed cracks growing in highly misoriented grains. Similar columnar grain structures have been observed by Cloots et al. [106]. Numerous cracks have been detected transverse to the laser scan direction, and SEM image analysis indicated a dendritic structure of solidification cracking. The cracking was attributed to Zr segregation at grain boundaries, as Zr is known to be a solidus depressant.

Based on crack face morphology analysis, Chauvet et al.[107] suggested solidification cracking occurs in the Ni-Co-Cr-Mo-Al-Ti-B superalloy manufactured by electron beam powder bed fusion technique (E-PBF). Segregation of B increases the solidification range in this alloy and increases the susceptibility of the alloy to solidification cracking. Atom Probe Tomography (APT) revealed the presence of this element on the grain boundaries. Constitutional undercooling during the solidification of the melt pool of Ni-based superalloys can lead to formation of low melting point in grain boundaries. When the next layers are applied, these phases melt locally in the HAZ of the sample, resulting in cracking in the presence of tensile residual stress. This cracking mechanism has been studied in limited number of studies, as it is hard to distinguish it from solidification cracking. However, it has been suggested that at higher energy density values, as the volume of HAZ increases, the liquation cracking mechanism is more active[108]. Coming back to LPBF of CM247LC, Carter et al [37] printed cuboidal samples with different energy densities and showed that, at high values, crack walls have dendritic structures which indicate solidification cracking (Figure 23a, and b). On the other hand, at lower values, they noticed that most of the cracks have smooth walls and are

elongated along the building direction with carbide precipitates in the vicinity of the cracks, which is indicative of the DDC mechanism (Figure 23c, and d).

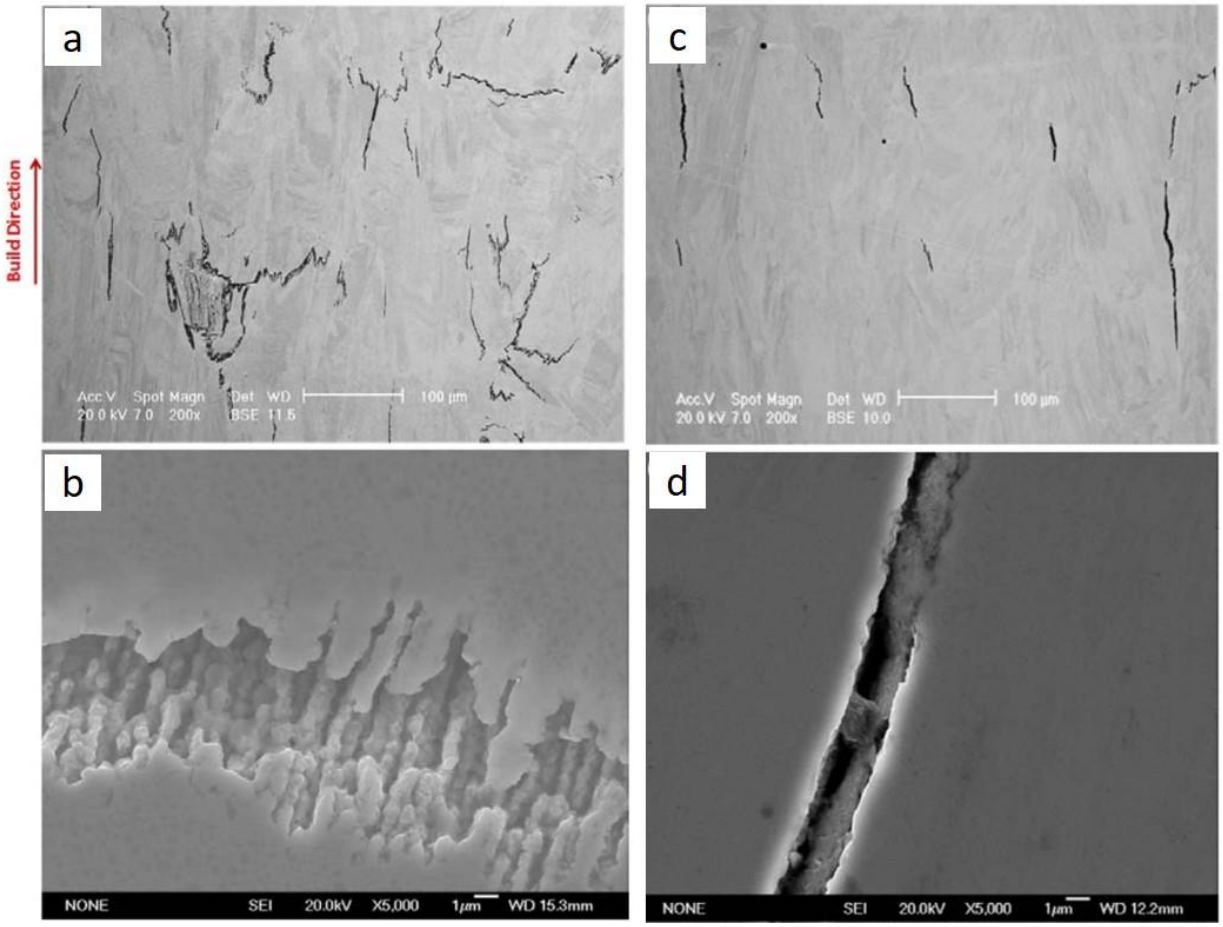

Figure 23. a) Optical image of cracks in CM247LC printed with high energy density, b) a higher magnification shows a dendritic shape of the crack walls. c) Micrograph showing cracks when printing with a low energy density, d) zoom on the cracks clean edges indicating solid state cracking [37].

Prasad et al. [109] observed variations in crack density in printed Hastelloy X samples, as a result of changes in printing energy density. They show that there is higher chance for crack formation at higher energy density values, due to increased residual stresses.

A few studies have been conducted to mitigate cracking in Ni-based superalloys through process modification, and mainly focused on the effect of preheating and scanning strategies. Ramsperger et al.[110] applied high temperature preheating (1040 °C) on the base plate and managed to print crack-free CMSX-4 cubes manufactured by E-PBF. Hagedorn et al.[111] used the same approach for the L-PBF process and obtained crack-free CM247LC samples by preheating the substrate to 1200 °C. The results of these studies

confirm that preheating the build plate is an effective solution to print crack free Ni-based superalloys; however, this approach is mainly limited to the E-PBF process, since providing such a high preheating temperature is complicated in most L-PBF machines. Carter et al.[38] investigated the influence of scan strategy on L-PBF fabricated CM247LC and found that a simple back and forth scan strategy resulted in a homogenous microstructure that was less susceptible to cracking compared to island scanning strategy

The effect of AM process parameters on microstructures is also of interest for bulk metallic glass alloys. Sohrabi et al. [112] cladded a layer of Zr-based metallic glass (MG) on an aluminum baseplate using laser additive manufacturing (AM) . Hardness test results presented in Figure 24, indicate a significant increase in the coated layer hardness values by increasing the laser power. Microstructural observation reveal that increasing the energy density increased the melt pool and the HAZ sizes, thereby promoting crystallization and higher hardness.

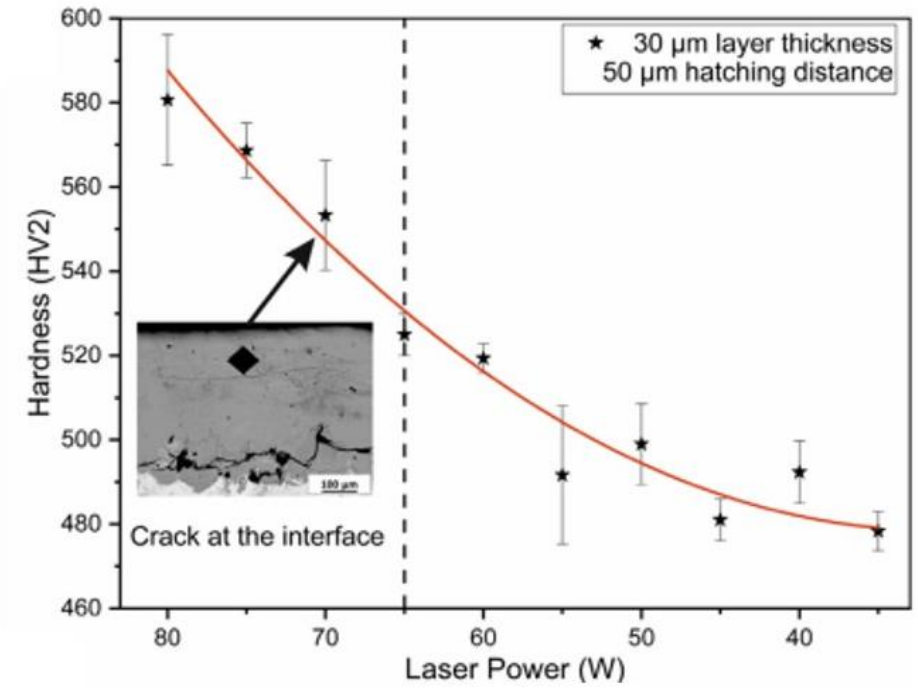

Figure 24. Effect of laser power on the hardness (HV2) values of a bulk metallic glass coating, at fixed layer thickness and hatching distance [112].

Order-disorder phase transformations in red gold alloys is another interesting feature which will be investigated in this thesis. In Au-Cu alloys around 50 at% Cu (Figure 25), the alloy goes through an order-

disorder phase transformation at 410°C [113]. The stable high temperature phase is a disordered cubic phase (α), while below 410 °C, an ordered tetragonal phase forms (AuCuI).

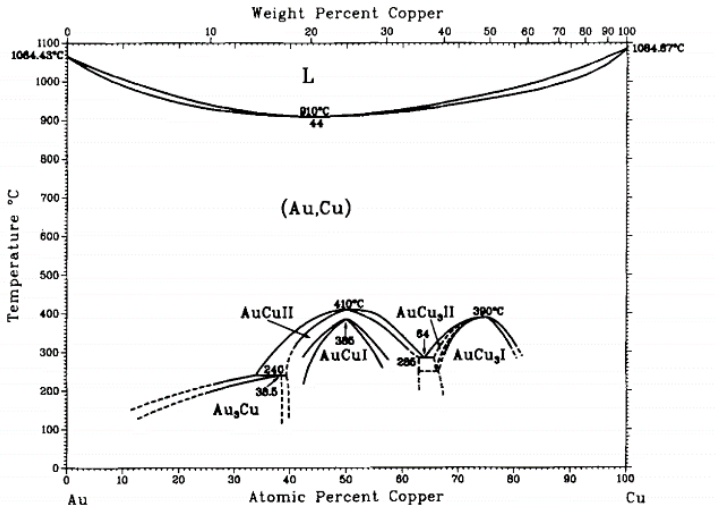

Figure 25. Phase diagram Au-Cu [113]

The disordered lattice is a face centered cubic (FCC) A1 lattice with gold and copper atoms randomly distributed on the atomic sites. The ordered phase with a tetragonal lattice is a $L1_0$ structure with alternate (002) planes of gold and copper atoms (Figure) [114].

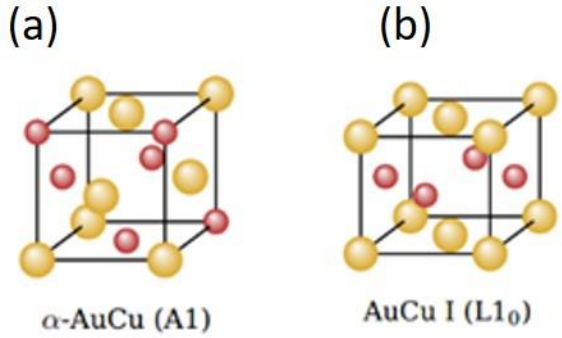

Figure 26. Cubic and tetragonal lattices in equiatomic AuCu [114]

The ordered phase significantly hardens the material, and this feature is beneficial for watch and jewelry applications where resistance against scratch is desired. The ordering transformation in gold alloys has been investigated in different studies since the middle of the 20th century, to understand the temperature ranges in which this transformation occurs [115–117]. Kuczynsky and et al. [118] also studied the kinetics of

ordering of AuCu through resistivity measurements and metallography. The kinetics was found to significantly depend on temperature and on the previous annealing treatment. Recently, the effect of plastic deformation and the thermo-mechanical history on the ordering phase transformation and its kinetic have been detailed[119,120]. In addition, the effect of stress on variant selection during the $A1 \rightarrow L1_0$ (disorder-order) transformation has been investigated[121–123]. All studies were however performed on cast samples, i.e. the $A1 \rightarrow L1_0$ phase transformation in additively manufactured red-gold alloy has never been studied so far. Fast heating and cooling rates during the L-PBF process, and reheating cycles inherent to AM, in combination with residual stresses in as-built samples, make red-gold alloys susceptible to partially undergo phase transformation during processing or post-processing.

Chapter 3: Scope of the thesis

In this chapter, we define the statement and the main objectives of the thesis. The proposed structure follows.

3.1. Thesis outline and objectives

In the context of this PhD, we propose to treat the following question:
«Why is it important to understand the thermomechanical treatments induced by L-PBF, and how does it help to control the final microstructure/properties? »
The thermal history plays an important role on the final microstructure and the state of stress of the printed parts. Crack formation in Ni-based super alloys, and phase transformations in red gold alloys are examples of microstructure evolutions related to thermal cycles induced by the L-PBF process.

The proposed methodology consists in analyzing the L-PBF process at different scales, to understand and quantify the thermomechanical conditions operating during the process, and their influence on microstructures and properties.
The laser beam interacts with powders particles, which behave differently from bulk solid materials. Therefore, Chapter 4 starts by investigating the “micro scale” (a few tenth of microns), looking at parameters like absorptivity and thermal conductivity in the powder bed and in the liquid, and thermodynamic quantities like the material enthalpy. Processing parameters induce various laser dwelling times and operating temperature distributions in the part, which will affect the amount of liquid and the melt pool geometry in the steady state.
The “meso scale” (typically a few hundreds of microns) study, involving dedicated numerical finite element simulations, is then needed to predict the melt pool formation and to find the optimal processing conditions. This predictive modelling approach helps, in a second step, defining a translation rule, capable of adjusting processing parameters for new materials and L-PBF machines (Chapters 4, 5).

Melt pool geometry and temperature distribution during manufacturing provide the tools to a better understanding and control of microstructures and stresses, defined at the “macro scale” (a few mm) (Chapters 6-10).

Summarizing the scope of the thesis, we propose a multiscale journey, going from laser/matter interaction to the effects of process parameters on the melt pool formation, to thermal histories during the manufacturing process. The latter are used to understand and better control phenomena such as cracking in the CM247LC alloy, and phase transformations in red-gold alloys. These two phenomena indeed relate directly to the thermal cycles and stress states induced by the process.

The thesis contains 11 chapters, and is constructed in a cumulative manner, from seven distinct paper manuscripts, which have been published, submitted, or are about to be submitted to international peer-reviewed journals.

Chapter 1 – Introduction.

This chapter provides a short introduction to AM techniques, and more precisely to the L-PBF process, with its main applications and characteristics. Selected topics related to the L-PBF process are discussed such as to provide the background for subsequent chapters.

Chapter 2 – State of the art.

This chapter describes some of the literature knowledge related to the micro, meso and macro scales previously defined and inherent to the LPBF process. The chapter should help the reader understanding the context in which the seven papers have been written.

Chapter 3 – Scope of the thesis

This chapter presents the thesis objectives and its structure. The multiscale approach is illustrated with Figure 27, giving at the same time the outline of the thesis.

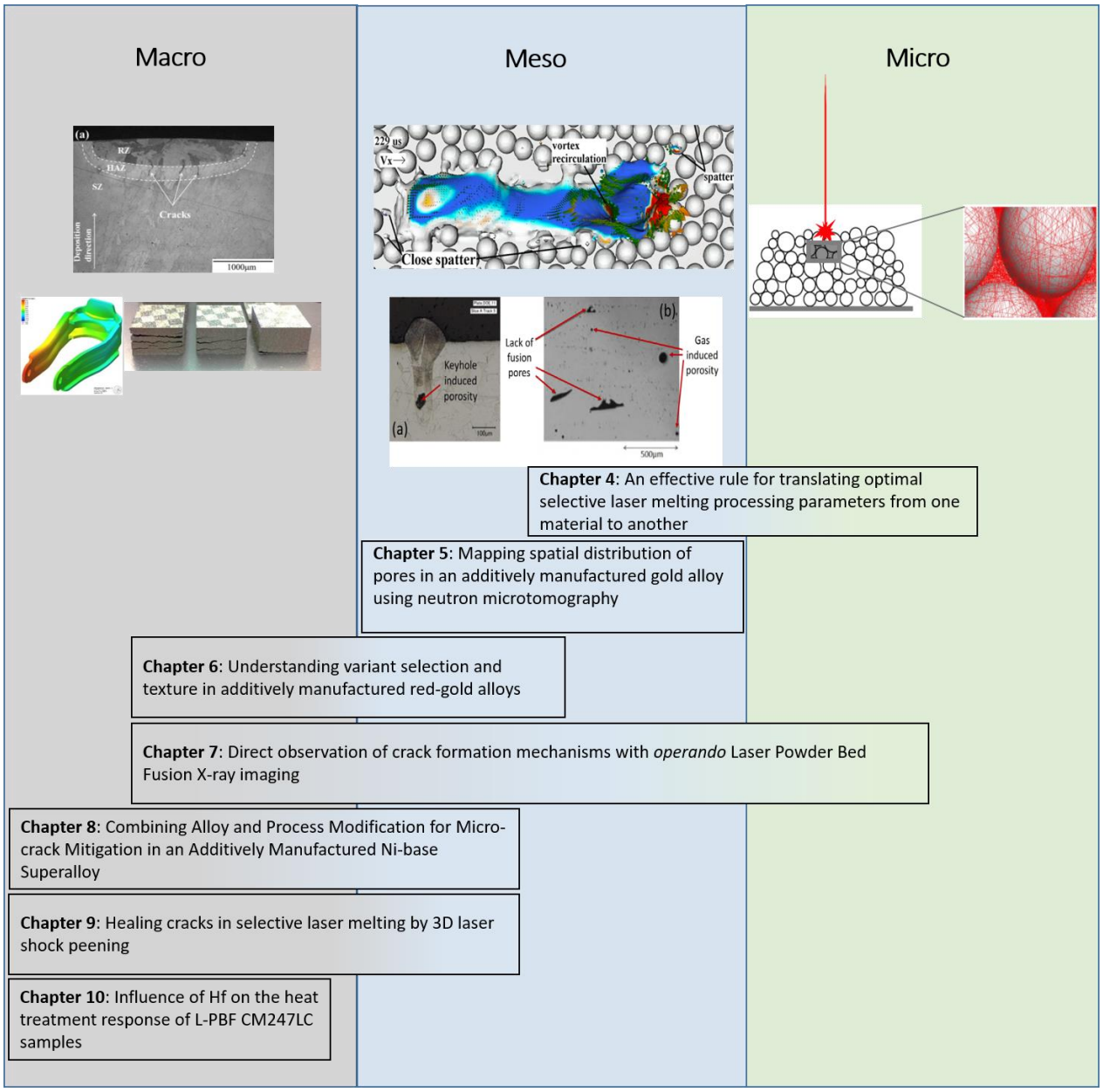

Figure 27. Thesis outline and chapters structure schematically represented. Images in this figure are taken from [53,124–127].

Chapter 4 – An effective rule for translating optimal selective laser melting processing parameters from one material to another

The primary goal of this chapter is to derive a "translation rule" in order to adjust optimal process parameters from one material to another. Laser/powder interaction is described by the powder absorptivity, a key parameter which takes into account a number of powder particles properties (chemical composition, surface

roughness, powder morphology, and size distribution) and helps identify different melt pool regimes during the manufacturing process. The translation rule itself is built on the notion of normalized enthalpy.

Chapter 5 – Mapping Spatial Distribution of Pores in an Additively Manufactured Gold Alloy Using Neutron Microtomography

Both 2D cross sections and a 3D nondestructive characterization technique are used to evaluate the porosity content of printed red gold samples. Neutron tomography is used to visualize the distribution of pores with 10 μm spatial resolution. In addition, imaging with neutrons proves to be an interesting alternative technique to X-rays, when the latter have a too small penetration depth. This is the case for gold alloys, known to be quasi opaque to X-Rays.

Chapter 6 – Understanding variant selection and texture in additively manufactured red-gold alloys

Order-disorder phase transformations are other examples of metallurgical evolutions occurring in additive manufacturing or during post-processing. In this chapter, we investigate the effect of the stress state induced by LPBF on variant selection during the disorder-order transformation in red-gold samples with different types of post processing (as-built, Laser Shock Peened (LSP), and annealed samples). It is concluded that the stress state at the early stages of the transformation is the one which will dictate the final texture.

Chapter 7 – Direct observation of crack formation mechanisms with *operando* Laser Powder Bed Fusion X-ray imaging

High-speed synchrotron X-ray imaging in combination with a miniaturized L-PBF set-up that reproduces real processing conditions are utilized to study the cracking mechanisms during manufacturing of the CM247LC alloy. Complementary post-mortem inspection of crack morphology, and thermal simulations supported by *operando* X-ray diffraction-based measurements are combined such as to better understand the cracking mechanisms.

Chapter 8 (supplementary chapter) - Combining Alloy and Process Modification for Micro-crack Mitigation in an Additively Manufactured Ni-base Superalloy

Micro-crack mechanisms occurring during manufacturing of the CM247LC alloy are reviewed, and the effects of the process parameters and chemical composition are analyzed. Both numerical and physical simulations (using a Gleeble machine) are conducted in order to reveal the active cracking mechanisms.

Chapter 9 (supplementary chapter) - Healing cracks in selective laser melting by 3D laser shock peening

Understanding the main cracking mechanisms occurring during LPBF in relation to processing parameters lead to different solutions for reducing cracking in the CM247LC alloy. This chapter indicates how 3D Laser Shock Peening (LSP) can be one of them, significantly reducing the amount of cracks in L-PBF CM247LC samples.

Chapter 10 (supplementary chapter) - Influence of Hf on the heat treatment response of additively manufactured Ni-base superalloy CM247LC (paper 6)

In previous chapters, segregation of Hf during the L-PBF process and its effects on the solidification range of CM247LC have been discussed. Modifying the chemical composition can be one approach leading to a reduction in crack density of up to 98 %. In this chapter, different heat treatments and mechanical tests are conducted to investigate the effect of Hf removal in this alloy.

Chapter 11 – Conclusions and future perspectives.

The main results and achievements presented during the thesis are summarized in this chapter. Finally, potential paths for further research in this field are proposed.

References:

[1] G.N. Levy, R. Schindel, J.P. Kruth, Rapid manufacturing and rapid tooling with layer manufacturing (LM) technologies, state of the art and future perspectives, CIRP Ann. - Manuf. Technol. 52 (2003) 589–609. doi:10.1016/S0007-8506(07)60206-6.

[2] T.T. Wohlers, W. Associates, R.I. Campbell, T. Caffrey, Wohlers Report 2016: 3D Printing and Additive Manufacturing State of the Industry : Annual Worldwide Progress Report, Wohlers Associates, 2016. https://books.google.ch/books?id=YHUJkAEACAAJ.

[3] K. Kempen, E. Yasa, L. Thijs, J.-P. Kruth, J. Van Humbeeck, Microstructure and mechanical properties of Selective Laser Melted 18Ni-300 steel, Phys. Procedia. 12 (2011) 255–263. doi:https://doi.org/10.1016/j.phpro.2011.03.033.

[4] K. Kempen, L. Thijs, J. Van Humbeeck, J. Kruth, Mechanical properties of AlSi10Mg produced by Selective Laser Melting, 39 (2012) 439–446. doi:10.1016/j.phpro.2012.10.059.

[5] A.N. Ag, AMPOWER REPORT 2020 - Additive manufacturing Management Summary, AMPOWER GmbH % Co. KG. (2020).

[6] D. Gu, Y.-C. Hagedorn, W. Meiners, G. Meng, R.J.S. Batista, K. Wissenbach, R. Poprawe, Densification behavior, microstructure evolution, and wear performance of selective laser melting processed commercially pure titanium, Acta Mater. 60 (2012) 3849–3860. doi:https://doi.org/10.1016/j.actamat.2012.04.006.

[7] O. Yilmaz, A.A. Ugla, Shaped metal deposition technique in additive manufacturing: A review, Proc. Inst. Mech. Eng. Part B J. Eng. Manuf. 230 (2016) 1781–1798. doi:10.1177/0954405416640181.

[8] C.Y. Yap, C.K. Chua, Z.L. Dong, Z.H. Liu, D.Q. Zhang, L.E. Loh, S.L. Sing, Review of selective laser melting: Materials and applications, Appl. Phys. Rev. 2 (2015) 0–21. doi:10.1063/1.4935926.

[9] U. Scipioni Bertoli, A.J. Wolfer, M.J. Matthews, J.P.R. Delplanque, J.M. Schoenung, On the limitations of Volumetric Energy Density as a design parameter for Selective Laser Melting, Mater. Des. 113 (2017) 331–340. doi:10.1016/j.matdes.2016.10.037.

[10] K.G. Prashanth, S. Scudino, T. Maity, J. Das, J. Eckert, Is the energy density a reliable parameter for materials synthesis by selective laser melting?, Mater. Res. Lett. 5 (2017) 386–390. doi:10.1080/21663831.2017.1299808.

[11] J. Mutua, S. Nakata, T. Onda, Z. Chen, Optimization of selective laser melting parameters and in fl

uence of post heat treatment on microstructure and mechanical properties of maraging steel, Mater. Des. 139 (2018) 486–497. doi:10.1016/j.matdes.2017.11.042.

[12] E. Liverani, S. Toschi, L. Ceschini, A. Fortunato, Effect of selective laser melting (SLM) process parameters on microstructure and mechanical properties of 316L austenitic stainless steel, J. Mater. Process. Tech. 249 (2017) 255–263. doi:10.1016/j.jmatprotec.2017.05.042.

[13] W.M. Tucho, V.H. Lysne, H. Austbø, A. Sjolyst-kverneland, Investigation of effects of process parameters on microstructure and hardness of SLM manufactured SS316L, J. Alloys Compd. 740 (2018) 910–925. doi:10.1016/j.jallcom.2018.01.098.

[14] A. Sola, A. Nouri, Microstructural porosity in additive manufacturing: The formation and detection of pores in metal parts fabricated by powder bed fusion, J. Adv. Manuf. Process. 1 (2019) e10021. doi:10.1002/amp2.10021.

[15] Y. Zhang, L. Wu, X. Guo, S. Kane, Y. Deng, Y.-G. Jung, J.-H. Lee, J. Zhang, Additive Manufacturing of Metallic Materials: A Review, J. Mater. Eng. Perform. 27 (2018) 1–13. doi:10.1007/s11665-017-2747-y.

[16] K. Zeng, D. Pal, B.E. Stucker, A Review of Thermal Analysis Methods in Laser Sintering and Selective Laser Melting, Proc. Solid Free. Fabr. Symp. (2012) 796–814. http://utwired.engr.utexas.edu/lff/symposium/proceedingsArchive/pubs/Manuscripts/2012/2012-60-Zeng.pdf%5Cnhttp://utwired.engr.utexas.edu/lff/symposium/proceedingsArchive/pubs/Table of Contents/2012_TOC.cfm.

[17] J.C. Ion, H.R. Shercliff, M.F. Ashby, Diagrams for laser materials processing, Acta Metall. Mater. 40 (1992) 1539–1551. doi:10.1016/0956-7151(92)90097-X.

[18] A.A. Martin, N.P. Calta, S.A. Khairallah, J. Wang, P.J. Depond, A.Y. Fong, V. Thampy, G.M. Guss, A.M. Kiss, K.H. Stone, C.J. Tassone, J. Nelson Weker, M.F. Toney, T. van Buuren, M.J. Matthews, Dynamics of pore formation during laser powder bed fusion additive manufacturing, Nat. Commun. 10 (2019) 1–10. doi:10.1038/s41467-019-10009-2.

[19] H. Ki, P.S. Mohanty, J. Mazumder, Multiple reflection and its influence on keyhole evolution, J. Laser Appl. 14 (2002) 39–45. doi:10.2351/1.1449885.

[20] R. Rai, G.G. Roy, T. Debroy, A computationally efficient model of convective heat transfer and solidification characteristics during keyhole mode laser welding, J. Appl. Phys. 101 (2007). doi:10.1063/1.2537587.

[21] G.K. Lewis, E. Schlienger, Practical considerations and capabilities for laser assisted direct metal deposition, Mater. Des. 21 (2000) 417–423. doi:10.1016/S0261-3069(99)00078-3.

[22] P. Mercelis, J.P. Kruth, Residual stresses in selective laser sintering and selective laser melting, Rapid Prototyp. J. 12 (2006) 254–265. doi:10.1108/13552540610707013.

[23] O. Fergani, F. Berto, T. Welo, S.Y. Liang, Analytical modelling of residual stress in additive manufacturing, Fatigue Fract. Eng. Mater. Struct. 40 (2017) 971–978. doi:10.1111/ffe.12560.

[24] X. Song, M. Xie, F. Hofmann, T. Illston, T. Connolley, C. Reinhard, R.C. Atwood, L. Connor, M. Drakopoulos, L. Frampton, A.M. Korsunsky, Residual stresses and microstructure in Powder Bed Direct Laser Deposition (PB DLD) samples, Int. J. Mater. Form. 8 (2015) 245–254. doi:10.1007/s12289-014-1163-1.

[25] A. V. Gusarov, M. Pavlov, I. Smurov, Residual stresses at laser surface remelting and additive manufacturing, Phys. Procedia. 12 (2011) 248–254. doi:10.1016/j.phpro.2011.03.032.

[26] J. Ding, P. Colegrove, J. Mehnen, S. Ganguly, P.M.S. Almeida, F. Wang, S. Williams, Thermo-mechanical analysis of Wire and Arc Additive Layer Manufacturing process on large multi-layer parts, Comput. Mater. Sci. 50 (2011) 3315–3322. doi:10.1016/j.commatsci.2011.06.023.

[27] F. Brückner, D. Lepski, E. Beyer, Modeling the Influence of Process Parameters and Additional Heat Sources on Residual Stresses in Laser Cladding, J. Therm. Spray Technol. 16 (2007) 355–373. doi:10.1007/s11666-007-9026-7.

[28] B. Vranchen, Study of Residual Stresses in Selective Laser Melting, (2016). https://lirias.kuleuven.be/bitstream/123456789/542751/1/thesis+Bey+Vrancken+v01-06-2016+FINAL-compressed.pdf.

[29] J.-P. Kruth, J. Deckers, E. Yasa, R. Wauthlé, Assessing and comparing influencing factors of residual stresses in selective laser melting using a novel analysis method, Proc. Inst. Mech. Eng. Part B J. Eng. Manuf. 226 (2012) 980–991. doi:10.1177/0954405412437085.

[30] V. Manvatkar, A. De, T. DebRoy, Spatial variation of melt pool geometry, peak temperature and solidification parameters during laser assisted additive manufacturing process, Mater. Sci. Technol. 31 (2015) 924–930. doi:10.1179/1743284714Y.0000000701.

[31] V. Manvatkar, A. De, T. Debroy, Heat transfer and material flow during laser assisted multi-layer additive manufacturing, J. Appl. Phys. 116 (2014) 1–8. doi:10.1063/1.4896751.

[32] H.L. Wei, J. Mazumder, T. DebRoy, Evolution of solidification texture during additive manufacturing, Sci. Rep. 5 (2015) 1–7. doi:10.1038/srep16446.

[33] T.G. Spears, S.A. Gold, In-process sensing in selective laser melting (SLM) additive manufacturing, (2016). doi:10.1186/s40192-016-0045-4.

[34] V.D. Divya, R. Muñoz-Moreno, O.M.D.M. Messé, J.S. Barnard, S. Baker, T. Illston, H.J. Stone, Microstructure of selective laser melted CM247LC nickel-based superalloy and its evolution through heat treatment, Mater. Charact. 114 (2016) 62–74. doi:10.1016/j.matchar.2016.02.004.

[35] N. Kalentics, N. Sohrabi, H.G. Tabasi, S. Griffiths, J. Jhabvala, C. Leinenbach, A. Burn, R.E. Logé, Healing cracks in selective laser melting by 3D laser shock peening, Addit. Manuf. 30 (2019) 100881. doi:10.1016/j.addma.2019.100881.

[36] S. Griffiths, H. Ghasemi Tabasi, T. Ivas, X. Maeder, A. De Luca, K. Zweiacker, R. Wróbel, J. Jhabvala, R.E. Logé, C. Leinenbach, Combining alloy and process modification for micro-crack mitigation in an additively manufactured Ni-base superalloy, Addit. Manuf. 36 (2020). doi:10.1016/j.addma.2020.101443.

[37] L.N. Carter, M.M. Attallah, R.C. Reed, Laser Powder Bed Fabrication of Nickel-Base Superalloys: Influence of Parameters; Characterisation, Quantification and Mitigation of Cracking, Superalloys 2012. (2012) 577–586. doi:doi:10.1002/9781118516430.ch64.

[38] L.N. Carter, C. Martin, P.J. Withers, M.M. Attallah, The influence of the laser scan strategy on grain structure and cracking behaviour in SLM powder-bed fabricated nickel superalloy, J. Alloys Compd. 615 (2014) 338–347. doi:10.1016/j.jallcom.2014.06.172.

[39] X. Wang, L.N. Carter, B. Pang, M.M. Attallah, M.H. Loretto, Microstructure and yield strength of SLM-fabricated CM247LC Ni-Superalloy, Acta Mater. 128 (2017) 87–95. doi:10.1016/j.actamat.2017.02.007.

[40] K. Puebla, L. E. Murr, S. M. Gaytan, E. Martinez, F. Medina, R. B. Wicker, Effect of Melt Scan Rate on Microstructure and Macrostructure for Electron Beam Melting of Ti-6Al-4V, Mater. Sci. Appl. 03 (2012) 259–264. doi:10.4236/msa.2012.35038.

[41] S. Ocylok, E. Alexeev, S. Mann, A. Weisheit, K. Wissenbach, I. Kelbassa, Correlations of melt pool geometry and process parameters during laser metal deposition by coaxial process monitoring, Phys. Procedia. 56 (2014) 228–238. doi:10.1016/j.phpro.2014.08.167.

[42] J. Gockel, J. Beuth, K. Taminger, Integrated control of solidification microstructure and melt pool

dimensions in electron beam wire feed additive manufacturing of ti-6al-4v, Addit. Manuf. 1 (2014) 119–126. doi:10.1016/j.addma.2014.09.004.

[43] M. v. Allmen, A. Blatter, Laser-Beam Interactions with Materials, 2nd ed., Springer-Verlag Berlin Heidelberg, 1995. doi:10.1007/978-3-642-57813-7.

[44] W.E. King, H.D. Barth, V.M. Castillo, G.F. Gallegos, J.W. Gibbs, D.E. Hahn, C. Kamath, A.M. Rubenchik, Observation of keyhole-mode laser melting in laser powder-bed fusion additive manufacturing, J. Mater. Process. Technol. 214 (2014) 2915–2925. doi:10.1016/j.jmatprotec.2014.06.005.

[45] A. Kaplan, A model of deep penetration laser welding based on calculation of the keyhole profile A model of deep penetration laser welding based on calculation of the I keyhole profile, J. Phys. D Appl. Phys. J. Phys. D Appt. Phys. 27 (1994) 1805–1814. doi:10.1088/0022-3727/27/9/002.

[46] M. Svensson, U. Ackelid, Titanium alloys manufactured with electron beam melting mechanical and chemical properties, 2010.

[47] K. Darvish, Z.W. Chen, T. Pasang, Reducing lack of fusion during selective laser melting of CoCrMo alloy: Effect of laser power on geometrical features of tracks, Mater. Des. 112 (2016) 357–366. doi:10.1016/j.matdes.2016.09.086.

[48] T. Mukherjee, J.S. Zuback, A. De, T. DebRoy, Printability of alloys for additive manufacturing, Sci. Rep. 6 (2016) 1–10. doi:10.1038/srep19717.

[49] M. Tang, P.C. Pistorius, J.L. Beuth, Prediction of lack-of-fusion porosity for powder bed fusion, Addit. Manuf. 14 (2017) 39–48. doi:10.1016/j.addma.2016.12.001.

[50] Z.H. Shen, S.Y. Zhang, J. Lu, X.W. Ni, Mathematical modeling of laser induced heating and melting in solids, Opt. Laser Technol. 33 (2001) 533–537. doi:10.1016/S0030-3992(01)00005-6.

[51] D. Sowdari, P. Majumdar, Finite element analysis of laser irradiated metal heating and melting processes, Opt. Laser Technol. 42 (2010) 855–865. doi:10.1016/j.optlastec.2009.11.022.

[52] J. Trapp, A.M. Rubenchik, G. Guss, M.J. Matthews, In situ absorptivity measurements of metallic powders during laser powder-bed fusion additive manufacturing, Appl. Mater. Today. 9 (2017) 341–349. doi:10.1016/j.apmt.2017.08.006.

[53] C.D. Boley, S.A. Khairallah, A.M. Rubenchik, Calculation of laser absorption by metal powders in additive manufacturing, Appl. Opt. 54 (2015) 2477. doi:10.1364/AO.54.002477.

[54] M.A. Ordal, L.L. Long, R.J. Bell, S.E. Bell, R.R. Bell, R.W. Alexander, C.A. Ward, Optical properties of the metals Al , Co , Cu , Au , Fe , Pb , Ni , Pd , Pt , Ag , Ti , and W in the infrared and far infrared, 22 (1983) 1099–1120.

[55] Mark Fox, Optical Properties of Solids, Second Edi, Oxford University Press, Oxford, United Kingdom, 2010.

[56] D. Bergström, The Absorptance of Metallic Alloys to Nd : YAG and Nd : YLF Laser Light, 2005.

[57] M. Schmid, S. Zehnder, P. Schwaller, B. Neuenschwander, M. Held, U. Hunziker, J. Zürcher, Measuring optical properties on rough and liquid metal surfaces, Proc ALT12. (2012). doi:10.12684/alt.1.78.

[58] J. Winter, S. Rapp, M. Schmidt, H.P. Huber, Ultrafast laser processing of copper: A comparative study of experimental and simulated transient optical properties, Appl. Surf. Sci. 417 (2017) 2–15. doi:10.1016/j.apsusc.2017.02.070.

[59] M.A. Havstad, W. Mclean, S.A. Self, M.A. Havstad, W.M. Ii, Apparatus for the measurement of the optical constants and thermal radiative properties of pure liquid metals from 0 . 4 to 10 μm Apparatus for the measurement of the optical constants and thermal radiative properties of pure liquid metals from 0 . 4 to 1, 1971 (2014). doi:10.1063/1.1143984.

[60] T.E. Faber, N. V Smith, Optical Measurements on Liquid Metals Using a New Ellipsometer, J. Opt. Soc. Am. 58 (1968) 102–108. doi:10.1364/JOSA.58.000102.

[61] S. Krishnan, K.J. Yugawa, P.C. Nordine, Optical properties of liquid metals studied by spectroscopic ellipsometry, in: Proc.SPIE, 1996. doi:10.1117/12.246250.

[62] A.M. Prokhorov, Laser heating of metals, A. Hilger, Bristol; Philadelphia, 1990.

[63] E. Siegel, Optical Reflectivity of Liquid Metals at their Melting Temperatures, Phys. Chem. Liq. 5 (1976) 9–27. doi:10.1080/00319107608084103.

[64] V. Gunenthiram, P. Peyre, M. Schneider, M. Dal, F. Coste, R. Fabbro, Analysis of laser–melt pool–powder bed interaction during the selective laser melting of a stainless steel, J. Laser Appl. 29 (2017) 022303. doi:10.2351/1.4983259.

[65] J. Mohelnikova, Materials for reflective coatings of window glass applications, Constr. Build. Mater. 23 (2009) 1993–1998. doi:10.1016/j.conbuildmat.2008.08.033.

[66] U.E. Klotz, D. Tiberto, F. Held, U.E. Klotz, D. Tiberto, F. Held, “ Additive Manufacturing of 18-

Karat Yellow-Gold alloys ,” in: Jewel. Technol. Forum, 2017.

[67] K. Ujihara, Reflectivity of metals at high temperatures, J. Appl. Phys. 43 (1972) 2376–2383. doi:10.1063/1.1661506.

[68] C.D. Boley, S.A. Khairallah, A.M. Rubenchik, Modeling of powder absorption in additive manufacturing, Opt. InfoBase Conf. Pap. (2014) 15–16. doi:10.1364/cleo_at.2014.am1l.5.

[69] M. Khan, P. Dickens, Selective Laser Melting (SLM) of pure gold, Gold Bull. 43 (2010) 114–121. doi:10.1007/BF03214976.

[70] E.F. Sichani, S. Kohl, M. Schmidt, J. Kruth, J.R. Duflou, On plasma formation in CO 2 fusion laser cutting of stainless steel, 39 (2012) 197–203. doi:10.1016/j.phpro.2012.10.030.

[71] Y. Kawahito, K. Kinoshita, N. Matsumoto, S. Katayama, Visualization of refraction and attenuation of near-infrared laser beam due to laser-induced plume, J. Laser Appl. 21 (2009) 96–101. doi:10.2351/1.3110058.

[72] J. Ye, S.A. Khairallah, A.M. Rubenchik, M.F. Crumb, G. Guss, J. Belak, M.J. Matthews, Energy Coupling Mechanisms and Scaling Behavior Associated with Laser Powder Bed Fusion Additive Manufacturing, Adv. Eng. Mater. 1900185 (2019) 1–9. doi:10.1002/adem.201900185.

[73] J. Greses, P.A. Hilton, C.Y. Barlow, W.M. Steen, Plume attenuation under high power Nd : yttritium – aluminum – garnet laser welding Plume attenuation under high power Nd : yttritium – aluminum – garnet laser welding, 9 (2016).

[74] M. Bayat, A. Thanki, S. Mohanty, A. Witvrouw, S. Yang, J. Thorborg, N.S. Tiedje, J.H. Hattel, Keyhole-induced porosities in Laser-based Powder Bed Fusion (L-PBF) of Ti6Al4V: High-fidelity modelling and experimental validation, Addit. Manuf. 30 (2019) 100835. doi:https://doi.org/10.1016/j.addma.2019.100835.

[75] C. Deng, J. Kim, S. Oh, H. Ki, Electrodynamic simulation of energy absorption in laser keyhole welding of zinc-coated and uncoated steel sheets, J. Mater. Process. Technol. 231 (2016) 412–421. doi:https://doi.org/10.1016/j.jmatprotec.2016.01.011.

[76] S.A. Khairallah, A.A. Martin, J.R.I. Lee, G. Guss, N.P. Calta, J.A. Hammons, M.H. Nielsen, K. Chaput, E. Schwalbach, M.N. Shah, M.G. Chapman, T.M. Willey, A.M. Rubenchik, A.T. Anderson, Y.M. Wang, M.J. Matthews, W.E. King, Controlling interdependent meso-nanosecond dynamics and defect generation in metal 3D printing, Science (80-.). 368 (2020) 660–665. doi:10.1126/science.aay7830.

[77] B. Hu, S. Hu, J. Shen, Y. Li, Modeling of keyhole dynamics and analysis of energy absorption efficiency based on Fresnel law during deep-penetration laser spot welding, Comput. Mater. Sci. 97 (2015) 48–54. doi:https://doi.org/10.1016/j.commatsci.2014.09.031.

[78] Z.H. Shen, S.Y. Zhang, J. Lu, X.W. Ni, Mathematical modeling of laser induced heating and melting in solids, 33 (2001) 533–537.

[79] X.C. Wang, T. Laoui, J. Bonse, J.P. Kruth, B. Lauwers, L. Froyen, Direct Selective Laser Sintering of Hard Metal Powders: Experimental Study and Simulation, Int. J. Adv. Manuf. Technol. 19 (2002) 351–357. doi:10.1007/s001700200024.

[80] C.D. Boley, A.M. Rubenchik, Modeling of laser interactions with composite materials, Appl. Opt. 52 (2013) 3329–3337. doi:10.1364/AO.52.003329.

[81] P. Meakin, R. Jullien, Restructuring effects in the rain model for random deposition, J. Phys. 48 (1987) 1651–1662. doi:10.1051/jphys:0198700480100165100.

[82] O. Pannitz, J.T. Sehrt, Transferability of process parameters in laser powder bed fusion processes for an energy and cost efficient manufacturing, Sustain. 12 (2020) 1–14. doi:10.3390/su12041565.

[83] S.D. Jadhav, J. Vleugels, J.-P. Kruth, J. Van Humbeeck, K. Vanmeensel, Mechanical and electrical properties of selective laser-melted parts produced from surface-oxidized copper powder, Mater. Des. Process. Commun. 0 (2019) e94. doi:10.1002/mdp2.94.

[84] V. Lindström, O. Liashenko, K. Zweiacker, S. Derevianko, V. Morozovych, Y. Lyashenko, C. Leinenbach, Laser powder bed fusion of metal coated copper powders, Materials (Basel). 13 (2020). doi:10.3390/MA13163493.

[85] S.D. Jadhav, S. Dadbakhsh, J. Vleugels, J. Hofkens, P. Van Puyvelde, S. Yang, J.-P. Kruth, J. Van Humbeeck, K. Vanmeensel, Influence of Carbon Nanoparticle Addition (and Impurities) on Selective Laser Melting of Pure Copper, Mater. . 12 (2019). doi:10.3390/ma12152469.

[86] U.E. Klotz, D. Tiberto, F. Held, Optimization of 18-karat yellow gold alloys for the additive manufacturing of jewelry and watch parts, Gold Bull. 50 (2017) 111–121. doi:10.1007/s13404-017-0201-4.

[87] U.E. Klotz, D. Tiberto, F. Held, U.E. Klotz, D. Tiberto, F. Held, “ Additive Manufacturing of 18-Karat Yellow-Gold alloys ,” in: Jewel. Technol. Forum 2, 2017.

[88] J. Ciurana, L. Hernandez, J. Delgado, Energy density analysis on single tracks formed by selective

laser melting with CoCrMo powder material, Int. J. Adv. Manuf. Technol. 68 (2013) 1103–1110. doi:10.1007/s00170-013-4902-4.

[89] H. Gong, K. Rafi, H. Gu, G.D. Janaki Ram, T. Starr, B. Stucker, Influence of defects on mechanical properties of Ti–6Al–4V components produced by selective laser melting and electron beam melting, Mater. Des. 86 (2015) 545–554. doi:https://doi.org/10.1016/j.matdes.2015.07.147.

[90] U. Scipioni Bertoli, A.J. Wolfer, M.J. Matthews, J.P.R. Delplanque, J.M. Schoenung, On the limitations of Volumetric Energy Density as a design parameter for Selective Laser Melting, Mater. Des. 113 (2017) 331–340. doi:10.1016/j.matdes.2016.10.037.

[91] S. Ghouse, S. Babu, R.J. Van Arkel, K. Nai, P.A. Hooper, J.R.T. Jeffers, The influence of laser parameters and scanning strategies on the mechanical properties of a stochastic porous material, Mater. Des. 131 (2017) 498–508. doi:10.1016/j.matdes.2017.06.041.

[92] M. Thomas, G.J. Baxter, I. Todd, Normalised model-based processing diagrams for additive layer manufacture of engineering alloys, Acta Mater. 108 (2016) 26–35. doi:10.1016/j.actamat.2016.02.025.

[93] R. Rai, J.W. Elmer, T.A. Palmer, T. Debroy, Heat transfer and fluid flow during keyhole mode laser welding of tantalum, Ti-6Al-4V, 304L stainless steel and vanadium, J. Phys. D. Appl. Phys. 40 (2007) 5753–5766. doi:10.1088/0022-3727/40/18/037.

[94] D.W. Bäuerle, Laser Processing and Chemistry, 4th ed., Springer-Verlag Berlin Heidelberg, 2011. doi:10.1007/978-3-642-17613-5.

[95] T.C. Chawla, D.L. Graff, R.C. Borg, G.L. Bordner, D.P. Weber, D. Miller, Thermophysical properties of mixed oxide fuel and stainless steel type 316 for use in transition phase analysis, Nucl. Eng. Des. 67 (1981) 57–74. doi:10.1016/0029-5493(81)90155-2.

[96] D.B. Hann, J. Iammi, J. Folkes, A simple methodology for predicting laser-weld properties from material and laser parameters, J. Phys. D. Appl. Phys. 44 (2011). doi:10.1088/0022-3727/44/44/445401.

[97] P. Promoppatum, S.C. Yao, Analytical evaluation of defect generation for selective laser melting of metals, Int. J. Adv. Manuf. Technol. 103 (2019) 1185–1198. doi:10.1007/s00170-019-03500-z.

[98] A.M. Kiss, A.Y. Fong, N.P. Calta, V. Thampy, A.A. Martin, P.J. Depond, J. Wang, M.J. Matthews, R.T. Ott, C.J. Tassone, K.H. Stone, M.J. Kramer, A. van Buuren, M.F. Toney, J. Nelson Weker, Laser-Induced Keyhole Defect Dynamics during Metal Additive Manufacturing, Adv. Eng. Mater. 21

(2019) 1–7. doi:10.1002/adem.201900455.

[99] W.E. King, H.D. Barth, V.M. Castillo, G.F. Gallegos, J.W. Gibbs, D.E. Hahn, C. Kamath, A.M. Rubenchik, Observation of keyhole-mode laser melting in laser powder-bed fusion additive manufacturing, J. Mater. Process. Technol. 214 (2014) 2915–2925. doi:10.1016/j.jmatprotec.2014.06.005.

[100] J. Yu, D. Kim, K. Ha, J.B. Jeon, W. Lee, Strong feature size dependence of tensile properties and its microstructural origin in selectively laser melted 316L stainless steel, Mater. Lett. 275 (2020) 128161. doi:10.1016/j.matlet.2020.128161.

[101] C.L. Druzgalski, A. Ashby, G. Guss, W.E. King, T.T. Roehling, M.J. Matthews, Process optimization of complex geometries using feed forward control for laser powder bed fusion additive manufacturing, Addit. Manuf. 34 (2020) 101169. doi:10.1016/j.addma.2020.101169.

[102] E. Stathatos, G.C. Vosniakos, Efficient temperature regulation through power optimization for arbitrary paths in Laser Based Additive Manufacturing, CIRP J. Manuf. Sci. Technol. 33 (2021) 133–142. doi:10.1016/j.cirpj.2021.03.008.

[103] T. DebRoy, H.L. Wei, J.S. Zuback, T. Mukherjee, J.W. Elmer, J.O. Milewski, A.M. Beese, A. Wilson-Heid, A. De, W. Zhang, Additive manufacturing of metallic components – Process, structure and properties, Prog. Mater. Sci. 92 (2018) 112–224. doi:10.1016/j.pmatsci.2017.10.001.

[104] X. Tan, Y. Kok, Y.J. Tan, M. Descoins, D. Mangelinck, S.B. Tor, K.F. Leong, C.K. Chua, Graded microstructure and mechanical properties of additive manufactured Ti-6Al-4V via electron beam melting, Acta Mater. 97 (2015) 1–16. doi:10.1016/j.actamat.2015.06.036.

[105] T.H. Becker, M. Beck, C. Scheffer, Microstructure and mechanical properties of Direct Metal Laser Sintered Ti- 6Al-4V, South African J. Ind. Eng. 26 (2015) 1–10. doi:10.7166/26-1-1022.

[106] M. Cloots, P.J. Uggowitzer, K. Wegener, Investigations on the microstructure and crack formation of IN738LC samples processed by selective laser melting using Gaussian and doughnut profiles, Mater. Des. 89 (2016) 770–784. doi:10.1016/j.matdes.2015.10.027.

[107] E. Chauvet, P. Kontis, E.A. Jägle, B. Gault, D. Raabe, C. Tassin, J.J. Blandin, R. Dendievel, B. Vayre, S. Abed, G. Martin, Hot cracking mechanism affecting a non-weldable Ni-based superalloy produced by selective electron Beam Melting, Acta Mater. 142 (2018) 82–94. doi:10.1016/j.actamat.2017.09.047.

[108] M. Zhong, H. Sun, W. Liu, X. Zhu, J. He, Boundary liquation and interface cracking characterization

in laser deposition of Inconel 738 on directionally solidified Ni-based superalloy, Scr. Mater. 53 (2005) 159–164. doi:10.1016/j.scriptamat.2005.03.047.

[109] K. Prasad, M. Obana, Y. Ishii, A. Ito, S. Torizuka, The effect of laser scanning strategies on the microstructure, texture and crystallography of grains exhibiting hot cracks in additively manufactured Hastelloy X, Mech. Mater. 157 (2021) 103816. doi:10.1016/j.mechmat.2021.103816.

[110] M. Ramsperger, R.F. Singer, C. Körner, Microstructure of the Nickel-Base Superalloy CMSX-4 Fabricated by Selective Electron Beam Melting, Metall. Mater. Trans. A Phys. Metall. Mater. Sci. 47 (2016) 1469–1480. doi:10.1007/s11661-015-3300-y.

[111] Y.-C. Hagedorn, J. Risse, W. Meiners, N. Pirch, K. Wissenbach, R. Poprawe, Processing of nickel based superalloy MAR M-247 by means of High Temperature - Selective Laser Melting (HT - SLM), in: 6th Int. Conf. Adv. Res. Virtual Phys. Prototyp., Leira, Portugal, 2013: pp. 291–295. https://www.scopus.com/record/display.uri?eid=2-s2.0-84892160456&origin=inward&txGid=d74095b9c9e07874cfd19ca5f4b5c522.

[112] N. Sohrabi, R.S. Panikar, J. Jhabvala, A.R. Buch, S. Mischler, R.E. Logé, Laser coating of a Zr-based metallic glass on an aluminum substrate, Surf. Coatings Technol. 400 (2020) 126223. doi:https://doi.org/10.1016/j.surfcoat.2020.126223.

[113] H. Okamoto, D.J. Chakrabarti, D.E. Laughlin, T.B. Massalski, The Au-Cu (Gold-Copper) system, J. Phase Equilibria. 8 (1987) 454–474. doi:10.1007/BF02893155.

[114] J. Hennig, Phase Transformations in 18-Carat Gold Alloys Studied by Mechanical Spectroscopy, 4635 (2010).

[115] G. Borelius, On the equilibrium and kinetics of the order-disorder transformations in alloys, J. Inst. Met. 74 (1948) 17–31.

[116] J.L. O'Brien, G.C. Kuczynski, X-Ray study of the kinetics of ordering in AuCu, Acta Metall. 7 (1959) 803–806.

[117] M. Hirabayashi, S. Ogawa, An X-ray Study of Ordering Processes in CuAu Single Crystals, J. Phys. Soc. Japan. 11 (1956) 907–914. doi:10.1143/JPSJ.11.907.

[118] G.C. Kuczynski, R.F. Hochman, M. Doyama, Study of the kinetics of ordering in the alloy AuCu, J. Appl. Phys. 26 (1955) 871–878. doi:10.1063/1.1722112.

[119] M. Garcia-Gonzalez, S. Van Petegem, N. Baluc, M. Dupraz, V. Honkimaki, F. Lalire, H. Van

Swygenhoven, Influence of thermo-mechanical history on the ordering kinetics in 18 carat Au alloys, Acta Mater. 191 (2020) 186–197. doi:https://doi.org/10.1016/j.actamat.2020.03.032.

[120] M. Garcia-Gonzalez, S. Van Petegem, N. Baluc, S. Hocine, M. Dupraz, F. Lalire, H. Van Swygenhoven, Enhanced precipitate growth at reduced temperatures during chemical ordering in deformed red gold alloys, Scr. Mater. 170 (2019) 129–133. doi:10.1016/j.scriptamat.2019.05.038.

[121] M.N.D. Larcher, C. Cayron, A. Blatter, R. Soulignac, R.E. Loge, Electron backscatter diffraction study of variant selection during ordering phase transformation in L10-type red gold alloy, J. Appl. Crystallogr. 52 (2019) 1202–1213. doi:10.1107/S1600576719011890.

[122] M.N.D. Larcher, C. Cayron, A. Blatter, R. Soulignac, R.E. Logé, The thermally activated distortion with amplification effect and related variant selection in red gold alloys, Acta Mater. 198 (2020) 242–256. doi:10.1016/j.actamat.2020.07.064.

[123] M.N.D. Larcher, Phase transformation induced distortions in red gold alloys, EPFL, 2021. doi:10.5075/epfl-thesis-8381.

[124] T. DebRoy, H.L. Wei, J.S. Zuback, T. Mukherjee, J.W. Elmer, J.O. Milewski, A.M. Beese, A. Wilson-Heid, A. De, W. Zhang, Additive manufacturing of metallic components – Process, structure and properties, Prog. Mater. Sci. 92 (2018) 112–224. doi:10.1016/j.pmatsci.2017.10.001.

[125] S.A. Khairallah, A.T. Anderson, A. Rubenchik, W.E. King, Laser powder-bed fusion additive manufacturing: Physics of complex melt flow and formation mechanisms of pores, spatter, and denudation zones, Acta Mater. 108 (2016) 36–45. doi:10.1016/j.actamat.2016.02.014.

[126] A. Mostafa, D. Shahriari, I.P. Rubio, V. Brailovski, M. Jahazi, M. Medraj, Hot compression behavior and microstructure of selectively laser-melted IN718 alloy, Int. J. Adv. Manuf. Technol. 96 (2018) 371–385. doi:10.1007/s00170-017-1522-4.

[127] K. Kempen, L. Thijs, B. Vrancken, S. Buls, J. Van Humbeeck, J.P. Kruth, Producing crack-free, high density M2 HSS parts by Selective Laser Melting: Pre-heating the baseplate, 24th Int. SFF Symp. - An Addit. Manuf. Conf. SFF 2013. (2013) 131–139.

Chapter 4

An effective rule for translating optimal selective laser melting processing parameters from one material to another

Hossein Ghasemi-Tabasi[1], Jamasp Jhabvala[1], Eric Boillat[1], Toni Ivas[1], Rita Drissi-Daoudi[1], Roland E. Logé[1]

1. Thermomechanical Metallurgy Laboratory (LMTM) – PX Group Chair, Ecole Polytechnique Fédérale de Lausanne (EPFL), CH-2002 Neuchâtel, Switzerland.

H. Ghasemi-Tabasi, J. Jhabvala, E. Boillat, T. Ivas, R. Drissi-Daoudi, R.E. Logé, An effective rule for translating optimal selective laser melting processing parameters from one material to another, Addit. Manuf. 36 (2020) 101496. doi:10.1016/j.addma.2020.101496.

Contribution:
Hossein Ghasemi Tabasi designed the model and experiments, and conducted the manufacturing, sample analysis, interpretation of results and wrote the manuscript.

Abstract:

Selective Laser Melting (SLM) or Laser Powder Bed Fusion (L-PBF) is the most studied laser-based additive manufacturing process for metals and alloys. One important issue in SLM is the time-consuming identification of a process window leading to quasi fully dense parts (> 99.8%), usually based on trials and errors. As some metal powders may be very expensive, and therefore not suitable for a whole battery of tests, a method to infer optimal parameters from one material to another would be highly beneficial. In this study, we use bronze as a test material for optimizing SLM parameters, before translating these parameters to red gold and 316L steel. The concept of normalized enthalpy is used to take into account the differences in thermal and optical properties among the different materials. A translation rule is derived for the prediction of optimal processing conditions, based on the ones found for the test material. One important input for this translation rule is the powder absorptivity, which is measured at the appropriate laser wavelength and at room temperature. This approach eventually leads to the highest reported density for an additive manufactured 18-carat gold alloy (99.81% relative density), to the authors' knowledge. Finite element (FEM) simulations justify the translation rule formulation by showing the importance of the laser/powder interactions during the SLM process, leading to a finite penetration depth of the laser in the powder bed due to multiple reflections. The FEM calculations indicate that a significant part of the laser energy is directly absorbed by the powder during the manufacturing process when operating in near-optimal conditions.

Keywords: laser powder bed fusion; powder absorptivity; gold alloy; translation rule; finite element simulation**.**

1. Introduction

Additive manufacturing (AM) enables the production of intricate internal and external geometries unattainable by conventional manufacturing methods. These can be achieved with short production times and minimal custom tooling [1]. Among different AM techniques, the SLM (also called Laser Powder Bed Fusion (L-PBF)) process has received the most focus. Producing AM parts using the SLM technique requires a significant number of trials and errors cycles to optimize the process parameters, in relation with the metallic powder and its physical and chemical properties [2–4]. The process optimization is not only time consuming, but it also needs to be repeated when moving from one machine to another. The primary objective is usually to produce parts without defects such as porosity and cracks [5,6]. This objective becomes a real challenge when dealing with materials like gold, due to their high

reflectivity at the standard laser wavelength (infrared). Moreover, in commercial SLM machines, a non-negligible amount of powder is needed to fill the powder supply, which makes the situation difficult for expensive alloys. This does not prevent SLM to find an increasing interest in the jewelry and watch industries [7–13]. One way to deal with the time consuming and/or expensive trial and error procedure is to mathematically define translation rules which can predict optimum processing conditions for one material based on those found for another material.

Different strategies have been considered to define or predict optimized SLM parameters. They often determine one or several variables which are allowed to vary within a specific range of values. Some studies have shown a relation between the Volume Energy Density (VED), and the final part porosity content, and the strategy then consists in keeping about the same VED from one material to another [14]. The volume energy density is given by:

$$\mathrm{VED} = \frac{\alpha \,.\, \mathrm{P}}{\mathrm{V}.\,\mathrm{h}.\,\mathrm{L}} \tag{1}$$

Where α is the material absorptivity, P the laser power (W), V the laser speed (m/s), h the hatching distance (m), and L the layer thickness (m). However, the VED does not consider all essential quantities, and it is well known that different sets of parameters in Equation (1) may lead to the same VED but different melt pool depths [14], which in turn lead to different part qualities. In other words, there are not enough material related parameters in the VED equation, such that this quantity could be used for translation rules [15].

An alternative to the VED criterion is the construction of process maps based on material and laser process parameters. There are several studies describing the correlations of the melt pool geometry with laser parameters and material properties [16–22]. Ion et al. [23] have applied analytical heat flow parameters in order to develop laser processing diagrams through dimensionless numbers which predict the heating, melting, and evaporation zones for different types of laser and material. The reported tables and diagrams are useful to quantify regimes in different laser processes such as welding, heating, cutting, and cladding. The keyhole formation threshold has been used in several studies as a fundamental model to find the optimum conditions [24–30]. Hann et al. [27] plotted dimensionless graphs to find the transition zone between the conduction mode and the keyhole mode, considering an energy balance between the input and the dissipated energy - which introduced the so-called normalized enthalpy - and comparing it to a normalized melt pool depth. Equations 2 and 3 express the normalized enthalpy $\overline{\Delta H}$, and the normalized melt pool depth $\bar{d}$:

$$\overline{\Delta H} = \frac{\Delta H}{\Delta h} = \frac{\alpha P}{\rho(C\Delta T + L_m)\sqrt{\pi\omega^3 VD}} \quad (2)$$

$$\bar{d} = \frac{d}{\omega} \quad (3)$$

where α is the absorptivity of the bulk material, P is the laser power (W), ρ the density ($\frac{kg}{m^3}$), C the specific heat ($\frac{J}{kg.K}$), ΔT the difference between the melting and initial temperature (K), L_m the latent heat of melting ($\frac{kJ}{kg}$), ω the laser spot radius (m), V the laser speed ($\frac{m}{s}$), D the thermal diffusivity ($\frac{m^2}{s}$), and d the melt pool depth (m). A master curve valid for different materials has been found by plotting the normalized melt pool depth as a function of the normalized enthalpy $\bar{d}$ ($\overline{\Delta H}$). Going to high values of the normalized enthalpy results in keyhole formation, and increases the slope of the $\bar{d}$ ($\overline{\Delta H}$)function [27]. In welding processes, an appropriate process parameters optimization is required to set a balance between different forces inside the melt pool such as to have a stable keyhole [31]. However, high energy densities lead to high evaporation on the melt surface. As a result, a complex liquid flow develops in which instability and collision of the keyhole walls may result in keyhole porosities [32]. Therefore, even though the keyhole mode is frequently helpful for welding to deliver deep penetration and thin bead welds, it is not recommended in AM because of the risk for porosity formation. The conduction mode [33,34] is preferred instead, i.e. the one at lower normalized enthalpy values, where keyholes do not form yet. On the other hand, insufficient heat input during laser processing leads to incomplete melting of the powders and the so-called lack of fusion porosities, which must clearly be avoided. Optimal conditions therefore lie in a transition zone between keyhole and conduction modes: this is where the formation of porosities is expected to be the lowest. Experimental welding data for different materials are in a good agreement with this model, and they all align well with the master curve when varying the process parameters [27].

The above model has been used for additive manufacturing in different studies. King et al. [30] combined the laser process parameters into a graph, based on normalized enthalpy and normalized melt pool depth. The results suggest that the model is useful to identify close to optimum process windows; however, a much higher normalized enthalpy was obtained at the transition zone between conduction and keyhole modes, compared to welding. Scipioni Bertoli et al. [14] did not observe a sharp transition between conduction and keyhole modes, and their normalized enthalpy at the transition point was also different from the study by King et al. [30]. Alternate versions of the normalized enthalpy expression have been proposed, e.g. by adding dimensionless parameters to characterize the melt pool [35,36] or

heat conduction [37] during the SLM process. M. Thomas et al. [38] extended the approach devised by Ion et al. [23] to plot dimensionless graphs based on additive manufacturing process parameters and their model provides useful information for predicting the final microstructure of AM parts; however, it does not provide information concerning the transition zone between different melt pool modes (conduction, keyhole). L. Johnson et al. [39] used characteristic length scales of the melt pool as a printability metric for the SLM process. In their numerical calculation they consider phase transformation between solid, liquid and vapor, neglecting the powder properties, and define artificially high absorptivity and conductivity for the vapor phase. The reported maps provide useful information for different melt pool modes based on laser power and scanning speed; however like in [38], the model fails to clearly capture a transition zone between melt pool modes for different materials.

SLM shares some characteristics with laser welding. However, in the SLM process, the laser interacts with powders which have completely different responses from bulk solid materials in welding. Laser/powder interaction is also a function of the powder size distribution and layer thickness. In processes such as laser cutting, drilling, and welding, when a high power laser irradiates the surface of the material, a part of the beam energy is transferred to the piece by heat conduction. The surface can also melt and even vaporize [40]. When dealing with powders, multiple scattering, and powder geometry effects play a major role in determining the effective optical properties [41]. These aspects have been studied both empirically and by numerical simulation. To simplify the model of light absorption in the powder, in earlier studies, the powder is assumed to be a homogeneous continuum body [42,43]. In their theoretical study, Boley et al. [41] considered the powder bed as randomly distributed particles. Using the ray-tracing method, these authors found that the powder absorption was much larger than the value measured on a flat metal surface, due to multiple light scattering. A real powder bed is made of particles of variable sizes and which are not densely packed, which also influences the absorption [44,45]. The numerical computation reveals that a flat metallic surface or an isolated sphere has a reduced absorptivity compared to powder particles. Multiple reflections inside the powder bed give an effective absorption coefficient which can also be higher than that of the liquid surface [43]. Trapp et al. [46] measured the absorption value for 316L stainless steel powder, and found that higher ratios of the beam size to the particles size increase the chance for multiple reflections and lead to higher absorptivity.
The experimental evaluation of absorption through temperature measurements is not easy since absorptivity depends on different factors such as laser intensity, angle of incidence, wavelength, temperature, surface chemistry (oxidation), surface roughness, and contamination. As an example, for gold, various absorption models have been considered [47,48]. Gold in the solid-state is known to be very reflective in nature. While other metals like iron, palladium, aluminum, and platinum show a relatively lower reflectivity of 60-70% at the infrared wavelength, copper, silver and gold show almost total reflectivity [49]. Therefore, the surface reflects most of the incident laser energy, and melting these

metals by laser is difficult despite their low melting point. However, when using powders, the finite penetration depth of light inside the powder bed significantly increases the absorption compared to the bulk solid state [13,41].

The selective laser melting of tin bronze (CuSn10) powder has been studied in previous studies[50,51]. The first step of this work is to investigate optimum SLM processing conditions for bronze (CuSn8), i.e. those leading to the lowest porosity content. A second step then consists in transferring SLM parameterization results from CuSn8 to red gold and 316L steel, using an appropriate translation rule. In previous studies mentioned earlier, authors considered different states of the material for the absorptivity values, i.e. bulk surface ([14,30,35,37,38,52,53], liquid surface [36], and vapor state [39]). In our study, one important ingredient of the translation rule is the *powder* absorptivity, which takes into account the chemical composition, surface roughness, powder morphology, and size distribution [54]. For one specific material, most of the thermophysical properties of the powder particles mainly depend on their shape and size distributions, and on their spatial arrangement. Their temperature evolution is actually very small compared to their variation between powder, bulk solid and liquid state values; this means that room temperature measurements are meaningful even if processing also operates at higher temperatures. For instance, the powder thermal conductivity variation between room temperature and the sintering temperature with temperature is more than 100 times lower than the change from the powder to the bulk solid and the liquid state [55–57]. In the same way, the powder absorptivity evolution over the same temperature interval is negligible compared to the difference associated to the transformation into bulk solid or liquid state [58,59].

The proposed translation rule is finally validated by SLM experiments on red gold and 316L steel, and justified through finite element simulations using different values of absorptivity for the liquid, bulk solid and powders, while considering a finite optical penetration depth of the laser in the powder bed. The optimal condition acquired from the model is defined based on the density and porosity content of the samples. In order to be able to study the effect of the process parameters on the final porosity content of the printed samples, one need to use powder with good flow ability and acceptable internal pores. The generality of the approach is verified by considering a different laser spot size when printing 316L steel samples.

2. Experimental

2.1 Manufacturing process

Commercially gas-atomized bronze CuSn8 (92 wt.% Cu, 8 wt.% Sn) and 18-carat red gold (75 wt.% Au, 20.5 wt.% Cu, 4.5 wt.% Ag) powders provided by Heraeus Group were used in this study. 316L steel samples were printed with gas-atomized powder (12 wt.% Ni, 17 wt.% Cr, 2.5 wt.% Mo, 2.3 wt.% Si, 1.0 wt.% Mn, 0.03 wt.% C) provided by Oerlikon. The received powder particles had a

spherical shape with some small porosity and very fine rare satellite particles (Figure 1). The powder particle size distributions and their relative densities are listed in Table 1. The relative density of the powder bed was measured using the Powder Tester HOSOKAWA MICRON CORPORATION machine (supplementary section S1).

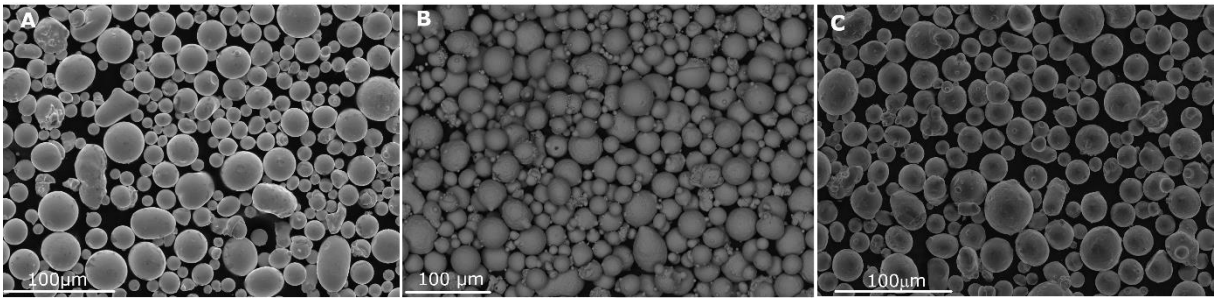

Figure 1. SEM images of the A) 18-carat red gold, B) bronze, and C) 316L gas atomized powders morphologies.

Table1. Bronze, red-gold, and 316L powders particles details.

	D10 (µm)	D50 (µm)	D90 (µm)	Relative density %
Bronze	20.11	31.11	44.25	59.7
Red-gold	13.77	26.63	40.84	54.8
316L	18.24	30.04	45.65	55.3

SLM experiments used an in-house machine (Figure 2), intended for research activities [60], and designed for operating with only a few dozen grams of powder. It is equipped with a 500 W fiber SPI laser, with a wavelength of 1070 nm and with the possibility to use two different laser spot sizes (65 µm and 85 µm). Optimization of SLM parameters was done under a nitrogen atmosphere, with oxygen content controlled below 200 ppm throughout the process.

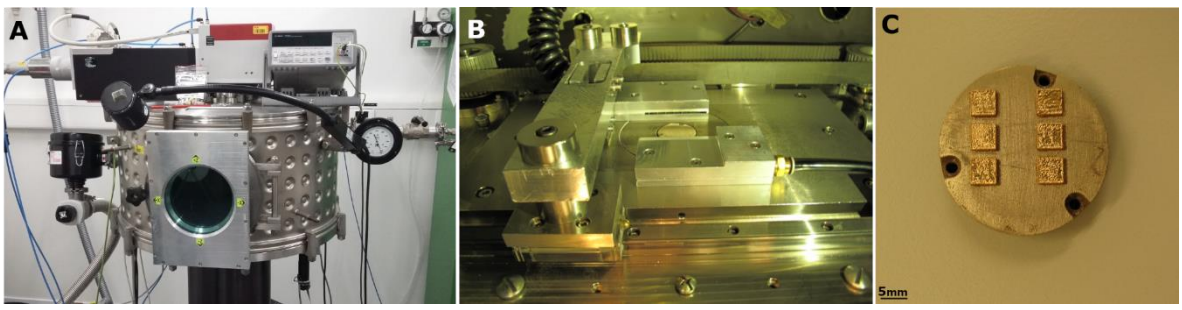

Figure 2. A) In-house SLM machine, B) printing plate, powder deposition, and gas flow system, and C) example of printed bronze samples.

2.2 Optical properties measurements

Powder and bulk material absorptivities of the different materials were measured for wavelengths from 900 to 1200 nm with a Perkin Elmer Lambda900 spectrophotometer. For the powder particles, the measurements were done in both transmission and reflection modes. Figure 3 indicates different phenomena occurring during the optical measurement of the powder layer with the spectrophotometer. The measured layer thickness of the powder is around 40 μm, which corresponds well to the SLM layer thickness in our experiments. The measured reflectivity and transmitivity of the powder bed are named R and T, respectively.

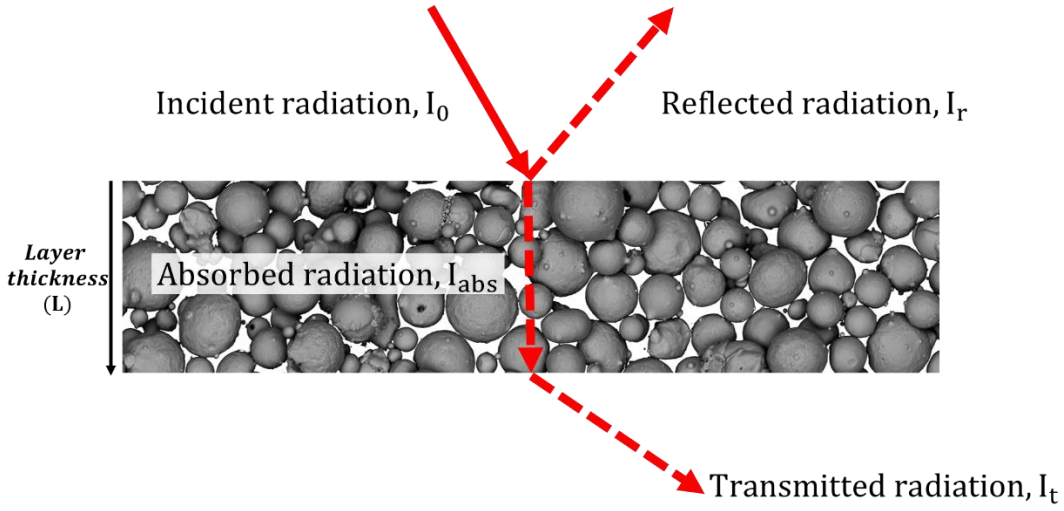

Figure 3. Schematic view of beam reflection, transmission, and absorption inside the powder bed during the optical properties measurement with the spectrophotometer.

The amount of light (per unit area of the top surface) penetrating inside the powder layer is equal to:

$$I_0 - I_r = (1 - R)\, I_0 = \alpha_p I_0 \tag{4}$$

where I_0 is the intensity of the light on the top surface, I_r is the intensity of the reflected light, and α_p is the *total powder absorptivity*. A part of the penetrating light in the powder bed is absorbed within the powder layer (I_{abs}) and the remaining part is transmitted at the other side of the layer (I_t). We can then define the *powder layer absorptivity* (α_{p_layer}) by:

$$I_{abs} = I_0 - I_r - I_t = (1 - R - T) I_0 = \boldsymbol{\alpha_{p\_layer}} I_0 \tag{5}$$

One could object that, during the SLM process, the fraction of light reaching the bottom side of the layer will be either absorbed or back-reflected by the substrate or the previously solidified layers. However, due to the surface roughness induced by SLM processing which reduces reflectivity, and the fact that

back-reflections go in all directions [61,62], we assume that the amount of light really contributing to the local heating of the powder layer under the laser spot is closer to α_{p_layer} than α_p. Such an assumption would require proper simulations at the right scale to be validated [63,64].

The optical penetration depth in the powder bed is calculated from the spectrophotometer measurements. In a homogeneous medium, the radiation intensity perpendicular to the medium surface decays according to the Beer-Lambert law [49]. The intensity of the transmitted radiation (I_t) at a distance L from the material layer top surface (Figure 3) is then:

$$I_t = I_0 T = \alpha_p I_0 e^{-\frac{L}{\delta}} \quad (6)$$

where L is the layer thickness, and δ the optical penetration depth defined as the depth at which the beam intensity falls to 1/e of the top surface value. In other words, $\alpha_p I_0$ indicates the amount of light entering the powder layer and $e^{-\frac{L}{\delta}}$ the intensity decay at distance L from the top surface. With the same approach as Equation (6), the amount of absorbed intensity inside the powder bed (I_{abs}) will be:

$$I_{abs} = \alpha_p I_0 (1 - e^{-\frac{L}{\delta}}) \quad (7)$$

which then defines the relation between α_p and α_{p_layer} :

$$\alpha_p = \frac{I_{abs}}{I_0(1-e^{-\frac{L}{\delta}})} = \frac{\boldsymbol{\alpha_{p\_layer}}}{(1-e^{-\frac{L}{\delta}})} \quad (8)$$

For red gold powders, the effect of a heat treatment was also considered such as to quantify the change of absorptivity related to oxidation of the powder particles surface [65]. The oxide formation is in fact used in several studies to increase absorptivity and reduce the porosity content in the final part [12,66]. In this study, the chosen heat treatment was four hours at 200°C.

2.3 Samples characterization

2D optical microscopy analysis was conducted using a Leica DM6000M microscope to evaluate the distribution of pores within the SLM samples, and measure the melt pool geometries. The samples were ground using a SiC paper up to 2500 grit size and then polished with a suspension of alumina particles until 0.25µm. For each sample, three different parallel sections (5×5mm) were evaluated at a magnification of 10X. The stitching of the figures was done using the software tool of the Leica microscope. To characterize the melt pools, bronze samples were etched with a H_2O + 25ml NH_3 + 5ml H_2O_2 solution, and red gold samples with a cyanide-based solution. Diluted Aqua regia solution (75ml HCl+ 25ml HNO_3+ 100ml H_2O) was used to characterize the melt pool of the 316L printed samples.

The porosity distribution was characterized by 2D image analysis of the three metallographic cross-sections, using the ImageJ software with a plugin [30], and the values are reported with a fractional uncertainty of maximum 0.08%.

2.4 Finite element simulations

A dedicated finite element simulation software has been developed for the modeling of the SLM process [67]. In this code, the powder bed is considered as a homogeneous medium, which has effective properties (absorptivity, thermal conductivity, optical penetration depth, density).

The mesh in the parallelepiped computation domain Ω (the powder bed and its surrounding) is illustrated in Figure 4. Five different zones can be distinguished based on the (isotropic) mesh size; mesh adaptation follows the laser scanning direction such as to keep the laser spot at the center of the most refined zone. The mesh extends in the z-direction by extrusion of the 2D mesh shown in Figure 4. The elements in the coarse and fine mesh are tetrahedra and orthogonal prisms, respectively [68]. The elements sizes are determined based on the heat source spatial distribution and considering the needed accuracy for the computation of thermal conduction within the powder and at the interface between the powder and the bulk solid or liquid.

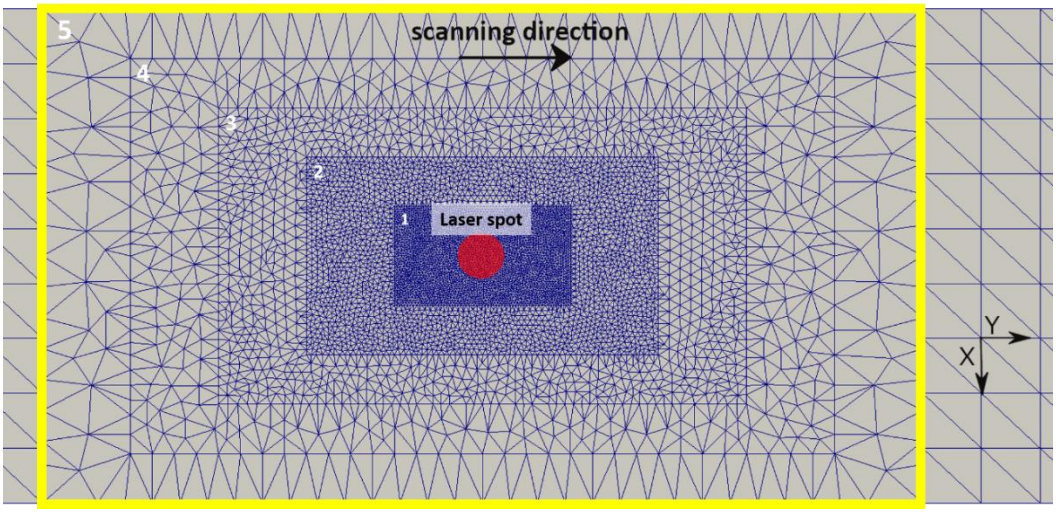

Figure 4. Top view of the non-conformal mesh used in finite element simulations of the SLM process. Five different zones are defined inside the moving mesh (indicated by the yellow box), which follows the laser scanning during the simulation. The laser scanning plane is the (x, y) plane. . The maximum areas (mm^2) of the elements in the (x, y) plane are, 0.00000625, 0.000025, 0.0001, 0.0004, and 0.0016, for zones 1, 2, 3, 4, and 5, respectively.

Different optical properties are considered for the solid, liquid and powder states. The light penetration inside the powder bed is defined by Equation (6). Generally, for bulk metals, the light penetration depth

δ is very small (in the order of tens of nanometers) [69]; therefore, a surface heat source is used when dealing with the liquid or the bulk solid. However, for powders particles with sizes in the range 10-40 μ m, the penetration depth δ is of the order of several powder particle diameters [70]. Therefore, in the SLM process for which the powder bed thickness is lower than a hundred microns, the effect of the penetration depth in energy deposition is certainly not negligible [43]. For this reason, the laser heat source is modeled, in the powder bed, as a *volumetric* source.

In the finite element code, the temperature T and the enthalpy per unit mass u result from the heat transfer in Ω. The evolution of u follows from the heat diffusion equation, with appropriate boundary and initial conditions (Equations 9 to 11):

$$\rho\frac{\partial u}{\partial t} - \nabla(K\nabla T) = F, \qquad \text{in } \Omega \tag{9}$$

$$K\frac{\partial T}{\partial n} = \kappa(T_0 - T) + f, \qquad \text{on } \partial\Omega \tag{10}$$

$$u = u_0, \qquad \text{in } \Omega, \qquad \text{for } t = 0 \tag{11}$$

where K is the effective thermal conductivity, ρ the density, κ the thermal exchange coefficient between the domain and the environment (at a temperature T_0), F a volumetric heat source and f a surface heat source. $\frac{\partial T}{\partial n}$ is the normal outward derivative of the temperature on the surface boundary of the computational domain $\partial\Omega$. The temperature T is linked to the enthalpy per unit mass u by an algebraic equation:

$$T = \beta(u) \tag{12}$$

where β is a non-decreasing real-valued function of the real variable u. In our program, the function β is constructed according to the information on the heat capacity of the material and on the latent heats of its phase changes[71].

All material properties used in the numerical simulations are summarized in Tables 2 and 3. For all three materials, evolutions of properties with temperature are taken from the references listed in Table 3. For bronze and red gold alloy, due to a lack of experimental thermo-physical property data, fewer data points are available, compared to 316L. The computations considered the stabilized melt pool size (i.e. in quasi-steady state). The thermal conductivity of the powder particles is set two orders of magnitude smaller than that of the bulk solid state, due to the air gap between particles.

3. Results and discussions

3.1 Optimization of SLM parameters

Bronze samples (5×5×3mm) with different SLM parameters were printed. The analysis of samples is conducted to evaluate the distribution of pores within cross-sections. The selected optimal parameters, for a laser spot diameter of 85µm, were a power of 250 W, a scanning speed of 200 mm/s, a hatching distance of 150 µm and a layer thickness of 40 µm, leading to a relative density of 99.87%. Figure 5. -A illustrates a cross-section of one printed bronze sample with optimized parameters. Using the exact same parameters for the red gold sample gave a highly porous material (Figure 5. -B, 93% relative density), which clearly indicates the need for a translation rule.

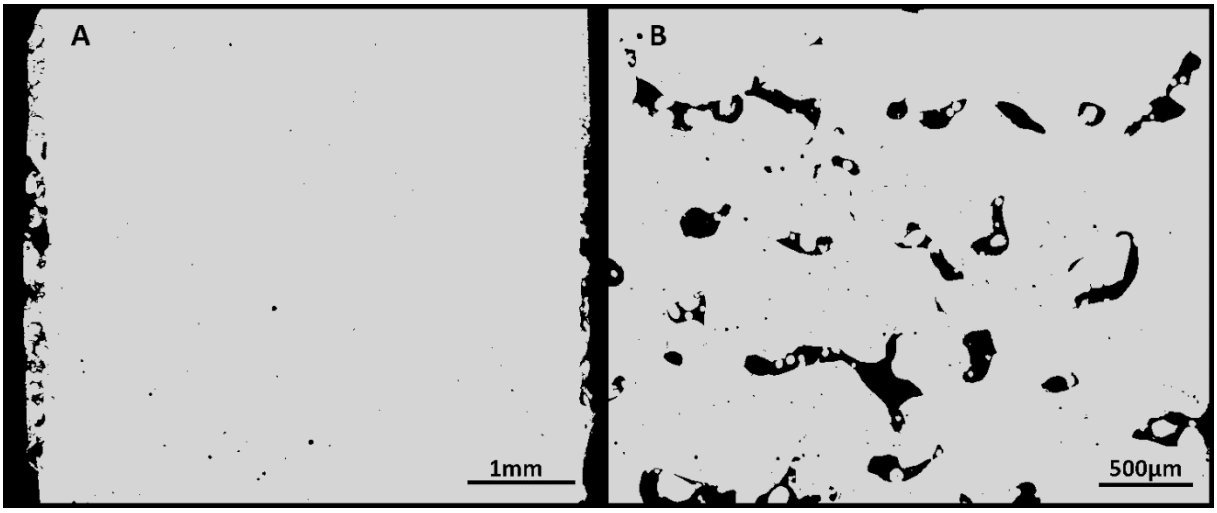

Figure 5. Optical micrographs (X-Y plane) of the A) optimized bronze sample, and B) manufactured red gold sample with the parameters used to obtain an optimized bronze sample in figure A).

3.2 Derivation of a translation rule from one material to another

Equation (2) is now rewritten with effective parameters taking into account the different states of the material involved in SLM (powder, liquid and bulk). $\overline{\Delta H}^j$ is the normalized enthalpy of the material j (in this work: bronze(B), red-gold(G), or 316L steel(S)) as a function of the processing conditions. Equations 13 and 14 express the normalized enthalpy $\overline{\Delta H}^j$, and the normalized melt pool depth $\bar{d}$:

$$\overline{\Delta H}^j = <\alpha>^j . M^j . \frac{P}{\sqrt{\omega^3 V}} \quad \text{with } M^j = \frac{1}{\rho(C\Delta T + L_m)\sqrt{\pi < D >}} \tag{13}$$

$$\bar{d} = \frac{d}{\omega} \tag{14}$$

where $< \alpha >^j$ is the effective absorptivity value of material j during the SLM process, and M^j contains all the other properties of the material as defined in section 1. $< D >$ is the effective diffusivity of the material. During the SLM process operating in the conduction mode, the laser interacts with both the powder and liquid phases and therefore, considering Equation (8), the incident power P_0 is distributed between the liquid and powder phases according to:

$$< \alpha >^j . P_0 = \alpha_p^j P_p + \alpha_l^j P_l = \frac{\boldsymbol{\alpha^j_{p\_layer}}}{(1 - e^{-\left(\frac{L^j}{\delta^j}\right)})} . P_p + \alpha_l^j . P_l \tag{15}$$

Where α_p^j and α_l^j are the powder and liquid absorptivities of material j, respectively, and P_p and P_l are the amount of incident power interacting with powder and liquid phases, respectively. From Equation (15), the effective absorptivity value is then:

$$< \alpha >^j = \frac{\boldsymbol{\alpha^j_{p\_layer}} . P_p}{(1 - e^{-\left(\frac{L^j}{\delta^j}\right)}) . P_0} + \frac{\alpha_l^j P_l}{P_0} \tag{16}$$

If we define $\frac{P_p}{P_0}$ as the fraction f_p of the incident laser power interacting with the powder particles, and $\frac{P_l}{P_0}$ as the fraction $f_l = 1 - f_p$ interacting with the liquid phase, we have:

$$< \alpha >^j = \frac{\alpha^j_{p-layer}}{\left(1-e^{-\left(\frac{L^j}{\delta^j}\right)}\right)} . f_p + \alpha_l^j . f_l = \alpha^j_{p\_layer}\left[\left(\frac{1}{1-e^{-\left(\frac{L^j}{\delta^j}\right)}}\right) . f_p + \left(\frac{\alpha_l^j}{\alpha^j_{p\_layer}}\right) . f_l\right] = G^j . \boldsymbol{\alpha^j_{p\_layer}} \tag{17}$$

where G^j is a material-dependent value.

Table 2 summarizes absorptivity values for different materials and different physical states. The absorptivity values were obtained from spectrophotometer measurements on a powder layer (α_{p_layer}, see Fig. 3) or a polished bulk solid (α_s). All measurements were done at room temperature, as discussed in section 1. In the infrared range, the red gold powder absorptivity increased after heat treatment by about 8%; however, it was still significantly lower than the bronze value. The reported optical properties of the liquid phases in Table 2 are taken from literature considering pure gold and pure copper [72,73] (approximating red gold and bronze, respectively). All other material parameters are given in Table 3.

Due to the lack of available thermophysical properties for liquid bronze and red gold, a few quantities were taken identical for the solid and the liquid.

In Table 2, liquid absorptivities are all significantly lower than the corresponding powder absorptivities, which gives an increased weight of the powder over the liquid when computing normalized enthalpies. Equation (13) describes the energy balance between the input energy of the laser source and the dissipation of the energy due to thermal losses. The thermal losses are mainly classified in radiation, vaporization and splattering, convection, and conduction losses [74]. From the experimental measurements and theoretical computations, the primary heat dissipation mechanism is conduction through the bulk solid phase [75,76]. Consequently, as a **first approximation (i)** we choose the thermal diffusivity of the solid phase (D_s) in Equation (13), instead of the effective diffusivity $< D >$, to describe the dissipation of the energy.

The input energy can be divided into the light absorbed by the melt pool, the powder bed, and at higher energies, by vapor plumes and plasma produced by the melt pool. In additive manufacturing, laser powers used for melting of the powder layer are in general lower than in welding applications, mainly to prevent porosities created by the keyhole regime. The absorbed laser light in vapor and plasma during low-power laser welding is around 15%, as discussed by R. Miller et.al [77]. In the SLM process, the conduction mode leads to minimal vaporization; thus, the majority of the energy is absorbed by the melt pool and the powder bed. The melt pool lifetime is directly proportional to the process parameters and thermal diffusivity [78,79]. For highly conductive materials such as bronze and gold, it is even shorter than for convention materials. Part of the heat absorbed by the melt pool is transferred to the surrounding material, but very little to the powders, due to their low thermal conductivity. Consequently, the energy used to melt the powder is essentially the one directly absorbed by multiple scattering of the laser beam coming on the powder bed. Since the exact value of $< \alpha >^j$ is not easily measurable as the laser interacts with different material states in unknown proportions, as a **second approximation (ii)**, we consider that in Equation (17), G^j is *material insensitive*, so that only the powder layer component $\alpha^j_{p\_layer}$ of the effective absorptivity is important when comparing different materials.

The combination of approximations (i) and (ii) finally leads to:

$$\overline{\Delta H}^j \approx \boldsymbol{\alpha}^{\mathbf{j}}_{\mathbf{p\_layer}} . M^j . \frac{P}{\sqrt{\omega^3 V}} \quad \text{with} \quad M^j = \frac{1}{\rho(C\Delta T + L_m)\sqrt{\pi D_s}} \tag{18}$$

Both approximations (i) and (ii) will be validated further in this paper by finite element simulations (section 3.4). Figure 6 is a schematic view of the SLM process and summarizes the assumptions which are considered to derive the translation rule below.

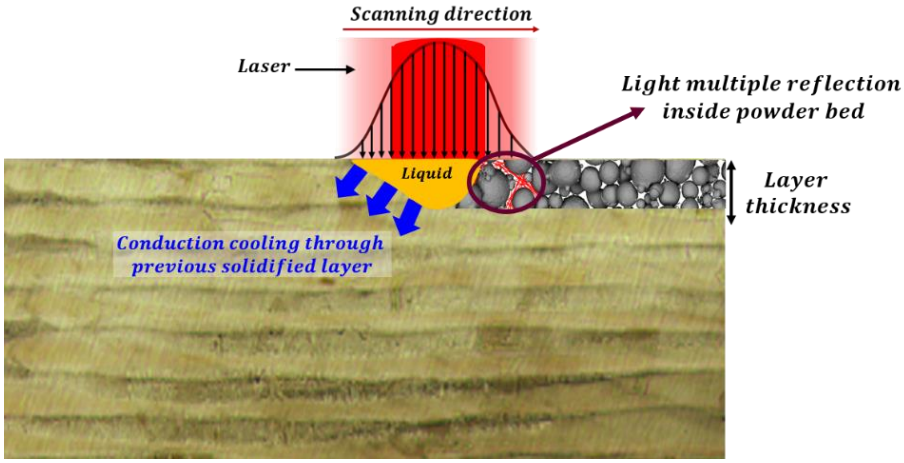

Figure 6. Schematic view of the SLM process indicating energy coupling and heat transfer paths considering the different states of the material (solid, liquid, powder).

Table 2. Optical properties of bronze, red gold, heat-treated red gold and 316L steel in the different states (solid (s), liquid (l), and powder (p)), at 1070 nm wavelength.

	α_s%	α_l%	α_{p_layer}%	δ (µm)
Bronze	11.05	11	44.27	27.30
Red Gold	10.8	10	20.82 (27.91)[a]	53.82(49.98)[a]
316L	29.05	20[80]	52.59	25.81

[a]. Thermally treated red gold powder

Table 3. Physical properties of solid (room temperature) /liquid (melting point) bronze, red gold, and 316L steel.

	Density (kg/m^3)	**Thermal diffusivity (m^2/s)**	**Specific heat (J/kg.K)**	**Melting/Boiling point point (K)**	**Latent heat of fusion/evaporation (kJ/kg)**
Bronze solid	8800[81]	1.8×10^{-5}[82]	371[83]	1163[83]	180[84]
Bronze Liquid	8800[a]	1.8×10^{-5} [a]	371[a]	2573[85]	1800
Red gold solid	15100[86]	2.1×10^{-5}	193[87]	1183[86]	62
Red gold liquid	15100[a]	2.1×10^{-5} [a]	193 [a]	3370[85]	620
316L solid	7900[88]	3.5×10^{-6}[88]	490[88]	1640[88]	260[88]
316L liquid	6920[88]	3.84×10^{-6}[88]	770[88]	3090[88]	7450[89]

[a]. same value for solid and liquid

The optimal normalized enthalpy value ($\overline{\Delta H^{opt}}$) in Equation (18), based on the powder absorptivity values of bronze or any other alloy A, $\alpha^{B}_{p\_layer}$ and $\alpha^{A}_{p\_layer}$ respectively, is:

$$\overline{\Delta H^{opt}} \approx \alpha^{B}_{p\_layer} \cdot M^{B} \cdot \left(\frac{P}{\sqrt{\omega^3 V}}\right)^{opt}_{B} = \alpha^{A}_{p\_layer} \cdot M^{A} \cdot \left(\frac{P}{\sqrt{\omega^3 V}}\right)^{opt}_{A} \quad (19)$$

From equation (19), the **translation rule** (20) follows, defining the optimal alloy A processing conditions:

$$\left(\frac{P}{\sqrt{\omega^3 V}}\right)^{opt}_{A} = \left(\frac{\alpha^{B}_{p\_layer}}{\alpha^{A}_{p\_layer}}\right) \cdot \left(\frac{P}{\sqrt{\omega^3 V}}\right)^{opt}_{B} \cdot \frac{M^{B}}{M^{A}} \quad , \quad (20)$$

where $\left(\frac{P}{\sqrt{\omega^3 V}}\right)^{opt}_{B}$ and $\left(\frac{P}{\sqrt{\omega^3 V}}\right)^{opt}_{A}$ represent the optimal SLM laser power and scanning speed for bronze and alloy A, respectively. Differences in laser spot size ω can also be accounted for.

3.3 Applying the translation rule to red gold and 316L

Normalized melt pool depths have been measured for the different investigated materials. Figure 7 shows the $\bar{d}(\overline{\Delta H})$ curve of the normalized melt pool vs the normalized enthalpy for bronze samples, considering only the powder layer contribution to $\overline{\Delta H}$ according to (18). Figure 7 captures well the transition between conduction and keyhole regimes, indicated by a significant change of the curve slope.

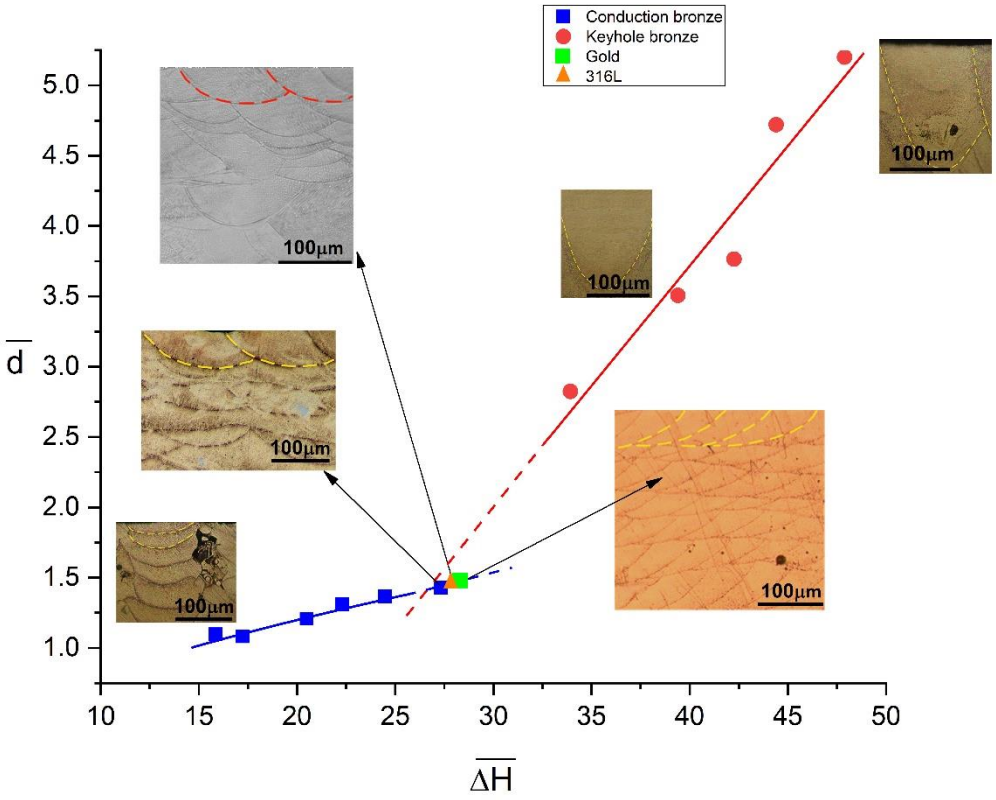

Figure 7. Normalized enthalpy of the printed bronze samples (Eq. (18)) versus the normalized melt pool depth. In green, the optimal conditions for the red gold sample. In black, the optimal conditions for 316L steel.

Translated parameters for printing red gold and 316L steel samples are listed in Table . They were determined by changing the laser power and speed such as to satisfy Equation (20). Only small adjustments were performed afterwards, leading to the optimum points for red gold and 316L represented by the green square and orange triangle in Figure . It is underlined that 316L steel was printed with a different laser spot size ω (65 µm instead of 85 µm), which explains the different hatching distance in Table 4, and also tests the generality of the translation rule. The hatching distance for the 316L steel sample has been chosen such as to keep about the same ratio between the beam diameter and the hatching distance as the one used for bronze.

Table 4. Bronze optimized parameters and translated ones for two different red gold powders and 316L steel.

	Power(W)	Speed(mm/s)	Hatching distance(µm)	Layer thickness(µm)	$\omega(\mu m)$
Bronze	250	200	150	40	42.5
Untreated red gold	500	188	150	40	42.5
Thermally treated red gold	375	200	150	40	42.5
316L	155	490	110	40	32.5

The analysis of microstructures confirms the very low porosity content in both red gold and 316L steel samples (Figures 8 and 9). These results show major improvements in printing gold alloy samples with a high relative density, compared to previous studies where the authors had to change the alloy composition to print samples with a reasonable density [11]. The porosity content for the thermally treated red gold powder sample is more important than for the untreated powder sample, which is attributed to the presence of oxide, known to promote porosity formation, and its stabilization and growth [90].

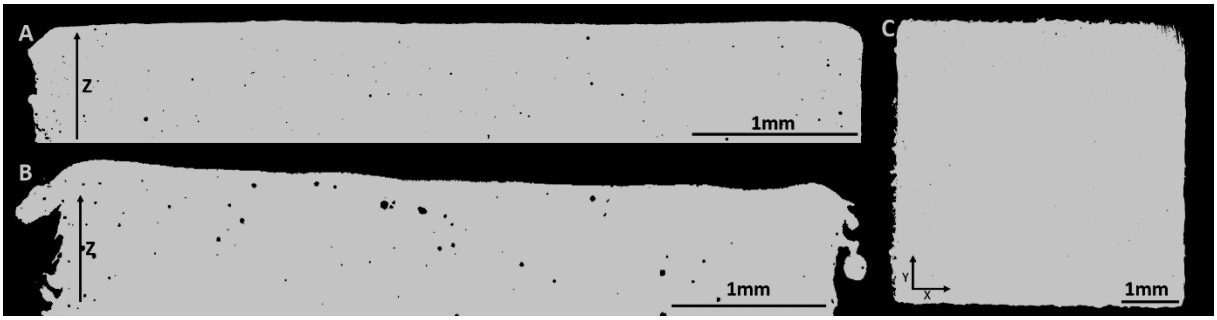

Figure 8. Micrographs of the printed red gold samples and 316L steel with translated parameters from bronze, A) untreated red gold, B) thermally treated red gold, and C) 316L steel.

The optimal normalized enthalpy ($\overline{\Delta H}$), normalized melt pool depth ($\bar{d}$), and relative densities values for bronze, red gold, and 316L samples are summarized in Figure 9. Process parameters slightly on the right of the optimal zone would bring closer to the onset of the keyhole mode, and, on the other hand, using parameters on the left side of the optimal point would decrease the melt pool size and increase the porosity content (see supplementary section S2). However, samples printed with process parameters close to the optimal zone always keep high relative densities compared to those with very different $\overline{\Delta H}$ values. This is in fact the interesting feature of the proposed model, as printing samples close to the reported optimal value guarantees low porosity content. The outcome is important not only when dealing with precious powders like gold, but also for any new material, for which the number of trials and errors is reduced.

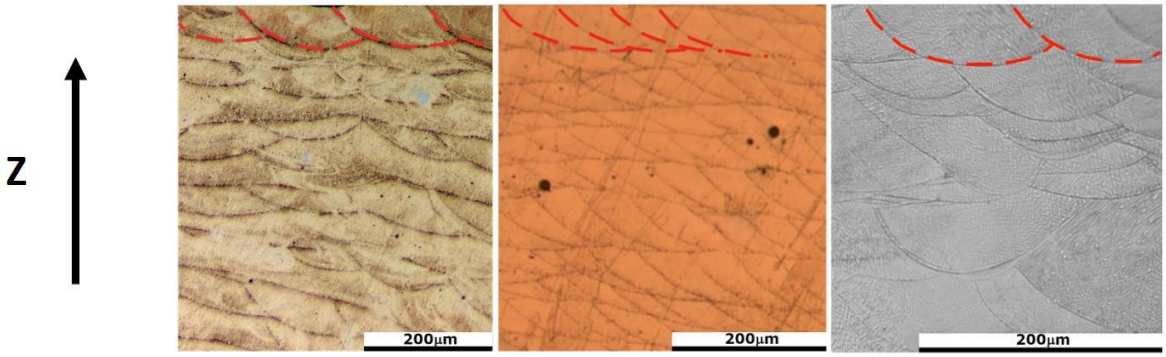

Material	Bronze	Red gold	316L
$\overline{\Delta H}$	27.34	28.31	27.90
$\bar{d}$	1.429	1.482	1.475
Relative density %	99.87	99.81(99.4)[a]	99.95

[a]. Thermally treated red gold powder

Figure 9. a) Micrographs showing the melt pool geometry (Note: the vertical arrow indicates the build-up direction) b) Normalized enthalpy, normalized melt pool values, and relative densities of bronze, red gold, and 316L samples printed using the translation rule.

3.4 Finite element simulations

Finite element simulations of SLM were performed in order to check the validity of the approximations made in the previous section: (i) consider the bulk solid value for the thermal diffusivity in Equation (18), and (ii) only consider the powder layer absorptivity in the translation rule (20).

Figure 10 shows the FEM simulated and experimental melt pool depth values for printed bronze samples, using the optical and physical parameters given in Tables 2 and 3. In the conduction mode, there is a good agreement with experiments, when considering three phases (powder, bulk solid, and melt) with different values of absorptivity and thermal diffusivity. Using the bulk solid value for the diffusivity (Table 3), the predicted melt pool sizes vary by less than 10%, which reasonably validates the assumption (i) recalled above.

As the fluid flow and the keyhole formation mechanism are not considered in the numerical model, the simulated melt pools depths in the keyhole mode are, as expected, strongly underestimated. However, since the optimal process zone corresponds to much lower normalized enthalpies (conduction mode), such calculations are actually not needed to validate our approximations (i) and (ii), and the resulting translation rule.

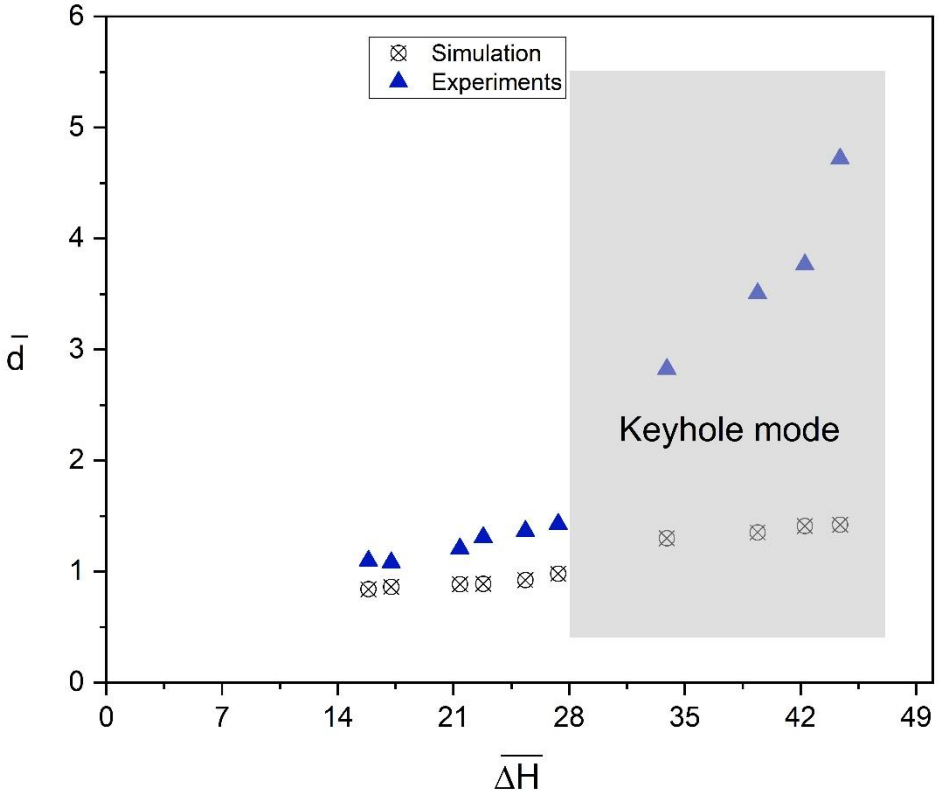

Figure 10. Experimental and simulated melt pool depth values for printed bronze samples.

Figure 11 (A-B) indicates the temperature distributions predicted by the finite element simulations applied to bronze and red gold, in steady-state conditions (the liquid phase appears in yellow to red). The selected SLM conditions are the identified optimal ones shown in Figure and detailed in Table 4. Thermal gradients look similar for both materials. However, the absolute values of temperatures are higher in red gold. Figure 11 (C-D) represent the laser intensity absorbed by the material and show how it distributes between the powder and the liquid. These results demonstrate a significant direct interaction between the laser source and the powder bed during the manufacturing process, besides the interaction with the melt pool. As described earlier, the penetration of the light into the depth of the powder bed is implemented in the code such that the heat source term becomes volumetric [89]. This feature is of high importance when defining a layer thickness ensuring metallurgical contact with the previously solidified material. The amount of light absorbed at the front of the melt pool as observed in the simulations influences the thermal interactions strongly, and therefore the melt pool geometry.

The changes in the laser power and scanning speed described in Table , using the translation rule, were based on approximations (i) and (ii). Approximation (ii) can be further investigated with the present simulations, looking at the interaction of the laser with both the powder bed and the liquid, and computing their relative contributions to thermal exchanges.

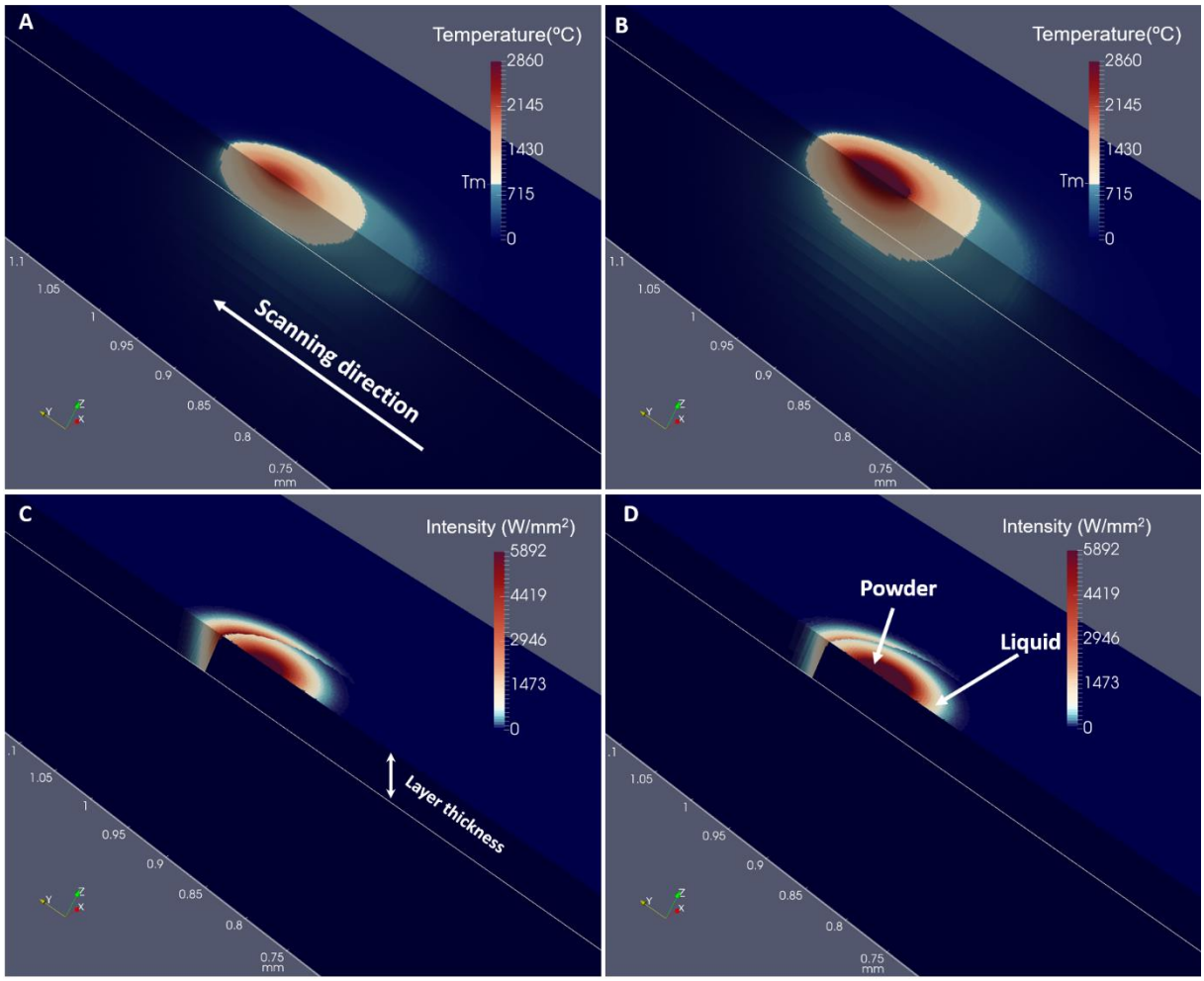

Figure 11. Simulation results of the SLM process for bronze and red gold, in optimal conditions. (A-B) temperature field in bronze and red gold (°C), respectively, (C-D) laser absorbed intensity (W/mm^2) for bronze and red gold, respectively.

Figure 12 indicates, in the steady-state, the fraction of the total absorbed power in bronze which goes to the powder bed $\left(\frac{\alpha_p^B \,.\, P_p}{<\alpha>^B .P_0}\right)$, for different normalized enthalpy values, while the complementary part is being absorbed by the liquid. For small values of $\overline{\Delta H}$ (faster scanning speed, lower laser power), the fraction absorbed by the powder is higher, and we conclude that powder absorption dominates the process. However, this regime leads to an increase in porosity content related to lack of fusion. At larger values of $\overline{\Delta H}$, the relative density increases and reaches its maximum at the near keyhole threshold, indicated by the green point in Figure 12. At this point, almost 26% of the power remains absorbed by the powder bed. Larger values of $\overline{\Delta H}$ lead to keyhole formation which cannot be modelled with the finite element model, as already mentioned, which means that the computed fraction of absorbed power in the liquid is most likely underestimated. Again, this is not an issue in practice, as we are only interested in the conduction mode regime.

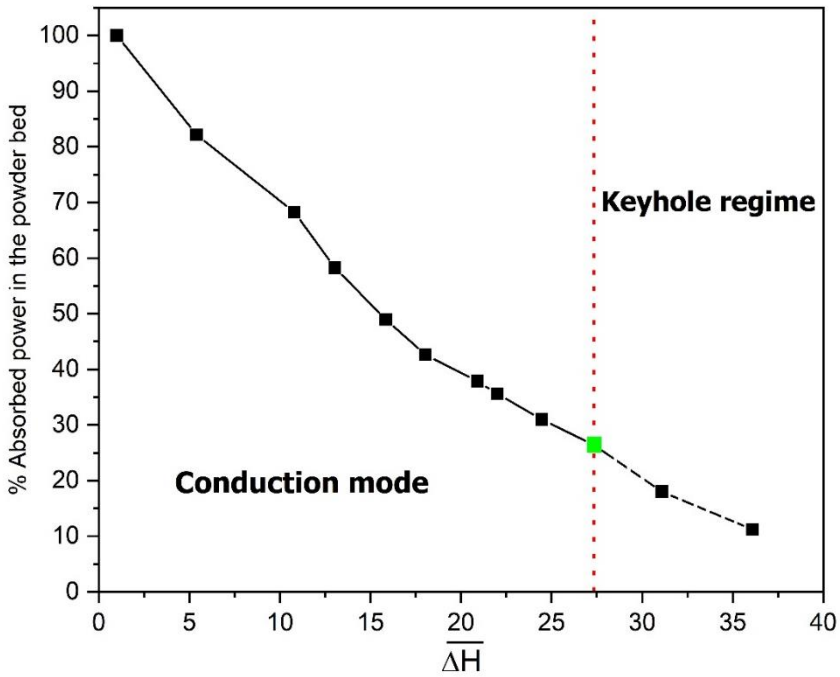

Figure 12. Simulated fraction of the total absorbed power in bronze going to the powder bed, after melt pool stabilization. The optimal processing condition (highest relative density) is highlighted in green. The dashed line corresponds to the keyhole regime, whose mechanism is not modeled, and is therefore only an extrapolation.

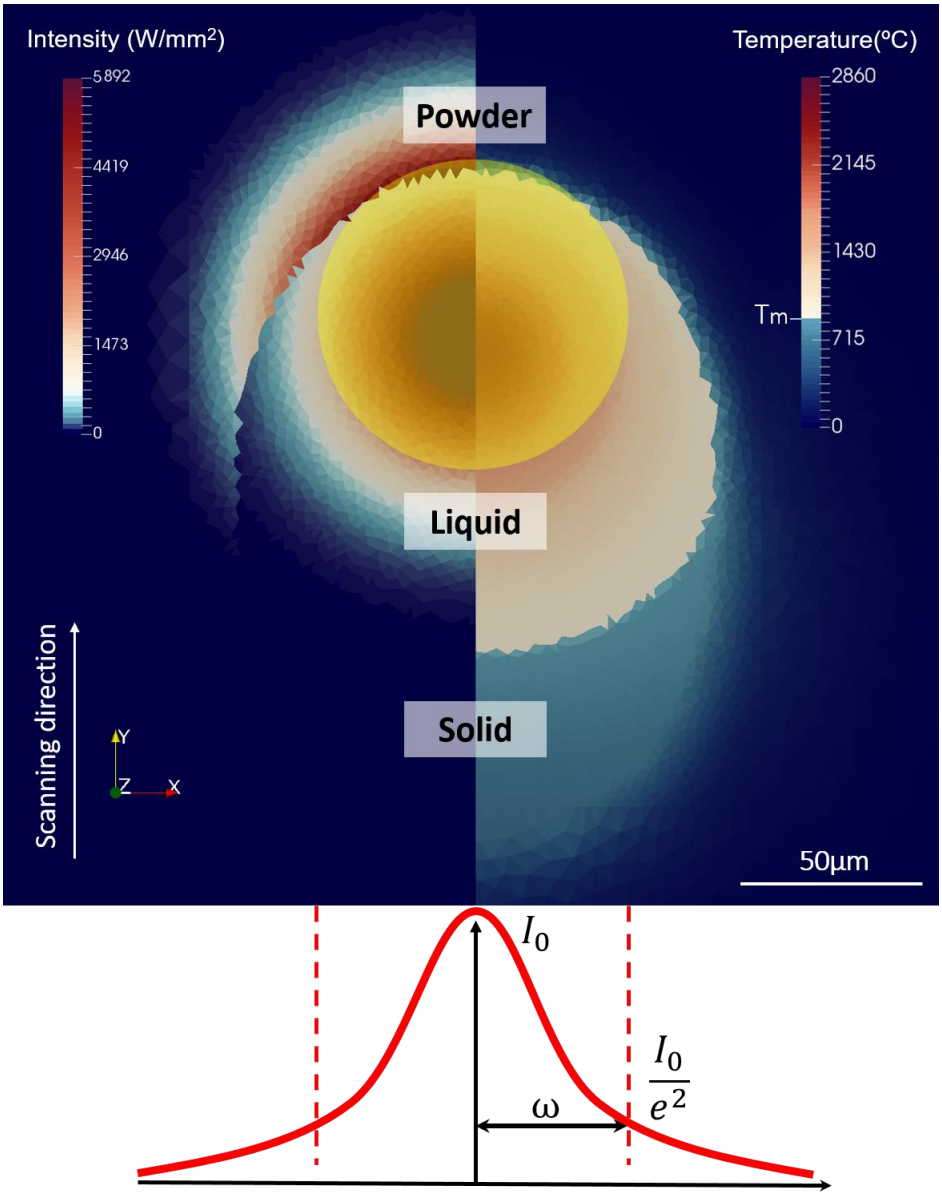

Figure 13. Simulated temperature distribution (right) and absorbed power intensity in powder bed and melt pool (W/mm^2) (left) in bronze, during the SLM process. The laser beam size (1/e^2) is represented by the yellow circle. A Gaussian profile schematically indicates the beam intensity distribution corresponding to the laser beam size.

Figure 13 indicates how the input power is distributed into the melt pool and the powder bed, compared to the beam location. The absorbed power is represented on the left part of the image, and the temperature field is given on the right side (the liquid phase appears in yellow to red). The beam spot size is superimposed (yellow circle), considering a spot size definition at 1/e^2 of the maximum intensity. With this definition, the laser beam mainly interacts with the liquid phase, however a small part of the beam and the tails of the Gaussian distribution do cover the powder bed as well, and this is particularly clear ahead of the melt pool, where the absorbed power is increased due to the higher absorptivity and

penetration depth of the powder. These results are in agreement with [36,46] where authors both numerically and experimentally studied the total absorptivity evolution during the SLM process. Their results indicate that the total absorptivity is dominated by the powder bed at the beginning of the melting process, still allowing multiple reflections to occur. Melting and wetting of the powder material also result in a relatively flat surface and reduce the total absorptivity. Moreover, from [91], it is also found that in the conduction mode, multiple reflections inside the powder bed occur in the front head of the melt pool. We can therefore conclude that powders essentially heat ahead of the melt pool due to light being directly absorbed by the powder particles.

To understand better the applicability of the translation rule, the ratio $G^j = \frac{\langle\alpha\rangle^j}{\alpha^j_{p\_layer}}$ is plotted in Figure 14 as a function of the normalized enthalpy, using the FEM calculated values of $\langle\alpha\rangle^j$.

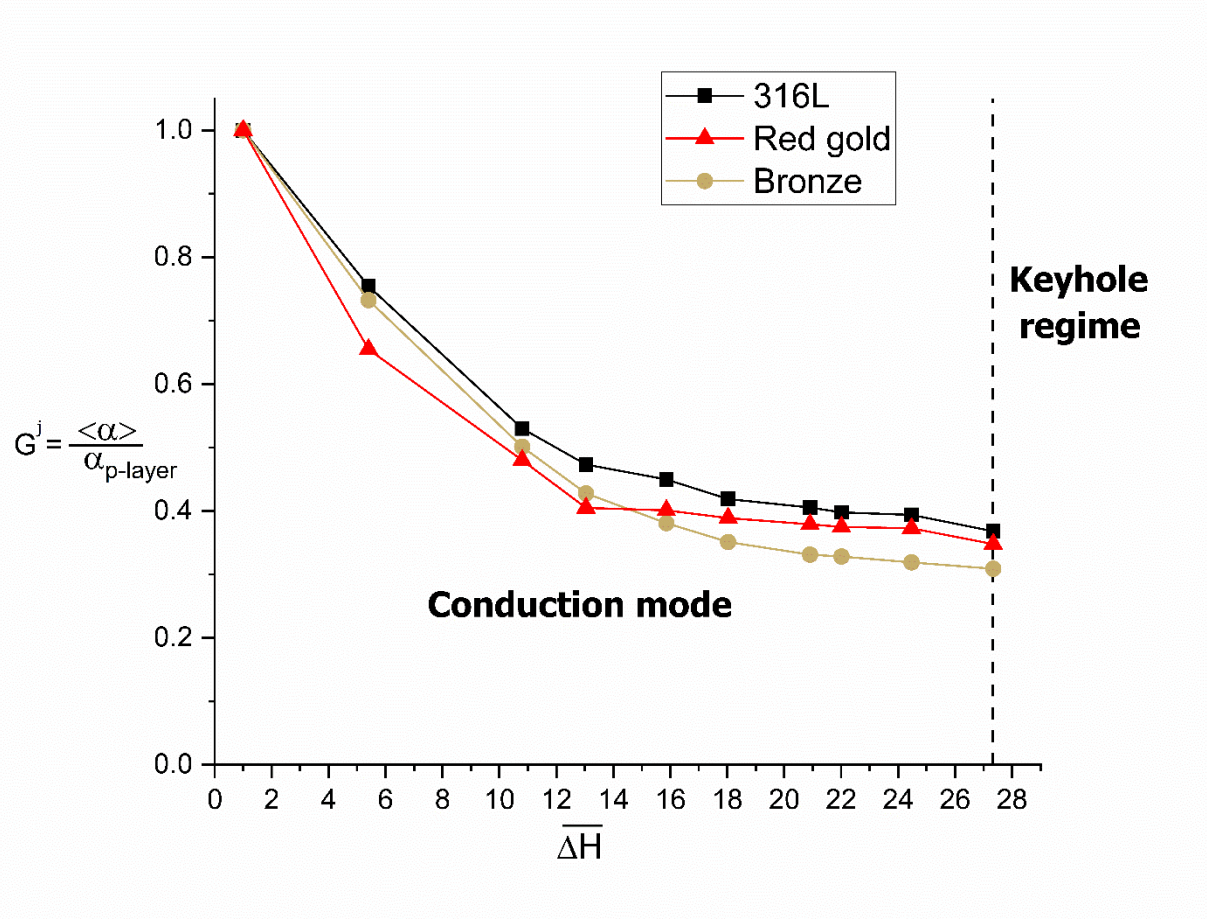

Figure 14. The ratio of simulated effective powder absorptivity to powder layer measured absorptivity, G^j, versus normalized enthalpy for bronze, red gold, and 316L steel, in the conduction mode. The vertical dotted line corresponds to the optimal $\overline{\Delta H}$, i.e. the near keyhole threshold.

At very small values of $\overline{\Delta H}$, G^j tends to 1 since there is not enough input energy to form a liquid phase, i.e. the laser only interacts with powder particles. For increasing values of $\overline{\Delta H}$, the powder contribution decreases. The G^j variation is systematically dominated by the higher reflectivity of the liquid phase (regardless of the material) in comparison to that of the powder bed.

We can notice that the value of G^j for different materials at different $\overline{\Delta H}$ values are quite similar, so that we can consider this value to be indeed *material insensitive*, especially when approaching the transition between the conduction mode and the keyhole regime. This can be summarized by the following equation (which is only valid for the conduction mode):

$$\left(\frac{\alpha^{B}_{p\_layer}}{\alpha^{A}_{p\_layer}}\right) \cong \left(\frac{\langle\alpha\rangle^{B}}{\langle\alpha\rangle^{A}}\right) \tag{21}$$

These results clearly validate the second approximation (ii) in the translation rule, i.e. the material insensitivity of the G^j value in Equation (17).

For the three materials covered in this study, G^j values at the optimal condition vary in the range 0.30-0.38. Considering typical layer thicknesses values used in the SLM process [92], optical penetration depths in the powder bed, and different values for liquid and powder absorptivities, it is possible to identify, from Equation (17), ranges of values for $\frac{L}{\delta}$ and $\frac{\alpha_l^j}{\alpha_p^j}$ which result in similar G^j values :

$$\left.\begin{array}{l} 0.1 < \frac{L}{\delta} < 3.5 \\ 0.1 < \frac{\alpha_l^j}{\alpha_p^j} < 0.4 \end{array}\right\} \quad \rightarrow \quad 0.30 < G^j < 0.38 \tag{22}$$

Any material for which relations (22) are satisfied should, in principle, be suitable for optimizing the SLM conditions through the translation rule. The supplementary section S3 gives additional details concerning the optical properties measured for powder and bulk materials investigated in this work.

In summary, it is here demonstrated that the proposed translation rule can predict optimal process parameters for a large range of materials, using a simple powder layer absorptivity measurement performed at room temperature.

The validity of the translation rule is related to the importance of the powder absorptivity ahead of the melt pool, when operating in the conduction mode. Light penetrates deeply into the powder bed and largely influences the overall thermal behavior of the melt pool. The story completely changes when entering the keyhole regime, as the complex melt pool geometry then starts absorbing most of the incident light and consequently removes the effect of the powder absorptivity [93,94].

4. Summary

In this study, a model has been developed to translate optimized SLM process parameters from one material to another, based on one simple measurement of powder absorptivity at room temperature. It has been applied to bronze, red gold and 316L stainless steel, and validated experimentally. Finite element simulations considering variable absorptivities and thermal properties for different materials and states justify the translation rule and its generality. The following conclusions can be drawn:

(1) SLM process parameters for bronze have been optimized to achieve a high relative density of 99.87 %. The optimized parameters correspond to the transition zone between conduction and keyhole modes, and are conveniently identified by plotting the normalized melt pool depth versus the normalized enthalpy of the material.

(2) The bronze optimized parameters have been translated to red gold and 316L steel, based on the difference in materials thermal properties and measured powder absorptivity. 2D image analysis of metallographic cross-sections show samples with excellent quality, and a porosity content equivalent to the bronze one. To the authors' knowledge, the amount of porosity results is the highest relative density (99.81%) achieved for an additively manufactured 18-carat gold alloy, when using an infrared laser.

(3) The temperature field and the laser power absorbed by the material during the SLM process have been numerically calculated using an in house finite element code. The simulation results indicate the importance of the powder absorptivity and light penetration inside the powder bed. Furthermore, the effective absorptivity of the material is following the same trend as the powder layer absorptivity, for different values of the normalized enthalpy, in the conduction mode. These results demonstrate that using the room temperature powder layer absorptivity for translating parameters from one material to another in SLM is valid.

(4) The generality of the translation rule has been checked by considering three different materials and two different laser spot sizes.

Further studies are ongoing in order to check the sensitivity of the model to $\overline{\Delta H}$ variations for different materials. The proposed translation rule will be further investigated by looking at the sample size and at

geometrical effects. In addition, an improvement in the finite element formulation will consider the light propagation in all three directions, as the current model only considers a propagation along the depth (z) direction. 3D propagation could be based on ray tracing models [63,64].

The proposed translation rule does not take into account all details of the SLM process (and many are important); however, it was demonstrated to be a powerful approach to translate the optimal parameters from one material to another, using straightforward measurements.

Acknowledgments

This work has been supported by the "Additive Manufacturing and Metallic Microstructures (AM3) " project. The project is funded by the Competence Center for Materials Science and Technology (CCMX) and by a Swiss industrial consortium. The generous support of PX Group to the LMTM laboratory is also highly acknowledged.

References

[1] G.N. Levy, R. Schindel, J.P. Kruth, Rapid manufacturing and rapid tooling with layer manufacturing (LM) technologies, state of the art and future perspectives, CIRP Ann. - Manuf. Technol. 52 (2003) 589–609. doi:10.1016/S0007-8506(07)60206-6.

[2] J. Mutua, S. Nakata, T. Onda, Z. Chen, Optimization of selective laser melting parameters and in fl uence of post heat treatment on microstructure and mechanical properties of maraging steel, Mater. Des. 139 (2018) 486–497. doi:10.1016/j.matdes.2017.11.042.

[3] E. Liverani, S. Toschi, L. Ceschini, A. Fortunato, Effect of selective laser melting (SLM) process parameters on microstructure and mechanical properties of 316L austenitic stainless steel, J. Mater. Process. Tech. 249 (2017) 255–263. doi:10.1016/j.jmatprotec.2017.05.042.

[4] W.M. Tucho, V.H. Lysne, H. Austbø, A. Sjolyst-kverneland, Investigation of effects of process parameters on microstructure and hardness of SLM manufactured SS316L, J. Alloys Compd. 740 (2018) 910–925. doi:10.1016/j.jallcom.2018.01.098.

[5] M. Tang, P.C. Pistorius, J.L. Beuth, Prediction of lack-of-fusion porosity for powder bed fusion, Addit. Manuf. 14 (2017) 39–48. doi:10.1016/j.addma.2016.12.001.

[6] B. Zhang, Y. Li, Q. Bai, Defect Formation Mechanisms in Selective Laser Melting: A Review, Chinese J. Mech. Eng. 30 (2017) 515–527. doi:10.1007/s10033-017-0121-5.

[7] F. Cooper, Sintering And Additive Manufacturing: The New Paradigm for the Jewelry Manufacturer, Proc. St. Fe Symp. Jewel. Manuf. Technol. (2012) 103–122.

[8] P.A.M. Damiano Zito, Silvano Bortolamei, Alessio Carlotto, Prof. Ilaria Cristofolini, Alessandro Loggi, Latest developments in Selective Laser Melting production of gold jewellery, in: St. Fe Symp., 2012: pp. 1–18.

[9] B.J. Fischer-buehner, P. Poliero, R. Bertoncello, A. Basso, L.G.S. A, J. Fischer-buehner, P. Poliero, R. Bertoncello, A. Basso, M. Poliero, Rapid Jewelry Manufacturing By Laser Melting of Precious Metal Powders (PLM): Fiction Or Future ?, Proc. St. Fe Symp. Jewel. Manuf. Technol. (2011) 177–202.

[10] D. Zito, A. Carlotto, A. Loggi, P. Sbornicchia, D. Maggian, S.A. Progold, T. Vi, M. Fockele, P. Unterberg, Optimization of the Main Selective Laser Melting Technology Parameters in the Production of Precious Metal Jewelry, Proc. St. Fe Symp. Jewel. Manuf. Technol. (2013) 1–20.

[11] U.E. Klotz, D. Tiberto, F. Held, Optimization of 18-karat yellow gold alloys for the additive manufacturing of jewelry and watch parts, Gold Bull. 50 (2017) 111–121. doi:10.1007/s13404-017-0201-4.

[12] U.E. Klotz, D. Tiberto, F. Held, U.E. Klotz, D. Tiberto, F. Held, " Additive Manufacturing of 18-Karat Yellow-Gold alloys ," in: Jewel. Technol. Forum 2, 2017.

[13] M. Khan, P. Dickens, Selective Laser Melting (SLM) of pure gold, Gold Bull. 43 (2010) 114–121. doi:10.1007/BF03214976.

[14] U. Scipioni Bertoli, A.J. Wolfer, M.J. Matthews, J.P.R. Delplanque, J.M. Schoenung, On the limitations of Volumetric Energy Density as a design parameter for Selective Laser Melting, Mater. Des. 113 (2017) 331–340. doi:10.1016/j.matdes.2016.10.037.

[15] S. Ghouse, S. Babu, R.J. Van Arkel, K. Nai, P.A. Hooper, J.R.T. Jeffers, The influence of laser parameters and scanning strategies on the mechanical properties of a stochastic porous material, Mater. Des. 131 (2017) 498–508. doi:10.1016/j.matdes.2017.06.041.

[16] L. Quintino, A. Costa, R. Miranda, D. Yapp, V. Kumar, C.J. Kong, Welding with high power fiber lasers - A preliminary study, Mater. Des. 28 (2007) 1231–1237. doi:10.1016/j.matdes.2006.01.009.

[17] J.J.S. Dilip, S. Zhang, C. Teng, K. Zeng, C. Robinson, D. Pal, B. Stucker, Influence of processing parameters on the evolution of melt pool, porosity, and microstructures in Ti-6Al-4V alloy parts fabricated by selective laser melting, Prog. Addit. Manuf. 2 (2017) 157–167. doi:10.1007/s40964-017-0030-2.

[18] A. Keshavarzkermani, E. Marzbanrad, R. Esmaeilizadeh, Y. Mahmoodkhani, U. Ali, P.D. Enrique, N.Y. Zhou, A. Bonakdar, E. Toyserkani, An investigation into the effect of process

parameters on melt pool geometry, cell spacing, and grain refinement during laser powder bed fusion, Opt. Laser Technol. 116 (2019) 83–91. doi:10.1016/j.optlastec.2019.03.012.

[19] C. Zhao, K. Fezzaa, R.W. Cunningham, H. Wen, F. De Carlo, L. Chen, A.D. Rollett, T. Sun, Real-time monitoring of laser powder bed fusion process using high-speed X-ray imaging and diffraction, Sci. Rep. 7 (2017) 3602. doi:10.1038/s41598-017-03761-2.

[20] R. Cunningham, C. Zhao, N. Parab, C. Kantzos, J. Pauza, K. Fezzaa, T. Sun, A.D. Rollett, Keyhole threshold and morphology in laser melting revealed by ultrahigh-speed x-ray imaging, Science (80-.). 363 (2019) 849–852. doi:10.1126/science.aav4687.

[21] E. Soylemez, High deposition rate approach of selective laser melting through defocused single bead experiments and thermal finite element analysis for Ti-6Al-4V, Addit. Manuf. 31 (2020) 100984. doi:10.1016/j.addma.2019.100984.

[22] J. Metelkova, Y. Kinds, K. Kempen, C. de Formanoir, A. Witvrouw, B. Van Hooreweder, On the influence of laser defocusing in Selective Laser Melting of 316L, Addit. Manuf. 23 (2018) 161–169. doi:10.1016/j.addma.2018.08.006.

[23] J.C. Ion, H.R. Shercliff, M.F. Ashby, Diagrams for laser materials processing, Acta Metall. Mater. 40 (1992) 1539–1551. doi:10.1016/0956-7151(92)90097-X.

[24] R. Rai, J.W. Elmer, T.A. Palmer, T. Debroy, Heat transfer and fluid flow during keyhole mode laser welding of tantalum, Ti-6Al-4V, 304L stainless steel and vanadium, J. Phys. D. Appl. Phys. 40 (2007) 5753–5766. doi:10.1088/0022-3727/40/18/037.

[25] D.W. Bäuerle, Laser Processing and Chemistry, 4th ed., Springer-Verlag Berlin Heidelberg, 2011. doi:10.1007/978-3-642-17613-5.

[26] T.C. Chawla, D.L. Graff, R.C. Borg, G.L. Bordner, D.P. Weber, D. Miller, Thermophysical properties of mixed oxide fuel and stainless steel type 316 for use in transition phase analysis, Nucl. Eng. Des. 67 (1981) 57–74. doi:10.1016/0029-5493(81)90155-2.

[27] D.B. Hann, J. Iammi, J. Folkes, A simple methodology for predicting laser-weld properties from material and laser parameters, J. Phys. D. Appl. Phys. 44 (2011). doi:10.1088/0022-3727/44/44/445401.

[28] P. Promoppatum, S.C. Yao, Analytical evaluation of defect generation for selective laser melting of metals, Int. J. Adv. Manuf. Technol. 103 (2019) 1185–1198. doi:10.1007/s00170-019-03500-z.

[29] A.M. Kiss, A.Y. Fong, N.P. Calta, V. Thampy, A.A. Martin, P.J. Depond, J. Wang, M.J.

Matthews, R.T. Ott, C.J. Tassone, K.H. Stone, M.J. Kramer, A. van Buuren, M.F. Toney, J. Nelson Weker, Laser-Induced Keyhole Defect Dynamics during Metal Additive Manufacturing, Adv. Eng. Mater. 21 (2019) 1–7. doi:10.1002/adem.201900455.

[30] W.E. King, H.D. Barth, V.M. Castillo, G.F. Gallegos, J.W. Gibbs, D.E. Hahn, C. Kamath, A.M. Rubenchik, Observation of keyhole-mode laser melting in laser powder-bed fusion additive manufacturing, J. Mater. Process. Technol. 214 (2014) 2915–2925. doi:10.1016/j.jmatprotec.2014.06.005.

[31] X. Jian, C.S. Wu, G. Zhang, J. Chen, A unified 3D model for an interaction mechanism of the plasma arc, weld pool and keyhole in plasma arc welding, J. Phys. D. Appl. Phys. 48 (2015). doi:10.1088/0022-3727/48/46/465504.

[32] S. Elena-manuela, U.T. Brasov, O. Dontu, Mechanism of keyhole formation and stability instationary laser welding, J. Phys. D. Appl. Phys. 35 (2002) 1570–1576.

[33] M. Rasch, C. Roider, S. Kohl, J. Strauß, N. Maurer, K.Y. Nagulin, M. Schmidt, Shaped laser beam profiles for heat conduction welding of aluminium-copper alloys, Opt. Lasers Eng. 115 (2019) 179–189. doi:10.1016/j.optlaseng.2018.11.025.

[34] E. Assuncao, S. Williams, D. Yapp, Interaction time and beam diameter effects on the conduction mode limit, Opt. Lasers Eng. 50 (2012) 823–828. doi:10.1016/j.optlaseng.2012.02.001.

[35] A.M. Rubenchik, W.E. King, S.S. Wu, Scaling laws for the additive manufacturing, J. Mater. Process. Tech. 257 (2018) 234–243. doi:10.1016/j.jmatprotec.2018.02.034.

[36] J. Ye, S.A. Khairallah, A.M. Rubenchik, M.F. Crumb, G. Guss, J. Belak, M.J. Matthews, Energy Coupling Mechanisms and Scaling Behavior Associated with Laser Powder Bed Fusion Additive Manufacturing, Adv. Eng. Mater. 1900185 (2019) 1–9. doi:10.1002/adem.201900185.

[37] R. Fabbro, Scaling laws for the laser welding process in keyhole mode, J. Mater. Process. Tech. 264 (2019) 346–351. doi:10.1016/j.jmatprotec.2018.09.027.

[38] M. Thomas, G.J. Baxter, I. Todd, Normalised model-based processing diagrams for additive layer manufacture of engineering alloys, Acta Mater. 108 (2016) 26–35. doi:10.1016/j.actamat.2016.02.025.

[39] L. Johnson, M. Mahmoudi, B. Zhang, R. Seede, X. Huang, J.T. Maier, H.J. Maier, I. Karaman, A. Elwany, R. Arróyave, Assessing printability maps in additive manufacturing of metal alloys, Acta Mater. 176 (2019) 199–210. doi:10.1016/j.actamat.2019.07.005.

[40] Z.H. Shen, S.Y. Zhang, J. Lu, X.W. Ni, Mathematical modeling of laser induced heating and melting in solids, 33 (2001) 533–537.

[41] C.D. Boley, S.A. Khairallah, A.M. Rubenchik, Calculation of laser absorption by metal powders in additive manufacturing, Appl. Opt. 54 (2015) 2477. doi:10.1364/AO.54.002477.

[42] D. Sowdari, P. Majumdar, Finite element analysis of laser irradiated metal heating and melting processes, Opt. Laser Technol. 42 (2010) 855–865. doi:10.1016/j.optlastec.2009.11.022.

[43] X.C. Wang, T. Laoui, J. Bonse, J.P. Kruth, B. Lauwers, L. Froyen, Direct Selective Laser Sintering of Hard Metal Powders: Experimental Study and Simulation, Int. J. Adv. Manuf. Technol. 19 (2002) 351–357. doi:10.1007/s001700200024.

[44] P. Meakin, R. Jullien, Restructuring effects in the rain model for random deposition, J. Phys. 48 (1987) 1651–1662.

[45] Y.H. Zhou, Z.H. Zhang, Y.P. Wang, G. Liu, S.Y. Zhou, Y.L. Li, J. Shen, M. Yan, Selective laser melting of typical metallic materials: An effective process prediction model developed by energy absorption and consumption analysis, Addit. Manuf. 25 (2019) 204–217. doi:https://doi.org/10.1016/j.addma.2018.10.046.

[46] J. Trapp, A.M. Rubenchik, G. Guss, M.J. Matthews, In situ absorptivity measurements of metallic powders during laser powder-bed fusion additive manufacturing, Appl. Mater. Today. 9 (2017) 341–349. doi:10.1016/j.apmt.2017.08.006.

[47] O. Loebich, The optical properties of gold, Gold Bull. 5 (1972) 2–10. doi:10.1007/BF03215148.

[48] J.N. Hodgson, The optical properties of gold, J. Phys. Chem. Solids. 29 (1968) 2175–2181. doi:10.1016/0022-3697(68)90013-9.

[49] Mark Fox, Optical Properties of Solids, Second Edi, Oxford University Press, Oxford, United Kingdom, 2010.

[50] C. Deng, J. Kang, T. Feng, Y. Feng, X. Wang, P. Wu, Study on the selective laser melting of CuSn10 powder, Materials (Basel). 11 (2018) 1–7. doi:10.3390/ma11040614.

[51] S. Scudino, C. Unterdörfer, K.G. Prashanth, H. Attar, N. Ellendt, V. Uhlenwinkel, J. Eckert, Additive manufacturing of Cu-10Sn bronze, Mater. Lett. 156 (2015) 202–204. doi:10.1016/j.matlet.2015.05.076.

[52] J. Ye, A.M. Rubenchik, M.F. Crumb, G. Guss, M.J. Matthews, Laser Absorption and Scaling Behavior in Powder Bed Fusion Additive Manufacturing of Metals, in: Conf. Lasers Electro-

Optics, Optical Society of America, San Jose, California, 2018: p. JW2A.117.

[53] H.G. Kim, W.R. Kim, O. Kwon, G.B. Bang, M.J. Ham, H.-K. Park, K.-H. Jung, K.M. Kim, C.-W. Lee, G.-H. Kim, Laser beam melting process based on complete-melting energy density for commercially pure titanium, J. Manuf. Process. 45 (2019) 455–459. doi:10.1016/j.jmapro.2019.07.031.

[54] J. Zhang, D. Gu, Y. Yang, H. Zhang, H. Chen, D. Dai, K. Lin, Influence of Particle Size on Laser Absorption and Scanning Track Formation Mechanisms of Pure Tungsten Powder during Selective Laser Melting, Engineering. (2019). doi:10.1016/j.eng.2019.07.003.

[55] D. Moser, S. Pannala, J. Murthy, Computation of Effective Thermal Conductivity of Powders for Selective Laser Sintering Simulations, J. Heat Transfer. 138 (2016) 1–9. doi:10.1115/1.4033351.

[56] N. Sakatani, K. Ogawa, Y. Iijima, M. Arakawa, R. Honda, S. Tanaka, Thermal conductivity model for powdered materials under vacuum based on experimental studies, AIP Adv. 7 (2017). doi:10.1063/1.4975153.

[57] J. Yin, H. Zhu, L. Ke, P. Hu, C. He, H. Zhang, X. Zeng, A finite element model of thermal evolution in laser micro sintering, Int. J. Adv. Manuf. Technol. 83 (2016) 1847–1859. doi:10.1007/s00170-015-7609-x.

[58] S.A. Khairallah, A. Anderson, Mesoscopic simulation model of selective laser melting of stainless steel powder, J. Mater. Process. Technol. 214 (2014) 2627–2636. doi:10.1016/j.jmatprotec.2014.06.001.

[59] U. Scipioni Bertoli, G. Guss, S. Wu, M.J. Matthews, J.M. Schoenung, In-situ characterization of laser-powder interaction and cooling rates through high-speed imaging of powder bed fusion additive manufacturing, Mater. Des. 135 (2017) 385–396. doi:10.1016/j.matdes.2017.09.044.

[60] J. Jhabvala, Study of the consolidation process under macro- and microscopic thermal effects in selective laser sintering and selective laser melting, EPFL PP - Lausanne, n.d. doi:10.5075/epfl-thesis-4609.

[61] J. Mingear, B. Zhang, D. Hartl, A. Elwany, Effect of process parameters and electropolishing on the surface roughness of interior channels in additively manufactured nickel-titanium shape memory alloy actuators, Addit. Manuf. 27 (2019) 565–575. doi:https://doi.org/10.1016/j.addma.2019.03.027.

[62] K.-E. Peiponen, T. Tsuboi, Metal surface roughness and optical reflectance, Opt. Laser Technol. 22 (1990) 127–130. doi:https://doi.org/10.1016/0030-3992(90)90022-V.

[63] A. V. Gusarov, I. Yadroitsev, P. Bertrand, I. Smurov, Model of Radiation and Heat Transfer in Laser-Powder Interaction Zone at Selective Laser Melting, J. Heat Transfer. 131 (2009) 072101. doi:10.1115/1.3109245.

[64] A. V. Gusarov, J.P. Kruth, Modelling of radiation transfer in metallic powders at laser treatment, Int. J. Heat Mass Transf. 48 (2005) 3423–3434. doi:10.1016/j.ijheatmasstransfer.2005.01.044.

[65] Y. Tokura, Optical and magnetic properties of transition metal oxides, Curr. Opin. Solid State Mater. Sci. 3 (1998) 175–180. doi:10.1016/S1359-0286(98)80085-5.

[66] S.D. Jadhav, J. Vleugels, J.-P. Kruth, J. Van Humbeeck, K. Vanmeensel, Mechanical and electrical properties of selective laser-melted parts produced from surface-oxidized copper powder, Mater. Des. Process. Commun. 0 (2019) e94. doi:10.1002/mdp2.94.

[67] T. Polivnikova, Study and Modelling of the Melt Pool Dynamics during Selective Laser Sintering and Melting, EPFL PP - Lausanne, n.d. doi:10.5075/epfl-thesis-6826.

[68] E. Boillat, Finite element methods on non-conforming grids by penalizing the matching constraint, ESAIM M2AN. 37 (2003) 357–372. https://doi.org/10.1051/m2an:2003031.

[69] D. Bergström, The Absorption of Laser Light by Rough Metal Surfaces, Luleå University of Technology, 2008.

[70] R. Glardon, N. Karapatis, V. Romano, Influence of Nd: YAG parameters on the selective laser sintering of metallic powders, CIRP Ann. - Manuf. Technol. 50 (2001) 133–136. doi:10.1016/S0007-8506(07)62088-5.

[71] J. Jhabvala, E. Boillat, R. Glardon, On the use of EBSD analysis to investigate the microstructure of gold samples built by selective laser melting, Gold Bull. 44 (2011) 113–118. doi:10.1007/s13404-011-0017-6.

[72] M. Schmid, S. Zehnder, P. Schwaller, B. Neuenschwander, M. Held, U. Hunziker, J. Zürcher, Measuring optical properties on rough and liquid metal surfaces, Proc ALT12. (2012). doi:10.12684/alt.1.78.

[73] K. Shankar, Thermophysical and optical property measurements of electromagnetically-leviated liquid metals, Rice University, 1989.

[74] M. Salcudean, M. Choi, R. Greif, A study of heat transfer during arc welding, Int. J. Heat Mass Transf. 29 (1986) 215–225. doi:https://doi.org/10.1016/0017-9310(86)90229-2.

[75] Y. Yang, M.F. Knol, F. van Keulen, C. Ayas, A semi-analytical thermal modelling approach

for selective laser melting, Addit. Manuf. 21 (2018) 284–297. doi:https://doi.org/10.1016/j.addma.2018.03.002.

[76] A. Plotkowski, M.M. Kirka, S.S. Babu, Verification and validation of a rapid heat transfer calculation methodology for transient melt pool solidification conditions in powder bed metal additive manufacturing, Addit. Manuf. 18 (2017) 256–268. doi:https://doi.org/10.1016/j.addma.2017.10.017.

[77] R. Miller, T. DebRoy, Energy absorption by metal-vapor-dominated plasma during carbon dioxide laser welding of steels, J. Appl. Phys. 68 (1990) 2045–2050. doi:10.1063/1.346555.

[78] Y. Tian, D. Tomus, P. Rometsch, X. Wu, Influences of processing parameters on surface roughness of Hastelloy X produced by selective laser melting, Addit. Manuf. 13 (2017) 103–112. doi:https://doi.org/10.1016/j.addma.2016.10.010.

[79] B. Fotovvati, S.F. Wayne, G. Lewis, E. Asadi, A Review on Melt-Pool Characteristics in Laser Welding of Metals, Adv. Mater. Sci. Eng. 2018 (2018). doi:10.1155/2018/4920718.

[80] T. Polivnikova, Study and modelling of the melt pool dynamics during Selective Laser Sintering and Melting, 6826 (2015) 107.

[81] Copper alloys, PX Group, (n.d.). https://www.pxgroup.com/sites/default/files/CuSn8_1.pdf.

[82] Copper-tin and Copper-tin-zinc casting alloys (Tin bronze), (2017). https://www.kupferinstitut.de/wp-content/uploads/2019/09/Infodruck-i.-25.pdf.

[83] UNS C52100 (CW453K) Phosphor Bronze, (2019). https://www.makeitfrom.com/material-properties/UNS-C52100-CW453K-Phosphor-Bronze.

[84] EN CC480K (CuSn10-C) Tin Bronze, (2018). https://www.makeitfrom.com/material-properties/EN-CC480K-CuSn10-C-Tin-Bronze.

[85] E. ToolBox, Solids - Melting and Boiling Temperatures, (2003). https://www.engineeringtoolbox.com/melting-points-solids-d_148.html.

[86] 18K red gold 5N, for universal use, PX Group, (n.d.). https://www.pxgroup.com/sites/default/files/0518.pdf.

[87] P. Sbornicchia, S. Rappo, D. Zito, V. Doppio, F. Tiso, G. Cepeda, S.A. Progold, Understanding Gold Alloy Features From Thermodynamic Phenomena, St. Fe Symp. Jewel. Manuf. Technol. 39 (2018) 517–560.

[88] C.S. Kim, Thermophysical properties of stainless steels, United States, 1975.

http://inis.iaea.org/search/search.aspx?orig_q=RN:07236394.

[89] T. Heeling, M. Cloots, K. Wegener, Melt pool simulation for the evaluation of process parameters in selective laser melting, Addit. Manuf. 14 (2017) 116–125. doi:10.1016/j.addma.2017.02.003.

[90] C.L.A. Leung, S. Marussi, M. Towrie, R.C. Atwood, P.J. Withers, P.D. Lee, The effect of powder oxidation on defect formation in laser additive manufacturing, Acta Mater. 166 (2019) 294–305. doi:10.1016/j.actamat.2018.12.027.

[91] S.A. Khairallah, A.A. Martin, J.R.I. Lee, G. Guss, N.P. Calta, J.A. Hammons, M.H. Nielsen, K. Chaput, E. Schwalbach, M.N. Shah, M.G. Chapman, T.M. Willey, A.M. Rubenchik, A.T. Anderson, Y.M. Wang, M.J. Matthews, W.E. King, Controlling interdependent meso-nanosecond dynamics and defect generation in metal 3D printing, Science (80-.). 368 (2020) 660–665. doi:10.1126/science.aay7830.

[92] T. DebRoy, H.L. Wei, J.S. Zuback, T. Mukherjee, J.W. Elmer, J.O. Milewski, A.M. Beese, A. Wilson-Heid, A. De, W. Zhang, Additive manufacturing of metallic components – Process, structure and properties, Prog. Mater. Sci. 92 (2018) 112–224. doi:10.1016/j.pmatsci.2017.10.001.

[93] B.J. Simonds, J. Sowards, J. Hadler, E. Pfeif, B. Wilthan, J. Tanner, C. Harris, P. Williams, J. Lehman, Time-Resolved Absorptance and Melt Pool Dynamics during Intense Laser Irradiation of a Metal, Phys. Rev. Appl. 10 (2018) 1. doi:10.1103/PhysRevApplied.10.044061.

[94] C. Van Gestel, Study of physical phenomena of selective laser melting towards increased productivity, EPFL, 2015. doi:10.5075/epfl-thesis-6817.

Supplementary materials

An effective rule for translating optimal selective laser melting processing parameters from one material to another

Hossein Ghasemi-Tabasi[1], Jamasp Jhabvala[1], Eric Boillat[1], Toni Ivas[1], Rita Drissi-Daoudi[1], Roland E. Logé[1]

1. Thermomechanical Metallurgy Laboratory (LMTM) – PX Group Chair, Ecole Polytechnique Fédérale de Lausanne (EPFL), CH-2002 Neuchâtel, Switzerland.

S1. Powder Tester HOSOKAWA MICRON CORPORATION:

The "Powder Tester" unit (Hosokawa Micron Corporation, Figure S2) can measure the relative density and the tapped density of powders with a graduated measuring cylinder. It can also supply the tapped bulk density. Before starting the measurement, the cup with defined volume should be weighted. In the next step, using the sieving system inside the machine, the cup is filled until powder particles start overflowing. The excess powder on top of the cup should be removed using a blade, in an angular movement avoiding to induce pressure. Finally, the filled cup is weighted, leading to the aerated density. The aerated density for each material divided by its bulk density provides relative density values.

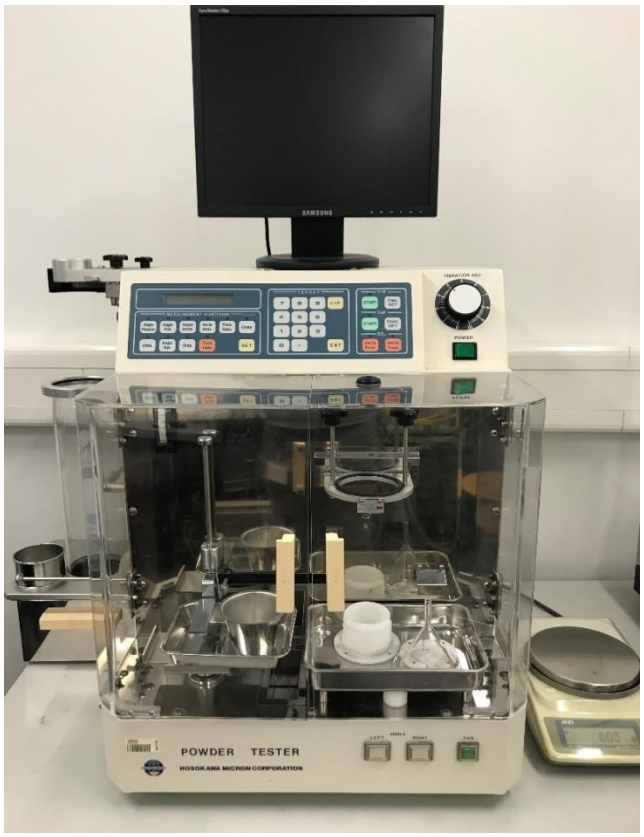

Figure S1. Powder Tester HOSOKAWA MICRON CORPORATION unit.

S2. 316L samples printed with process parameters close to the optimal value (delta_H 27.9)

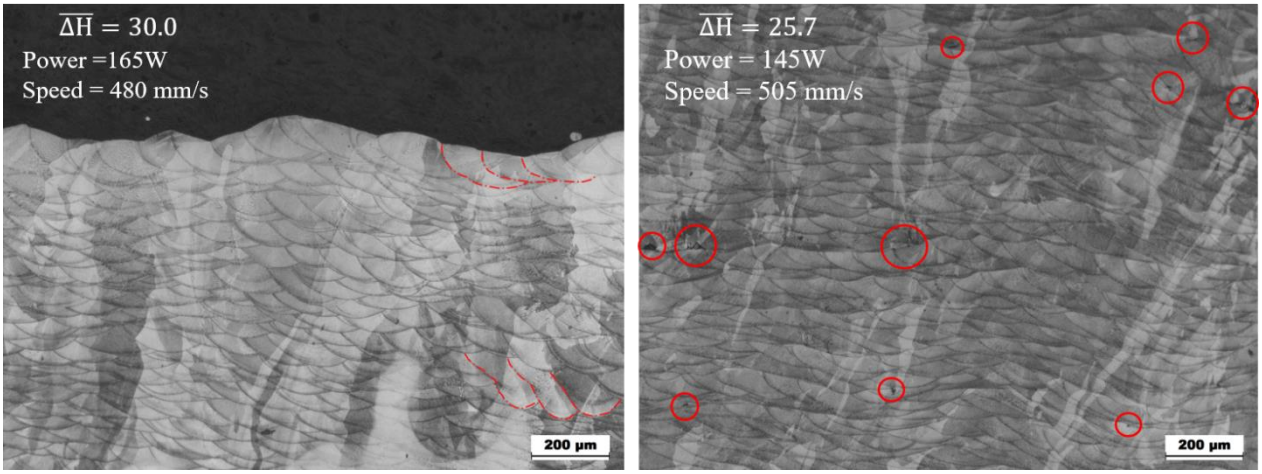

Figure S2. 316 L samples printed with slightly higher (left) and lower (right) normalized enthalpy than the reported optimal value. (Red circles indicate porosities at the melt pool borders).

S3. Results of optical properties measurements.

Optical properties of the materials measured by Perkin Elmer Lambda900 spectrophotometer are used in both experimental and numerical calculations. As illustrated in Figure 3, different phenomena occur during the optical characterization of the powder layer. Part of the beam reflects, part of it absorbs in the powder bed, and the rest transmits through the powder bed, which in the SLM process will reach the substrate or the previous solidified layers. Equations (4-8) explain the difference between α_p (part of the incident beam which has entered the powder layer, 1-R) and $\alpha_{p-layer}$, the part of the incident beam which has been absorbed within the powder layer (1-R-T). $\alpha_{p-layer}$ is used in calculations related to the translation rule, i.e. for calculating the normalized enthalpy from equation 18. It can be computed from R, and T. R is obtained with equation (4) from the incident beam intensity I_0, and the measured reflected intensity I_r. T is obtained with equation (6) from the incident beam intensity I_0, and the measured transmitted intensity I_t.

In finite element (FE) simulations, the light penetration inside the powder bed is defined from the Beer-Lambert law, right-hand side of equation (6), whose parameter δ is calibrated by knowing I_0, α_p= 1-R, and the layer thickness L. In FE simulations, L is of course replaced by the Z depth coordinate. Tables S2-S5 provide the reflectivity (R), transmitivity (T), total absorptivity (α_p), penetration depth (δ) and powder bed absorptivity ($\alpha_{p-layer}$) at different wavelengths (1200-900 nm) for bronze, red-gold, thermally-treated red-gold, and 316L stainless steel powder particles, respectively.

Table S2. Optical properties of bronze powder

Wavelength(nm)	**R**	**T**	$\boldsymbol{\alpha_p}$	$\boldsymbol{\alpha_{p\_layer}}$	**δ (mm)**
1200	0.4375	0.1354	0.5625	0.4271	0.02808
1190	0.4365	0.1350	0.5635	0.4285	0.02799
1180	0.4355	0.1350	0.5645	0.4295	0.02796
1170	0.4345	0.1349	0.5655	0.4306	0.02790
1160	0.4334	0.1348	0.5666	0.4318	0.02786
1150	0.4323	0.1347	0.5677	0.4330	0.02781
1140	0.4312	0.1346	0.5688	0.4342	0.02775
1130	0.4301	0.1344	0.5699	0.4355	0.02769
1120	0.4290	0.1341	0.5710	0.4369	0.02762
1110	0.4278	0.1338	0.5722	0.4384	0.02753
1100	0.4267	0.1335	0.5733	0.4398	0.02745
1090	0.4255	0.1333	0.5745	0.4412	0.02738
1080	0.4251	0.1334	0.5749	0.4415	0.02733
1070	0.4243	0.1330	0.5757	0.4427	0.02730
1060	0.4218	0.1324	0.5782	0.4458	0.02714
1050	0.4205	0.1321	0.5795	0.4474	0.02706
1040	0.4192	0.1319	0.5808	0.4489	0.02698
1030	0.4179	0.1316	0.5821	0.4505	0.02690
1020	0.4165	0.1313	0.5835	0.4522	0.02682
1010	0.4150	0.1311	0.5850	0.4539	0.02674
1000	0.4135	0.1308	0.5865	0.4557	0.02665
990	0.4121	0.1305	0.5879	0.4574	0.02657
980	0.4106	0.1303	0.5894	0.4591	0.02650
970	0.4089	0.1300	0.5911	0.4611	0.02641
960	0.4072	0.1297	0.5928	0.4631	0.02632
950	0.4055	0.1295	0.5945	0.4650	0.02624
940	0.4036	0.1291	0.5964	0.4673	0.02615
930	0.4018	0.1288	0.5982	0.4694	0.02605
920	0.3998	0.1286	0.6002	0.4716	0.02596
910	0.3979	0.1283	0.6021	0.4738	0.02587
900	0.3962	0.1281	0.6038	0.4757	0.02580

Table S3. Optical properties of red-gold powder

Wavelength(nm)	**R**	**T**	$\boldsymbol{\alpha_p}$	$\boldsymbol{\alpha_{p\_layer}}$	**δ (mm)**
1200	0.6104	0.1929	0.3896	0.1967	0.05689
1190	0.6099	0.1922	0.3901	0.1979	0.05651
1180	0.6093	0.1922	0.3907	0.1985	0.05637
1170	0.6089	0.1917	0.3911	0.1994	0.05613
1160	0.6084	0.1917	0.3916	0.1999	0.05600
1150	0.6077	0.1915	0.3923	0.2008	0.05579
1140	0.6072	0.1913	0.3928	0.2015	0.05560
1130	0.6066	0.1911	0.3934	0.2023	0.05539
1120	0.6059	0.1907	0.3941	0.2034	0.05510
1110	0.6052	0.1902	0.3948	0.2046	0.05476
1100	0.6045	0.1897	0.3955	0.2058	0.05446
1090	0.6038	0.1893	0.3962	0.2069	0.05415
1080	0.6032	0.1892	0.3968	0.2076	0.05401
1070	0.6030	0.1888	0.3970	0.2082	0.05382
1060	0.6012	0.1879	0.3988	0.2109	0.05314
1050	0.6003	0.1874	0.3997	0.2123	0.05281
1040	0.5995	0.1869	0.4005	0.2136	0.05249
1030	0.5985	0.1865	0.4015	0.2150	0.05216
1020	0.5974	0.1860	0.4026	0.2166	0.05180
1010	0.5962	0.1855	0.4038	0.2183	0.05144
1000	0.5951	0.1851	0.4049	0.2198	0.05110
990	0.5937	0.1847	0.4063	0.2216	0.05073
980	0.5923	0.1843	0.4077	0.2234	0.05039
970	0.5907	0.1839	0.4093	0.2254	0.04999
960	0.5890	0.1834	0.4110	0.2276	0.04958
950	0.5872	0.1830	0.4128	0.2298	0.04919
940	0.5852	0.1826	0.4148	0.2322	0.04874
930	0.5830	0.1820	0.4170	0.2350	0.04827
920	0.5806	0.1816	0.4194	0.2378	0.04777
910	0.5782	0.1811	0.4218	0.2407	0.04731
900	0.5764	0.1807	0.4236	0.2429	0.04695

Table S4. Optical properties of thermally treated red-gold powder

Wavelength(nm)	**R**	**T**	α_p	α_{p_layer}	**δ (mm)**
1200	0.5059	0.2283	0.4941	0.2658	0.05180
1190	0.5051	0.2276	0.4949	0.2673	0.05149
1180	0.5043	0.2274	0.4957	0.2683	0.05135
1170	0.5037	0.2277	0.4963	0.2686	0.05134
1160	0.5030	0.2278	0.4970	0.2692	0.05128
1150	0.5022	0.2280	0.4978	0.2698	0.05123
1140	0.5016	0.2281	0.4984	0.2703	0.05116
1130	0.5008	0.2281	0.4992	0.2711	0.05106
1120	0.5001	0.2280	0.4999	0.2719	0.05094
1110	0.4992	0.2277	0.5008	0.2731	0.05074
1100	0.4983	0.2274	0.5017	0.2743	0.05055
1090	0.4975	0.2271	0.5025	0.2754	0.05036
1080	0.4967	0.2268	0.5033	0.2765	0.05017
1070	0.4949	0.2260	0.5051	0.2791	0.04998
1060	0.4945	0.2259	0.5055	0.2796	0.04976
1050	0.4938	0.2258	0.5062	0.2804	0.04954
1040	0.4930	0.2254	0.5070	0.2816	0.04935
1030	0.4921	0.2252	0.5079	0.2827	0.04917
1020	0.4911	0.2249	0.5089	0.2840	0.04898
1010	0.4902	0.2245	0.5098	0.2853	0.04878
1000	0.4893	0.2242	0.5107	0.2865	0.04857
990	0.4882	0.2239	0.5118	0.2879	0.04839
980	0.4874	0.2236	0.5126	0.2890	0.04821
970	0.4864	0.2233	0.5136	0.2903	0.04803
960	0.4854	0.2231	0.5146	0.2915	0.04786
950	0.4845	0.2229	0.5155	0.2926	0.04770
940	0.4837	0.2226	0.5163	0.2937	0.04754
930	0.4828	0.2223	0.5172	0.2949	0.04738
920	0.4819	0.2221	0.5181	0.2960	0.04722
910	0.4810	0.2219	0.5190	0.2971	0.04707
900	0.4797	0.2218	0.5203	0.2985	0.04694

Table S5. Optical properties of 316L stainless steel powder

Wavelength(nm)	R	T	α_p	α_{p_layer}	δ (mm)
1200	0.3415	0.1408	0.6585	0.5177	0.02593
1190	0.3408	0.1406	0.6592	0.5186	0.02588
1180	0.3401	0.1408	0.6599	0.5191	0.02589
1170	0.3393	0.1410	0.6607	0.5197	0.02590
1160	0.3386	0.1412	0.6614	0.5202	0.02590
1150	0.3379	0.1413	0.6621	0.5208	0.02590
1140	0.3372	0.1415	0.6628	0.5213	0.02591
1130	0.3365	0.1416	0.6635	0.5219	0.02590
1120	0.3358	0.1417	0.6642	0.5225	0.02590
1110	0.3350	0.1418	0.6650	0.5232	0.02588
1100	0.3343	0.1418	0.6657	0.5239	0.02587
1090	0.3337	0.1418	0.6663	0.5245	0.02585
1080	0.3330	0.1418	0.6670	0.5252	0.02583
1070	0.3323	0.1418	0.6677	0.5259	0.02581
1060	0.3316	0.1418	0.6684	0.5266	0.02580
1050	0.3309	0.1418	0.6691	0.5273	0.02578
1040	0.3301	0.1419	0.6699	0.5280	0.02577
1030	0.3294	0.1419	0.6706	0.5287	0.02576
1020	0.3287	0.1419	0.6713	0.5294	0.02574
1010	0.3279	0.1420	0.6721	0.5301	0.02573
1000	0.3272	0.1421	0.6728	0.5307	0.02573
990	0.3264	0.1422	0.6736	0.5314	0.02572
980	0.3256	0.1423	0.6744	0.5321	0.02571
970	0.3248	0.1425	0.6752	0.5327	0.02571
960	0.3240	0.1427	0.6760	0.5333	0.02571
950	0.3231	0.1429	0.6769	0.5340	0.02571
940	0.3221	0.1431	0.6779	0.5348	0.02571
930	0.3211	0.1433	0.6789	0.5356	0.02572
920	0.3199	0.1436	0.6801	0.5365	0.02572
910	0.3188	0.1439	0.6812	0.5373	0.02573
900	0.3180	0.1442	0.6820	0.5378	0.02574

Tables S6 provides the reflectivity (R) values of polished bulk bronze, red-gold, and 316L samples.

Table S6. Reflectivity value of mirror polished bulk solid materials, at room temperature.

Wavelength (nm)	R (Bronze)	R (Red gold)	R (316L steel)
1200	0.8954	0.8962	0.7204
1190	0.8950	0.8958	0.7197
1180	0.8946	0.8954	0.7189
1170	0.8939	0.8949	0.7180
1160	0.8933	0.8947	0.7171
1150	0.8926	0.8943	0.7161
1140	0.8922	0.8939	0.7151
1130	0.8917	0.8936	0.7141
1120	0.8913	0.8934	0.7134
1110	0.8911	0.8931	0.7127
1100	0.8909	0.8929	0.7120
1090	0.8905	0.8925	0.7113
1080	0.8901	0.8922	0.7104
1070	0.8895	0.8918	0.7095
1060	0.8890	0.8913	0.7088
1050	0.8886	0.8907	0.7079
1040	0.8880	0.8901	0.7071
1030	0.8876	0.8895	0.7064
1020	0.8871	0.8890	0.7056
1010	0.8866	0.8882	0.7047
1000	0.8860	0.8873	0.7039
990	0.8853	0.8862	0.7030
980	0.8849	0.8849	0.7023
970	0.8843	0.8829	0.7015
960	0.8837	0.8799	0.7006
950	0.8830	0.8753	0.6998
940	0.8825	0.8680	0.6989
930	0.8822	0.8625	0.6982
920	0.8820	0.8625	0.6976
910	0.8816	0.8626	0.6967
900	0.8814	0.8623	0.6958

Chapter 5

Mapping Spatial Distribution of Pores in an Additively Manufactured Gold Alloy Using Neutron Microtomography

Hossein Ghasemi-Tabasi[1], Pavel Trtik[2], Jamasp Jhabvala[1], Michael Meyer[2], Chiara Carminati[2], Markus Strobl[2], Roland E. Logé[1]

1. Thermomechanical Metallurgy Laboratory (LMTM) – PX Group Chair, Ecole Polytechnique Fédérale de Lausanne (EPFL), CH-2002 Neuchâtel, Switzerland.
2. Laboratory for Neutron Scattering and Imaging (LNS), Paul Scherrer Institut, 5232 Villigen PSI, Switzerland

H. Ghasemi-Tabasi, P. Trtik, J. Jhabvala, M. Meyer, C. Carminati, M. Strobl, R.E. Logé, Mapping Spatial Distribution of Pores in an Additively Manufactured Gold Alloy Using Neutron Microtomography, Appl. Sci. . 11 (2021). doi:10.3390/app11041512.

Contribution:
Hossein Ghasemi Tabasi printed the gold samples. He analyzed the porosity content of the printed samples from mechanically polished 2D cross-sections, conducted the interpretation of the 3D results and wrote the manuscript.

Abstract

A crucial criterion for the quality of the additively manufactured parts is the porosity content for achieving an acceptable final relative density. In addition, for jewelry applications, visible pores are unacceptable at or in the vicinity of the surface. In this study, non-destructive 3D neutron microtomography is applied to map the spatial distribution of pores in additively manufactured red-gold samples. The 3D imaging assessment underlines the high relative density of the printed red-gold sample and indicates residual pore sizes are predominantly below the limit of concern for jewelry applications. The 3D maps of pores within printed samples highlight the effect of the scanning strategy on the final quality and location of pores in the printed samples. These results confirm that neutron microtomography is a novel and precise tool to characterize residual porosity in additively manufactured gold alloys and other higher-Z materials where such investigation using other non-destructive methods (such as X-rays) is challenging due to the limited penetration depth

Keywords*:* laser powder bed fusion; non-destructive investigations; gold alloy; neutron microtomography; porosity

1. Introduction

Additive Manufacturing (AM) refers to different technologies that produce a 3D part in a layer-by-layer mode. Laser powder bed fusion (L-PBF) -also known as selective laser melting (SLM)- is one of the most important powder bed fusion AM processes, which enables the manufacturing of very complex metallic objects from a computer-aided design (CAD) file. Printing parts with the L-PBF technology requires careful optimization of the process parameters, which depend on the metallic powder and its physical and chemical properties [1,2]. Materials with high reflectivity and high thermal conductivity, such as gold and its alloys, are usually difficult to process, because they are hard to be heated and kept in a stable molten state. Moreover, for printing in commercial machines, a non-negligible amount of metallic powder is needed to fill the powder supply, which tends to make AM of gold alloys rather uneconomic. Despite these obstacles, L-PBF of precious metals including gold receives increasing interest, in particular from the jewelry and the watch industries [3–7].

One of the main success criteria for the AM produced parts is the porosity content. The occurrence of pores in gold alloys produced by AM is very difficult to be avoided. At the same time, it is critical for applications in jewelry and watches to minimize porosity and in particular such that could be visible on the material surface. The latter implies that the pore size, especially in the surface region, is required to be smaller than approximately 15-20 microns. Otherwise, the pores can be observed with the naked eye, and even if they

are located in close vicinity of the surface, they can appear later due to material wear. Conventionally, porosity in a bulk material can be investigated using the Archimedes method, microscopy, or X-ray tomography. However, all these methods are of limited use for AM produced gold alloys. The Archimedes method [8] has been used in different studies in order to evaluate the relative density of parts [9,10]. In L-PBF processing, due to the geometrical constraints and/or partial consolidation of powder particles, there might be particles left inside of pores after build completion [11]. Since the immersion liquid used cannot wet rough surfaces efficiently and also does not take these internally trapped powders into consideration, the Archimedes method is not a very reliable technique to precisely measure the porosity content in L-PBF samples. Furthermore, as the size of the precious metal samples is usually limited, the confidence level of the Archimedes method is low. Above all, the Archimedes method does not provide any information about the pore size and spatial distributions within the material, which are important parameters with respect to the above-mentioned requirements [12]. Likewise, the high cost associated with material loss also seriously limits the use of optical microscopy on mechanical sectioning of representative volumes. Klotz et al. [7] conducted a full process study on the L-PBF of yellow gold alloys and analyzed the porosities in the printed samples by mechanical polishing. The effects of the heat treatment and alloying addition (Fe and Ge) on the optical reflectivity and, as a result, on the final porosity have been analyzed. The average porosity using untreated powder particles was in the order of 3 to 4%. With the use of thermal heat treatment and alloying, Klotz et al. could decrease the final porosity to 0.7%, and 0.3-0.1%, respectively. They used the addition of Ge to the yellow gold chemical composition to lower the solidus temperature, which provided an easier condition to melt the material. Moreover, the addition of Fe increased the oxidation of the powder particles and as a result, decreased their reflectivity. In general, quantitative investigations can be performed using X-ray tomography [13–18]. For example, Cai et al. [19] observed the internal structure of AlSi10Mg L-PBF printed samples to investigate the effect of the process parameters on the final porosity content, and to provide knowledge to control the quality of the L-PBF parts. However, the penetration depth of X-rays in gold alloys is rather limited [20], which makes the investigation of representative volume elements hardly possible.

Neutron tomography provides a viable alternative to visualize the distribution of pores in additively manufactured samples [21]. Here, the recent advances in the available instrumentation has been utilized [22][23] that allow resolution of features with dimensions of a few micrometres [24]. The neutron cross-section of gold and hence the penetration depth of thermal neutrons for gold alloys is such that it provides excellent transmission imaging contrast conditions for samples in the range of several millimeters in thickness. Thus, imaging with neutrons has evolved to be a highly suitable experimental technique for

studying the relationship between porosity and L-PBF processing parameters in samples opaque to x-rays. While a proof-of-concept neutron microtomography experiment with high-resolution detector capability at Paul Scherrer Institut (PSI) [25] recently demonstrated the feasibility to assess porosity in gold with about 10 µm spatial resolution, here we focus on the assessment of porosity in gold alloy samples of representative volumes manufactured by L-PBF.

2. Materials and Methods

Two samples of 18-carat red gold alloy ($Au_{511}Cu_{433}Ag_{56}$, expected density 15.2 g cm^{-3}) of the intended size of 2 × 2 × 2 mm^3 have been printed with an in-house customized L-PBF machine, dedicated to research activities and designed for operating with a low amount of powder [26], using the process parameters shown in Table 1. In the L-PBF processes, the scanning of the laser beam for each layer follows specific patterns called scanning strategies, and the hatching distance defines the separation between two consecutive laser tracks [27]. In this study, two different scanning strategies are used, parallel and crosshatch. The parallel scan path is the most frequently applied scanning strategy for L-PBF in which parallel unidirectional tracks are traced with a fixed distance (hatching distance) between adjacent tracks. At the end of each track, there is a discontinuous jump of the laser beam from the end of one track to the beginning of the next track. The crosshatch scanning strategy consists of two parallel scan paths, which are perpendicular to each other, and both are applied on each layer [28]. The L-PBF machine is equipped with a 500 W fiber SPI laser, with a wavelength of 1070 nm and a laser spot diameter of 85 µm. Information on the applied optimization process via experiments and simulation can be found in [26]. First analyses confirm major improvements in printing gold samples with high relative density, compared e.g. to previous studies where the chemical composition of the alloy had to be altered to print samples with a reasonably low amount of porosity [7].

Table 1. L-PBF process parameters for two red gold samples.

Sample	Power(W)	Speed(mm/s)	Hatching distance(µm)	Layer thickness(µm)	Scanning strategy
1	210	220	100	40	Parallel
2	230	200	70	40	Crosshatch

The process parameters were selected such as to reach the highest possible relative density in one sample (Sample 1), and allowing for a higher porosity content and higher amount of partially melted zones in the other (Sample 2). This is done in order to not only investigate a sample of low porosity from a process that

is assumed optimized, but also to establish confidence in the method by detecting higher porosity from a less optimized process.

The presented investigation has been performed with the high-resolution imaging detector[29] of PSI at the D50 beamline of the ILL (Institute Laue Langevin)[30]. Neutron microscope installed at ILL-D50 beamline allowed for the 2D images of Siemens star positioned at the contact with scintillator screen showed the spatial resolution of approximately 5 μm [29]. The scintillator screen ($^{157}Gd_2O_2S$:Tb [31]) of the detector system has been positioned at 11.13 m downstream the 30 mm-diameter pinhole, thus providing a neutron beam collimation ratio of 371. The light emitted from the scintillator has been captured by a CCD camera (Andor iKon-L, 2048 × 2048 pixels, 13.5 μm pixel size). Due to the fivefold magnification of the high-resolution detector, the effective pixel size of the acquired images was 2.7 μm, and the available image field of view (FOV) was 5.5 × 5.5 mm^2.

The samples were attached to sample holders using UV-hardening glue, and both were scanned in a single tomographic run using 375 projections evenly distributed between 0° and 359.04°. Five images with 30-second exposure time were acquired for each angular position that were after the white spot (gamma-ray artifacts) removal averaged in a single projection image. The tomographic measurement was complemented with the acquisition of 100 open beam images without sample, 30 dark current images as well as the acquisition of black body (BB) images for background correction according to references [32],[33]. The individual projections were aligned during post-processing to correct for the sample positioning instabilities using an alignment algorithm originally developed for X-ray ptychographic tomography [34]. The tomographic dataset was reconstructed using the MuhRec software [35]. Ring artifacts were suppressed by a combined wavelet-Fourier stripe cleaning algorithm [36]. The tomographic dataset was then post-processed by the Kiptool software [37] using an edge-preserving smoothing inverse scale space (ISS) filter [38]. The dataset visualizations and quantitative analysis was subsequently performed using Avizo 3D visualization software.

The linear attenuation coefficient (LAC) of the gold alloy has been found to be about 6.55 cm^{-1}. This value is in rather good agreement with the theoretically predicted value (6.43 cm^{-1}) [39] the mentioned red gold alloy composition at 2.8Å neutron wavelength (peak wavelength of the neutron spectrum at D50 beamline). The porosity has been segmented using the Otsu method [40], setting the global threshold between gold alloy and hollow space to 3.226 cm^{-1}. Subsequently, the closed porosity volume fractions in both samples have been analyzed

3. Results and discussion

Figure 1 concisely summarizes the results of the porosity quantification based on the neutron microtomography and shows the 3D renderings of both samples, revealing the sample shape and the spatial distribution of the closed pores (in blue) larger than 10 micrometres in equivalent diameter. The pore size distributions of the closed pores differ significantly between the two samples, and for the large pores (larger than 10 micrometres), the fractions are 0.012% and 0.047%, respectively.

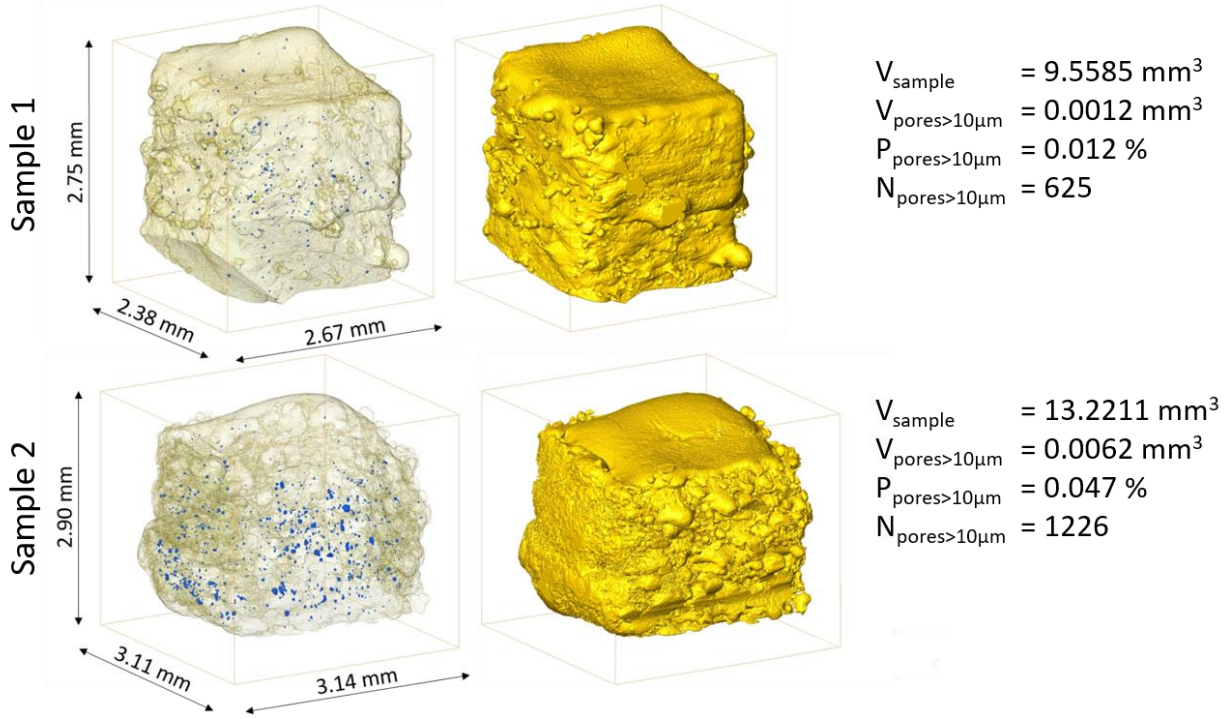

Figure 1. 3D renderings of the L-PBF printed red gold samples revealing sample shapes and their closed porosities in blue. For each sample, the number of pores > 10 µm (all pores which are larger than 10 µm) and their volume relative to the total sample volume has been quantified.

Higher laser power and lower hatching distance used in the manufacturing process of sample 2 increased the heat accumulation [41] and, as a result, the amount of sintered powder at the border of the samples. Moreover, in the crosshatch scanning strategy, which is used for Sample 2, the laser passes two times in each layer, in 2 directions perpendicular to each other, which also increases the total heat input and leads to

the formation of large fractions of sintered powders at the sample edges. In contrast, in Sample 1, using optimal process parameters and a parallel scanning strategy, the fraction of sintered powder at the sample surface is reduced. These surface features explain the relatively large difference between the total volumes of Sample 1 and Sample 2.

The investigated samples have been printed with an in-house customized L-PBF machine that is not equipped with contour correction algorithms. Such options exist in some machines and they may improve the samples quality (e.g. its final shape) at the borders and edges [42].

Figure 2 shows optical microscopy images acquired after neutron microtomography, following the mechanical sectioning of the samples (Figure 2b and 2e). Juxtaposed are the corresponding sections from the 3D neutron microtomography reconstructions (Figure 2a and 2d). The location of the corresponding section in the neutron tomographic datasets is difficult to be identified exactly for several reasons: (a) the real metallographic sections may not necessarily be planar, (b) the preparation of the metallographic section may lead to relocation of some parts of the sample, in particular within the sintered zones at the edges of the sample. Despite this fact, the image comparison indicates a very good match between 2D optical microscopy and 3D neutron microtomography cross-sections.

Figures 2c and 2f show the pore size distribution based on the neutron microtomography (3D) and optical microscopy (2D). The neutron tomography data reveals the following. The number of individual pore entities in Sample 2 is almost two-times larger compared to Sample 1, with a considerable number of large pores (larger than 30 micrometres). The pore size distribution indicates that almost 88% of the total porosity in Sample 1 is composed of pores smaller than 15 μm (critical pore size for watch and jewelry industry), which are generally due to entrapped gas in powder particles [43]. There are only six pores in the entire sample volume with an equivalent diameter larger than 30μm. On the other hand, Sample 2 exhibits a larger number of pores, in particular also with increased sizes (90 pores larger than 30 μm), and only 55% of the total porosity corresponds to pores smaller than 15 μm. These results show a significant improvement in the choice of the optimum process parameters for printing red gold samples and highlight the effect of the scanning strategy on the final quality of the printed samples. Although the initial porosity entrapped in powder particles cannot fully account for the total amount of porosities in the printed samples, increasing powder quality would further improve density, e.g., by using the plasma rotating electrode process (PREP) [43,44].

Pore size analysis from the optical microscopy cross-sections indicates that most of the pores are actually much smaller than 10 micrometres (Figure 2c and 2f) and are thus below the current resolution of the neutron

microtomography datasets. However, the comparison of relative densities from the optical 2D section and the corresponding 2D slice of the 3D data (see Figure 2a to 2d) reveals that the contribution of pores smaller than 10 micrometres to the total relative density of the printed samples is negligible. Density values acquired from 2D optical microscopy (99.73% and 98.35% for Samples 1 and 2, respectively), and from the corresponding 2D slices of 3D neutron microtomography data (99.81% and 98.42% for Samples 1 and 2, respectively) are indeed very close. The difference in relative density with and without considering pores smaller than 10micrometres in the equivalent diameter is less than 0.1%. It should be noted that in 2D optical microscopy cross-sections, there is a contribution of open porosity to what appears to be closed porosity; however, the provision of the 3D datasets reveals such artefacts.

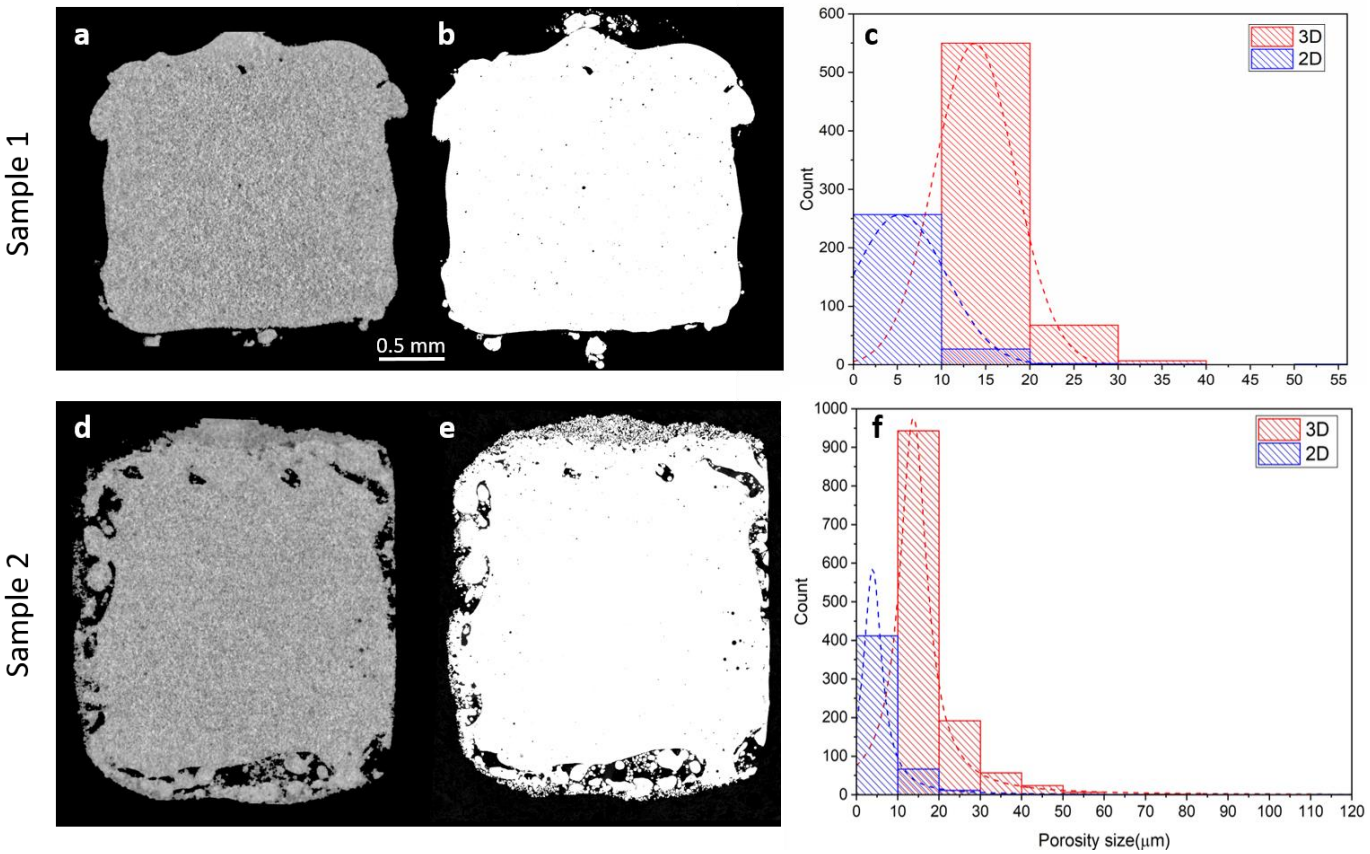

Figure 2. Comparison of the neutron microtomography (a,d) sections and their equivalent optical microscopy (b, e) sections. Graphs c and f show pore size distributions extracted from the full volume of the 3D neutron microtomography datasets and from a single slice of optical microscopy (b, e) sections, respectively.

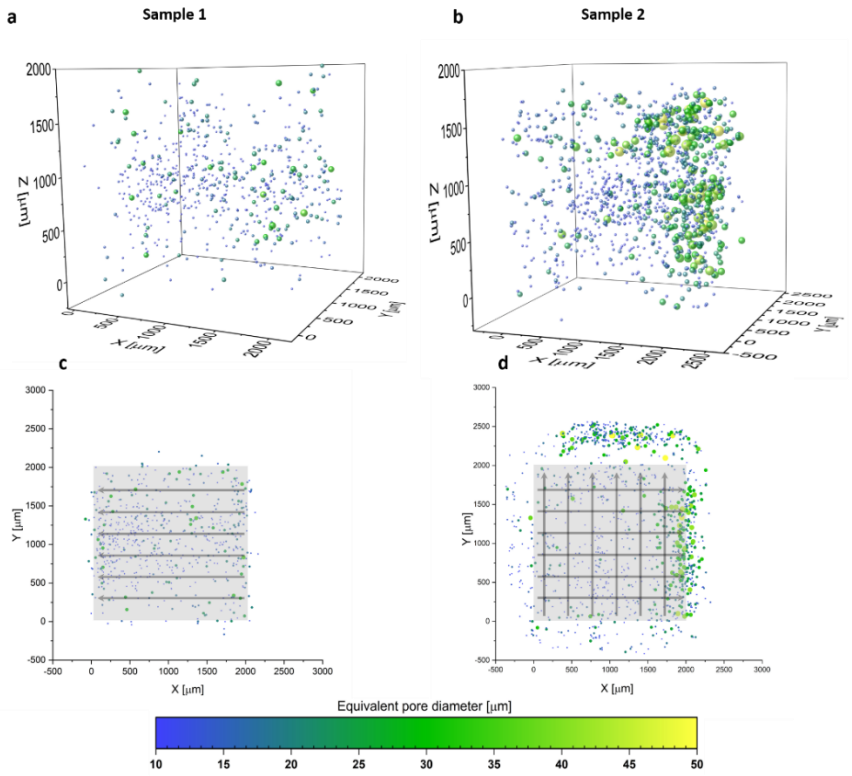
a
Sample 1
b
Sample 2
Z [µm]
X [µm]
Y [µm]
c
d
Equivalent pore diameter [µm]
10
15
20
25
30
35
40
45
50

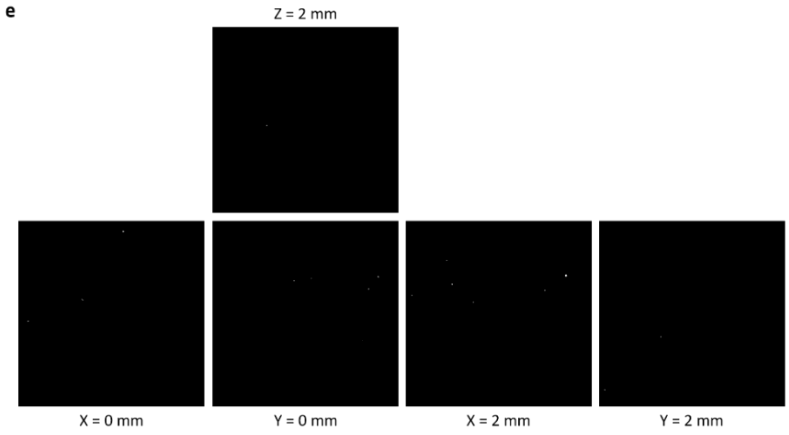
e
Z = 2 mm
X = 0 mm
Y = 0 mm
X = 2 mm
Y = 2 mm

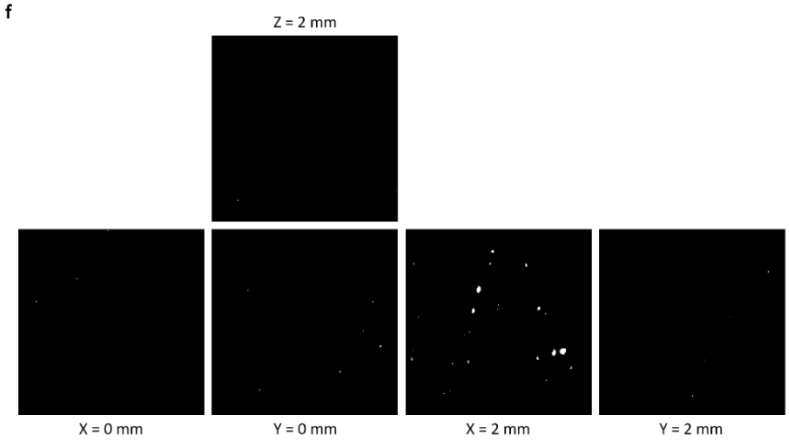
f
Z = 2 mm
X = 0 mm
Y = 0 mm
X = 2 mm
Y = 2 mm

Figure 3. 3D (a, b) and X-Y (c, d) plane projections of visualized pores, with illustrated laser scanning strategies. Most of the pores are located at the end of the laser tracks, where laser-off events occur. Figures (e) and (f) represent the distribution of the pores at the surfaces of the target shape printed samples 1 and 2, respectively (The pores are in white).

Figure 3 shows the 3D distribution of pores in Samples 1 and 2, with equivalent diameter colour coding. Figures 3c and 3d give distributions from the top view, along the building direction, revealing pore locations with respect to the intended production volume. A strong correlation with the scanning strategy is observed. Although pores in Sample 1 are much more homogeneously distributed than in Sample 2, in both samples, most of the pores are located at specific surface regions, corresponding to laser off events. Laser off events refer to the end of the scanning along each scan line, where the scanning speed changes to lower values before the laser is completely turned off, resulting in a local increase of heat input, causing material evaporation and porosity formation [45]. A larger fraction of pores appear in particular outside the intended sample production volume. This is much more pronounced in the case of Sample 2, manufactured with lower hatching distance and higher laser power (see Table 1). In sample 1, this type of porosity is significantly lower and limited to 9 % (volume-wise 10 %) of the total number of closed pores larger than 10 micrometres. In contrast, these amount to 52 % (54 % volume-wise) in Sample 2.

However, in the jewelry and watch industries, part contours are post-processed with surface treatments to ensure mirror-polished surfaces. Our interest; therefore, mainly lies in the porosity within the target shape of the samples. Figures 3e and 3f represent the distribution of visualized pores at the surface of the target shape of the printed samples. The results indicate very few pores are found at the target surface of Sample 1. On Sample 2, significant porosity is revealed at the target surface. Considering the surface with the highest porosity in both samples, relative density at the surface for Sample 1 is 99.98%, whereas for sample 2 it is only about 99.60 %.

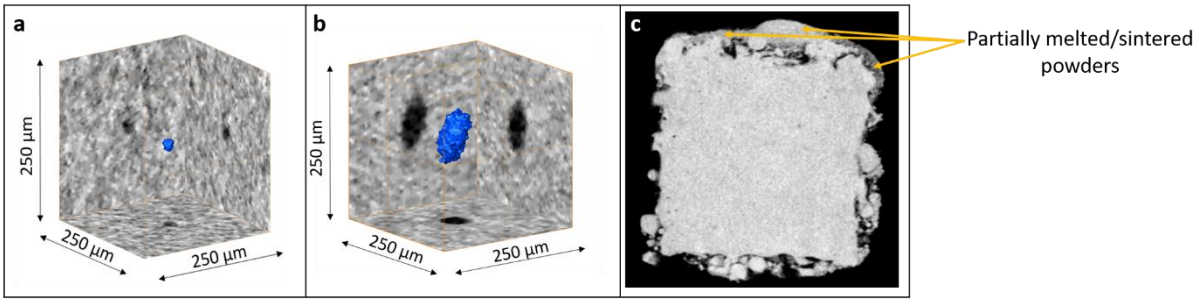

Figure 4. Different types of porosities in L-PBF printed red gold samples characterized by neutron microtomography. a) Round pore, b) large keyhole pore, and c) partially melted/sintered powders on the edge of the printed sample.

3D analysis of pore morphologies in additively manufactured samples helps to distinguish different types of pores. Most of the pores in Samples 1 and 2 are close to spherical. These round pores (e.g. Figure 4a) form due to the injection of dissolved gas at the liquid-solid interface. Spherical pores typically have four different origins: (i) The moisture absorbed by the powder particles in the ambient atmosphere, ii) shielding gas during the manufacturing process, (iii) gas entrapped inside the powder particles during the powder atomization process, and (iv) entrapment of the gas during the manufacturing process due to alloy vapors inside the molten pool [46,47].

Figure 4b shows an example of a large pore in Sample 2, which can be assumed to have formed due to a keyhole collapse and shrinkage, during L-PBF processing. The higher energy density used for printing Sample 2 increases the chance for keyhole formation [48]. Figure 4b indicates a prolate spheroid shape pore located close to the sample edge. As discussed earlier, higher energy densities at the end of a laser track lead to keyhole pore formation. Considering the physical limitations of the laser scanning system optics, stabilizing the energy density by varying the laser power is a solution to solve this problem[43,49]. This emphasises the fact that process parameters modification is a practical approach to control defect formation (pores, cracks, etc.) in the final printed samples[50,51].

Irregular pores located in the vicinity of the parts surface are due to partially melted /sintered/entrapped metallic powder particles, which stick to and agglomerate on the outer edge of the melt pool. These residual powders are associated with the presence of complex voids, which can be distinguished from other types of defects [52,53]. The specific process parameters of Sample 2 (i.e., higher power, lower speed, smaller hatching distance) lead to higher energy density which accumulates more heat during the printing process. This heat input diffuses up to hundreds of micrometres from the melt pool and increases the temperature of the surrounding powder. Some of the powder grains will thus sinter or partially melt, leading to their agglomeration to the solidified surfaces [54], as visualized in Figure 4c. Due to their sub-10-micrometers size, the induced porosities cannot be analyzed in detail with 3D neutron microtomography. However, the partially melted zones exhibit significantly lower LAC than the well-processed zones, and can therefore be clearly distinguished (Figure 4c).

4. Conclusions

In summary, here it has been demonstrated that the direct additive manufacturing of gold alloys of very low total porosity is possible without the need of any additional post-processing or alloying. This makes the analyzed production parameters directly applicable for the production processes in the jewelry and watch industries. In addition, the results highlight the effect of the scanning strategy on the final quality and pores

distribution of the printed samples. Likewise, the results show that neutron microtomography is an excellent tool to characterize relevant residual porosity in additively manufactured gold alloys and other higher-Z materials.

Data Availability Statement: The data that support the findings of this study are available from the corresponding author upon reasonable request.

Acknowledgments: This work has been supported by the "Additive Manufacturing and Metallic Microstructures (AM3) "project. The project is funded by the Competence Center for Materials Science and Technology (CCMX) and by a Swiss industrial consortium. The generous support of PX Group to the LMTM laboratory is also highly acknowledged. We would like to express the deepest gratitude to Drs Duncan Atkins and Alessandro Tengattini (both ILL, Grenoble, France) for the assistance with setting up the Neutron Microscope detector at ILL-D50 beamline.

Conflicts of Interest: The authors declare that they have no known competing financial interests or personal relationships that could have appeared to influence the work reported in this paper.

References

[1] A. Masmoudi, R. Bolot, C. Coddet, Investigation of the laser–powder–atmosphere interaction zone during the selective laser melting process, J. Mater. Process. Technol. 225 (2015) 122–132. doi:https://doi.org/10.1016/j.jmatprotec.2015.05.008.

[2] Y. Pupo, K.P. Monroy, J. Ciurana, Influence of process parameters on surface quality of CoCrMo produced by selective laser melting, Int. J. Adv. Manuf. Technol. 80 (2015) 985–995. doi:10.1007/s00170-015-7040-3.

[3] F. Cooper, DMLM Supports: Are They the Jewelry Industry's New Sprue, Riser and Gate Feed?, St. FE Symp. Jelwelry Manuf. Technol. (2014) 1–22.

[4] B.J. Fischer-buehner, P. Poliero, R. Bertoncello, A. Basso, L.G.S. A, J. Fischer-buehner, P. Poliero, R. Bertoncello, A. Basso, M. Poliero, Rapid Jewelry Manufacturing By Laser Melting of Precious Metal Powders (PLM): Fiction Or Future ?, Proc. St. Fe Symp. Jewel. Manuf. Technol. (2011) 177–202.

[5] D. Zito, A. Carlotto, A. Loggi, P. Sbornicchia, D. Maggian, S.A. Progold, T. Vi, M. Fockele, P.

Unterberg, Optimization of the Main Selective Laser Melting Technology Parameters in the Production of Precious Metal Jewelry, Proc. St. Fe Symp. Jewel. Manuf. Technol. (2013) 1–20.

[6] D. Zito, A. Carlotto, A. Loggi, P. Sbornicchia, D. Bruttomesso, S.A. Progold, Definition and solidity idity of gold and platinum jewels produced using Selective Laser Melting SLM™ technology, St. Fe Symp. Jewel. Manuf. Technol. (2015) 439–470.

[7] U.E. Klotz, D. Tiberto, F. Held, Optimization of 18-karat yellow gold alloys for the additive manufacturing of jewelry and watch parts, Gold Bull. 50 (2017) 111–121. doi:10.1007/s13404-017-0201-4.

[8] Archimedes, Archimedes, ON FLOATING BODIES, BOOK I, in: Work. Arch., 2010: pp. 253–262. doi:10.1017/cbo9780511695124.019.

[9] A.B. Spierings, M. Schneider, R. Eggenberger, Comparison of density measurement techniques for additive manufactured metallic parts, Rapid Prototyp. J. 17 (2011) 380–386. doi:10.1108/13552541111156504.

[10] A.-F. Obaton, M.-Q. Lê, V. Prezza, D. Marlot, P. Delvart, A. Huskic, S. Senck, E. Mahé, C. Cayron, Investigation of new volumetric non-destructive techniques to characterise additive manufacturing parts, Weld. World. 62 (2018) 1049–1057. doi:10.1007/s40194-018-0593-7.

[11] L.W. Hunter, D. Brackett, N. Brierley, J. Yang, M.M. Attallah, Assessment of trapped powder removal and inspection strategies for powder bed fusion techniques, Int. J. Adv. Manuf. Technol. 106 (2020) 4521–4532. doi:10.1007/s00170-020-04930-w.

[12] A. du Plessis, P. Sperling, A. Beerlink, L. Tshabalala, S. Hoosain, N. Mathe, S.G. le Roux, Standard method for microCT-based additive manufacturing quality control 2: Density measurement, MethodsX. 5 (2018) 1117–1123. doi:10.1016/j.mex.2018.09.006.

[13] N. Limodin, L. Salvo, M. Suéry, M. DiMichiel, In situ investigation by X-ray tomography of the overall and local microstructural changes occurring during partial remelting of an Al-15.8 wt.% Cu alloy, Acta Mater. 55 (2007) 3177–3191. doi:10.1016/j.actamat.2007.01.027.

[14] I. Maskery, N.T. Aboulkhair, M.R. Corfield, C. Tuck, A.T. Clare, R.K. Leach, R.D. Wildman, I.A. Ashcroft, R.J.M. Hague, Quantification and characterisation of porosity in selectively laser melted Al-Si10-Mg using X-ray computed tomography, Mater. Charact. 111 (2016) 193–204. doi:10.1016/j.matchar.2015.12.001.

[15] G. Ziółkowski, E. Chlebus, P. Szymczyk, J. Kurzac, Application of X-ray CT method for discontinuity and porosity detection in 316L stainless steel parts produced with SLM technology, Arch. Civ. Mech. Eng. 14 (2014) 608–614. doi:10.1016/j.acme.2014.02.003.

[16] V. Aloisi, S. Carmignato, Influence of surface roughness on X-ray computed tomography

dimensional measurements of additive manufactured parts, Case Stud. Nondestruct. Test. Eval. 6 (2016) 104–110. doi:https://doi.org/10.1016/j.csndt.2016.05.005.

[17] J.C. Hastie, M.E. Kartal, L.N. Carter, M.M. Attallah, D.M. Mulvihill, Classifying shape of internal pores within AlSi10Mg alloy manufactured by laser powder bed fusion using 3D X-ray micro computed tomography: Influence of processing parameters and heat treatment, Mater. Charact. 163 (2020) 110225. doi:https://doi.org/10.1016/j.matchar.2020.110225.

[18] C.A. Moorehead, J.M. Sietins, J.J. Swab, Meso-scale microstructural agglomerate quantification in boron carbide using X-ray microcomputed tomography, Mater. Charact. 141 (2018) 177–185. doi:https://doi.org/10.1016/j.matchar.2018.04.053.

[19] X. Cai, A.A. Malcolm, B.S. Wong, Z. Fan, Measurement and characterization of porosity in aluminium selective laser melting parts using X-ray CT, Virtual Phys. Prototyp. 10 (2015) 195–206. doi:10.1080/17452759.2015.1112412.

[20] A.S. Tremsin, J. Rakovan, T. Shinohara, W. Kockelmann, A.S. Losko, S.C. Vogel, Non-Destructive Study of Bulk Crystallinity and Elemental Composition of Natural Gold Single Crystal Samples by Energy-Resolved Neutron Imaging, Sci. Rep. 7 (2017) 40759. doi:10.1038/srep40759.

[21] A.J. Brooks, J. Ge, M.M. Kirka, R.R. Dehoff, H.Z. Bilheux, N. Kardjilov, I. Manke, L.G. Butler, Porosity detection in electron beam-melted Ti-6Al-4V using high-resolution neutron imaging and grating-based interferometry, Prog. Addit. Manuf. 2 (2017) 125–132. doi:10.1007/s40964-017-0025-z.

[22] P. Trtik, E.H. Lehmann, Isotopically-enriched gadolinium-157 oxysulfide scintillator screens for the high-resolution neutron imaging, Nucl. Instruments Methods Phys. Res. Sect. A Accel. Spectrometers, Detect. Assoc. Equip. 788 (2015). doi:10.1016/j.nima.2015.03.076.

[23] P. Trtik, J. Hovind, C. Grünzweig, A. Bollhalder, V. Thominet, C. David, A. Kaestner, E.H. Lehmann, Improving the Spatial Resolution of Neutron Imaging at Paul Scherrer Institut - The Neutron Microscope Project, in: Phys. Procedia, Grindelwald, Switzerland, 2015: pp. 169–176. doi:10.1016/j.phpro.2015.07.024.

[24] P. Trtik, E.H. Lehmann, Progress in High-resolution Neutron Imaging at the Paul Scherrer Institut-The Neutron Microscope Project, J. Phys. Conf. Ser. 746 (2016). doi:10.1088/1742-6596/746/1/012004.

[25] P. Trtik, Neutron microtomography of voids in gold, MethodsX. 4 (2017). doi:10.1016/j.mex.2017.11.009.

[26] H. Ghasemi-Tabasi, J. Jhabvala, E. Boillat, T. Ivas, R. Drissi-Daoudi, R.E. Logé, An effective rule for translating optimal selective laser melting processing parameters from one material to another,

Addit. Manuf. 36 (2020) 101496. doi:10.1016/j.addma.2020.101496.

[27] Sanjay Kumar, Additive Manufacturing Processes, 1st ed., Springer International Publishing, 2019. doi:10.1007/978-3-030-45089-2.

[28] B. AlMangour, D. Grzesiak, J.-M. Yang, Scanning strategies for texture and anisotropy tailoring during selective laser melting of TiC/316L stainless steel nanocomposites, J. Alloys Compd. 728 (2017) 424–435. doi:https://doi.org/10.1016/j.jallcom.2017.08.022.

[29] P. Trtik, M. Meyer, T. Wehmann, A. Tengattini, D. Atkins, E.H. Lehmann, M. Strobl, PSI 'Neutron Microscope' at ILL-D50 Beamline - First Results, Neutron Radiogr. - WCNR-11. 15 (2020) 23–28. doi:10.21741/9781644900574-4.

[30] A. Tengattini, N. Lenoir, E. Andò, B. Giroud, D. Atkins, J. Beaucour, G. Viggiani, NeXT-Grenoble, the Neutron and X-ray tomograph in Grenoble, Nucl. Instruments Methods Phys. Res. Sect. A Accel. Spectrometers, Detect. Assoc. Equip. 968 (2020) 163939. doi:10.1016/j.nima.2020.163939.

[31] J. Crha, J. Vila-Comamala, E. Lehmann, C. David, P. Trtik, Light Yield Enhancement of 157-Gadolinium Oxysulfide Scintillator Screens for the High-Resolution Neutron Imaging, MethodsX. 6 (2019) 107–114. doi:10.1016/J.MEX.2018.12.005.

[32] P. Boillat, C. Carminati, F. Schmid, C. Grünzweig, J. Hovind, A. Kaestner, D. Mannes, M. Morgano, M. Siegwart, P. Trtik, P. Vontobel, E.H. Lehmann, Chasing quantitative biases in neutron imaging with scintillator-camera detectors: A practical method with black body grids, Opt. Express. 26 (2018). doi:10.1364/OE.26.015769.

[33] C. Carminati, P. Boillat, F. Schmid, P. Vontobel, J. Hovind, M. Morgano, M. Raventos, M. Siegwart, D. Mannes, C. Gruenzweig, P. Trtik, E. Lehmann, M. Strobl, A. Kaestner, Implementation and assessment of the black body bias correction in quantitative neutron imaging, PLoS One. 14 (2019) e0210300. doi:10.1371/journal.pone.0210300.

[34] M. Guizar-Sicairos, A. Diaz, M. Holler, M.S. Lucas, A. Menzel, R.A. Wepf, O. Bunk, Phase tomography from x-ray coherent diffractive imaging projections, Opt. Express. 19 (2011). doi:10.1364/OE.19.021345.

[35] A.P. Kaestner, MuhRec - A new tomography reconstructor, Nucl. Instruments Methods Phys. Res. Sect. A Accel. Spectrometers, Detect. Assoc. Equip. 651 (2011). doi:10.1016/j.nima.2011.01.129.

[36] B. Münch, P. Trtik, F. Marone, M. Stampanoni, Stripe and ring artifact removal with combined wavelet - Fourier filtering, Opt. Express. 17 (2009). doi:10.1364/OE.17.008567.

[37] C. Carminati, M. Strobl, A. Kaestner, KipTool, a general purpose processing tool for neutron imaging data, SoftwareX. 10 (2019). doi:10.1016/j.softx.2019.100279.

[38] A. Kaestner, E. Lehmann, M. Stampanoni, Imaging and image processing in porous media research,

(2008). doi:10.1016/j.advwatres.2008.01.022.

[39] D. Brown, P. Kienzle, Neutron activation and scattering calculator, (2015) https://www.ncnr.nist.gov/resources/activation/itl. https://www.ncnr.nist.gov/resources/activation/.

[40] N. Otsu, Threshold selection method from gray-level histograms, IEEE Trans Syst Man Cybern. SMC-9 (1979) 62–66. doi:10.1109/tsmc.1979.4310076.

[41] Z. Dong, Y. Liu, W. Wen, J. Ge, J. Liang, Effect of hatch spacing on melt pool and as-built quality during selective laser melting of stainless steel: Modeling and experimental approaches, Materials (Basel). 12 (2018). doi:10.3390/ma12010050.

[42] A. du Plessis, Effects of process parameters on porosity in laser powder bed fusion revealed by X-ray tomography, Addit. Manuf. 30 (2019) 100871. doi:10.1016/j.addma.2019.100871.

[43] T. DebRoy, H.L. Wei, J.S. Zuback, T. Mukherjee, J.W. Elmer, J.O. Milewski, A.M. Beese, A. Wilson-Heid, A. De, W. Zhang, Additive manufacturing of metallic components – Process, structure and properties, Prog. Mater. Sci. 92 (2018) 112–224. doi:10.1016/j.pmatsci.2017.10.001.

[44] H. Qi, M. Azer, A. Ritter, Studies of standard heat treatment effects on microstructure and mechanical properties of laser net shape manufactured INCONEL 718, Metall. Mater. Trans. A Phys. Metall. Mater. Sci. 40 (2009) 2410–2422. doi:10.1007/s11661-009-9949-3.

[45] A.M. Mancisidor, F. Garciandia, M.S. Sebastian, P. Álvarez, J. Díaz, I. Unanue, Reduction of the residual porosity in parts manufactured by selective laser melting using skywriting and high focus offset strategies, Phys. Procedia. 83 (2016) 864–873. doi:10.1016/j.phpro.2016.08.090.

[46] L. Bian, N. Shamsaei, J. Usher, Laser-Based Additive Manufacturing of Metal Parts: Modeling, Optimization, and Control of Mechanical Properties, 1st ed., CRC Press, Inc., Boca Raton, FL, USA, 2017.

[47] M. Renderos, A. Torregaray, M.E. Gutierrez-Orrantia, A. Lamikiz, N. Saintier, F. Girot, Microstructure characterization of recycled IN718 powder and resulting laser clad material, Mater. Charact. 134 (2017) 103–113. doi:https://doi.org/10.1016/j.matchar.2017.09.029.

[48] R. Cunningham, C. Zhao, N. Parab, C. Kantzos, J. Pauza, K. Fezzaa, T. Sun, A.D. Rollett, Keyhole threshold and morphology in laser melting revealed by ultrahigh-speed x-ray imaging, Science (80-.). 363 (2019) 849–852. doi:10.1126/science.aav4687.

[49] A.A. Martin, N.P. Calta, S.A. Khairallah, J. Wang, P.J. Depond, A.Y. Fong, V. Thampy, G.M. Guss, A.M. Kiss, K.H. Stone, C.J. Tassone, J. Nelson Weker, M.F. Toney, T. van Buuren, M.J. Matthews, Dynamics of pore formation during laser powder bed fusion additive manufacturing, Nat. Commun. 10 (2019) 1–10. doi:10.1038/s41467-019-10009-2.

[50] N.T. Aboulkhair, N.M. Everitt, I. Ashcroft, C. Tuck, Reducing porosity in AlSi10Mg parts processed

by selective laser melting, Addit. Manuf. 1–4 (2014) 77–86. doi:https://doi.org/10.1016/j.addma.2014.08.001.

[51] S. Griffiths, H. Ghasemi Tabasi, T. Ivas, X. Maeder, A. De Luca, K. Zweiacker, R. Wróbel, J. Jhabvala, R.E. Logé, C. Leinenbach, Combining alloy and process modification for micro-crack mitigation in an additively manufactured Ni-base superalloy, Addit. Manuf. 36 (2020). doi:10.1016/j.addma.2020.101443.

[52] G. Kasperovich, J. Haubrich, J. Gussone, G. Requena, Correlation between porosity and processing parameters in TiAl6V4 produced by selective laser melting, Mater. Des. 112 (2016) 160–161. doi:10.1016/j.matdes.2016.09.040.

[53] J. Lee, J. Choe, J. Park, J.-H. Yu, S. Kim, I.D. Jung, H. Sung, Microstructural effects on the tensile and fracture behavior of selective laser melted H13 tool steel under varying conditions, Mater. Charact. 155 (2019) 109817. doi:https://doi.org/10.1016/j.matchar.2019.109817.

[54] M. Jamshidinia, R. Kovacevic, The influence of heat accumulation on the surface roughness in powder-bed additive manufacturing, Surf. Topogr. Metrol. Prop. 3 (2015). doi:10.1088/2051-672X/3/1/014003.

Chapter 6

Understanding variant selection and texture in additively manufactured red-gold alloys

Hossein Ghasemi-Tabasi[1], Margaux N.D. Larcher[1], Cyril Cayron[1], Nikola Kalentics[1], Jamasp Jhabvala[1], Eric Boillat, Roland E. Logé[1]

1. Thermomechanical Metallurgy Laboratory (LMTM) – PX Group Chair, École Polytechnique Fédérale de Lausanne (EPFL), CH-2002 Neuchâtel, Switzerland.

The manuscript will be submitted to the Materials Research Letters journal.

Contribution:
Hossein Ghasemi Tabasi printed the gold samples and conducted the microstructure and EBSD analyses. He wrote the manuscript.

Abstract

Laser-Powder Bed Fusion (L-PBF) has an increasing interest in the jewelry and watch industries. Printing gold alloys parts is a challenge due to the high reflectivity and thermal conductivity of these materials. Recent studies show an improvement in printing gold using the L-PBF process; however, the impact of the $A1 \rightarrow L1_0$ phase transformation on additively manufactured red-gold alloy has not been studied so far. In this work, 3D printed red-gold samples with different post processing - as-built, Laser Shock Peened (LSP), and annealed samples - have been heat treated at 250 ºC to investigate by Electron Backscatter Diffraction (EBSD) the effect of the sample stress states on variant selection during the phase transformation. The results indicate that textures after the heat-treatment strongly depend on the stress state in the early stages of the phase transformation. This stress state therefore determines the final spatial distribution of lattice strains in the L-PBF part.

Keywords: Laser powder bed fusion (L-PBF); Red-gold alloy; Variant selection; Electron backscatter diffraction (EBSD); Order–disorder transformation

Additive manufacturing (AM), also referred to as 3D printing, allows a sample to be built up layer by layer by material addition. Among different AM techniques, the Laser Powder Bed Fusion (L-PBF) has received the most focus. In the L-PBF process, a layer of powder is deposited on a substrate and the laser selectively melts the powder particles according to the computer-aided design (CAD) file [1].

A result of the deposition of liquid material on a solid substrate with lower temperature or previous solidified layers, is the existence of high temperature gradients and generation of residual stresses [2]. Spatial thermal gradients due to localized heating and cooling, and associated thermal expansion and contraction, including those coming from phase transformations (solid-liquid, or solid-solid), explain the generation of residual stresses in L-PBF. Restricted thermal shrinkage is the main reason for the presence of high tensile residual stresses in regions near the upper surface of the part under construction. After printing, tensile stresses on the top of the part are compensated by compressive stresses underneath, such as to satisfy stress equilibrium [3]. Laser Shock Peening (LSP) has recently been used in AM to transform the tensile residual stresses into compressive ones, in the near surface region [4–6], which permits to improve the mechanical properties of the piece[7].

Due to the high thermal gradients during the printing and the strong residual stresses remaining in the final piece, the processing is even more challenging when performed on a material undergoing a phase transformation. It is particularly the case for red-gold alloys with a composition close to the equiatomic

AuCu, undergoing an order-disorder phase transformation A1→$L1_0$ around 400°C [8]. At high temperature, the stable phase is a disordered f.c.c. (face centered cubic) lattice A1 with random distribution of gold and copper atoms on the crystallographic sites. When slowly cooled from high temperature, the tetragonal distortion of the lattice associated with the ordering of the atoms leads to the AuCuI phase, a f.c.t. (face centered tetragonal) superlattice of type $L1_0$ composed of alternate (002) planes of gold and copper. As local diffusion is needed for the atomic ordering, the phase transformation can be prevented by a high cooling rate, and the f.c.c. phase can be maintained in a metastable state at room temperature. However, the kinetics of the phase transformation highly depends on the temperature of the previous annealing treatment [9]. When the material is quenched from a high temperature, the formation of small f.c.t. domains is often inevitable [9,10].

After quenching, the f.c.t. phase can be obtained from retained f.c.c by a subsequent heat treatment under 400°C often called hardening heat treatment. The f.c.t. phase is beneficial for the mechanical properties of the material and is often used in industry for increasing the hardness and yield stress [11]. However, the phase transformation is also known for inducing strong macroscopic distortion in the material, that can even lead to cracking [11–14]. In a recent study [15], the macroscopic distortion of red-gold alloys was proved to be induced by very small levels of stress in the material through the Thermally Activated Distortion with Amplification (TADA) effect. This singular behavior is explained as follows. First, the stress is released by classical stress-induced variant selection, and second, the amplification is caused by the persistence of the initial variant selection during the continuation of the phase transformation. This variant selection has been proved to persist during further heat treatment even under opposite loading[16].

Due to the strong residual stresses in final printed parts, an important variant selection is expected during a hardening heat treatment on nearly 100% f.c.c. as-built pieces. In this study, we quantify residual stresses effects on the texture of 3D printed red-gold after hardening treatment. In particular, we show that surprisingly, the strong compressive stress induced by the LSP treatment after L-PBF printing has no impact on the final texture of the f.c.t. phase. This behavior is explained by the formation of small f.c.t. domains with tensile variant selection during printing, which persist despite the subsequent LSP induced compressive stress.

L-PBF experiments were performed with an in-house machine developed for research activities [17] and designed for operating with only a few dozen grams of powder. It is equipped with a 500 W fiber SPI laser, with a wavelength of 1070 nm and laser spot size of 65 µm. A bronze alloy (CuSn8) of composition 92 wt.% Cu, 8 wt.% Sn (expected density 8.79 $g.cm^{-3}$) and an 18-carat red-gold of composition 75 wt.% Au, 20.5 wt.% Cu, 4.5 wt.% Ag (expected density 15.2 $g.cm^{-3}$) were investigated. The powders, which were provided

by Heraeus Group, are composed of spherical particles with D50 of 31 µm and 26 µm for red-gold and bronze, respectively. Table 1 summarizes the process parameters used to print the samples.

Table 1. L-PBF process parameters and post treatments for bronze and red-gold samples.

	Power(W)	Speed(mm/s)	Hatching distance(µm)	Layer thickness(µm)	Laser beam diameter (µm)
Bronze	200	275	100	40	65
Red-gold	320	200	100	40	65

The laser parameters optimization process via experiments and simulations can be found in [18,19]. Bronze and red-gold samples are printed with the same normalized enthalpy, such as to reach 99.81% relative density. 5×5×1.5 mm red-gold samples were printed with the crosshatch scanning strategy to reach a symmetric stress distribution along the in plane x and y-axes (z being the building direction). Table 2 summarizes the post-processing treatments applied on 3 different red-gold samples.

Table 2. Different post processing treatments applied on as-built L-PBF red-gold samples. The treatments are applied sequentially from left to right, for each sample.

	Annealing at 600 ºC for 1h	LSP	Hardening heat treatment at 250 ºC for 3h
Sample 1	×	×	✓
Sample 2	×	✓	✓
Sample 3	✓	✓	✓

While still being attached to the baseplate, some samples were treated with laser shock peening (LSP) using a Nd:YAG SAGA HP laser from Thales company. The LSP parameters are listed in Table 3. The LSP treatment introduces a compressive stress state in the x-y plane, in the near top surface region of the sample. The same treatment was done on both red-gold and bronze samples.

Table 3. LSP process parameters

Wavelength	1064nm
Pulse duration	6.3ns
Spot size diameter	1mm
Pulse energy	0.5J
Power density	7.2 GW/cm^2
Frequency	5Hz
Overlap%	80

The use of bronze samples in this study aims at measuring the residual stress in the as-built and LSP treated states, using the hole drilling method, assuming these are close to the ones obtained in red-gold. Indeed, the minimum sample dimensions to measure the residual stress using this technique are 12×12×5 mm, which would require large amounts of red-gold powder. Although the stress state in the as-built L-PBF and LSP-treated samples has been investigated in previous studies [7,20], the 12×12×5 mm bronze samples are printed here to verify the state of the stress (and not the exact values) obtained with the cross-hatched L-PBF scanning strategy. The choice of CuSn8 as a model material relates to the mechanical properties, comparable to those of red-gold [21].

For the final microscopic observations, the red-gold samples are cut in half along the building direction. The cross section surface is then manually grinded, polished down to 1 µm and finally electropolished in a solution given in [22], during 20 sec at 27 V. The EBSD maps are acquired across the sample with a Gemini 450 (Zeiss) field emission gun scanning electron microscope, operating at 30 kV. The acquisition is performed with a Symmetry camera and the Aztec acquisition software (Oxford Instruments). The step size is chosen around 1 µm in order to scan a zone large enough to quantify variant selection in a reasonable amount of time. As the hardening heat treatment gives rise to a fully transformed state, only the f.c.t. phase is taken into account in the EBSD software.

After printing, the as–built red-gold Sample 1 was heat-treated at 250°C for 3h, in order to induce the phase transformation. X-ray diffraction and hardness analyses confirm that the as-built sample is almost 100% f.c.c just after printing, and it is almost fully transformed to the f.c.t phase after the hardening heat treatment (see Supplementary section S1). It is known that as-built L-PBF samples display tensile stress on the top surface and compressive ones in the region below [7,20,23]. Hole drilling measurements performed on the

bronze samples (Supplementary S2) confirm that the stress in the x-y plane is indeed tensile on top of the sample, with the chosen scanning strategy. A large EBSD map is performed along the x-z cross section of the samples, as represented in Figure 1-a. The f.c.t. domains represented in IPFx and y (Figure 1-c and 1-c) display the same coloring features: the top of the sample is mainly blue and green and the very bottom shows some red domains. This coloring is an indication of a strong texture caused by the variant selection. The blue and green domains correspond to the variants which have their extension axes in the x-y plane (extension variants), while the red domains have their contraction axis in the x-y plane (contraction variants) [24]. The texture in this sample is therefore in good agreement with the presence of tensile stresses near the top surface of the sample [24].

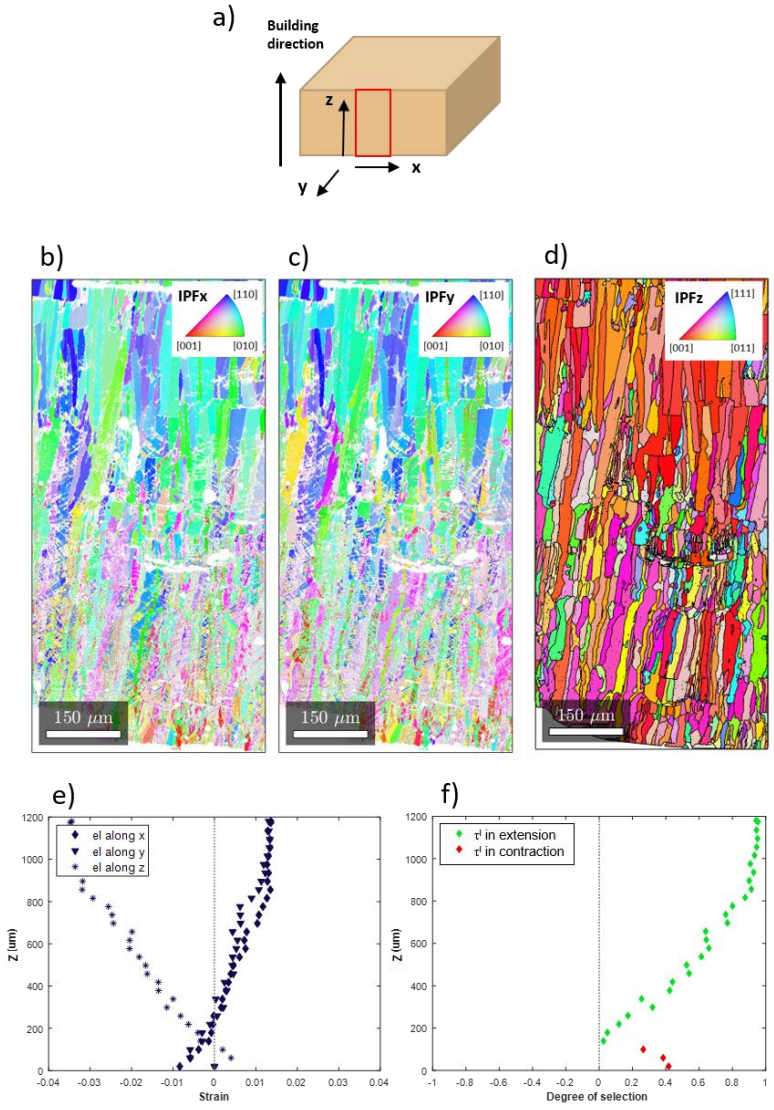

Figure 1: a) Schematic representation of the samples and location of the EBSD map. EBSD maps of Sample 1. F.c.t. domains represented in b) IPFx c) IPFy. d) The reconstructed parent f.c.c. grains in IPFz coloring. e) Evolution of the average lattice strain along the three sample directions with the depth z (0 is the bottom and 1200 µm is the top of the sample) and f) corresponding degree of variant selection.

Figure 1-d shows the high temperature f.c.c. parent grains, reconstructed from the EBSD data with the Mtex toolbox from Matlab [25]. The IPFz coloring shows a strong initial texture with all grains in reddish color, which means that {001} planes are perpendicular to the building discretion z. This initial texture is taken into account in the calculation of the degree of variant selection.

In order to quantitatively analyze the variant selection, the Matlab routine detailed in [24] is adapted to a biaxial stress distribution. The variant selection analysis is based on the calculation of the mechanical work of formation of one variant W. This work is expressed as the Frobenius product of σ, the macroscopic stress tensor, by ε^l, the lattice strain tensor, i.e. $W = \sigma : \varepsilon^l$.

The crosshatch L-PBF scanning strategy results in an approximately symmetric residual stress distribution along x and y (see Supplementary section S2). In addition, the profile of average lattice strain $\bar{\varepsilon}^l$ (Figure1-e) is very similar in the x and y directions, which indicates a symmetric distribution of the variant selection in the x and y directions. This is consistent with the symmetric residual stresses.

For the above reasons, we make the assumption that the stress state is equibiaxial, as expressed by the relation (1). In addition, shear stresses and the normal stress in the z-direction are set to 0 since they would have no impact on the analysis.

$$\boldsymbol{\sigma} = \begin{pmatrix} \sigma_x & 0 & 0 \\ 0 & \sigma_x & 0 \\ 0 & 0 & 0 \end{pmatrix} \quad (1)$$

The mechanical work associated to the transformation can then be expressed as $W = \sigma_x\left(\bar{\varepsilon}_x^l + \bar{\varepsilon}_y^l\right)$. The degree of variant selection τ defined in [24]. The average work value $\overline{W}$ is compared to the hypothetical equi-repartition of the three variants within each grain ($\overline{W}_{equi}$), and also to the case where only the maximal work variant is present in each grain ($\overline{W}_{max}$). It can be simplified and expressed in terms of lattice strains in equation (2).

$$\tau = \frac{\bar{W} - \bar{W}_{equi}}{\bar{W}_{max} - \bar{W}_{equi}} = \frac{\left(\bar{\varepsilon}_x^l + \bar{\varepsilon}_y^l\right) - \left(\bar{\varepsilon}_x^l + \bar{\varepsilon}_y^l\right)_{equi}}{\left(\bar{\varepsilon}_x^l + \bar{\varepsilon}_y^l\right)_{max} - \left(\bar{\varepsilon}_x^l + \bar{\varepsilon}_y^l\right)_{equi}} \quad (2)$$

Figure 1-f shows the evolution of the degree of variant selection τ across the thickness of the Sample 1. It confirms that extension variants are selected on top of the sample. In addition, a small compressive lattice strain is observed close to the bottom of the sample. The variant selection on top of the sample is almost maximal (close to 1), which has not been observed so far in conventional samples [15,24]. In addition, the average lattice strain on the top surface is very close to the one derived from the change of the crystallographic unit cell, i.e. 1.5% in extension and -3.9% in compression. This result is explained by the strong initial texture of the sample. For comparison, the strain in a non-textured polycrystal was computed in [15] as 1.12% in extension and -2.24% in contraction.

In order to study the influence of a compressive stress on the final texture, the LSP treatment is performed on another as-built red-gold Sample 2, in its f.c.c. phase. The LSP treatment induces compressive stress in the region near the top surface[4]. Sample 2 is then heat-treated at 250 °C for 3h, to induce the phase transformation. It is expected that the compressive stress near the top surface leads to variant selection with the contraction axis of the f.c.t. lattice in the x-y plane (contraction variants).

The EBSD map of the cross section of Sample 2 is presented in Figure 2. The IPFx and IPFy coloring of the f.c.t. variants in Figure 2-a, and 2-b shows the same texture as in Sample 1. This result is confirmed by the evolution of the degree of variant selection with z, given in Figure 2-d, again similar to that of Sample 1 (Figure 1). This distribution of variant selection is not consistent with the LSP induced compressive stress in the sample before the phase transformation. Yet, the presence of high compressive stresses on the top part of the sample has been confirmed by hold drilling measurements on the equivalent bronze sample (Supplementary section S2).

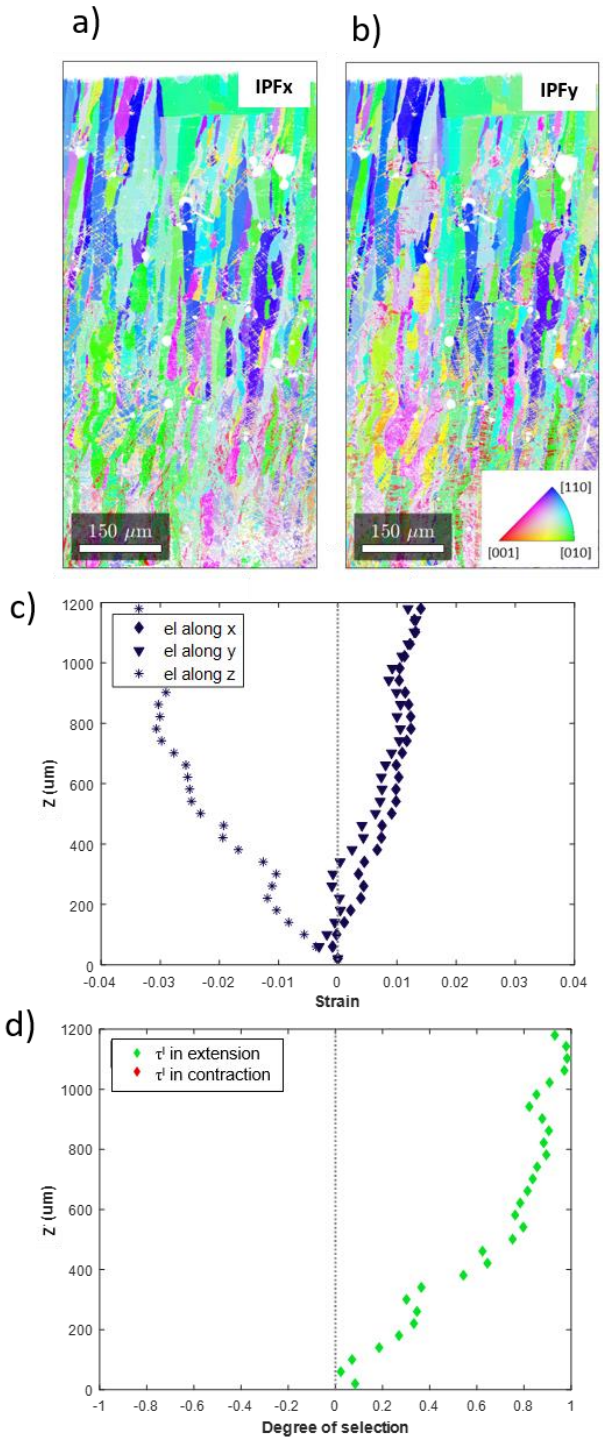

Figure 2: EBSD map of Sample 2 after ordering heat treatment with the f.c.t. domains in a) IPFx coloring and b) IPFy coloring. c) Evolution with z of the average lattice strain along the three sample directions and d) corresponding degree of variant selection.

As a comparison, another red-gold Sample 3 has been heat treated at 600 ºC for 45 minutes after printing, in order to re-initialize the thermo-mechanical history of the material [26]. The sample is then water

quenched to prevent the f.c.c. → f.c.t. transformation. Similarly to Sample 2, the LSP treatment is conducted to introduce compressive stresses near the top surface of the sample, and this operation is followed by a heat treatment at 250 ºC for 3h to induce the phase transformation. The EBSD map of Sample 3 is presented in Figure 3. This time, and unlike Sample 2, the texture in Sample 3 is consistent with the presence of compressive stresses on top of the sample (Figure 3). The red IPFx and IPFy coloring of the f.c.t. variants in Figure 3-a and 3-b indicates the presence of contraction variants on top of the sample. The lattice distortion evolution with z plotted in Figure 3-c shows a contraction along the x and y directions, and an extension along the z direction near the top surface. The lattice distortion is slightly different in the x and y directions, but the tendency is similar. The variant selection analysis is performed as described for Samples 1 and 2, and plotted in Figure 3-d. The variant selection as a function of z confirms the over-representation of contraction variants in the top half of the sample and extension variants in the bottom part. This profile is in good agreement with the expected stress profile induced by the LSP treatment [4].

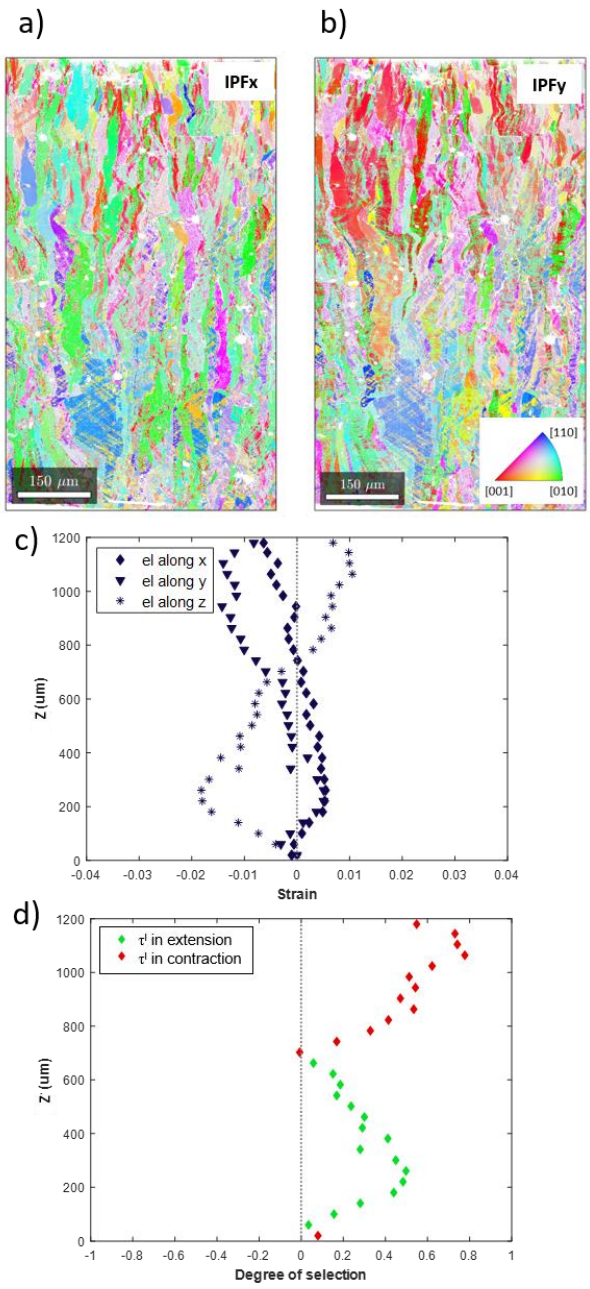

Figure 3: EBSD map of Sample 3 after ordering heat treatment with the f.c.t. domains in a) IPFx coloring and b) IPFy coloring. c) Evolution with z of the average lattice strain along the three sample directions and d) corresponding degree of variant selection.

The discrepancy between the textures of Sample 2 and Sample 3 is of interest as the two samples have undergone the same LSP and hardening treatments. The only difference between the two samples is the intermediate heat treatment at 600°C, before LSP. The variant selection profile in Sample 3 indicates that the LSP treatment has the expected effect on the material. The compressive stress on top of the sample (confirmed by the hole drilling measurements) induced contraction variant selection. The fact there is no

effect of the LSP treatment on Sample 2 demonstrates a mechanism preventing the expected variant selection. This effect is removed by the intermediate annealing at 600°C.

Although XRD measurements show no presence of the f.c.t. phase after printing (Supplementary S1), small nuclei of ordered f.c.t. phase are likely to be formed due to the non-negligible heating of the samples during L-PBF processing. Finite element simulations confirm that the temperature increases sufficiently high for the ordering phase transformation to take place during the deposition of new layers [18,27] (see also Supplementary section S3). According to [15], the variant selection is determined by the stress state at the very beginning of the phase transformation. If the stress is removed after these early stages, the variant selection keeps proceeding the same way, as the phase transformation continues. In a companion paper [16], it is proved that the persistence of the variant selection can even occur under opposite loading. The phenomenon of persistence of variant selection is at the origin of the surprising absence of LSP treatment effect on the variant selection and final texture in Sample 2.

In conclusion, variant selection along the cross section of additively manufactured red-gold samples has been quantified by EBSD, using the maximal work criterion. Despite the change of stress state induced by LSP treatment before the hardening heat treatment, the variant selection in the LSP treated sample (Sample 2) and the as-built sample (Sample 1) is the same This result is explained by the persistence of variant selection, whereby the formation of small f.c.t. domains in the printed sample occurs in the near surface region under tensile stress conditions. The extension variant selection initiated during L-PBF does not change and the f.c.t. domains will continue to grow accordingly, even if the stress state is subsequently changed by LSP. The small amount of f.c.t. phase can however be totally removed with an annealing treatment at 600°C followed by quenching (Sample 3). This approach then enables the subsequent LSP treatment to trigger the expected contraction variant selection and form a new texture after phase transformation.

Reference

[1] C.Y. Yap, C.K. Chua, Z.L. Dong, Z.H. Liu, D.Q. Zhang, L.E. Loh, S.L. Sing, Review of selective laser melting: Materials and applications, Appl. Phys. Rev. 2 (2015) 0–21. doi:10.1063/1.4935926.

[2] L.G. Hector, R.B. Hetnarski, Thermal Stresses in Materials Due to Laser Heating, in: R.B.B.T.-T.S.I. V Hetnarski (Ed.), Mech. Math. Methods–Series Handbooks, North-Holland, Amsterdam, 1996: pp. 453–531. doi:https://doi.org/10.1016/B978-044481571-2/50006-6.

[3] B. Vranchen, Study of Residual Stresses in Selective Laser Melting, KU LEUVEN, 2016. https://lirias.kuleuven.be/bitstream/123456789/542751/1/thesis+Bey+Vrancken+v01-06-2016+FINAL-compressed.pdf.

[4] N. Kalentics, E. Boillat, P. Peyre, S. Ćirić-Kostić, N. Bogojević, R.E. Logé, Tailoring residual stress profile of Selective Laser Melted parts by Laser Shock Peening, Addit. Manuf. 16 (2017) 90–97. doi:10.1016/j.addma.2017.05.008.

[5] N. Kalentics, A. Burn, M. Cloots, R.E. Logé, 3D laser shock peening as a way to improve geometrical accuracy in selective laser melting, Int. J. Adv. Manuf. Technol. 101 (2019) 1247–1254. doi:10.1007/s00170-018-3033-3.

[6] N. Kalentics, N. Sohrabi, H.G. Tabasi, S. Griffiths, J. Jhabvala, C. Leinenbach, A. Burn, R.E. Logé, Healing cracks in selective laser melting by 3D laser shock peening, Addit. Manuf. 30 (2019) 100881. doi:10.1016/j.addma.2019.100881.

[7] N. Kalentics, M.O.V. de Seijas, S. Griffiths, C. Leinenbach, R.E. Logé, 3D laser shock peening – A new method for improving fatigue properties of selective laser melted parts, Addit. Manuf. 33 (2020) 101112. doi:https://doi.org/10.1016/j.addma.2020.101112.

[8] H. Okamoto, D.J. Chakrabarti, D.E. Laughlin, T.B. Massalski, The Au-Cu (Gold-Copper) system, J. Phase Equilibria. 8 (1987) 454–474. doi:10.1007/BF02893155.

[9] G.C. Kuczynski, R.F. Hochman, M. Doyama, Study of the kinetics of ordering in the alloy AuCu, J. Appl. Phys. 26 (1955) 871–878. doi:10.1063/1.1722112.

[10] T. Shiraishi, M. Ohta, Low temperature ageing in equiatomic CuAu and Cu-Au-Pd ternary alloys, J. Mater. Sci. 24 (1989) 1049–1052. doi:10.1007/BF01148796.

[11] M. Garcia-Gonzalez, S. Van Petegem, N. Baluc, S. Hocine, M. Dupraz, F. Lalire, H. Van Swygenhoven, Enhanced precipitate growth at reduced temperatures during chemical ordering in deformed red gold alloys, Scr. Mater. 170 (2019) 129–133. doi:10.1016/j.scriptamat.2019.05.038.

[12] A.Y. Volkov, V.A. Kazantsev, Impact of the initial state on the structure and properties of the ordered CuAu alloy, Phys. Met. Metallogr. 113 (2012) 62–71. doi:10.1134/S0031918X12010127.

[13] M. Ohta, T. Shiraishi, R. Ouchida, M. Nakagawa, S. Matsuya, Shape restoration effect associated with order-disorder transformation in equiatomic AuCu and AuCu-Ga alloys, J. Alloys Compd. 265 (1998) 240–248. doi:10.1016/S0925-8388(97)00307-1.

[14] S. Kohara, G.C. Kuczynski, Internal stresses during ordering, Acta Metall. 4 (1956) 221–222. doi:10.1016/0001-6160(56)90149-3.

[15] M.N.D. Larcher, C. Cayron, A. Blatter, R. Soulignac, R.E. Logé, The thermally activated distortion with amplification effect and related variant selection in red gold alloys, Acta Mater. 198 (2020) 242–256. doi:10.1016/j.actamat.2020.07.064.

[16] M. Larcher, C. Cayron, A. Blatter, R. Souligance, R.E. Logé, No Title, In prepara (2021).

[17] J. Jhabvala, Study of the consolidation process under macro- and microscopic thermal effects in selective laser sintering and selective laser melting, EPFL PP - Lausanne, n.d. doi:10.5075/epfl-thesis-4609.

[18] H. Ghasemi-Tabasi, J. Jhabvala, E. Boillat, T. Ivas, R. Drissi-Daoudi, R.E. Logé, An effective rule for translating optimal selective laser melting processing parameters from one material to another, Addit. Manuf. 36 (2020) 101496. doi:10.1016/j.addma.2020.101496.

[19] H. Ghasemi-Tabasi, P. Trtik, J. Jhabvala, M. Meyer, C. Carminati, M. Strobl, R.E. Logé, Mapping Spatial Distribution of Pores in an Additively Manufactured Gold Alloy Using Neutron Microtomography, Appl. Sci. . 11 (2021). doi:10.3390/app11041512.

[20] J.L. Bartlett, X. Li, An overview of residual stresses in metal powder bed fusion, Addit. Manuf. 27 (2019) 131–149. doi:https://doi.org/10.1016/j.addma.2019.02.020.

[21] C. Deng, J. Kang, T. Feng, Y. Feng, X. Wang, P. Wu, Study on the selective laser melting of CuSn10 powder, Materials (Basel). 11 (2018) 1–7. doi:10.3390/ma11040614.

[22] R. Wolf, Electropolishing of gold and gold-rich alloys, Micron. 8 (1977) 171–172. doi:10.1016/0047-7206(77)90021-8.

[23] Y. Liu, Y. Yang, D. Wang, A study on the residual stress during selective laser melting (SLM) of metallic powder, Int. J. Adv. Manuf. Technol. 87 (2016) 647–656. doi:10.1007/s00170-016-8466-y.

[24] M.N.D. Larcher, C. Cayron, A. Blatter, R. Soulignac, R.E. Logé, Electron backscatter diffraction study of variant selection during ordering phase transformation in L10 -type red gold alloy, J. Appl. Crystallogr. 52 (2019) 1–12. doi:10.1107/S1600576719011890.

[25] F. Bachmann, R. Hielscher, H. Schaeben, Texture Analysis with MTEX – Free and Open Source Software Toolbox, Solid State Phenom. 160 (2010) 63–68. doi:10.4028/www.scientific.net/ssp.160.63.

[26] M. Garcia-Gonzalez, S. Van Petegem, N. Baluc, M. Dupraz, V. Honkimaki, F. Lalire, H. Van Swygenhoven, Influence of thermo-mechanical history on the ordering kinetics in 18 carat Au alloys, Acta Mater. 191 (2020) 186–197. doi:https://doi.org/10.1016/j.actamat.2020.03.032.

[27] S. Hocine, H. Van Swygenhoven, S. Van Petegem, Verification of selective laser melting heat source models with operando X-ray diffraction data, Addit. Manuf. 37 (2021) 101747. doi:10.1016/j.addma.2020.101747.

[28] N. Sohrabi, J. Jhabvala, G. Kurtuldu, M. Stoica, A. Parrilli, S. Berns, E. Polatidis, S. Van Petegem, S. Hugon, A. Neels, J.F. Löffler, R.E. Logé, Characterization, mechanical properties and dimensional accuracy of a Zr-based bulk metallic glass manufactured via laser powder-bed fusion, Mater. Des. 199 (2021) 109400. doi:https://doi.org/10.1016/j.matdes.2020.109400.

[29] U. Scipioni Bertoli, G. Guss, S. Wu, M.J. Matthews, J.M. Schoenung, In-situ characterization of laser-powder interaction and cooling rates through high-speed imaging of powder bed fusion additive manufacturing, Mater. Des. 135 (2017) 385–396. doi:10.1016/j.matdes.2017.09.044.

[30] P.A. Hooper, Melt pool temperature and cooling rates in laser powder bed fusion, Addit. Manuf. 22 (2018) 548–559. doi:10.1016/j.addma.2018.05.032.

Supplementary Material

Understanding variant selection and texture in additively manufactured red-gold alloys

Hossein Ghasemi-Tabasi[1], Margaux N.D. Larcher[1], Cyril Cayron[1], Nikola Kalentics[1], Jamasp Jhabvala[1], Eric Boillat, Roland E. Logé[1]

1. Thermomechanical Metallurgy Laboratory – PX Group Chair, École Polytechnique Fédérale de Lausanne (EPFL), CH-2002 Neuchatel, Switzerland

S1. XRD, and hardness analysis of the red-gold samples

XRD characterization of the samples is done with a PanAlytical Empyrean diffractometer (Theta-Theta, 240 mm), equipped with aPIXcel-1D detector in reflection mode using Cu-Kα radiation.

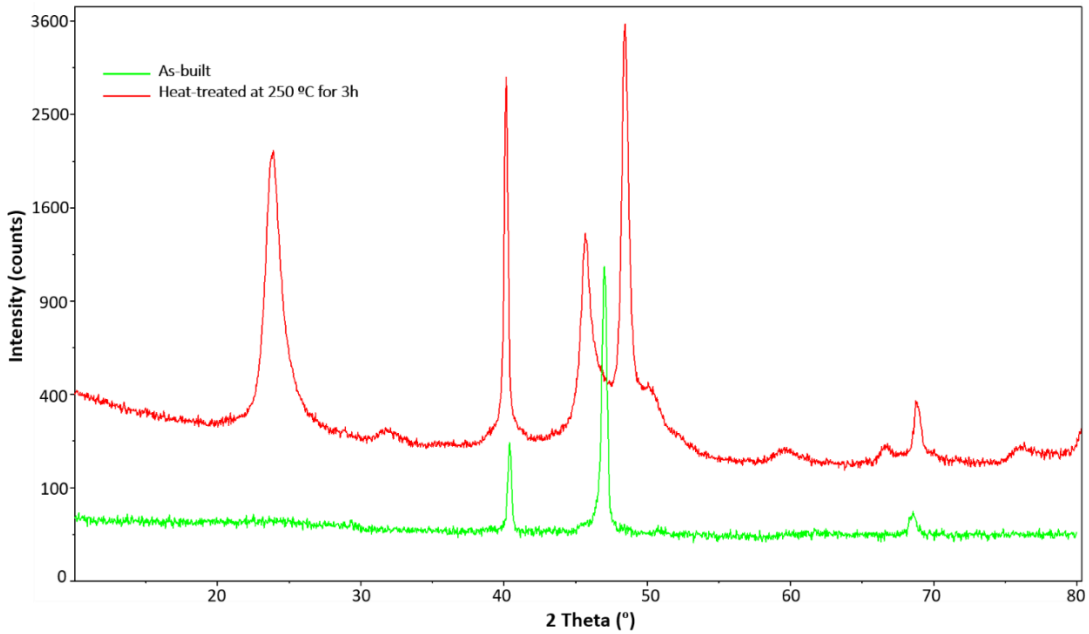

Figure S1. Laboratory XRD pattern (Cu-Kα radiation) of the as-built and heat-treated red-gold samples.

Vickers microhardness tests are conducted with 1-kgf (HV 1) and a dwell time of 10 s with a QnessQ10A machine.

Table S1. The hardness of the as-built and heat-treated red-gold samples.

Samples	Hardness (HV1)
As-built	175 ± 4
Heat-treated at 250 ºC for 3h	304 ± 8

XRD, and hardness analysis indicate that as-built samples consist of almost 100% f.c.c phase, whereas after keeping the sample 3h at 250 ºC, the microstructure is almost fully transformed to f.c.t.

S2. Hole drilling measurement on as-built and LSP-treated bronze samples

The hole-drilling method is a semi-destructive standardized method to measure residual stresses in a material. It leads to a local redistribution of the stresses, and thus, a measurable deformation of the hole. A strain gauge pasted on the surface of the material measures the hole deformation at each step of the drilling. Thanks to different models, the stress can be calculated as a function ot the depth from the top surface, up to 1mm, by steps of 10µm. In this work, the industrial machine MTS3000-Restan by SINT technologies is used. It is a fully automated machine, which can drill and acquire the deformation at each step without external intervention. Figure S2 indicates a schematic view of the crosshatch scanning strategy and the residual stress curves measured for a bronze sample in the as–built and LSP treated states.

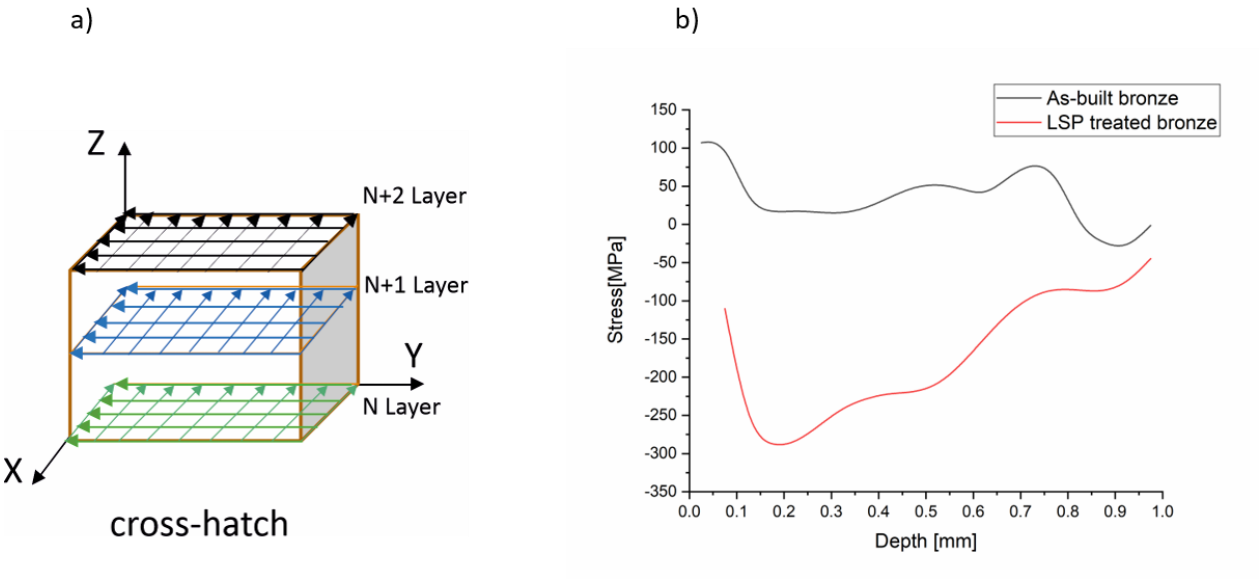

Figure S2. a) Schematic view of the scanning strategy used in printing bronze and red-gold samples, and b) residual stress curves measured for the bronze samples in the as–built and LSP treated conditions.

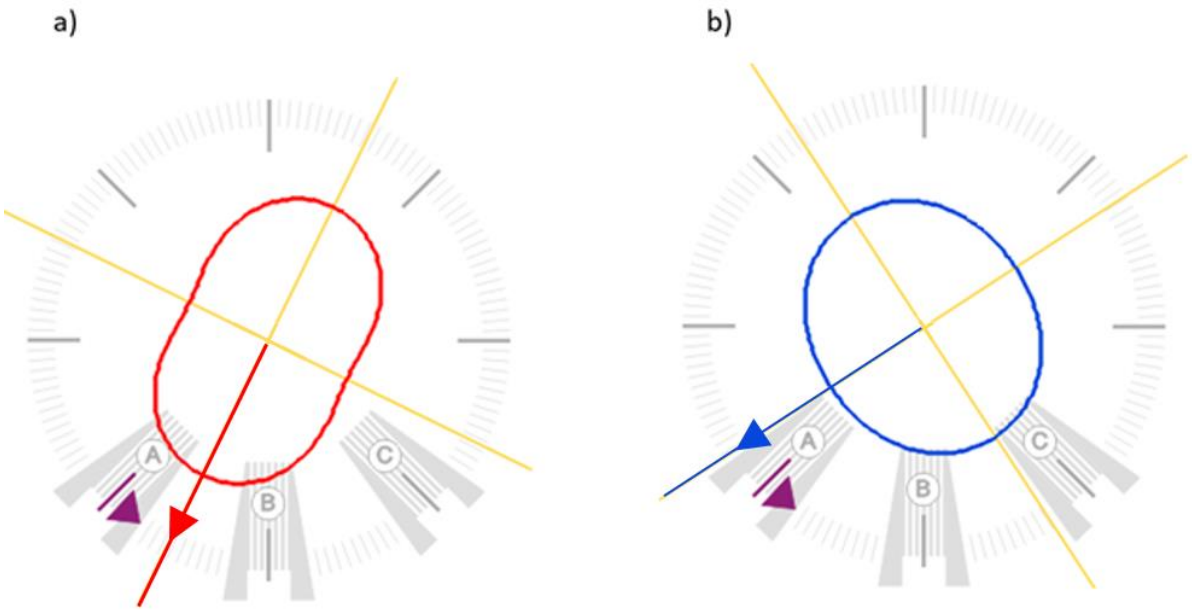

Figure S3. Residual stress spatial distribution close to the top surface (X-Y) for a) as-built, and b) LSP treated bronze samples. the residual stress principal direction is highlighted by red anb blue line and arrow representative of tensile and compressive residual stress, respectively.

The spatial distribution of residual stresses is shown in Figure S3. Elongation of the circular line in specific direction shows the residual stress principal direction (red line for tensile and blue line for compressive residual stress value). Figure S3-a indicates that tensile residual stresses in the as-built sample are present in all directions, with higher magnitude in one direction. The LSP-treated sample has a more isotropic compressive residual stress, as shown in figure S3-b.

S3. Numerical simulation of the L-PBF process

To better understand the temperature distribution during the manufacturing process, we performed numerical simulations of the LPBF process. A dedicated finite element simulation software has been developed for the modeling of the L-PBF process. In this code, the powder bed is considered as a

homogeneous medium, which has effective properties (absorptivity, thermal conductivity, optical penetration depth, density) (for more details, see [18,28]).

Figure S4 indicates the temperature distribution during the L-PBF process of the red-gold sample with the process parameters listed in the manuscript (Table 1). In the zone below the top surface, the temperature is high enough for phase transformation to occur in the red-gold sample. However, due to the fast heating and cooling rates during the manufacturing process [29,30], we expect only small nuclei of the ordered phase to form, with no significant growth. Figure S4-c indicates the temperature evolution at given sample locations (A on top surface and B, 120µm below the top surface, which represents 3 L-PBF layers), during three successive laser parallel line tracks. The results show that when considering a standard hatching distance (100µm), heat affected zones in the vicinity of the melt pool reach sufficiently high temperatures for triggering phase transformation (the white zone in figure S4-b). As indicated in Figure S4-c, a given material point remains for a very short time in this temperature range. On the other hand, the L-PBF process implies a number of thermal cycles, due to the deposition of successive layers.

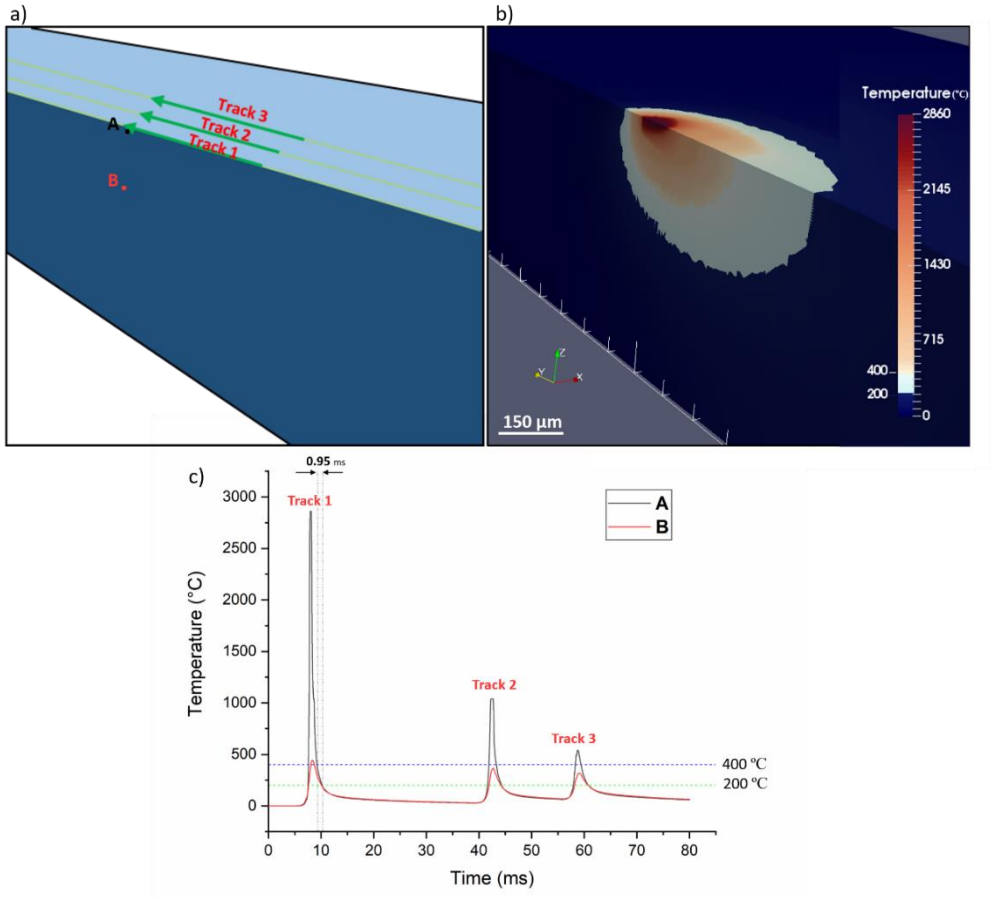

Figure S4. Simulated temperature field (°C) in a red-gold sample during L-PBF processing. a) Schematic view of three adjacent laser tracks, b) temperature distribution on the top surface of the sample and in the depth, and c) evolution of temperature at point A and point B, during the printing of three adjacent tracks.

[1] H. Ghasemi-Tabasi, J. Jhabvala, E. Boillat, T. Ivas, R. Drissi-Daoudi, R.E. Logé, Addit. Manuf. 36 (2020) 101496.

[2] N. Sohrabi, J. Jhabvala, G. Kurtuldu, M. Stoica, A. Parrilli, S. Berns, E. Polatidis, S. Van Petegem, S. Hugon, A. Neels, J.F. Löffler, R.E. Logé, Mater. Des. 199 (2021) 109400.

[3] U. Scipioni Bertoli, G. Guss, S. Wu, M.J. Matthews, J.M. Schoenung, Mater. Des. 135 (2017) 385–396.

[4] P.A. Hooper, Addit. Manuf. 22 (2018) 548–559.

Chapter 7

Direct observation of crack formation mechanisms with *operando* Laser Powder Bed Fusion X-ray imaging

Hossein Ghasemi-Tabasi[1], Charlotte de Formanoir[1], Steven Van Petegem[2], Jamasp Jhabvala[1], Samy Hocine[2,3], Eric Boillat[1], Navid Sohrabi[1], Federica Marone[4], Daniel Grolimund[4], Helena Van Swygenhoven[2,3], Roland E. Logé[1]

1. Thermomechanical Metallurgy Laboratory (LMTM) – PX Group Chair, École Polytechnique Fédérale de Lausanne (EPFL), CH-2002 Neuchâtel, Switzerland
2. Photons for Engineering and Manufacturing, Paul Scherrer Institute, Forschungsstrasse 111, 5232 Villigen PSI, Switzerland
3. Neutrons and X-rays for Mechanics of Materials, IMX, École Polytechnique Fédérale de Lausanne (EPFL), Route Cantonale, 1015 Lausanne, Switzerland
4. Swiss Light Source, Paul Scherrer Institute, 5232 Villigen, Switzerland

Manuscript is submitted to Acta Materialia and is under review (Manuscript number A-21-1439)

Contribution:

Hossein Ghasemi Tabasi printed the CM247LC samples (ex-situ and operando experiments), ran the numerical simulations, analyzed the acquired data from the operando experiments (Imaging and diffraction) and characterized the printed samples by optical microscopy and SEM. He wrote the manuscript.

Abstract

Laser powder bed fusion (L-PBF) is a versatile additive manufacturing process that can print geometrically complex metal parts for a variety of applications. However, poor control of defect formation during processing hampers its widespread industrial adoption. Many materials suffer from a high crack susceptibility during L-PBF, which results in degraded mechanical properties, and is an obstacle to the certification of critical parts. In order to unveil the mechanisms of crack formation in a prone-to-cracking nickel-based superalloy, we employ for the first time high-speed synchrotron X-ray imaging in combination with a miniaturized L-PBF set-up that reproduces real processing conditions. This unique set-up provides *operando* imaging of crack formation during L-PBF. Complementary post-mortem inspection of crack morphology and thermal simulations supported by *operando* X-ray diffraction-based measurements of the temperature evolution allow to identify the cracking mechanism and to differentiate hot cracking from liquation.

Keywords: Laser powder bed fusion; Operando X-ray imaging; Ni superalloy; Cracking; Segregation.

1. Introduction

Additive Manufacturing (AM) refers to different technologies that produce three-dimensional parts in a layer-by-layer mode. Due to its high technological and economic impact, the interest for AM has increased dramatically in recent years[1]. Laser Powder Bed Fusion (L-PBF), also known as Selective Laser Melting (SLM), is a highly versatile, and one of the most studied AM processes for metals. It enables the manufacturing of very complex metallic objects by selectively melting successive layers of powder based on a computer-aided design (CAD) file. From a metallurgical point of view, the complex thermal history that the material undergoes during L-PBF differs substantially from conventional processing. It is characterized by a succession of fast melting, fast solidification (cooling rates ~ 10^6 °C.s^{-1}), and cyclic remelting or reheating in the vicinity of the melt pool. The thermal gradients induced by the process and the large degree of shrinkage occurring during solidification create high residual stresses and favor crack formation [2–6].

The CM247LC nickel-based superalloy is a γ′-strengthened Ni superalloy, which is of particular interest due to its excellent mechanical, creep, wear, and oxidation properties at both ambient and elevated temperatures [7–10]. However, this alloy contains high amounts of Al and Ti and is considered vulnerable to cracking due to $L1_2$ Ni_3(Al, Ti) precipitation [11,12]. In literature, several mechanisms are reported to be responsible for cracking during the manufacturing of CM247LC alloy. Solidification cracking, liquation cracking and ductility dip cracking (DDC) are the main mechanisms that have been suggested [13–18].

Solidification cracking occurs in the last stages of solidification, due to a combination of solute-rich liquid entrapment between solid interfaces and tensile residual stresses that pull the interfaces apart [13–15,19,20]. Liquation cracking results from the micro-segregation that takes place during fast solidification, which locally lowers the solidus point. When an adjacent line scan or additional layer is processed, localized melting and associated cracking occur in the heat-affected zone [13–15,21]. Finally, ductility reduction in a [0.5 $T_{solidus}$ – $T_{solidus}$] temperature range has been reported in Ni-based superalloys. As is the case for solidification and liquation cracking, the presence of residual stress within this temperature range results in the so-called "ductility dip cracking" (DDC) [16–18,22].

Kalentics et al. [13] observed solidification and liquation cracks in as-built CM247LC samples. Griffiths et al. [14] suggested that micro-cracking in CM247LC was attributed to both solidification and liquation cracking. Gleeble experiments on as-built CM247LC L-PBF samples showed that a liquation cracking mechanism is most likely active in the heat-affected zone of laser tracks. Both numerical simulations and chemical analysis suggested that Hf influences the freezing range of the alloy and makes it susceptible to cracking.

Liquation cracking was also reported in as-built samples of IN738LC (another γ'-strengthened Ni superalloy) [23]. The presence of low melting point alloying components at the vicinity of the crack surface is evidence for this cracking mechanism [14,16,23].

Carter et al. [17] studied L-PBF-printed CM247LC samples and observed high-angle grain boundaries near the cracks, thus concluding that DDC is the main cracking mechanism in this alloy. The microstructure consists of columnar grains containing slightly misorientated cells elongated along the build direction. TEM analysis revealed the presence of small carbides within the cells, inter- and intra-cellular γ' precipitates, and a high density of dislocations at the grain and cell boundaries. These observations support the DDC mechanism[16,18].

The origin of cracking in additively manufactured γ'-strengthened Ni-based superalloys is thus still a matter of debate. So far, only post-mortem crack examinations have been performed and no observation of cracking *during* additive manufacturing of CM247LC samples in real condition is reported in the literature. *In-situ* X-ray imaging is a powerful technique to investigate the formation of defects in metals during thermal processing. In recent years, several fast *in-situ* radiography measurements have been performed during laser processing. These experiments mostly focus on the study of melt pool dynamics [24,25,34–39,26–33], on the formation and elimination of pores [25,28,40–43], and on the generation of spatters [25,44–48]. Despite its importance for the final mechanical integrity of L-PBF parts, there exists little literature on the *in-situ* observation. Preliminary work demonstrated the feasibility of observing cracks in an aluminum alloy 6061[49,50]. Their geometry and interaction with porosities was emphasized from single laser line tracks,

with however a simplified setup consisting of cuboidal solid specimens with no powder layer on top[50]. Whenever the aforementioned *in-situ* studies use a powder-bed system, the chosen configuration faces several limitations. It systematically consists of two plates that are transparent to X-rays and separated by a few hundred microns, between which a substrate is sandwiched. In most cases, a 100µm-thick single layer of powder is manually applied on top of the substrate [24,25,35,36,41], whereas in other cases the X-ray experiments are directly performed on the bare substrate, without any powder bed, to enhance clarity [26,35,41,50]. This two-plate setup can be considered as a quasi-2D configuration, which captures the evolution of a single layer melt track rather than the whole 3D character of the L-PBF process. Because the thickness and width of the substrate and powder bed are restricted to a few hundred microns, heat extraction from the melt pool strongly differs from what takes place in larger three-dimensional parts. This questions to what extent this type of set-up is representative of real powder bed additive manufacturing conditions. Regardless of the mechanism at play, most crack formation mechanisms during L-PBF are promoted by tensile residual stresses, which tend to accumulate through several layers. It is therefore essential to monitor the printing of several layers to observe cracking during the L-PBF process. To that end, a miniaturized L-PBF device [51,52] optimized for usage at synchrotron beamlines and reproducing real processing conditions at a small scale, is employed in the present study, the first ever to report imaging of cracking phenomena during L-PBF in real conditions. *Operando* radiography, combined with post-process SEM and EDX analyzes and thermal simulations, provides valuable information on the conditions of crack initiation and the possible cracking mechanisms taking place during processing. Complementary *operando* X-ray diffraction experiments are used to monitor the evolution of temperature during processing and relate it to the simulated results.

2. Experimental method

2.1. Materials and Fabrication

Commercial gas-atomized CM247LC powder provided by Oerlikon Metco (Pfaeffikon, Switzerland) was used in this study. Powder size distribution was 15 – 45 µm with a D_{50} of approximately 30 µm. The chemical composition of the powder is listed in Table 1 [14]. The *operando* radiography experiments were performed with a miniaturized L-PBF device developed at the Paul Scherrer Institut (Switzerland). It mimics a commercial L-PBF device and is optimized for usage at synchrotron beamlines. A detailed description of the device can be found in [51,52]. The laser source is a 500 W redPOWER® continuous wave (CW) Fiber Laser (SPI Lasers Ltd, UK), operating at a wavelength of 1070 ± 10nm. The laser beam is collimated as a parallel Gaussian beam into a 2-axis SuperScan III deflection-scanning unit (Raylase GmbH, Germany) with a 15 mm input aperture. Two fused silica mirror galvanometers allow scanning the laser beam over the

power bed. The beam is focused down to a ø100 µm spot size through an F-Theta lens (Sill Optics, Germany). Both laser and scanning units are controlled via an SP-ICE-3 board and the WeldMARK software (Raylase GmbH, Germany). Before and during operation the chamber is flushed with Ar-gas. Furthermore, on the recoater a gas-outlet is mounted, which blows Ar-gas over the powder bed.

The laser process parameters were determined based on ex-situ analysis preliminary to the *operando* experiments (Table 2).

Table 1. Chemical composition of the CM247LC powder

wt. %	**Al**	**W**	**Co**	**Cr**	**Ta**	**Hf**	**Ti**	**Mo**	**C**	**Fe**	**B**	**Zr**	**Ni**
CM247LC	5.71	9.93	9.24	8.62	3.08	1.37	0.73	0.54	0.06	0.02	0.017	0.006	Bal

Table 2. Processing parameters

Laser characteristics	
Spot diameter ($1/e^2$)	100 µm
Power	160 W
Scanning speed	220 mm/s
Hatch distance	100 µm
Scanning strategy	Bi-directional
Powder bed	
Base plate material	316L stainless steel
Pre-heating temperature	25°C
Layer thickness	40 µm

The printed samples were cut along the build direction and polished mechanically by SiC papers up to 2500 grit size and then polished by diamond suspension until 1 µm. To reveal the microstructure around the cracks, polished samples were etched with the Kalling solution (25ml Ethanol +25ml HCl +2.25g CuCl2) for one minute. Crack morphology analysis was done using a Zeiss-Gemini2 field emission scanning electron microscope. SEM-EDX analysis was performed at 15 keV.

2.2. *Operando* synchrotron X-ray imaging

The *Operando* X-ray imaging experiments were performed at the TOmographic Microscopy and Coherent rAdiology experimenTs (TOMCAT) beamline of the Swiss Light Source using an in-house built L-PBF device[51,52]. Figure 1 displays a schematic view of the setup. The miniaturized L-PBF device was mounted on a dedicated stage and tilted by 20 degrees compared to the direction of the incoming X-ray beam. The edge of the powder bed was illuminated by a parallel X-ray beam with energies ranging between

approximately 10 and 55 keV. The polychromatic radiation emerging from the source was filtered with 5 mm of Sigradur (50% power filter) and 0.525 mm of Si. The transmitted beam was recorded with a custom-made 4× microscope [53], coupled to the in-house developed GigaFRoST detector [54]. This detector exhibits a 2016x2016 pixels CMOS imaging chip with 11µm pixel size and 12-bit nominal dynamic range. Its novel readout system provides continuous and sustained data streaming up to almost 8GB/s to a dedicated high-performance data backend server. To optimize the visibility of crack observation, the microscope was positioned at a relatively large distance from the sample (70cm). This resulted in an enhanced contrast for edges. The experiments were performed at an acquisition frequency of 10 kHz. This was achieved by reducing the region of interest to 672 × 512 pixels, equivalent to a field-of-view of 1.85 × 1.41mm^2 (width × height). The optics consist of the custom-made microscope with 4× magnification and a high numerical aperture of 0.35, resulting in an effective pixel size of 2.75µm. Prior to the *operando* radiography experiments 8×2×0.4 mm^3 cuboids were printed near the edge of the build plate (Figure 1c). During the *operando* radiography experiment, a single layer was printed with the same process parameters while a series of radiographs were captured at 10'000 frames per second for a total duration of 1.5s. Figure S1 in the supplementary materials indicates some examples of printed CM247LC samples. All the acquired data were Flat-Field Corrected (FFC) using MATLAB R2018a[29] and an average flat-field image computed out of 10 consecutive frames. The contrast of corrected images was adjusted by Fiji and GIMP using color balance and color curve adjustment features. Supplementary figure S2 displays a picture of the mounted setup at the TOMCAT beam line of the Swiss Light Source.

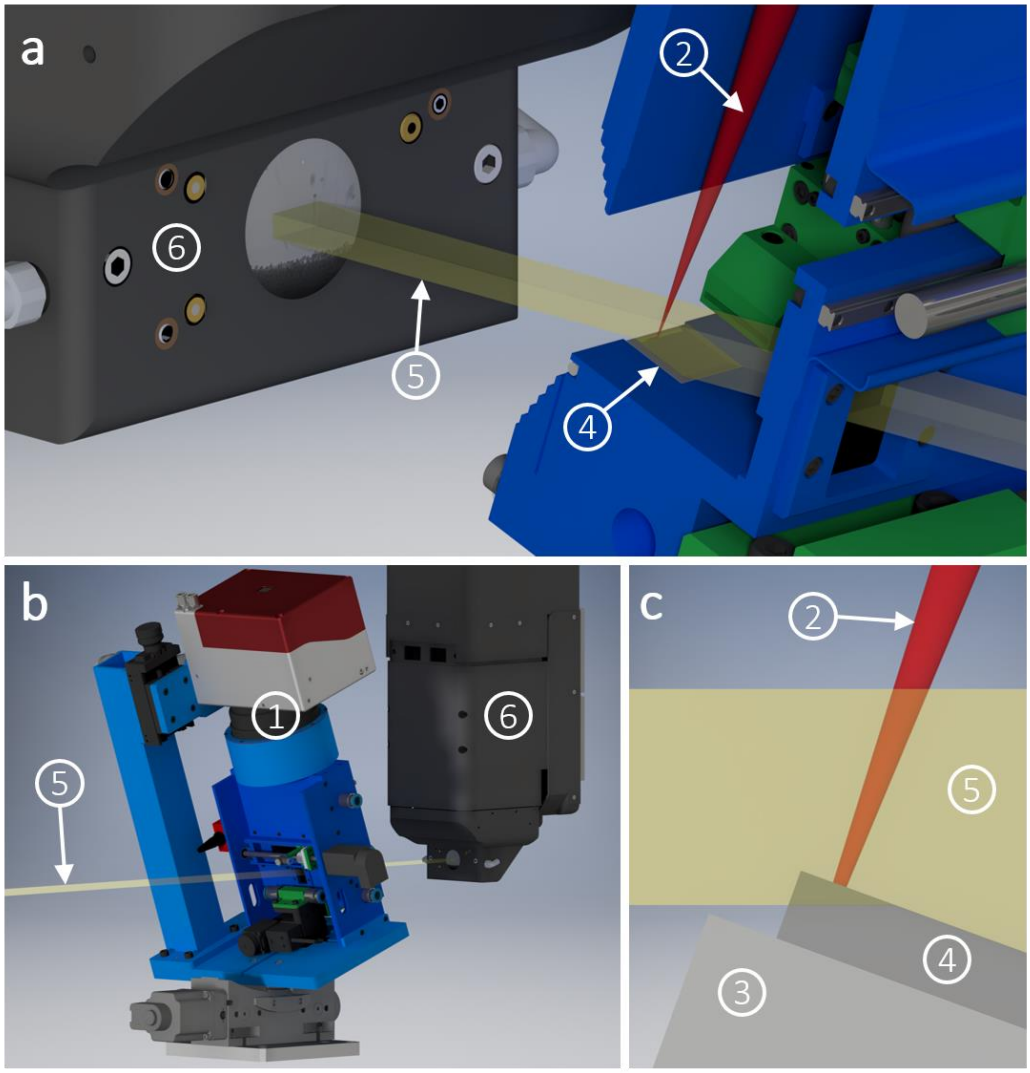

Figure 1. Schematic view of the *operando* radiography setup at the TOMCAT beamline. a), b) open build chamber of the miniaturized L-PBF machine and the camera in two different views, and c) zoom on the build plate and the printed sample to highlight the volume in which data is acquired during the *operando* experiment. A 2-axis scanning head (1) deflects the laser beam (2) on to a 12 × 12 mm^2 build plate (3) and the sample (4). A parallel X-ray beam (5) passes through the sample (figure 1c) and reaches the microscope (6).

As the sample is tilted compared to the incoming beam, the interpretation of the radiographs is not straightforward. Figure 2 displays a 3D schematic of the *operando* experiment for the first and final printed track of a given layer, together with representative features in the 2D projected images. This includes powder particles, solidified material, spatters, pores, and cracks. A more detailed discussion on the observed contrasts of these features can be found in the Supplementary Materials S3.

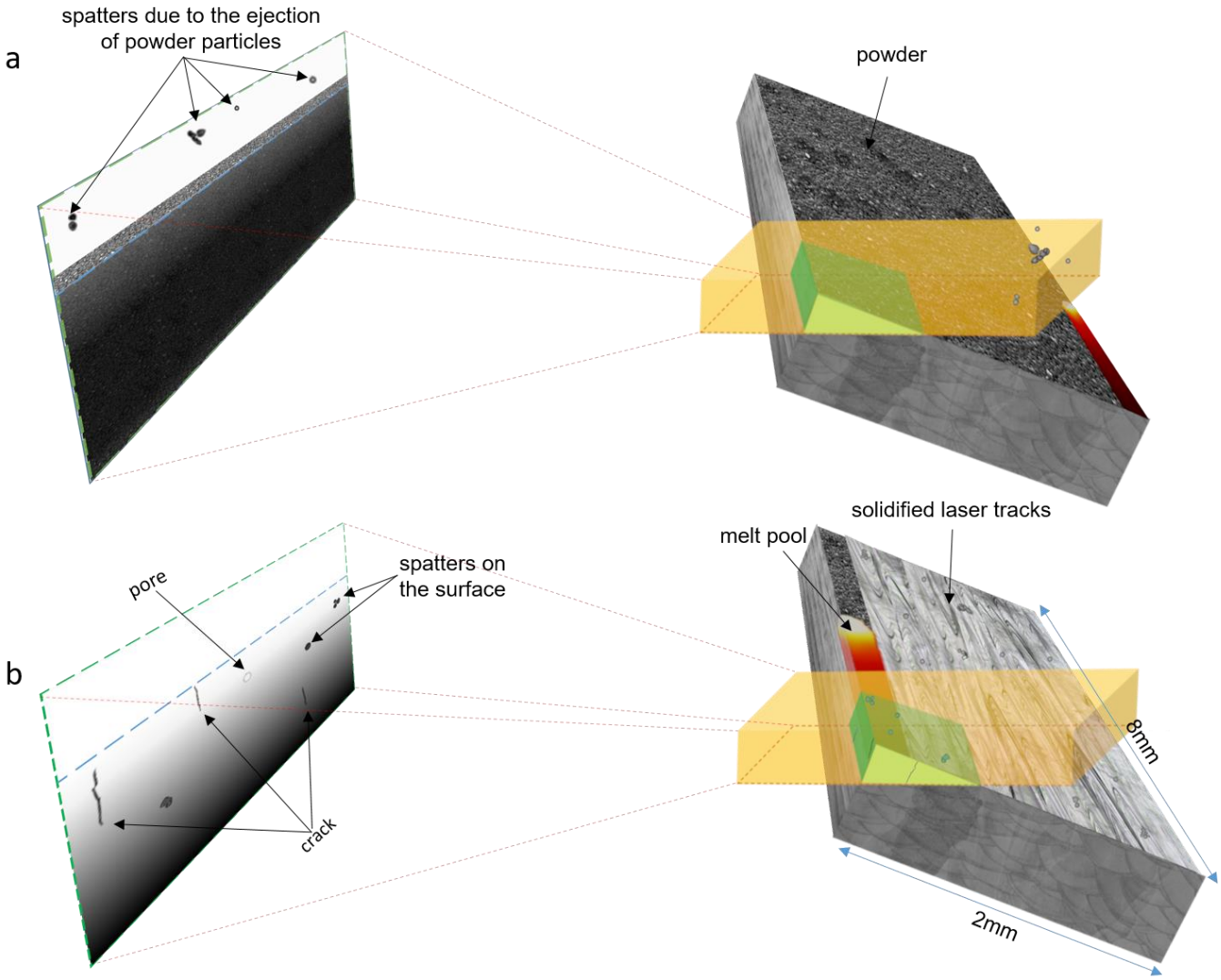

Figure 2. 3D schematic of the *operando* radiography experiments. Two representative cases, i.e. at the beginning (a) and at the end (b) of the printing of a layer, are depicted to illustrate the type of features that can be observed: spatters and powder particles, cracks and pores. The volume of material analyzed during the experiment is highlighted in green and the corresponding projected 2D image can be seen on the left. Powder particles on the top surface exhibit a darker contrast, whereas pores appear brighter. Cracks exhibit a dark contrast, as explained in Supplementary Materials S3. At the beginning of the process, (a) due to the printing of the first tracks at the back of the sample and the ejection of powder particles in the vicinity of the melt pool, some spatters appear in the images. After printing the last tracks near the edge of the sample, i.e. in the green volume, cracks and pores appear in this region and can be observed in the 2D images (b). In the last tracks (b), due to denudation effects, a much lower amount of powder particles is present on the top surface compared to the first tracks (a). For visibility purposes the different features (melt pool, cracks, pores, X-ray beam) represented in the schematic are not at the right scale.

2.3. *Operando* synchrotron X-ray diffraction

The *operando* X-ray diffraction experiments were performed at the MicroXAS beamline of the Swiss Light Source (SLS) using the same L-PBF device and processing parameters as for the X-ray imaging experiments. The X-ray beam had an energy of 17 keV and was focused to a projected spot size of 80 x 80 μm^2. Figure S3 in Supplementary Materials displays a picture of the L-PBF device mounted at MicroXAS. The experiments are performed in reflection mode, where the X-ray beam is positioned in the center of the sample. The diffracted beam is recorded by a 1M EIGER detector, developed at the Paul Scherrer Institute. During printing, 4-bit 2D diffraction patterns are recorded at a frequency of 20kHz. Azimuthal integration was done with pyFAI, resulting in 1D images with an angular range between 10° and 70°.

Figure S3 in Supplementary Materials shows a representative intensity vs diffraction and time plot. When the laser passes the area illuminated by the X-ray beam, the diffraction peaks change their position due to thermal expansion and contraction. This can be expressed as a change in lattice strain, which, in turn, is converted into a change in temperature using temperature-dependent thermal expansion coefficients [55]. Here, it is assumed that the thermal effects on the lattice constant are significantly larger compared to the effects of residual stresses and chemical composition[51].

2.4. Numerical simulations

A dedicated numerical simulation software has been developed to model the L-PBF process. The powder bed is considered as a homogeneous medium, with effective properties such as absorptivity, optical penetration depth, density, thermal conductivity, etc. Thermophysical properties vary according to the material state (powder, solid, and liquid). The absorptivity of powder particles is 57%, as measured with a Perkin Elmer Lambda900 spectrophotometer at 1070 nm wavelength[56]. Thermophysical properties and their evolutions with temperature are taken from [14,57–60]. To validate simulated temperatures, the values are compared with *operando* x-ray experiments. The simulation is done using the same process parameters and scanning strategies as for the *operando* experiments. Simulated temperatures are averaged over the x-ray beam probed zone, in the same way as the *operando* x-ray experiment does. More details on the finite element simulation framework are available in a recently published paper [56].

3. Results and discussion

3.1. *Operando* observation of crack formation

During the experiments, two particularly distinct crack-related features could be observed: 1) formation, growth, and remelting of cracks after interaction with the melt pool, and 2) growth of existing cracks after interaction with the heat-affected zone (HAZ).

Figure 3 shows five snapshots during the printing of two adjacent tracks. The contrast was chosen to highlight pores and cracks; spatters are not visible here. At $t = t_0$ the laser passes position A with the scanning direction to the left. After 2.7ms, (not shown here, see Supplementary Movie 1 in page 176) a crack appears and grows towards the top surface. The fully-grown crack after 4.4ms can be seen in Figure 3b. Similar features were found in other samples, as illustrated in Supplementary Figure S6. During printing of the adjacent track, the laser reaches again the (2D-projected) position A after 13.5ms (Figure 3c). After the laser has passed, the contrast of the top part of the crack disappears, indicating that it was remelted (Figure 3d). However, with a 2.9 ms delay (see Supplementary Movie 1 in page 176), the crack starts growing again towards the top surface (Figure 3d, and 3e).

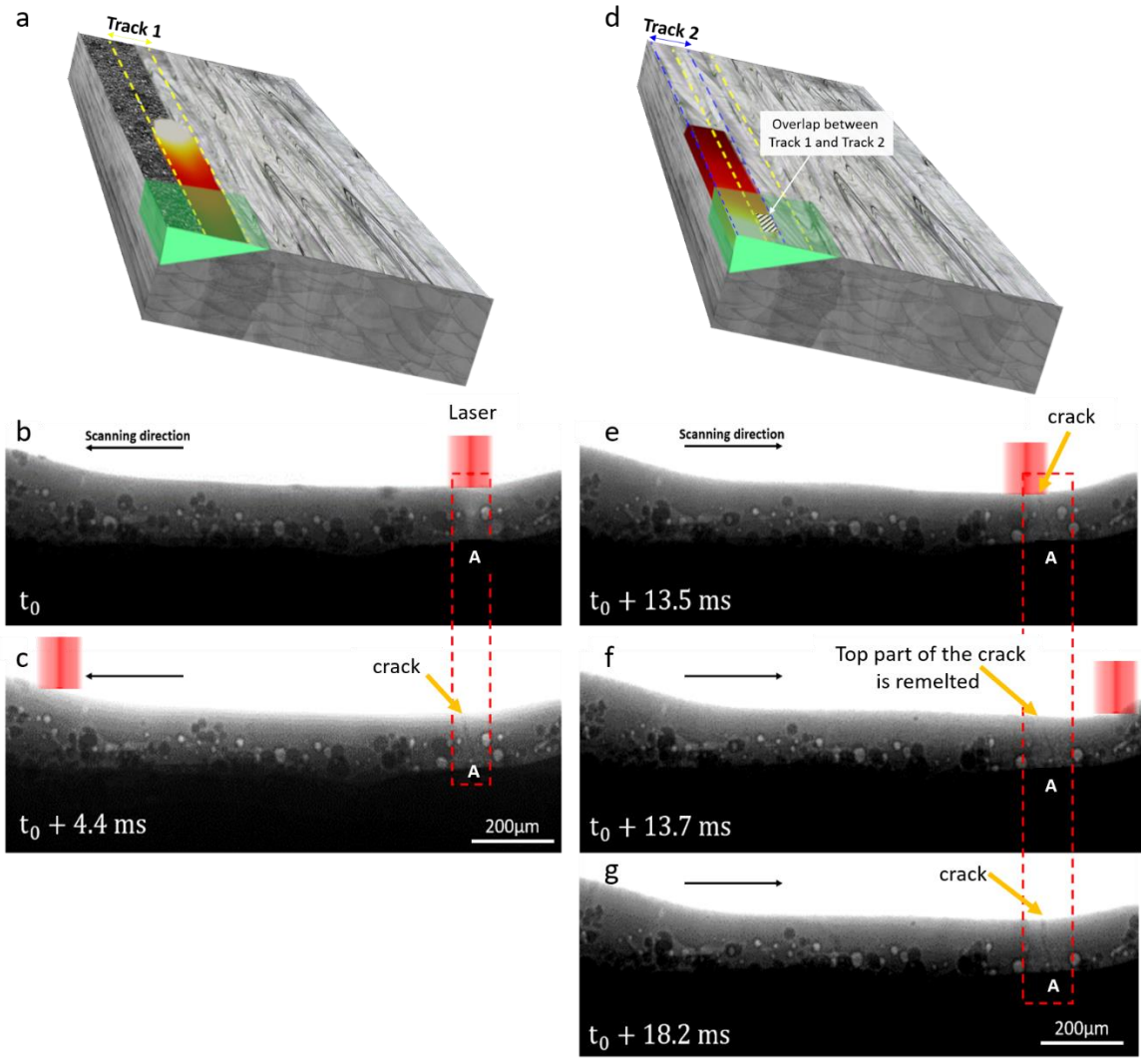

Figure 3. Radiographs acquired during L-PBF of CM247LC. a) The position of the track (Track 1) observed in b) and c) is shown schematically. b) At $t = t_0$, the laser reaches point A. The crack starts appearing at the same location 2.7 ms later. c) The crack is

clearly visible at t = t_0 + 4.4 ms. d) The position of the track (Track 2) observed in e), f) and g) is shown schematically. e)f) During printing of the next line scan, the crack is partially remelted. Track 2 remelts the top part of the crack. Considering the overlaps between two adjacent tracks, the striped part in d) indicates the zone in which the crack formed. The crack starts growing again towards the surface with a 2.9 ms delay. g)A radiograph at t = t_0 + 18.2 ms clearly shows the fully regrown crack. See Supplementary Movie 1 for a better observation of the crack formation.

In Figure 4a, a crack is already present in position B. When the laser passes in B (figure 4b), no visible change in the morphology and length of the crack is observed. Knowing the exact location of the crack with respect to the laser along the depth of the sample is not straightforward in transmission mode. However, as the crack does not appear to be remelted by the laser in Figure 3b, it can be assumed that the crack in B is not located in the laser beam path but rather in an adjacent track, i.e. in the HAZ. A similar interaction between an existing crack and the HAZ can be seen in Supplementary Figure S7. After 2.2 ms, the crack starts growing towards the surface; the fully grown crack is visible in Figure 4c. During the next laser track, when reaching point B (Figures 4d and 4e), the top part of the crack disappears, indicating that the crack is now located in the laser beam path and is being remelted. After 2.4 ms, the crack propagates back to the surface; the fully grown crack is visible in Figure 4f.

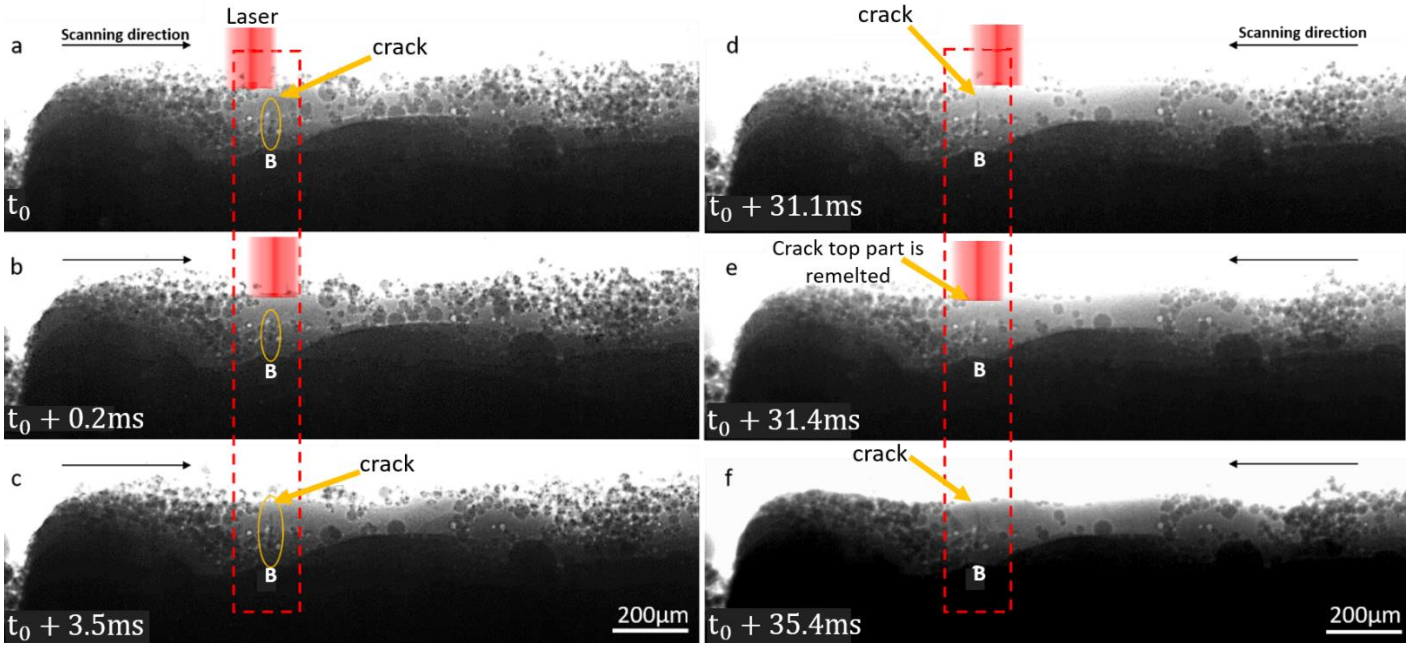

Figure 4. Radiographs acquired during L-PBF of CM247LC. a) At t = t_0, a crack is visible in B and b) the laser reaches the B position 0.2 ms later but does not appear to alter the crack morphology. 2.2 ms after the laser passes point B, the crack starts growing. The fully-grown crack is visible in c). d), e) During the next laser track, the top part of the crack is remelted, and with a 2.4 ms delay the crack starts growing again and reaches the surface. The fully-grown crack is clearly observable in f). See Supplementary Movie 2 in page 176 for a better observation of the crack formation.

3.2. Mechanisms of crack formation

The *operando* monitoring experiments reported in Figure 3 and Figure 4 systematically indicate a delay of about 2-3ms between laser-material interaction and crack formation or crack growth. In L-PBF of CM247LC, due to the fast heating and cooling cycles, micro-segregation occurs at the scale of the melt pool [14,61]. A large solidification range results in a large mushy zone, i.e. a liquid-solid mixture prone to cracking under tensile thermal stresses. Post-mortem SEM analysis of the cracks reveals a dendritic morphology, indicative of fracture occurring in the liquid phase, hence pointing towards solidification or liquation cracking. As highlighted in Figures 5a and 5b, crack propagation occurs preferentially along the cell boundaries.

The SEM-EDX analyses reported in Figures 5c and 5d indicate enrichment in Ta and Hf at the edge of cracks. It should be noticed that these SEM-EDX analyses are obtained after processing. Therefore, the successive L-PBF thermal cycles that occur after cracking partially homogenize the material chemistry in the crack vicinity, resulting in an underestimation of the micro-segregation that took place during solidification [14].

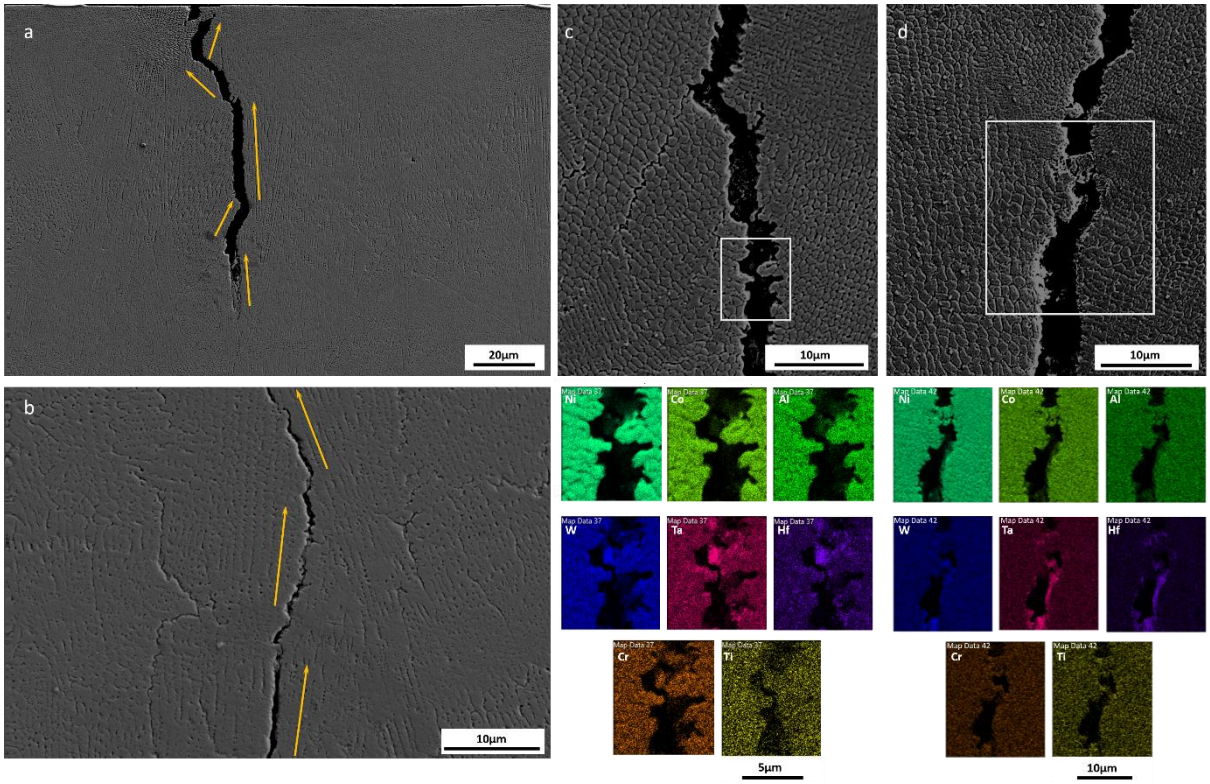

Figure 5. a, b) SEM secondary electron images indicate preferential propagation of cracks along grain boundaries (yellow arrows). c, d) SEM-EDX analysis highlighting element distribution in the vicinity of the cracks in as-built CM247LC samples.

The segregation of Hf and its effect on the solidification behavior of CM247LC has been investigated by Griffiths et. al [14]. Their calculated liquidus and solidus temperatures suggest that micro-segregation happens during the L-PBF process and can locally increase the solidification range from 150 to 525 °C, depending on the chemical composition of the segregated area. The solidus temperature can be locally reduced from 1249 to 858°C. Therefore, during the last stage of solidification, the entrapment of solute-rich liquid between solid interfaces and the tensile residual stresses due to solidification shrinkage and thermal contraction result in crack formation [11]. It can be hypothesized that the cracks observed in Figure 3, and Figures 4e, 4f, (also Figure S6, and point D in Figure S7 in the supplementary materials) which formed about 2-3 ms after laser exposure, originate from such a solidification cracking mechanism.

In order to relate the crack formation with the thermal history of the material, the temperature evolution during processing was evaluated using a finite element code described in [56,62]. The results of this simulation are reported in Figures 6b, 6c, and 6d (black curve). The simulations are supported experimentally by *operando* X-ray diffraction measurements obtained under the same processing conditions as the *operando* X-ray imaging experiments. The temperature evolution (blue curve in Figure 6d) was calculated from the experimentally measured change in lattice spacing using the thermal expansion coefficients tabulated in [55]. As shown in Figure 6, the simulated average temperature evolution (in the X-Ray probed zone) during processing fits well with the temperature derived from the X-ray diffraction experiments.

Based on this simulated temperature evolution, the time required for solidification at a point A located on the surface, at the center of the melt track, is estimated to 2.65 ms (Figure 6c, black curve), which agrees with the experimentally measured 2-3 ms time delay between laser exposure and cracking.

In addition, cracks may form in the HAZ, which is indicative of a liquation cracking mechanism caused by local melting of the solute-enriched grain boundaries.

Figure 6c (red curve) indicates the temperature evolution at a location B (100μm below the surface, the layer thickness being 40 μm), during the printing of three successive line tracks. The results show that when considering a standard hatching distance (100 μm), the heat-affected zones in previous layers and adjacent tracks both reach sufficiently high temperatures to locally melt the segregated zones. The formation of a thin liquid film combined with tensile residual stresses results in solid state cracking of the material. This cracking mechanism is observed in Figure 4c (point E in Figure S7 in the Supplementary Materials) where a pre-existing crack located in the HAZ grows after the laser beam passes.

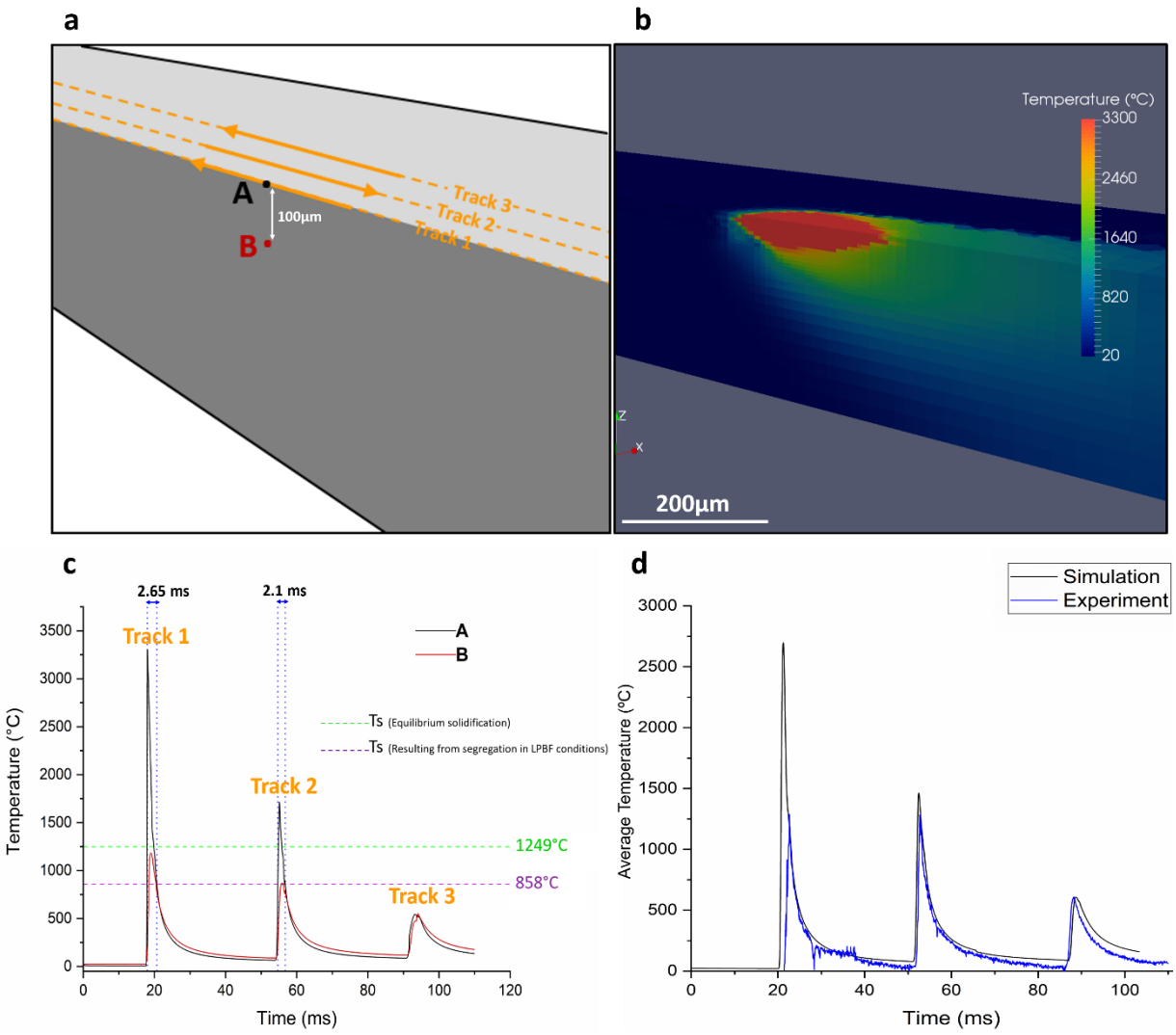

Figure 6. Finite element simulation indicating temperature evolution at the melt pool scale during L-PBF of CM247LC. a) Reference positions A and B with respect to the three laser line tracks considered in the simulation, b) temperature distribution when the laser reaches point A, and c) evolution of the temperature at point A and point B, during printing of the three adjacent tracks. The solidification time at point A is 2.65 ms after the first laser pass, which is comparable to the times needed for crack formation in the *operando* experiments. It can be seen in point B that heat transfer to the previously solidified layer is sufficient to locally melt segregated zones. d) The simulated temperatures are averaged over the X-ray probed zone and compared with the experimental values.

The above results provide direct evidence of the occurrence of solidification and liquation cracking in CM247LC, which were previously suggested as the main cracking mechanisms in this alloy [11,13,14] .

4. Summary

In summary, *operando* radiography allows the observation of crack formation and provides direct evidence of the cracking mechanisms taking place during L-PBF of the CM247LC nickel-based superalloy. We expect that a better understanding of cracking achieved in this study will stimulate the development of more accurate numerical simulations of the L-PBF process, and new approaches to achieve crack-free L-PBF nickel-based parts, such as to unravel the full industrial potential of AM technologies. Furthermore, the unique *operando* experimental setup employed here provides a broad range of information on various critical transient events that are beyond the scope of this paper, e.g. pore formation, melt pool dynamics, or spatter ejection. Hence, this set-up could be used for process optimization of different metals and alloys, validation of numerical simulations, and development of new material compositions better designed for L-PBF.

Declaration of Competing Interest

The authors declare that they have no known competing financial interests or personal relationships that could influence the work and results reported in this paper.

Acknowledgments

This work was supported by (1) the PREcision Additive Manufacturing of Precious metals Alloys (PREAMPA) project, funded by the ETH Board and the Swiss watch and precious metals industry; (2) the Additive Manufacturing and Metallic Microstructures (AM3) project, funded by the Competence Center for Materials Science and Technology (CCMX) and the Swiss watch and precious metals industry. We acknowledge the Paul Scherrer Institut, Villigen, Switzerland for the provision of synchrotron radiation beamtime at the TOMCAT and microXAS beamlines of the SLS. The authors kindly thank Dr. Christian Leinenbach and Dr. Seth Griffiths at Swiss Federal Laboratories for Materials Science and Technology (Empa) for providing the CM247LC powder. Special thanks to Dr. Milad Hamidi Nasab at EPFL for helping us in post processing and image analysis of the *operando* experimental data. The generous support of PX Group to the LMTM laboratory is also highly acknowledged.

Reference

[1] A. Gisario, M. Kazarian, F. Martina, M. Mehrpouya, Metal additive manufacturing in the commercial aviation industry: A review, J. Manuf. Syst. 53 (2019) 124–149. doi:10.1016/j.jmsy.2019.08.005.

[2] T. DebRoy, H.L. Wei, J.S. Zuback, T. Mukherjee, J.W. Elmer, J.O. Milewski, A.M. Beese, A. Wilson-Heid, A. De, W. Zhang, Additive manufacturing of metallic components – Process, structure and properties, Prog. Mater. Sci. 92 (2018) 112–224. doi:10.1016/j.pmatsci.2017.10.001.

[3] P.A. Hooper, Melt pool temperature and cooling rates in laser powder bed fusion, Addit. Manuf. 22 (2018) 548–559. doi:10.1016/j.addma.2018.05.032.

[4] V. Thampy, A.Y. Fong, N.P. Calta, J. Wang, A.A. Martin, P.J. Depond, A.M. Kiss, G. Guss, Q. Xing, R.T. Ott, A. van Buuren, M.F. Toney, J.N. Weker, M.J. Kramer, M.J. Matthews, C.J. Tassone, K.H. Stone, Subsurface Cooling Rates and Microstructural Response during Laser Based Metal Additive Manufacturing, Sci. Rep. 10 (2020) 1–9. doi:10.1038/s41598-020-58598-z.

[5] M. Opprecht, J.-P. Garandet, G. Roux, C. Flament, M. Soulier, A solution to the hot cracking problem for aluminium alloys manufactured by laser beam melting, Acta Mater. 197 (2020) 40–53. doi:https://doi.org/10.1016/j.actamat.2020.07.015.

[6] N.J. Harrison, I. Todd, K. Mumtaz, Reduction of micro-cracking in nickel superalloys processed by Selective Laser Melting: A fundamental alloy design approach, Acta Mater. 94 (2015) 59–68. doi:10.1016/j.actamat.2015.04.035.

[7] G.S. Reddy, K. Saurabh, D.M. Krishna, Numerical Simulation of Directionally Solidified CM247LC High Pressure Turbine Blade, in: Mater. Today Proc., Elsevier Ltd, 2017: pp. 7820–7830. doi:10.1016/j.matpr.2017.07.117.

[8] K. Prasad, R. Sarkar, K. Gopinath, Role of shrinkage pores, carbides on cyclic deformation behaviour of conventionally cast nickel base superalloy CM247LC® at 870°C, Mater. Sci. Eng. A. 654 (2016) 381–389. doi:10.1016/j.msea.2015.12.054.

[9] S. Griffiths, H. Ghasemi-Tabasi, A. De Luca, J. Pado, S.S. Joglekar, J. Jhabvala, R.E. Logé, C. Leinenbach, Influence of Hf on the heat treatment response of additively manufactured Ni-base superalloy CM247LC, Mater. Charact. 171 (2021) 110815. doi:https://doi.org/10.1016/j.matchar.2020.110815.

[10] Y.T. Tang, C. Panwisawas, J.N. Ghoussoub, Y. Gong, J.W.G. Clark, A.A.N. Németh, D.G.

McCartney, R.C. Reed, Alloys-by-design: Application to new superalloys for additive manufacturing, Acta Mater. 202 (2021) 417–436. doi:https://doi.org/10.1016/j.actamat.2020.09.023.

[11] J.N.D. J.C. Lippold, S.D. Kiser, Welding Metallurgy and Weldability of Nickel-base Alloys, Wiley, 2009.

[12] J.L. Caron, J.W. Sowards, Weldability of Nickel-Base Alloys, Elsevier, 2014. doi:10.1016/B978-0-08-096532-1.00615-4.

[13] N. Kalentics, N. Sohrabi, H.G. Tabasi, S. Griffiths, J. Jhabvala, C. Leinenbach, A. Burn, R.E. Logé, Healing cracks in selective laser melting by 3D laser shock peening, Addit. Manuf. 30 (2019) 100881. doi:10.1016/j.addma.2019.100881.

[14] S. Griffiths, H. Ghasemi Tabasi, T. Ivas, X. Maeder, A. De Luca, K. Zweiacker, R. Wróbel, J. Jhabvala, R.E. Logé, C. Leinenbach, Combining alloy and process modification for micro-crack mitigation in an additively manufactured Ni-base superalloy, Addit. Manuf. 36 (2020). doi:10.1016/j.addma.2020.101443.

[15] V.D. Divya, R. Muñoz-Moreno, O.M.D.M. Messé, J.S. Barnard, S. Baker, T. Illston, H.J. Stone, Microstructure of selective laser melted CM247LC nickel-based superalloy and its evolution through heat treatment, Mater. Charact. 114 (2016) 62–74. doi:10.1016/j.matchar.2016.02.004.

[16] L.N. Carter, M.M. Attallah, R.C. Reed, Laser Powder Bed Fabrication of Nickel-Base Superalloys: Influence of Parameters; Characterisation, Quantification and Mitigation of Cracking, Superalloys 2012. (2012) 577–586. doi:doi:10.1002/9781118516430.ch64.

[17] L.N. Carter, C. Martin, P.J. Withers, M.M. Attallah, The influence of the laser scan strategy on grain structure and cracking behaviour in SLM powder-bed fabricated nickel superalloy, J. Alloys Compd. 615 (2014) 338–347. doi:10.1016/j.jallcom.2014.06.172.

[18] X. Wang, L.N. Carter, B. Pang, M.M. Attallah, M.H. Loretto, Microstructure and yield strength of SLM-fabricated CM247LC Ni-Superalloy, Acta Mater. 128 (2017) 87–95. doi:10.1016/j.actamat.2017.02.007.

[19] H. Hyer, L. Zhou, A. Mehta, S. Park, T. Huynh, S. Song, Y. Bai, K. Cho, B. McWilliams, Y. Sohn, Composition-dependent solidification cracking of aluminum-silicon alloys during laser powder bed fusion, Acta Mater. 208 (2021) 116698. doi:https://doi.org/10.1016/j.actamat.2021.116698.

[20] T. Soysal, S. Kou, A simple test for assessing solidification cracking susceptibility and checking validity of susceptibility prediction, Acta Mater. 143 (2018) 181–197.

doi:https://doi.org/10.1016/j.actamat.2017.09.065.

[21] M. Qian, J.C. Lippold, The effect of annealing twin-generated special grain boundaries on HAZ liquation cracking of nickel-base superalloys, Acta Mater. 51 (2003) 3351–3361. doi:https://doi.org/10.1016/S1359-6454(03)00090-9.

[22] A.A.N. Németh, D.J. Crudden, D.E.J. Armstrong, D.M. Collins, K. Li, A.J. Wilkinson, C.R.M. Grovenor, R.C. Reed, Environmentally-assisted grain boundary attack as a mechanism of embrittlement in a nickel-based superalloy, Acta Mater. 126 (2017) 361–371. doi:https://doi.org/10.1016/j.actamat.2016.12.039.

[23] M. Cloots, P.J. Uggowitzer, K. Wegener, Investigations on the microstructure and crack formation of IN738LC samples processed by selective laser melting using Gaussian and doughnut profiles, Mater. Des. 89 (2016) 770–784. doi:10.1016/j.matdes.2015.10.027.

[24] Q. Guo, C. Zhao, M. Qu, L. Xiong, L.I. Escano, S.M.H. Hojjatzadeh, N.D. Parab, K. Fezzaa, W. Everhart, T. Sun, L. Chen, In-situ characterization and quantification of melt pool variation under constant input energy density in laser powder bed fusion additive manufacturing process, Addit. Manuf. 28 (2019) 600–609. doi:10.1016/j.addma.2019.04.021.

[25] C. Zhao, K. Fezzaa, R.W. Cunningham, H. Wen, F. De Carlo, L. Chen, A.D. Rollett, T. Sun, Real-time monitoring of laser powder bed fusion process using high-speed X-ray imaging and diffraction, Sci. Rep. 7 (2017) 3602. doi:10.1038/s41598-017-03761-2.

[26] N.P. Calta, A.A. Martin, J.A. Hammons, M.H. Nielsen, T.T. Roehling, K. Fezzaa, M.J. Matthews, J.R. Jeffries, T.M. Willey, J.R.I. Lee, Pressure dependence of the laser-metal interaction under laser powder bed fusion conditions probed by in situ X-ray imaging, Addit. Manuf. 32 (2020). doi:10.1016/j.addma.2020.101084.

[27] A.A. Martin, N.P. Calta, J.A. Hammons, S.A. Khairallah, M.H. Nielsen, R.M. Shuttlesworth, N. Sinclair, M.J. Matthews, J.R. Jeffries, T.M. Willey, J.R.I. Lee, Ultrafast dynamics of laser-metal interactions in additive manufacturing alloys captured by in situ X-ray imaging, Mater. Today Adv. 1 (2019) 100002. doi:https://doi.org/10.1016/j.mtadv.2019.01.001.

[28] R. Cunningham, C. Zhao, N. Parab, C. Kantzos, J. Pauza, K. Fezzaa, T. Sun, A.D. Rollett, Keyhole threshold and morphology in laser melting revealed by ultrahigh-speed x-ray imaging, Science (80-.). 363 (2019) 849–852. doi:10.1126/science.aav4687.

[29] C.L.A. Leung, S. Marussi, R.C. Atwood, M. Towrie, P.J. Withers, P.D. Lee, In situ X-ray imaging of

defect and molten pool dynamics in laser additive manufacturing, Nat. Commun. 9 (2018) 1355. doi:10.1038/s41467-018-03734-7.

[30] N.D. Parab, C. Zhao, R. Cunningham, L.I. Escano, K. Fezzaa, W. Everhart, A.D. Rollett, L. Chen, T. Sun, Ultrafast X-ray imaging of laser-metal additive manufacturing processes, J. Synchrotron Radiat. 25 (2018) 1467–1477. doi:10.1107/S1600577518009554.

[31] T. Sun, Probing Ultrafast Dynamics in Laser Powder Bed Fusion Using High-Speed X-Ray Imaging: A Review of Research at the Advanced Photon Source, Jom. 72 (2020) 999–1008. doi:10.1007/s11837-020-04015-9.

[32] C. Zhao, N.D. Parab, X. Li, K. Fezzaa, W. Tan, A.D. Rollett, T. Sun, Critical instability at moving keyhole tip generates porosity in laser melting, Science (80-.). 1086 (2020) 1080–1086.

[33] S.J. Wolff, S. Webster, N.D. Parab, B. Aronson, B. Gould, A. Greco, T. Sun, In-situ Observations of Directed Energy Deposition Additive Manufacturing Using High-Speed X-ray Imaging, Jom. 73 (2021) 189–200. doi:10.1007/s11837-020-04469-x.

[34] B.J. Simonds, J. Tanner, A. Artusio-Glimpse, P.A. Williams, N. Parab, C. Zhao, T. Sun, Simultaneous high-speed x-ray transmission imaging and absolute dynamic absorptance measurements during high-power laser-metal processing, Procedia CIRP. 94 (2020) 775–779. doi:10.1016/j.procir.2020.09.135.

[35] S.M.H. Hojjatzadeh, N.D. Parab, Q. Guo, M. Qu, L. Xiong, C. Zhao, L.I. Escano, K. Fezzaa, W. Everhart, T. Sun, L. Chen, Direct observation of pore formation mechanisms during LPBF additive manufacturing process and high energy density laser welding, Int. J. Mach. Tools Manuf. 153 (2020) 103555. doi:10.1016/j.ijmachtools.2020.103555.

[36] Q. Guo, C. Zhao, M. Qu, L. Xiong, S.M.H. Hojjatzadeh, L.I. Escano, N.D. Parab, K. Fezzaa, T. Sun, L. Chen, In-situ full-field mapping of melt flow dynamics in laser metal additive manufacturing, Addit. Manuf. 31 (2020) 100939. doi:10.1016/j.addma.2019.100939.

[37] Y. Chen, S.J. Clark, C.L.A. Leung, L. Sinclair, S. Marussi, M.P. Olbinado, E. Boller, A. Rack, I. Todd, P.D. Lee, In-situ Synchrotron imaging of keyhole mode multi-layer laser powder bed fusion additive manufacturing, Appl. Mater. Today. 20 (2020) 100650. doi:10.1016/j.apmt.2020.100650.

[38] Y. Chen, S.J. Clark, L. Sinclair, C.L.A. Leung, S. Marussi, T. Connolley, R.C. Atwood, G.J. Baxter, M.A. Jones, I. Todd, P.D. Lee, Synchrotron X-ray Imaging of Directed Energy Deposition Additive Manufacturing of Titanium Alloy Ti-6242, Addit. Manuf. (2021) 101969.

doi:https://doi.org/10.1016/j.addma.2021.101969.

[39] Z. Gan, O.L. Kafka, N. Parab, C. Zhao, L. Fang, O. Heinonen, T. Sun, W.K. Liu, Universal scaling laws of keyhole stability and porosity in 3D printing of metals, Nat. Commun. 12 (2021) 2379. doi:10.1038/s41467-021-22704-0.

[40] A.A. Martin, N.P. Calta, S.A. Khairallah, J. Wang, P.J. Depond, A.Y. Fong, V. Thampy, G.M. Guss, A.M. Kiss, K.H. Stone, C.J. Tassone, J. Nelson Weker, M.F. Toney, T. van Buuren, M.J. Matthews, Dynamics of pore formation during laser powder bed fusion additive manufacturing, Nat. Commun. 10 (2019) 1–10. doi:10.1038/s41467-019-10009-2.

[41] S.M.H. Hojjatzadeh, N.D. Parab, W. Yan, Q. Guo, L. Xiong, C. Zhao, M. Qu, L.I. Escano, X. Xiao, K. Fezzaa, W. Everhart, T. Sun, L. Chen, Pore elimination mechanisms during 3D printing of metals, Nat. Commun. 10 (2019) 1–8. doi:10.1038/s41467-019-10973-9.

[42] S. Shevchik, T. Le-Quang, B. Meylan, F.V. Farahani, M.P. Olbinado, A. Rack, G. Masinelli, C. Leinenbach, K. Wasmer, Supervised deep learning for real-time quality monitoring of laser welding with X-ray radiographic guidance, Sci. Rep. 10 (2020) 1–12. doi:10.1038/s41598-020-60294-x.

[43] L. Sinclair, C.L.A. Leung, S. Marussi, S.J. Clark, Y. Chen, M.P. Olbinado, A. Rack, J. Gardy, G.J. Baxter, P.D. Lee, In situ radiographic and ex situ tomographic analysis of pore interactions during multilayer builds in laser powder bed fusion, Addit. Manuf. 36 (2020) 101512. doi:10.1016/j.addma.2020.101512.

[44] Z.A. Young, Q. Guo, N.D. Parab, C. Zhao, M. Qu, L.I. Escano, K. Fezzaa, W. Everhart, T. Sun, L. Chen, Types of spatter and their features and formation mechanisms in laser powder bed fusion additive manufacturing process, Addit. Manuf. 36 (2020) 101438. doi:10.1016/j.addma.2020.101438.

[45] Q. Guo, C. Zhao, L.I. Escano, Z. Young, L. Xiong, K. Fezzaa, W. Everhart, B. Brown, T. Sun, L. Chen, Transient dynamics of powder spattering in laser powder bed fusion additive manufacturing process revealed by in-situ high-speed high-energy x-ray imaging, Acta Mater. 151 (2018) 169–180. doi:10.1016/j.actamat.2018.03.036.

[46] L.I. Escano, N.D. Parab, L. Xiong, Q. Guo, C. Zhao, T. Sun, L. Chen, Investigating Powder Spreading Dynamics in Additive Manufacturing Processes by In-situ High-speed X-ray Imaging, Synchrotron Radiat. News. 32 (2019) 9–13. doi:10.1080/08940886.2019.1582281.

[47] J. Yin, D. Wang, L. Yang, H. Wei, P. Dong, L. Ke, G. Wang, H. Zhu, X. Zeng, Correlation between

forming quality and spatter dynamics in laser powder bed fusion, Addit. Manuf. 31 (2020) 100958. doi:https://doi.org/10.1016/j.addma.2019.100958.

[48] S.J. Wolff, H. Wu, N. Parab, C. Zhao, K.F. Ehmann, T. Sun, J. Cao, In-situ high-speed X-ray imaging of piezo-driven directed energy deposition additive manufacturing, Sci. Rep. 9 (2019) 1–14. doi:10.1038/s41598-018-36678-5.

[49] P.-J. Chiang, R. Jiang, R. Cunningham, N. Parab, C. Zhao, K. Fezzaa, T. Sun, A.D. Rollett, In Situ Characterization of Hot Cracking Using Dynamic X-Ray Radiography BT - Advanced Real Time Imaging II, in: J. Nakano, P.C. Pistorius, C. Tamerler, H. Yasuda, Z. Zhang, N. Dogan, W. Wang, N. Saito, B. Webler (Eds.), Springer International Publishing, Cham, 2019: pp. 77–85.

[50] N. Kouraytem, P.-J. Chiang, R. Jiang, C. Kantzos, J. Pauza, R. Cunningham, Z. Wu, G. Tang, N. Parab, C. Zhao, K. Fezzaa, T. Sun, A.D. Rollett, Solidification crack propagation and morphology dependence on processing parameters in AA6061 from ultra-high-speed x-ray visualization, Addit. Manuf. (2021) 101959. doi:https://doi.org/10.1016/j.addma.2021.101959.

[51] S. Hocine, H. Van Swygenhoven, S. Van Petegem, C.S.T. Chang, T. Maimaitiyili, G. Tinti, D. Ferreira Sanchez, D. Grolimund, N. Casati, Operando X-ray diffraction during laser 3D printing, Mater. Today. 34 (2020) 30–40. doi:10.1016/j.mattod.2019.10.001.

[52] S. Hocine, S. Van Petegem, U. Frommherz, G. Tinti, N. Casati, D. Grolimund, H. Van Swygenhoven, A miniaturized selective laser melting device for operando X-ray diffraction studies, Addit. Manuf. 34 (2020) 101194. doi:10.1016/j.addma.2020.101194.

[53] M. Buhrer, M. Stampanoni, X. Rochet, F. Buchi, J. Eller, F. Marone, High-numerical-aperture macroscope optics for time-resolved experiments, J. Synchrotron Radiat. 26 (2019) 1161–1172. https://doi.org/10.1107/S1600577519004119.

[54] R. Mokso, C.M. Schleputz, G. Theidel, H. Billich, E. Schmid, T. Celcer, G. Mikuljan, L. Sala, F. Marone, N. Schlumpf, M. Stampanoni, GigaFRoST: the gigabit fast readout system for tomography, J. Synchrotron Radiat. 24 (2017) 1250–1259. https://doi.org/10.1107/S1600577517013522.

[55] R. Rajendran, V. Petley, B. Rehmer, Dynamic elastic properties of aero-engine metallic isotropic materials, Proc. Inst. Mech. Eng. Part L J. Mater. Des. Appl. 227 (2013) 243–249. doi:10.1177/1464420712454071.

[56] H. Ghasemi-Tabasi, J. Jhabvala, E. Boillat, T. Ivas, R. Drissi-Daoudi, R.E. Logé, An effective rule for translating optimal selective laser melting processing parameters from one material to another,

Addit. Manuf. 36 (2020) 101496. doi:10.1016/j.addma.2020.101496.

[57] R.E. Aune, L. Battezzati, R. Brooks, I. Egry, H.J. Fecht, J.P. Garandet, M. Hayashi, K.C. Mills, A. Passerone, P.N. Quested, E. Ricci, F. Schmidt-Hohagen, S. Seetharaman, B. Vinet, R.K. Wunderlich, Thermophysical properties of IN738LC, MM247LC and CMSX-4 in the liquid and high temperature solid phase, in: Proc. Int. Symp. Superalloys Var. Deriv., 2005: pp. 467–476. doi:10.7449/2005/superalloys_2005_467_476.

[58] R. Przeliorz, M. Góral, Heat resistance and heat capacity of the selected nickel superalloys, Solid State Phenom. 227 (2015) 329–332. doi:10.4028/www.scientific.net/SSP.227.329.

[59] E.B. Curry, S. Sahoo, C. Herrera, I. Sochnikov, S. Pamir Alpay, R.J. Hebert, B.G. Willis, J. Qi, J.N. Hancock, Optical response of nickel-based superalloy Inconel-718 for applications in additive manufacturing, J. Appl. Phys. 127 (2020). doi:10.1063/5.0006006.

[60] L. Cao, X. Yuan, Study on the numerical simulation of the SLM molten pool dynamic behavior of a nickel-based superalloy on the workpiece scale, Materials (Basel). 12 (2019). doi:10.3390/ma12142272.

[61] I. Serrano-Munoz, T. Mishurova, T. Thiede, M. Sprengel, A. Kromm, N. Nadammal, G. Nolze, R. Saliwan-Neumann, A. Evans, G. Bruno, The residual stress in as-built Laser Powder Bed Fusion IN718 alloy as a consequence of the scanning strategy induced microstructure, Sci. Rep. 10 (2020) 14645. doi:10.1038/s41598-020-71112-9.

[62] T. Polivnikova, Study and Modelling of the Melt Pool Dynamics during Selective Laser Sintering and Melting, EPFL PP - Lausanne, n.d. doi:10.5075/epfl-thesis-6826.

Supplementary Materials

Direct observation of crack formation mechanisms with *operando* Laser Powder Bed Fusion X-ray imaging

Hossein Ghasemi-Tabasi[1], Charlotte de Formanoir[1], Steven Van Petegem[2], Jamasp Jhabvala[1], Samy Hocine[2,3], Eric Boillat[1], Navid Sohrabi[1], Federica Marone[4], Daniel Grolimund[4], Helena Van Swygenhoven[2,3], Roland E. Logé[1]

1. Thermomechanical Metallurgy Laboratory (LMTM) – PX Group Chair, École Polytechnique Fédérale de Lausanne (EPFL), CH-2002 Neuchâtel, Switzerland
2. Photons for Engineering and Manufacturing, Paul Scherrer Institute, Forschungsstrasse 111, 5232 Villigen PSI, Switzerland
3. Neutrons and X-rays for Mechanics of Materials, IMX, École Polytechnique Fédérale de Lausanne (EPFL), Route Cantonale, 1015 Lausanne, Switzerland
4. Swiss Light Source, Paul Scherrer Institute, 5232 Villigen, Switzerland

Table of contents

S1. Printed CM247LC samples

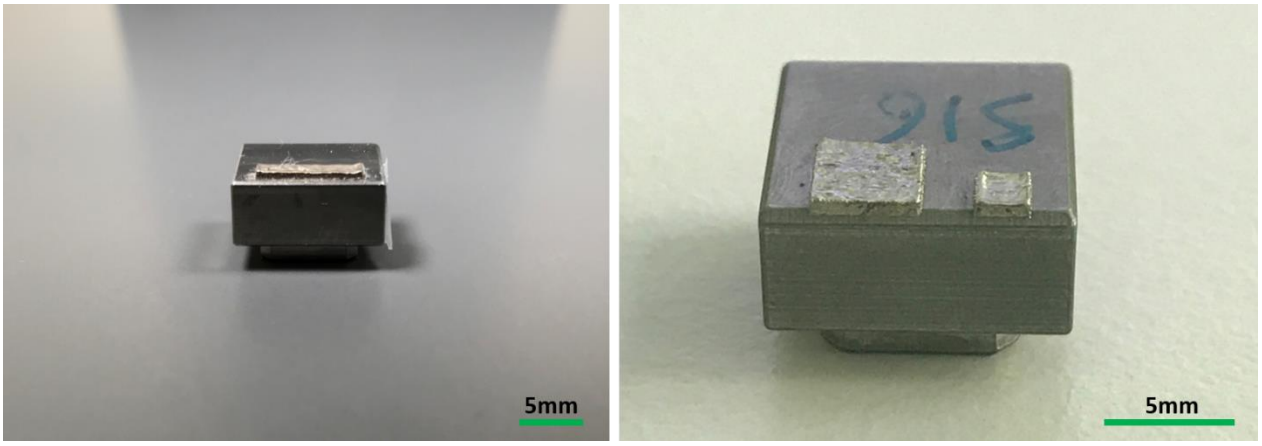

Figure S1. Examples of printed CM247LC during operando experiments. The miniaturized L-PBF device used in this study reproduces real processing conditions of samples of various sizes, and goes beyond the usual single-track experiments reported in previous in-situ X-Ray imaging experiments.

S2. Operando X-ray Imaging and diffraction experiments

Figure S2. The miniaturized L-PBF device mounted at the TOMCAT beam line of the Swiss Light Source.

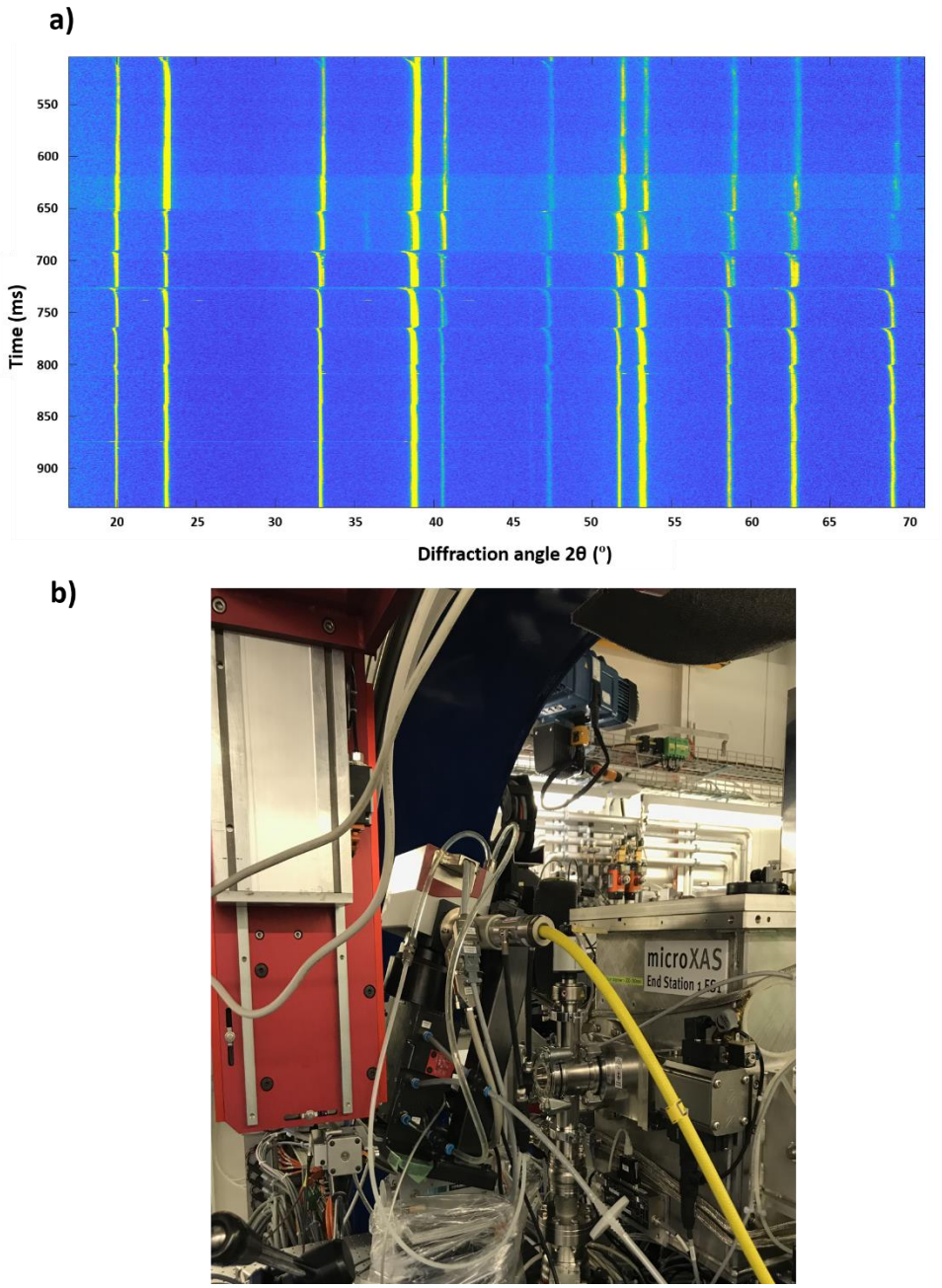

Figure S3. a) Phase evolution during printing of a single layer, shown as an intensity vs. diffraction angle and time, and b) the miniaturized L-PBF device mounted at micro-XAS beam line of the Swiss Light Source.

S3. Interpretation radiographs

The radiography experiments were performed with a polychromatic X-ray beam with an energy range 10-55keV. This provides the necessary flux to record radiographs with sufficient intensity at an acquisition rate of 10kHz. Furthermore, the detector was placed far away from the sample in order to create an edge enhancement effect. However, this introduces some counter-intuitive contrasts for certain microstructural features. In particular, in this mode, cracks show up as dark lines whereas pores result in bright discs. In order to prove that the dark lines are related to cracks, we have performed additional high-resolution 2D and 3D measurements on a printed sample using following parameters:

Table S1. Overview parameters for ex-situ high-resolution X-ray tomography experiments

Detector	pco.EDGE 5.5
Magnification	4x
Effective pixel size	1.65 µm^2
Sample-to-detector distance	48cm
High energy spectrum	30-55keV
Low energy spectrum	15-55keV

In a first measurement, radiographs were recorded with a polychromatic beam with different X-ray energy bandwidths, as shown in Table S1. Figures S4a and S4b display the corresponding radiographs. In both cases, pores show up as bright discs with a dark edge and powder particles or spatter on the sample surface as dark discs. However, cracks appear as bright lines in Fig. S4a and dark lines in Fig. S4b, as indicated by the black arrows.

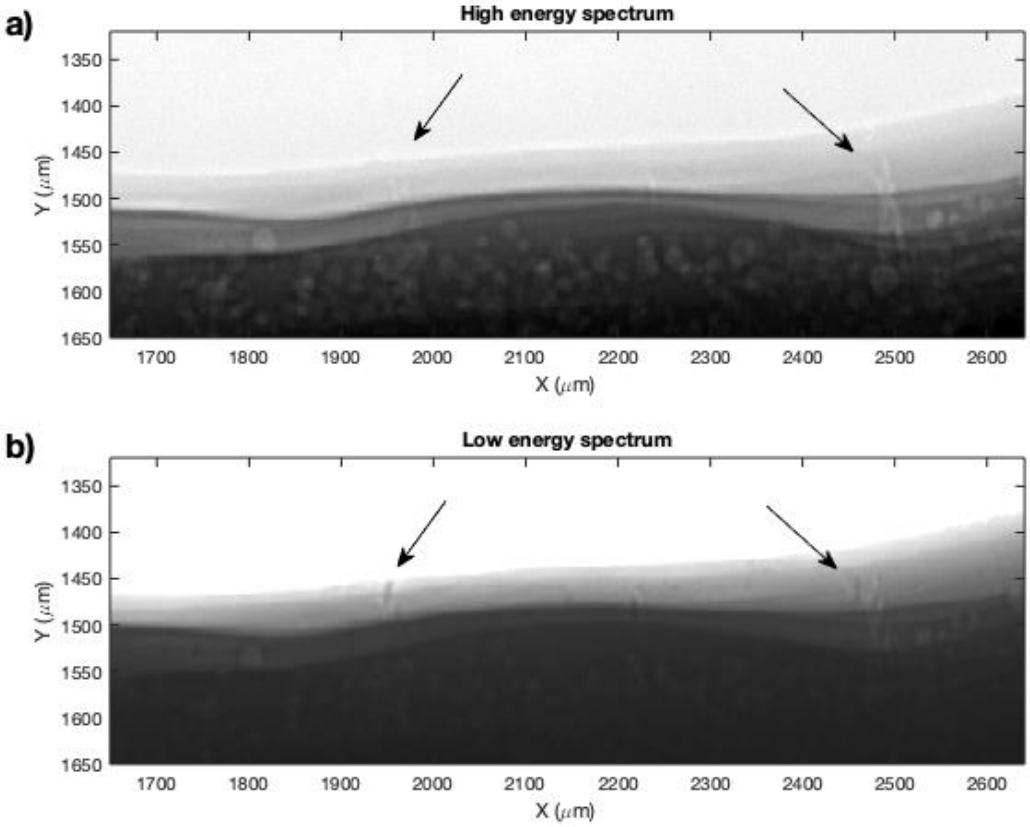

Figure S4. Influence of X-ray energy spectrum on contrast of cracks and pores.

In a second measurement, a high-resolution tomogram was recorded. Figure S5 shows a representative slice through the 3D reconstructed image. Several empty cracks and pores can be observed, in agreement with what was observed during the operando experiments.

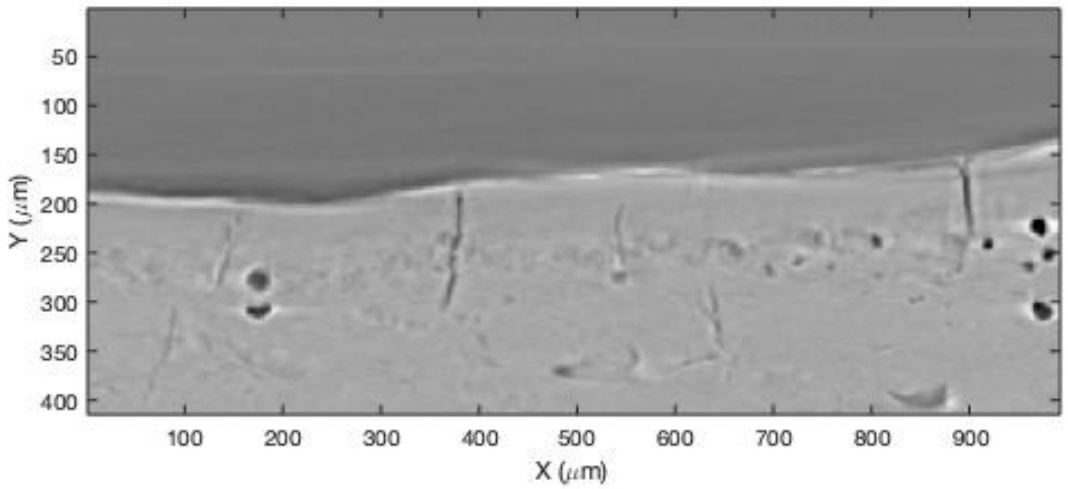

Figure S5. Reconstructed slice, showing the presence of multiple cracks and pores.

S4. Operando observation of crack formation:

Figure S6 shows two radiographs taken 4.8 ms apart while the laser passes. The contrast was chosen to highlight pores and cracks; spatters are not visible here. Figure S6-a shows the position of the laser beam at t_0 (position C). 1.9 ms after the laser has passed a crack has formed this position. Figure S6-b shows the fully-grown crack after it has reached the top surface. See Supplementary Movie S1 for a better observation of the crack formation.

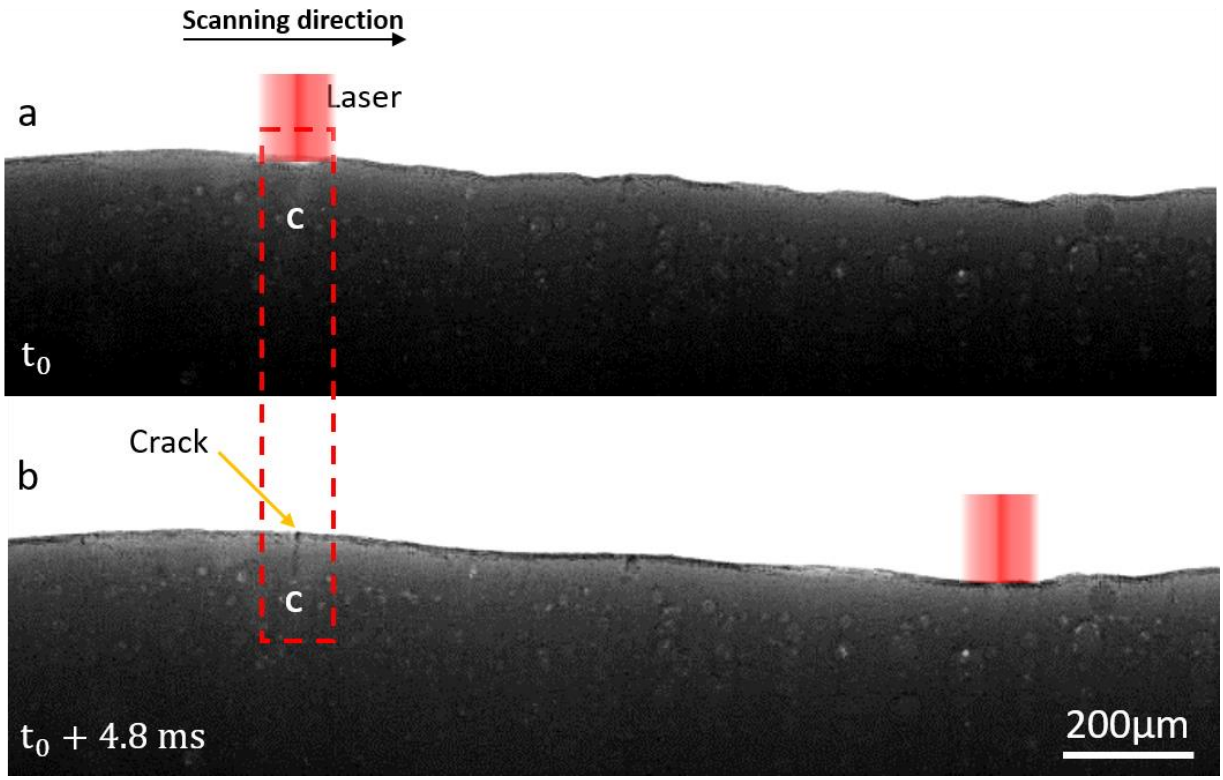

Figure S6. Radiographs acquired during L-PBF of CM247LC. a) At $t = t_0$, the laser reaches point C. A crack starts appearing in the same location 1.9 ms later. b) The crack is clearly visible at $t = t_0 + 4.8$ ms. See Supplementary Movie S1 for a better observation of the crack formation.

Figure S7 indicates the laser position and highlights two pre-existing cracks positioned in D and E. When the laser passes point E (figure S7-b), it does not visibly affect the crack. When reaching D, however, the laser removes part of the D crack. With a delay of 3.1 ms and 2.9 ms, cracks start growing in E and D, respectively. Supplementary Movie S2 depicts the crack evolution at these two points.

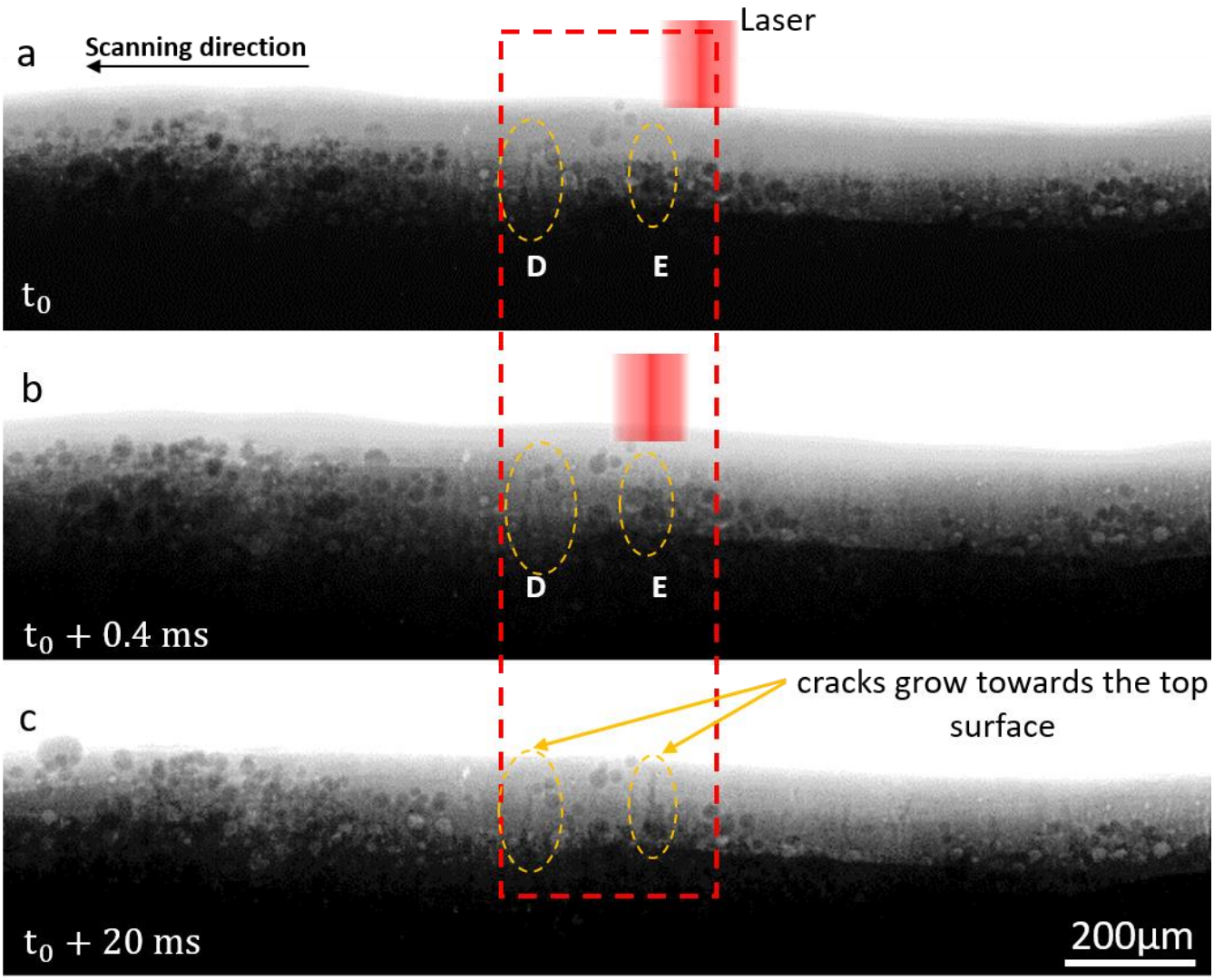

Figure S7. Radiographs acquired during L-PBF of CM247LC sample indicates a) laser position before reaching point E, and b) when laser reaches point E. The crack shape does not change in this case. However, when the laser reaches point D, part of the crack is remelted. c) Later, further crack evolutions are visible. See Supplementary Movie S2 for better observation of the crack morphology evolutions.

Chapter 8 (Supplementary)

Combining Alloy and Process Modification for Micro-crack Mitigation in an Additively Manufactured Ni-base Superalloy

S. Griffiths[1], H.Ghasemi-Tabasi[2], T. Ivas[2], X. Maeder[1], A. De Luca[1], K. Zweiacker[1], R. Wrobel[1], J. Jhabvala[2], R.E. Logé[2], C. Leinenbach[1]

1. Empa - Swiss Federal Laboratories for Materials Science and Technology, Überlandstrasse 129, 8600 Dübendorf, Switzerland
2. Thermomechanical Metallurgy Laboratory – PX Group Chair, Ecole Polytechnique Fédérale de Lausanne (EPFL), 2002 Neuchâtel, Switzerland

S. Griffiths, H. Ghasemi Tabasi, T. Ivas, X. Maeder, A. De Luca, K. Zweiacker, R. Wróbel, J. Jhabvala, R.E. Logé, C. Leinenbach, Combining alloy and process modification for micro-crack mitigation in an additively manufactured Ni-base superalloy, Addit. Manuf. 36 (2020). doi:10.1016/j.addma.2020.101443.

Contribution:
Hossein Ghasemi Tabasi took care of the Gleeble experiments and interpreted the results. In addition, he performed crack morphology and EDX analyses in order to study the liquation cracking mechanism in the printed samples. He wrote experimental and results sections on the Gleeble experiments (2.5, 3.3, and 3.4) and part of the discussion on the cracking mechanism (5.3) of the manuscript.

Abstract

The additive manufacturing (AM) of the γ` precipitation strengthened Ni-base superalloys still remains a challenge due to their susceptibility to micro-cracking. Post-processing, such as HIPing, has been shown to heal the micro-cracks but it remains desirable to prevent the micro-cracking from even occurring. Numerous studies highlighting potential mechanisms for micro-cracking exist but few solutions have been demonstrated. The intent of this study was to identify the micro-crack mechanisms and demonstrate how process and alloy modifications can reduce the micro-cracking. The micro-crack surfaces exhibit a dendritic appearance that is indicative of solidification cracking. Additionally, Gleeble experiments, simulating the L-PBF induced Heat Affected Zone (HAZ), were conducted below the γ` solvus temperature and reveal the existence of grain boundary liquation, indicative of liquation cracking. Two cracking mechanisms are thus coexisting during Laser Powder Bed Fusion (L-PBF) of CM247LC. Based on experimental evidence, reduction in the solidification interval of CM247LC was investigated as a candidate for micro-crack mitigation and a new alloy was developed. As Hf is found to have a significant influence on the freezing range of the alloy, a new CM247LC without Hf was produced and tested. The study also involved two separate and distinct processing conditions to highlight the importance of melt pool geometry on micro-crack density. Samples fabricated with the Hf-free CM247LC, CM247LC NHf, in combination with optimized processing conditions exhibit a reduction in crack density of 98 %. This study demonstrates the importance of both processing conditions and alloy chemistry on micro-cracking in L-PBF fabricated γ` hardening Ni-base superalloys.

1. Introduction

Additive manufacturing (AM) refers to a group of manufacturing techniques that are used to produce near net shape monolithic parts in a layer-by-layer fashion. For metallic materials, AM typically refers to either (i) Laser Powder Bed Fusion (L-PBF), (ii) Electron Beam Powder bed fusion (E-PBF), or (iii) Direct Energy Deposition (DED). In the PBF techniques, a layer of metallic powder is consolidated with either a laser (L-PBF) or an electron source (E-PBF). In DED, a stream of powder, or wire, is deposited into the focal point of a laser. The process, whether PBF or DED, in a simplistic way, can be viewed as a fusion welding process; therefore, many of the disadvantages associated with the rapid melting and solidification of metal, such as high residual stresses, undesirable metastable phases, and cracking apply to AM. This implies that only weldable alloys, such as Ti-6Al-4V, and 316 stainless steels are well suited for AM, however, the high geometric freedom AM offers in comparison to conventional manufacturing techniques [1] means there is a desire to process all alloys with AM, even those considered to have poor weldability, such as the nickel-base superalloys.

The nickel-base superalloys can be subdivided into two classes (i) solid-solution strengthened alloys, and (ii) precipitation strengthened alloys. The solid-solution strengthened superalloys, and a few precipitation strengthened superalloys, such as IN 718, are known to have good weldability; however,

the superalloys that contain high amounts of Al and Ti, to produce the $L1_2$ $Ni_3(Al,Ti)$ precipitation, such as CM247LC, are considered less weldable and are subject to cracking [2]. Micro-cracking of welded precipitation strengthened Ni-base superalloys can be attributed to the following mechanisms:

1. Solidification Cracking: Solidification cracking occurs during the final stages of solidification when the solute-rich liquid becomes trapped between two solid interfaces. Shrinkage strain resulting from the liquid to solid phase transformation in combination with thermal contraction strain result in the remaining liquid being pulled apart (liquid has negligible shear strength). [3]
2. Liquation Cracking: Liquation cracking occurs in the heat-affected zone (HAZ) of a melt track. Micro-segregation of elements during solidification of the metal, whether from casting or from a previous melt track, in the case of AM, results in grain boundaries and/or interdendritic areas having a depressed solidus point due to the changed chemical composition. When these boundaries are subjected to elevated temperatures in the HAZ they liquefy and become susceptible to tearing. Liquation can also be the result of molten metal wetting and penetrating grain boundaries of previously solidified material. [3]
3. Strain Age Cracking (SAC): When a superalloy is undergoing a solutionizing heat treatment it will pass through the aging temperature upon heating. Precipitation of the strengthening phase, typically γ'-Ni_3M, during the ramp will result in reduced ductility. If the residual stresses generated during processing, or from the precipitation itself (lattice mismatch), are not able to relax before the material loses ductility (from precipitation), then cracking can occur. [2,4]
4. Ductility Dip Cracking (DDC): Nickel-base superalloys are subject to a reduction in ductility at a temperature between the solidus (T_s) and 0.5 T_s. If sufficient strain exists in the material while at this temperature range then the material will crack. One suggested mechanism for the loss of ductility is grain boundary shearing. [3]

Numerous studies focusing both on microstructure and defect formation have been published on the PBF of precipitation strengthened Ni-base superalloys [5–12]. Carter et al. [12] investigated the microstructure of L-PBF fabricated CM247LC and observed a columnar grain microstructure, with a <001> texture oriented parallel to the build direction, separated by regions of fine grains. The bimodal grain distribution was attributed to the scan strategy (chess strategy). They observed a majority of cracking in the highly misorientated fine-grain regions and attributed the cracking to DDC. Wang et al. [6] performed a detailed TEM analysis on L-PBF fabricated CM247LC (as-fabricated condition) and observed columnar grains that were comprised of several 700 nm wide cells (low angle grain boundary). The cell boundaries had a high dislocation density and contained Hf/W/Ti/Ta-rich precipitates. A high density of 10 nm diameter γ`($Ni_3Al$) particles was observed within the cells and 50 nm diameter γ` was observed on the cell boundaries. It was hypothesized that the presence of Hf/W/Ti/Ta-rich precipitates and γ` led to dislocation accumulation at the cell boundaries. Divya et al. [7] also studied the

microstructure and defect formation of L-PBF fabricated CM247LC. Electron Backscatter Diffraction (EBSD) analysis revealed several 500 nm diameter cells with small misorientations (less than 4°) making up a single grain. Similar to Wang et al., Divya et al. observed 50 nm diameter carbides, 50 nm diameter γ`, and a high density of dislocations on the cell boundaries. Cracking was observed as well, however, they disputed the DDC mechanism, as the cracking was located mainly on cellular boundaries.

Cloots et al. [8] investigated the L-PBF of IN738LC and observed a similar columnar grain structure oriented along the build direction. Cracking was observed transverse to the laser scan direction, and SEM imaging inside of the cracks revealed a dendritic structure characteristic of solidification cracking. Atom Probe Tomography (APT) analysis of a grain boundary revealed high levels of Zr segregation, which is known to be a solidus depressant. Ramsperger et al. [10] studied the processing of E-PBF fabricated CMSX-4 and attributed its cracking to high internal stresses when part dimensions exceeded a certain value. The elevated processing temperatures associated with E-PBF also resulted in in-situ γ` precipitation. Chauvet et al. [9] performed an extensive study on cracking mechanisms affecting an unspecified Ni-Co-Cr-Mo-Al-Ti-B superalloy processed by E-PBF and concluded that a solidification cracking mechanism was at play based on the morphology observed on crack faces. Higher angle grain boundaries were found to be more susceptible to cracking than lower angle grain boundaries, which was attributed to the higher angle grain boundaries remaining wetted at lower temperatures (due to increased boundary energy), which in turn increases the solidification cracking susceptibility. APT studies revealed the presence of borides, which are known to depress the solidus temperature, on the grain boundaries.

A few different approaches to micro-crack mitigation in PBF fabricated Ni-base superalloys have been reported in the literature, which can be categorized as the following: (i) alloy modification, (ii) process modification, and (iii) post-processing. Carter et al. [5] utilized X-ray Computerized Tomography (CT) scans, on a L-PBF fabricated CM247LC, to highlight the effectiveness of post-process Hot Isostatic Pressing (HIP) at healing internal micro-cracks. Surface cracks can not be healed with HIPing. Research into crack mitigation via process modification are mostly focused on the effects of pre-heating [10,13] and scan strategies [5]. Ramsperger et al. [10] reported crack-free CMSX-4 samples fabricated by E-PBF when using high fabrication temperatures (1040°C and above), which is possible in E-BPF due to the E-beam preheating. Hagedorn et al. [13] obtained L-PBF fabricated crack-free CM247LC by preheating the baseplate to 1200 °C. Carter et al. [5] investigated the influence of scan strategy on L-PBF fabricated CM247LC and found that a simple back and forth scan strategy resulted in a homogenous microstructure that was less susceptible to cracking. One novel approach to process modification is the 3D Laser Shock Peening (LSP) approach demonstrated by Kalentics et al. [14]. In this method, LSP was applied between layers during the L-PBF fabrication of CM247LC in order to impart a compressive residual stress which induces crack healing through a reverse brazing mechanism. Crack mitigation through alloy modification has also been a successful technique. Harrison et al. [15] showed reduced

cracking in an L-PBF fabricated Hastelloy X, modified with increased solid-solution strengthening elements, improving the material strength. Engeli et al. [16] investigated the L-PBF processability of several batches of IN738LC and found that a Si content lower than 0.02 wt% was required to produced crack-free samples.

Each of the crack mitigation approaches listed above have advantages and disadvantages, and successful processing of precipitation strengthened Ni-base superalloys will require some combination of the different approaches. Post-process HIPing is effective at micro-crack healing; however, it is an additional manufacturing step that will increase production time and cost. Sample preheating has proved to be a viable option for successfully PBF fabrication of the precipitation strengthened Ni-base superalloys; however, it remains only well suited for the E-PBF process since a majority of L-PBF machines do not have the ability to operate at such high temperatures. Alloy modification and/or control of impurity levels is another successful strategy but again, it does not always lead to crack-free parts. A better understanding of the underlying mechanisms is required in order to modify the process and alloys for successful production level AM of the precipitation strengthened Ni-base alloys.

The aim of this study is to investigate the underlying micro-crack mechanisms and to mitigate cracking via alloy and process modification of L-PBF fabricated CM247LC. Cracking mechanisms were investigated in the commercial CM247LC alloy and based on microstructural investigations, a new Hf-free variant of CM247LC was developed to mitigate the micro-cracking mechanism observed. Two different processing conditions are presented to highlight the influence of melt pool geometry, specifically depth and width, on micro-crack mitigation.

2. Experimental Methods

2.1. Materials and Additive Manufacturing

Unmodified CM247LC and a modified version of CM247LC, CM247LC NHf (Hf-free), were inert-gas atomized by Oerlikon Metco (Pfaeffikon, Switzerland). Chemical composition was measured by inductively coupled plasma optical emission spectrometry (ICP-OES) and combustion analysis (for carbon) and is listed in Table 1. Both batches of powder had a 15 – 45 μm size range and a D_{50} of approximately 32 μm.

Table 1. Chemical composition of the powders used in the study.

wt. %	Al	B	C	Co	Cr	Fe	Hf	Mo	Ni	Ta	Ti	W	Zr
CM247LC	5.71	0.017	0.06	9.24	8.62	0.02	1.37	0.54	Bal	3.08	0.73	9.93	0.006
CM247LC NHf	5.56	0.01	0.07	9.14	8.36	0.07	0.005	0.53	Bal	3.18	0.63	9.48	0.018

Two distinct processing conditions were utilized for this study: Condition 1 and Condition 2. Condition 1 samples (10 × 10 × 10 mm cubes) were fabricated on a Concept M2 (Concept Laser, Germany) equipped with a 200 W 1070 nm fiber-laser operating in continuous wave mode with a Gaussian intensity distribution and a 90 μm spot size ($1/e^2$). The Concept M2 was modified by adding an aluminum support structure to hold an 80 mm diameter build plate instead of the standard 245 × 245 mm build plate. Condition 2 samples (8 × 8 × 8 mm cubes) were fabricated on a Sisma MySint 100 (Sisma S.p.A., Italy) equipped with a 200 W 1070 nm fiber-laser operating in continuous wave mode with a Gaussian intensity distribution and a 55 μm spot size ($1/e^2$). The Condition 1 samples were built on an 80 mm diameter stainless steel build plate and the Condition 2 samples were built on 100 mm and 34.5 mm diameter stainless steel build plates. All samples were processed with a bidirectional scan strategy (90 degree rotation between layers, except for two samples processed without layer rotation for surface analysis) with border contour. Argon shielding gas (99.996 % Ar) was used in both machines (Condition 1 < 0.8 % O_2, Condition 2 < 0.5 % O_2). The optimized parameter set, shown in Table 2, for each condition were identified via independent parameter surveys on each machine that focused on achieving the highest density (lowest porosity) parts.

The Volumetric Energy Density (VED) of the two processing conditions was calculated with Eq. 1:

$$\mathrm{VED} = \frac{\mathrm{P}}{\mathrm{V.h.d}} \tag{1}$$

where P is the laser power, v is the scan velocity, h is the hatch spacing, and d is the layer thickness.

In addition to the VED, the normalized enthalpy, first proposed by Hann et al [17] (the exact form given here is from Rubenchik et. al [18].), was calculated with Eq. 2:

$$\frac{\Delta \mathrm{H}}{\mathrm{h_s}} = \frac{\alpha \mathrm{P}.2^{\frac{3}{4}}}{\rho \mathrm{C} \mathrm{T_m} \sqrt{\pi \omega^3 \mathrm{V} \mathrm{D}}} \tag{2}$$

where ΔH is the input enthalpy, h_s is the enthalpy of the solid at the melting point, α is the absorptivity, ρ is the density, C is the specific heat at melting, T_m is the melting temperature, D is the thermal diffusivity, and ω is the radius of the spot size, was calculated in order to simplify comparisons between the two conditions. The VED and normalized enthalpies are presented in Table 2. Thermo-physical property data (from [19,20]) used in the calculation of normalized enthalpy is given in Supplement Table 2.

Table 2. Processing parameters used in this study.

Condition	Spot Size (µm, $1/e^2$)	Power (W)	Scan Speed (mm/s)	Hatch Spacing (mm)	Contour Spacing (mm)	Layer Thickness (µm)	VED (J/mm^3)	Normalized Enthalpy
1	90	200	600	0.105	0.075	30	106	26.3
2	55	175	750	0.075	0.100	30	104	43.2

2.2. Microstructure and Defect Characterization

Sample cubes for microstructure and defect characterization were sectioned in half, parallel to the build direction, cold-mounted in epoxy, ground, polished with monocrystalline diamond suspension and finally lapped with 50 nm colloidal silica. Some samples were etched with Glyceregia (15 ml HCl, 10 ml glycerol, 5 ml NHO_3) for melt pool and microstructure analysis. Scanning Electron Microscope (SEM) analysis was performed with a FEI NanoSEM 230 in secondary and backscatter electron imaging mode. Electron Backscatter Diffraction (EBSD) was performed on Tescan Lyra3 SEM equipped with a Symmetry camera from Oxford Instruments (UK) and operated at 20 kV with a 10 nA beam current.

Lamellae for scanning transmission electron microscopy (STEM) analysis were prepared from the aforementioned sample cubes (lamellae is perpendicular to build direction) using an FEI Helios NanoLab 600i focused ion beam (FIB). The selected area electron diffraction (SAED) data were obtained at 200 kV with a JEOL 2200FS microscope. An FEI Titan Themis microscope equipped with a probe spherical aberration corrector and a SuperEDX system (ChemiSTEM technology) with four silicon drift detectors for energy-dispersive X-ray (EDX) spectroscopy, was used for STEM analysis. The microscope was operated at 300 kV with a beam convergence semi-angle of 25 mrad. The annular dark field (ADF) detector have a inner and outer collection semi-angles of 66 and 200 mrad, respectively. The Bright Field (BF) detector had collection angles of 35 mrad. STEM-EDX spectrum images (with background correction) were pre-filtered (5 pixel average) for semi-quantification and displayed as wt. % (Figure 2) and net intensity maps (Figure 8).

2.3. Crack Density Analysis

Three independent studies were conducted to compare the micro-crack density between CM247LC and CM247LC NHf samples. Samples fabricated for comparison between the two alloys were identical except for the alloy used i.e., same build plate size, same number and geometry of samples on the build plate, same parameters, etc. Crack density analyses were conducted on optical images captured with a Leica VZ700C microscope with automatic image stitching at 200x magnification. Approximately 100 images were stitched together to generate one uncompressed image of an entire cross section (parallel to the build direction). Each sample was ground, repolished, and imaged numerous times in order to improve statistics (Condition 1: 5 times, Condition 2: 5 times, Condition 2 repeat: 4 times). Optical

image analysis for crack density comparisons was performed with ImageJ [21]. Uncompressed stitched images, merged together as one image, of the sample cross section were filtered with a 3 pixel median filter. Next, the images were manually thresholded to generate a binary image. The binary images of the cracks were analyzed with the Analyze Particle function in ImageJ. Particles under 20 pixels in size, touching edges, and with a circularity above 0.35 (ensuring pores were not counted) were ignored. Each crack was fitted as an ellipse. To differentiate cracks from horizontal lack of fusion defects, ellipses that were within ± 10 degrees of the horizontal axis (perpendicular to build direction) were ignored. Crack density for each sample is reported as an average of the numerous measurements taken per sample.

2.4. Thermodynamic Calculations

Scheil-Gulliver (no diffusion in solid, complete mixing in the liquid) and equilibrium solidification calculations were performed with the TCNI5 database in ThermoCalc. The Scheil-Gulliver calulations were performed with a nominal CM247LC composition that is listed in the Supplement.

2.5. Gleeble Experiments

In order to simulate cracking in the HAZ of the L-PBF samples (CM247LC and CM247LC NHf samples), Gleeble experiments were conducted using a Gleeble 3800 machine. Xu et al. have used this thermomechanical simulation technique to study the microstructure evolution in the HAZ of IN738LC samples produced by laser solid forming process [18]. In the Gleeble machine, the samples are heated by Joule effect, under vacuum, at a rate of 250 °C/s until 1250 °C, followed by water-quenching. The temperature is screened with thermocouples welded to the surface of the samples. Due to thermal expansion during the test, in combination with the constraints of the grips, the samples were subjected to 5 MPa compressive stress.The testing setup of the Gleeble experiments is shown in Supplement Figure 1.

2.6. Differential Scanning Calorimetry

The phase transformation temperatures, in as-fabricated CM247LC and CM247LC NHf (Condition 2), were determined by differential scanning calorimetry (DSC) measurements, conducted using a NETZSCH DSC 404C Pegasus thermal analyzer. Samples of 22.2 mg were used for both alloys, with their surfaces ground down to P4000 to ensure a better thermal conduction with the crucible. The experiments were carried out under argon atmosphere (99.9999% Argon) with a flow rate of 40 ml/min. The Al_2O_3 crucibles were heated at a rate of 10 K/min from room temperature to 1430°C, and cooled down at the same rates. Only the heating thermograms are considered in this study.

3. Results of L-PBF Processing of Standard CM247LC

3.1. As-Fabricated Microstructure

The Condition 1 and 2 as-fabricated microstructures of the CM24LC alloy is displayed in Figure 1. The melt pools are highlighted by dashed lines in Figures 1(a) and 1(b). The melt pools dimensions are ~175 µm wide and ~105 µm deep for samples produced using Condition 1 (Figure 1(a)), and ~180 µm wide and ~55 µm deep for samples produced using Condition 2 (Figure 1(b)). No significant differences were observed between the melt pool dimensions of the samples fabricated on the 100 mm diameter and the 34.5 mm build plate of Condition 2 (Supplement Figure 2). Regardless of the processing condition, in the as-fabricated condition, the samples are characterized by a grain microstructure predominately composed of columnar grains ranging from a few microns to ~50 µm in width, oriented parallel to the build direction (Figures 1(c) and 1(d)). Columnar grain regions are composed of ~1 µm wide substructures, later identified as cells (Figures 1(e) and 1(f)). EBSD Inverse Pole Figures (IPF) maps of Condition 1 and Condition 2 as-fabricated samples are shown in Figure 2. The EBSD IPF maps show elongated grains parallel to the build direction, as observed in the BSE images. The grains have a (100) fiber texture in the build direction. The high angle grain boundaries (HAGB, > 10°) represent 56 % and 36% of the total grain boundaries in Condition 1 and Condition 2 samples, respectively. The grain size (HAGB) in Condition 1 samples is ~ 30 - 50 µm wide and hundreds of µms in length, and the grain size (HAGB) in Condition 2 samples is ~40 – 80 µm wide and hundres of µms in length. The Condition 2 sample shows more distinct sub-grain structures marked by low angle boundaries cells inside the larger grains.

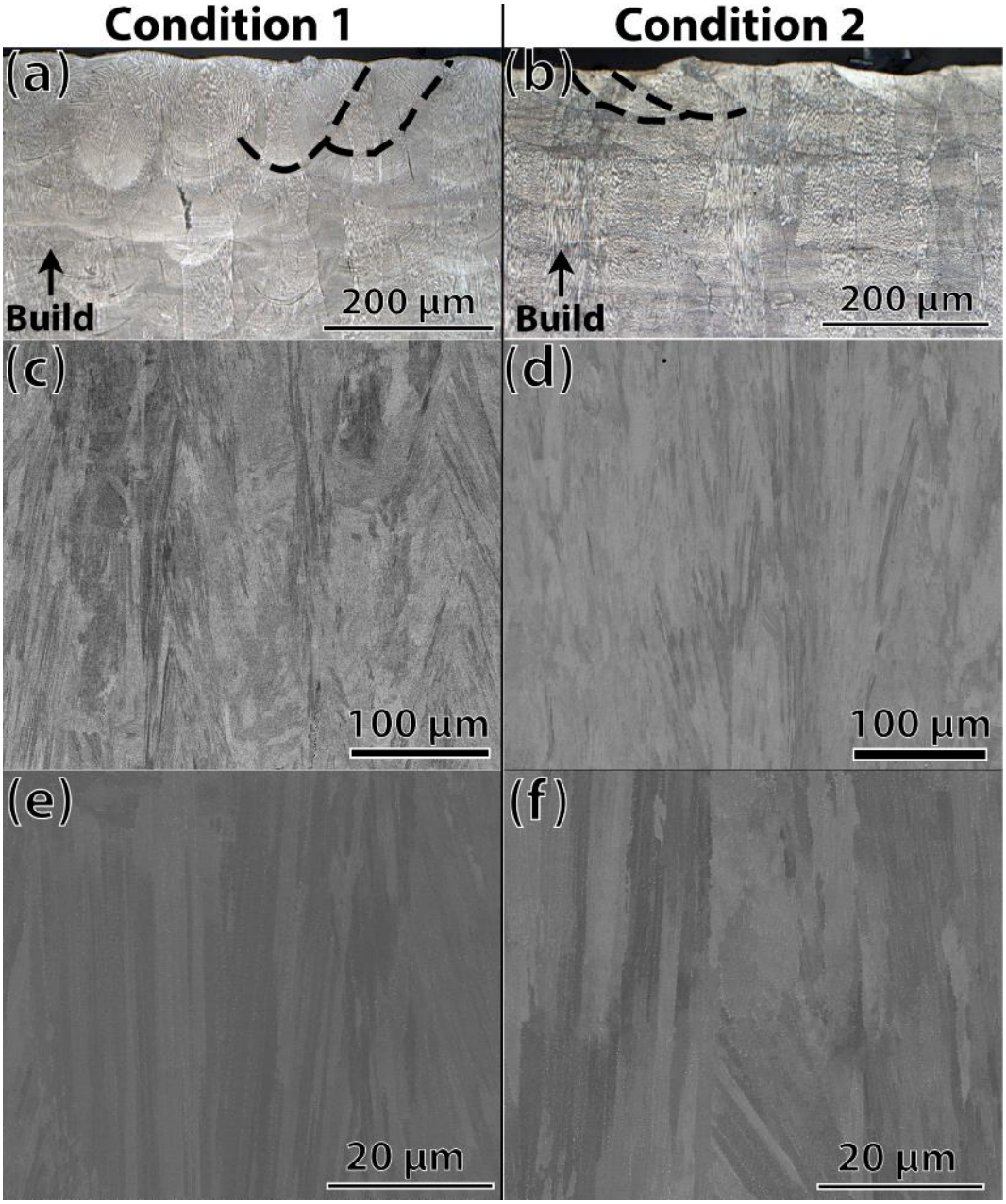

Figure 1. Microstructure of CM247LC samples in the as-fabricated condition, fabricated using Condition 1 (a,c,e), and Condition 2 (b,d,f). a,b) Optical images, with highlighted melt pool boundaries (dashed black lines). c,d) Backscatter electron images showing the columnar grain structure. e,f) Higher magnification backscatter electron images showing a cellular substructure.

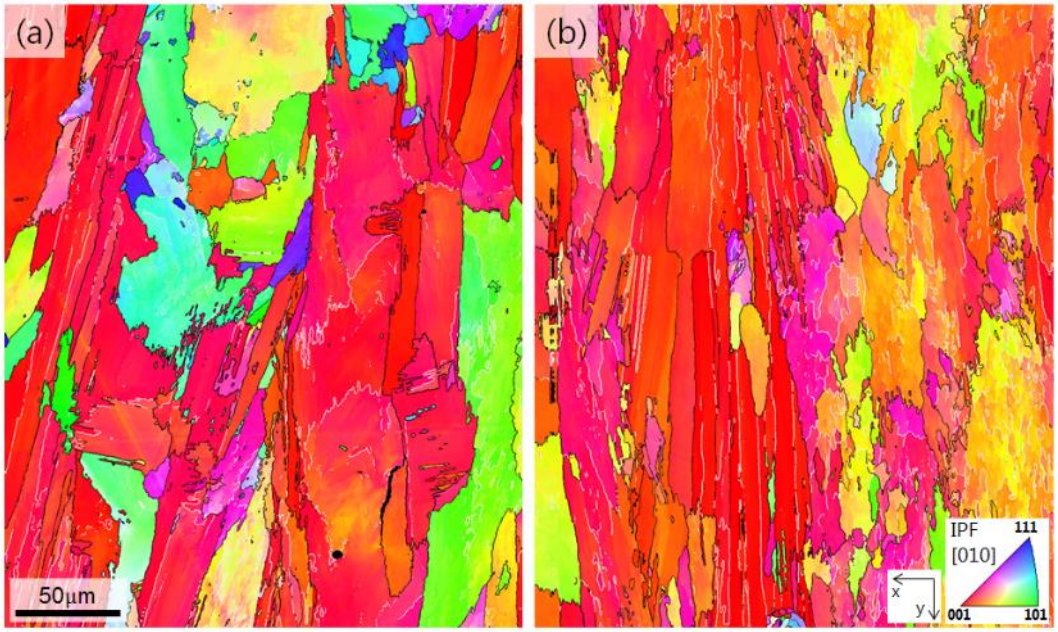

Figure 2. EBSD IPF maps of samples fabricated with Condition 1 (a) and Condition 2 (b). The IPF color is shown for the Y direction which is parallel to the solidification direction. White lines: low angle boundaries > 2°; black lines: high angle boundaries > 10°. Map sizes are 250 x 300 µm with 100 nm step size.

Scanning Transmission Electron Microscopy (STEM) was used to investigate the presence of secondary phases and characterize the solute distribution. Fig. 3 shows (a) ADF-STEM and (b) BF-STEM image, as well as (c) a series of STEM-EDX maps of the as-fabricated condition (transverse microstructure showing). The cell structure ranges from ~500 nm to ~1 µm in diameter (Fig. 3(a)). A high dislocation density is observed on the cell boundaries (Fig. 3(b), larger image in Supplement Fig. 3). Precipitates ~55 nm in diameter and rich in Ti/Hf/Ta/W/C are located on the cell boundaries and are presumed to be carbides (Fig. 3(c)). A X-Ray diffraction (XRD) pattern of an as-fabricated Condition 2 sample (See Supplement Fig. 4) did not reveal the presence of superlattice peaks of the γ` phase; however, a selected area electron diffraction (SAD) pattern (Supplement Fig. 5) did reveal 100- and 110-type superlattice reflections of the $L1_2$ (γ`) structure. TEM dark-field imaging and HR-STEM imaging were attempted in order to image the γ` precipitates, but the precipitates could not be imaged, likely due to the small size. Significant micro-segregation was observed; Hf, Al, and Ti partitioning to the cell boundaries and W, Co, and Ni partitioning to the cell cores (Fig. 3(c)). STEM-EDX semi-quantification values (line profiles are shown in Supplement Fig. 6) and the calculated effective partition coefficients are presented in Table 2. Levels of Hf enrichment varied considerably between grain boundaries, being estimated at 4 wt.% Hf in Fig. 3(c), while 20 wt.% Hf was measured on another boundary (Supplement Figs. 7 and 8). Zirconium K lines were observed in the EDX spectra but no partitioning of the Zr was observed. In a prior study, we have shown similar segregation behavior in samples fabricated with the same parameters as Conditions 1 except with a chess scanning strategy [14].

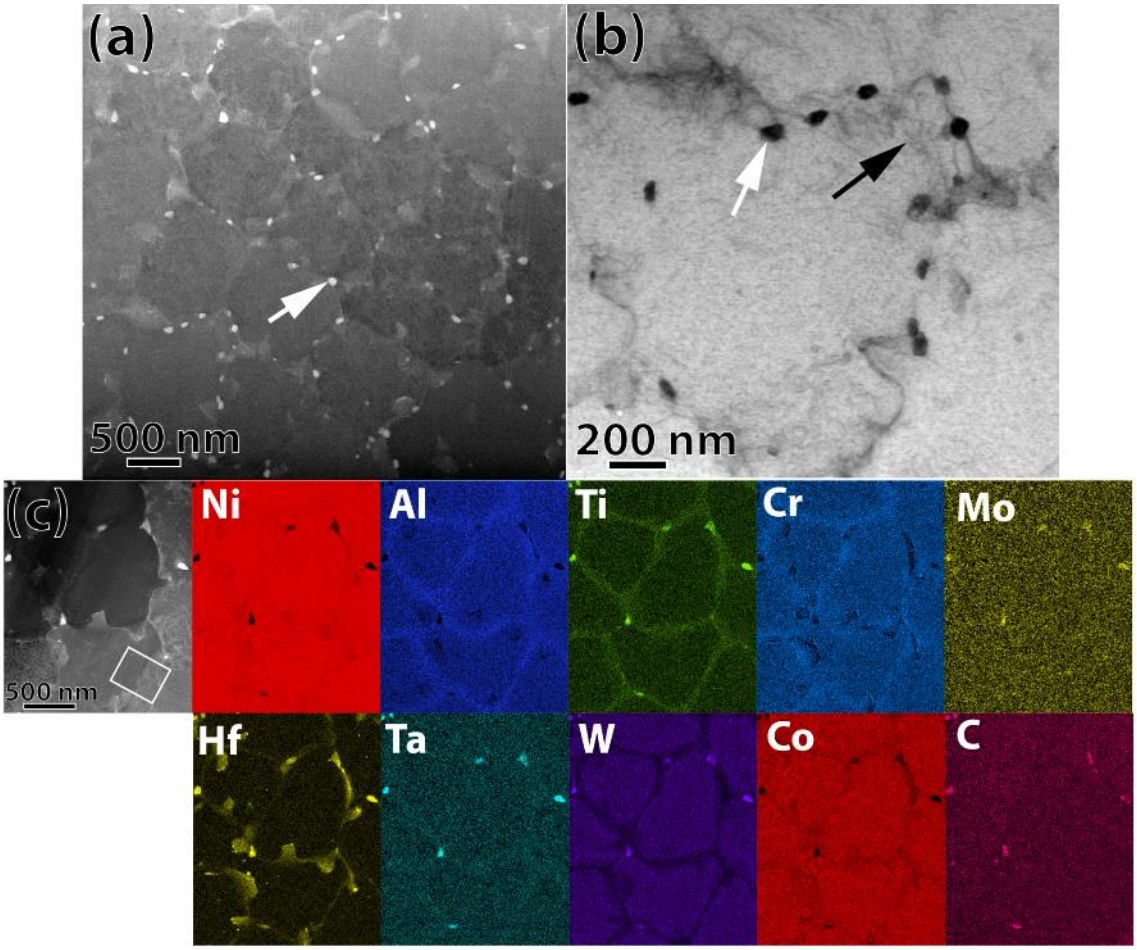

Figure 3. STEM characterization of the as-fabricated microstructure (transverse section) of a CM247LC sample fabricated with Condition 2 a) ADF-STEM image showing ~0.5-1 µm diameter cells, surrounded by grain boundary precipitates, assumed to be carbides (bright particles highlighted by white arrow). b) BF-STEM image showing a high dislocation density (area highlighted by black arrow) on the cell boundaries. c) STEM-EDX map of cell boundaries. Precipitates are enriched in Ti/Hf/Ta/W/C and are presumed to be carbides. The chemical analysis is performed using the Al-K, Ti-K, Cr-K, Hf-L, Ta-L, W-L, Co-K, Ni-K, Mo-K, Zr-K, and C-K lines.

Table 3. STEM-EDX semi-quantification values taken from the area highlighted by the white box in Figure 3(c), highlighting the segregation behaviors of the various elements in as-fabricated CM247LC. Effective partition coefficients k` (Cell / Boundary composition) are calculated. The chemical analysis is performed using the Al-K, Ti-K, Cr-K, Hf-L, Ta-L, W-L, Co-K, Ni-K, and Mo-K lines

	Al	**Co**	**Cr**	**Hf**	**Mo**	**Ni**	**Ta**	**Ti**	**W**
Cell wt. %	4.7	9.3	7.5	2.3	1.9	60	4.5	1.0	8.5
Boundary wt. %	4.1	8.6	8.1	4.1	1.9	59	5.5	1.5	6.5
k`	0.87	1.1	0.93	0.56	1.0	1.0	0.81	0.73	1.3

3.2. Micro-cracking in the as-fabricated samples

The density of both Condition 1 and Condition 2 samples was measured at >99.9 % with the Archimedes method and using a nominal density of CM247LC of 8.54 g/cm^3; however, the presence of defects such as micro-cracks, pores, and lack of fusion suggest that the density is slightly lower. The top surface of an as-fabricated (Condition 1) bi-directionally scanned sample (no rotation between layers) is shown in Fig. 4. Micro-cracks ~200 to 300 μm in length are oriented perpendicular to the beam travel. Similar observations were also made on the samples with bidirectional scanning and a 90° rotation between the layers. Micro-crack density was fairly uniform throughout the cross-section of Condition 1 samples, but Condition 2 samples did have a higher occurrence of micro-cracking ~300 μm from the side edge (visible in optical images presented later Fig. 11).

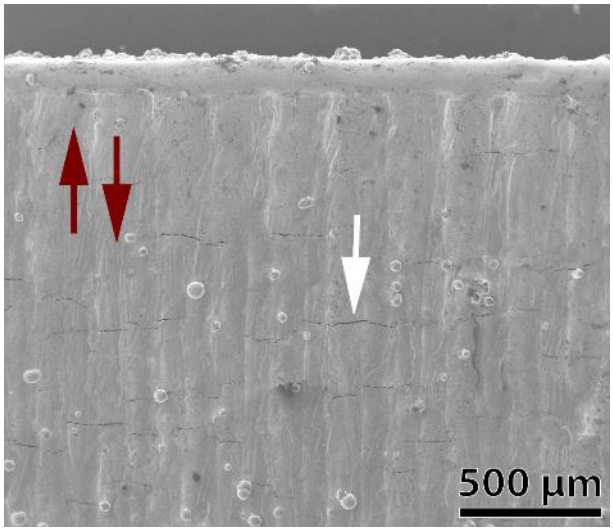

Figure 4. SE image of top surface of as-fabricated CM247LC cube (Condition 1). Cracking (one crack highlighted by white arrow) is perpendicular to the direction of laser travel (is indicated by the red arrows).

Figure 5 (a,b,d,e) presents BSE images of parallel and perpendicular cross sections of CM247LC samples (Condition 1 and 2 samples) . In the BSE image of a parallel cross section, micro-cracks ~100 μm in length are oriented parallel to the build direction (Figure 5(a)). In the images of the perpendicular cross sections, micro-cracks are observed oriented both parallel and perpendicular to the image frame (Figure 5(b)), which represent the X and Y scanning directions. Higher magnification imaging of a crack, both in parallel and perpendicular cross sections, reveals that cracking occurs on cell/grain boundaries, Figure 5(d) and (e). SE images of a representative micro-cracks observed in samples fabricated from both conditions are shown in Figures 5(c) and 5(f). The crack surfaces have a rough appearance indicative of fracture in the liquid phase [19]. Micro-crack location and morphology did not appreciably change between the two machines, only the crack density is higher in samples produced using Condition 1. In a prior study, we have shown similar crack appearance for cracks in samples fabricated with the sample parameters as Conditions 1 except with a chess scanning strategy [14].

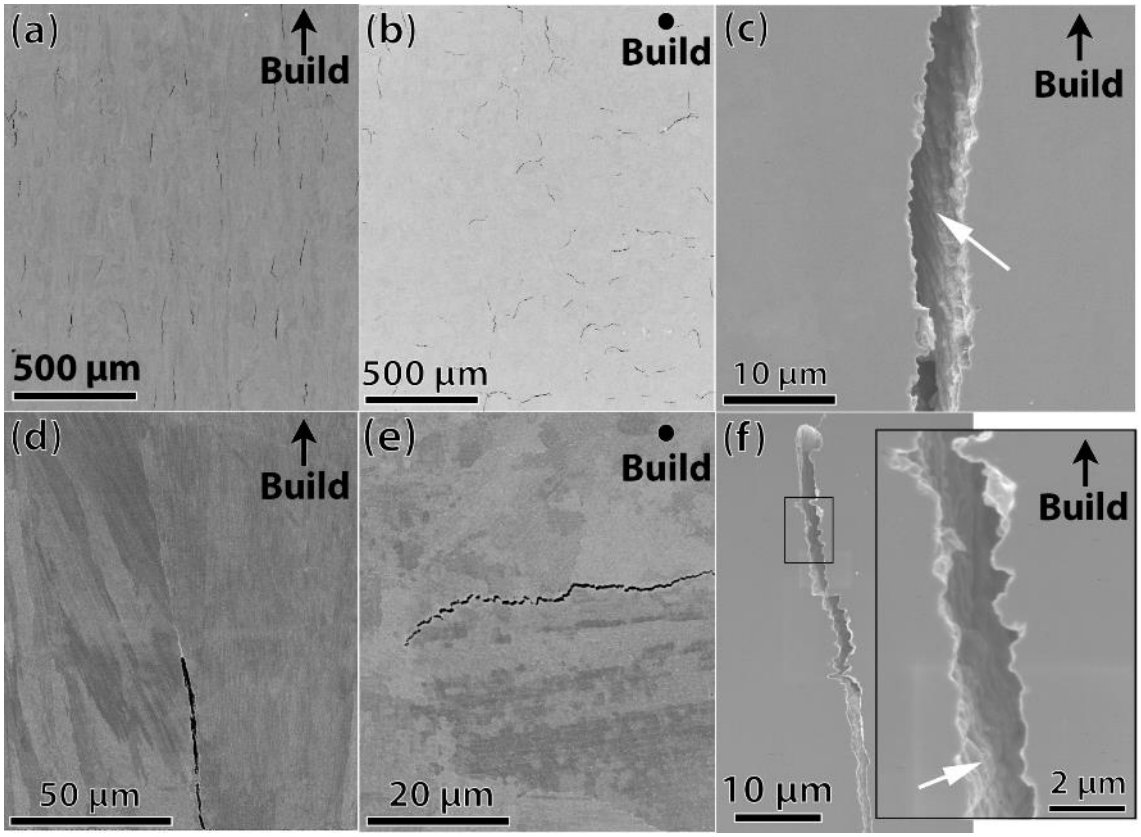

Figure 5: Electron microscope images taken from CM247LC samples fabricated from a,b,c) Condition 1 and d,e,f) Condition 2. a,d) BSE Image of a parallel cross section. b, e) BSE image of perpendicular cross section. c, d) SE image showing the features (white arrows) on the crack surfaces.

3.3. Gleeble Test Results

Gleeble tests have been conducted to further investigate the cracking mechanisms that may occur in the Heat Affected Zone (HAZ) during processing. The as-fabricated (Condition 2) CM247LC samples were heated up to 1250 °C at a rate of 250 °C/s and then water-quenched. Figure 6(a) indicates a specific part of the as-fabricated CM247LC sample that was chosen for investigation, prior to the experiment. The same zone has been imaged again after the experiment. A zone with the appearance of a grain boundary remelting and solidification after the fast heating/cooling was observed (Figure 6(b-c)). SEM-EDX analysis indicates significant Hf enrichment on the remelted and re-solidified grain boundary after the Gleeble experiment (Figure 6 d and e).

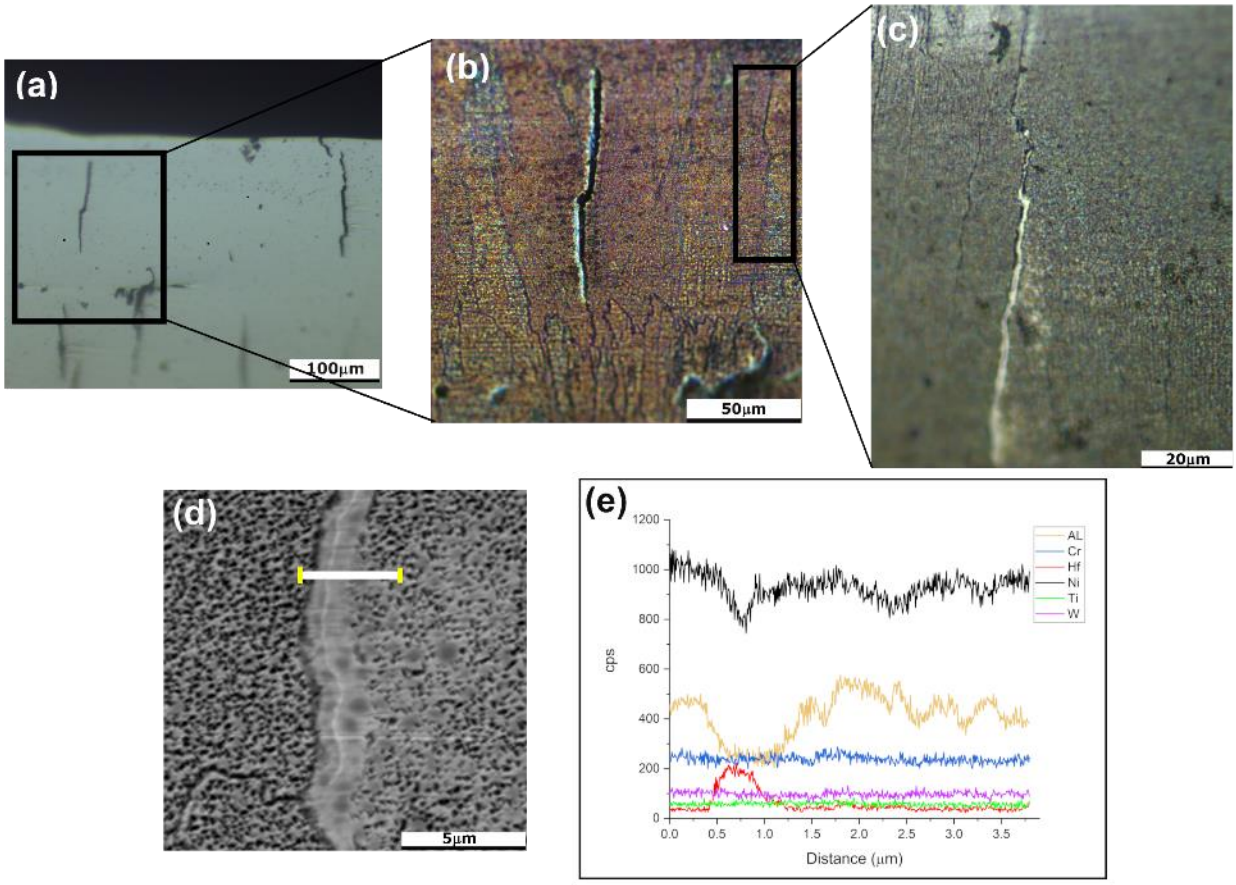

Figure 6. a) Optical image showing a specific area of the as-built sample before the Gleeble test. b) Optical microscope images taken from the same zone as (a) after the fast heating and cooling treatment in the Gleeble machine, c) higher magnification optical image shows a thin 1 µm wide film formed after Gleeble test. d) Higher magnification SE image of the observed film, and e) SEM-EDX line scan analysis of the region. All images are parallel to the build direction.

3.4. Microstructure and potential micro-crack formation mechanisms in CM247LC

The processing parameters utilized for Condition 1 and Condition 2 led to different melt pool profiles and incidence of HAGBs. While the melt pool profiles differ, the general microstructure, fine columnar grains composed of cells oriented predominately in the build direction, is similar between the two conditions. The influence of the processing parameters on the microstructure and micro-crack density will be discussed in Section 5.3.

The observed grain microstructure, fine columnar grains with a (100) fiber texture oriented parallel to the build direction, is similar to that observed in L-PBF fabricated CM247LC studies by Wang et al. [6] and Divya et al. [7]. The observed grains were composed of ~1 µm cells with dislocations and carbides located on the boundaries, also similar to the aforementioned studies. Unlike the studies of Wang et al. and Divya et al., we were not able to directly observe the γ` phase. The appearance of superlattice reflections in the SAED patters, characteristic of γ` precipitates, prove that it is present in the as-fabricated samples used in this study, but likely at nm to sub-nm sizes. The chemical micro-segregation observed is similar to that observed in the other CM247LC L-PBF studies. The effective partition

coefficients (Table II) of the various elements is comparable, except for Cr, to those observed in cast Ni/base superalloys, suggesting that the segregation tendencies do not significantly differ between L-PBF fabricated and conventionally cast alloys [20,21]. However, unlike the controlled solidification (controlled thermal gradients and interface velocities) typically encountered in superalloy casting, the L-PBF solidification conditions will vary substantially, leading to differences in micro-segregation within a single melt pool. This variation was shown by the observation of boundaries with 4 wt.% Hf enrichment and another boundary with up to 20 wt.% Hf enrichment. It should also be noted that the STEM-EDX measurements of the micro-segregation are ex-situ and actual levels of micro-segregation during solidification may be higher. Adjacent passes of the laser and additional building layers will result in a HAZ. The high temperatures in the HAZ in combination with the abundant short-circuit diffusion paths, may result in a partial homogenization. Therefore, actual levels of micro-segregation during solidification are likely different than that observed.

The remelted Hf-enriched grain boundaries observed after the Gleeble experiment is indicative of liquation cracking. During the L-PBF process, in the HAZ of the samples, cracks form due to the presence of a liquid film and the presence of tensile residual stresses that pulls the liquid films apart. Unlike in liquation cracking, the remelted grain boundaries in the Gleeble experiment remained closed. This can be attributed to the fact that the sample was under a 5 MPa compressive stress due to thermal expansion, hence, the remelted grain boundaries were kept closed, which prevents their cracking.

Analysis of the micro-crack fracture faces (Figure 5(c,f)) revealed a dendritic-like morphology indicative of fracture occurring in the liquid phase. In welding literature, micro-cracks with this appearance are attributed to solidification cracking [23]. While the crack faces analyzed all had morphology indicative of solidification cracking, the Gleeble test results show that a liquation cracking mechanism can be active during the L-PBF process. Susceptibility to liquation cracking is not surprising given the significant segregation observed. While most liquation and solidification cracks observed in welding literature will run parallel to the welding direction [26], a majority of the micro-cracks observed in this study are perpendicular to the direction of beam travel. Transverse solidification cracking has been reported in laser welding literature for welding of Ni-base superalloys [27] and Al alloys [28]. Park et al. utilized finite element modeling to show that, for high ratios of scan velocity over laser power, stresses parallel to the beam travel are highest, thus resulting in transverse cracking. Hu et al. [28] investigated transverse cracking in laser welded Al-alloys and found that the more elongated the thermal gradient was in the direction of beam travel (result of higher beam velocities) the higher the longitudinal stresses were and thus the greater transverse cracking.

4. Micro-Crack Mitigation – Alloy Design

Since the probable micro-cracking mechanisms at play have been identified as a combination of both solidification and liquation cracking, it is important to look at the factors that influence these mechanisms of cracking. Solidification and liquation cracking are influenced by a complex interplay

of both process and material related variables. Some of the major variables, but not all, that influence solidification cracking are listed below.

1. **Solidification Interval**: A large solidification range results in a large mushy zone (liquid-solid mixture). As solidification cracking occurs in the mushy zone, a larger solidification range will result in a larger region of susceptibility. [4]
2. **Amount of terminal liquid**: Peak crack susceptibility typically occurs with moderate levels of solute content. High values of solute can lead to large volumes of remaining liquid that can back fill any cracks that develop. With minimal to no solute, a grain boundary liquid film will not form and cracking will not occur. [4]
3. **Stress State**: Cracking cannot occur without a tensile stress. Both solidification shrinkage and thermal residual expansion/contraction provide the stress that can lead to fracture. The level of restraint on the solidifying material will influence the stress levels and therefore the cracking susceptibility. [19]
4. **Melt pool geometry/profile**: Teardrop shaped welds, welds with large depth to width ratios, and welds with concave profiles are all more susceptible to solidification cracking. [23]
5. **Surface tension of the terminal liquid**: The condition where a continuous liquid film is on a grain boundary is the most susceptible condition. If the liquid does not wet the grain boundaries, then bridging of grains occurs and cracking can be prevented. [4]
6. **Grain Boundary Orientation**: Grain boundaries can be classified as attractive or repulsive based on the misorientation angle between them. If the grain boundary misorientation exceeds a certain threshold, it becomes a repulsive boundary thus lowering the solidification temperature further. [29]
7. **Grain Morphology**: An equiaxed grain microstructure can more easily accommodate strains than a columnar grain microstructure and will be less susceptible to solidification cracking [30].

Stress state, melt pool geometry/profile, grain boundary misorientation, and grain morphology are all variables that are significantly influenced by the processing parameters. Some of the crack mitigation strategies based on addressing the aforementioned variables are discussed in the introduction. Many of these strategies are undesirable due to added processing steps and/or costly process modification that is not attainable in most commercial L-PBF machines. Process parameter optimization can lead to significant improvements (shown later) but the fact remains that L-PBF is a high energy density process. The high energy density typically results in high thermal gradients, and rapid heating and cooling, that in turn lead to columnar microstructures, and residual stresses that cannot be easily relaxed during the process. In order to broaden the processing window, the material specific variables need to be addressed as well. Variables such as solidification interval, amount of terminal liquid, and liquid surface tension

are primarily determined by the material itself. The second part of this work will thus focus on the influence of the solidification interval.

Intentionally reducing the solidification interval of an alloy implies modification of the alloy composition; typically, this is done via reducing the content of elements that preferentially segregate to the liquid ($k < 1$). Ni-base superalloys are complex alloys that contain several elements, for example, CM247LC has 13 main elements (Table 1), and the presence of many of those elements result in an increase in solidification interval. Typical culprits for solidification cracking in nickel-base superalloy welds are elevated levels of minor alloying elements such as P, S, B, C, and Zr [3]. While P and S are deleterious to mechanical properties and are kept to low levels, B and Zr serve as grain boundary strengtheners and are known to improve creep properties [31]. Ti is another element that can increase the susceptibility to solidification cracking; however, Ti is intentionally added for (i) raising the γ` solvus temperature, (ii) increasing the anti-phase boundary energy for γ`, and (iii) increasing the lattice parameter of γ`[31]. It is clear that intentionally reducing the alloy solidification interval via alloy modification will result in an alteration of mechanical properties; however, this consequence of alloy modification is not in the scope of the current study.

The STEM-EDX maps in Figure 2 reveal the enrichment of Al, Ti, C, Ta, and Hf on the cell boundaries. No Zr or B rich films were observed on the grain boundaries. Other STEM-EDX maps (not shown) have revealed minor Zr enrichment in carbides and Zr is known to exist in MC type carbides[2]. Out of the aforementioned elements, Hf has the lowest observed partition coefficient from the STEM-EDX data, $k` = 0.56$, and exists as continuous films on the cell boundaries. In the literature, Hf was originally added to Ni-base superalloys to improve ductility [31]. Hf also serves as an S scavenger and improves hot corrosion resistance. Hf additions are said to improve mechanical properties by promoting (i) eutectic γ/γ`at the grain boundaries and (ii) blocky MC carbide morphology instead of a script-like morphology at the grain boundaries [31]. Superalloys with elevated levels of Hf (~2.0 wt. %) generally display better castability (resistance to hot tearing) than alloys without Hf, despite Hf free alloys having a smaller solidification range [32,33]. This can be attributed to the presence of Hf increasing the volume fraction of eutectic γ/γ` and, eutectic melt, which results in improved back-feeding during the casting process [32,33]. As the solidification rates in L-PBF are much higher than in traditional superalloy casting, it is feasible that the volume fraction of the eutectic melt is reduced, as evidenced by the lack of observed γ/γ` eutectic. Since Hf is a very potent melting point depressant it a prime target element for studies on the influence of solidification range on the micro-cracking tendencies of L-PBF fabricated CM247LC.

The influence Hf has on the solidification behavior of CM247LC has been investigated via thermodynamic simulations. Figure 7 shows the results of a Scheil-Gulliver solidification calculation for a standard CM247LC composition and a Hf-free version of CM247LC. The liquidus and solidus temperatures, calculated by the Scheil-Gulliver solidification calculation of nominal CM247LC, are 1383 °C and 858 °C respectively, resulting in a 525 °C solidification interval. The liquidus and solidus

temperatures, calculated by the Scheil-Gulliver solidification calculation, of the Hf-free CM247LC are 1394 °C and 1241 °C respectively, resulting in a 153 °C solidification interval. The results show that removal of Hf will significantly reduce the solidification inverval of CM247LC. While Scheil-Gulliver solidification calculations are often used to simulate solidification behavior for AM processed superalloys [9,11], the approximation does not take into account solute build up at the solidification interface and may overstate actual micro-segregation [4]. Equilibrium solidification calculations (not shown) of CM247LC gives liquidus and solidus temperatures of 1383 °C and 1249 °C respectively, resulting in a 134 °C solidification interval. The same calculation performed with a Hf-Free version of CM247LC gives liquidus and solidus temperatures of 1394 °C and 1340 °C respectively, resulting in a 54 °C solidification interval. The Scheil-Gulliver model and equilibrium solidification represent the two extremes of solidification, with the actual solidus temperatures somewhere between those predicted by the two models. Regardless of the solidification mode, it is clear that Hf has a significant influence on the predicted solidification interval of the alloy. The next sections will focus on the results of experiments with a Hf free version of CM247LC, herein named CM247LC NHf.

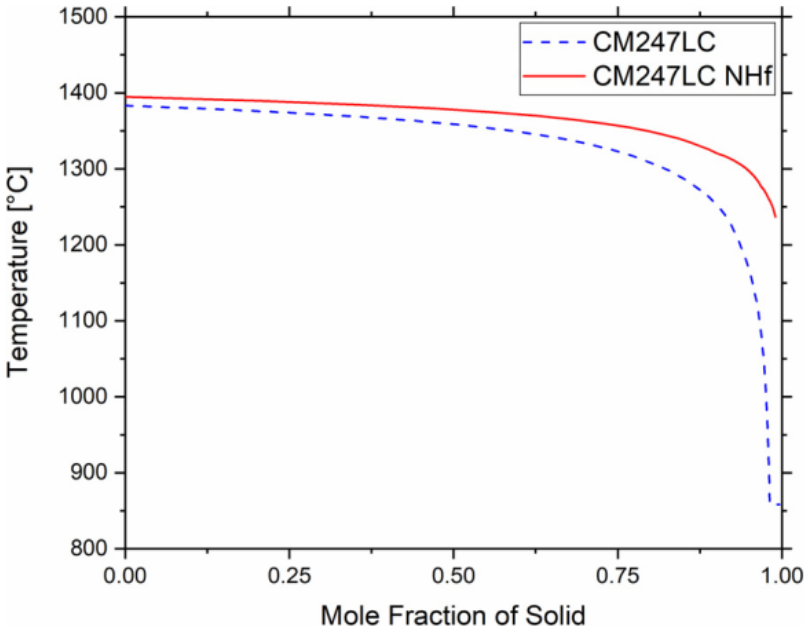

Figure 7: Scheil-Gulliver solidification curves for CM247LC and CM247LC NHf.

5. Processing of CM247LC NHf and comparison with CM247LC

5.1. Microstructure, Defects, and Thermal Analysis

Figures 8(a,b,c) show the microstructure of the as-fabricated condition of Condition 2 produced samples. The melt pools, highlighted by dashed lines in Figures 8(a), are approximately 200 µm wide and 60 µm in depth (Figure 8(a)), which correspond to an aspect ratio comparable to the one of the CM247LC alloy processed on the same machine (Supplement Figure 9 shows the CM247LC NHf processed with condition 1, Supplement Figure 10 shows additional optical images of Condition 2 samples). Similar to

the standard CM247LC samples, the as-fabricated condition of CM247LC NHf display a grain microstructure predominately composed of fine columnar grains oriented parallel to the build direction (Figures 8(b)). Columnar grain regions are composed of ~1 µm wide substructures, later identified as cells (Figure 8(c)).

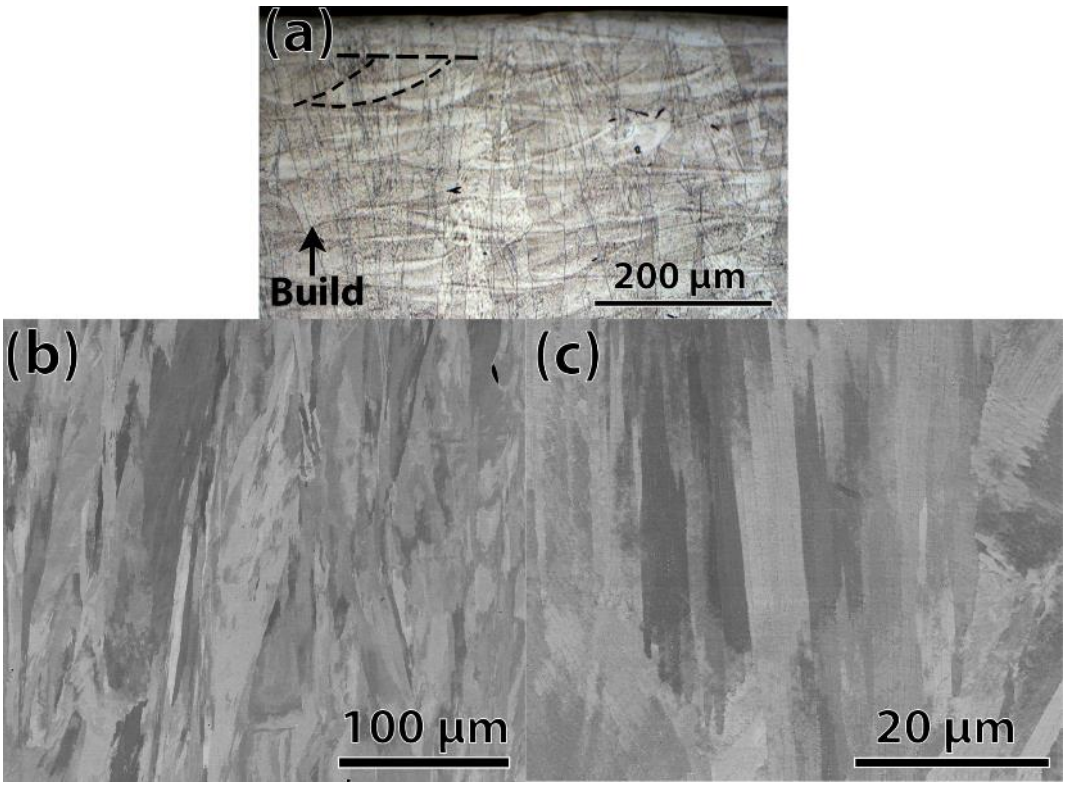

Figure 8: Microstructure of as-fabricated CM247LC NHf (Machine 2, 100 mm). (a) Optical image of an etched sample. Melt pools are highlighted by a dashed line. b,c) BSE images showing the elongated grain and subcellmicrostructure.

Figure 9 shows an (a) ADF-STEM image, a (b) BF-STEM image, and a series of (c) STEM-EDX maps taken from a Condition 2 produced sample in the as-fabricated condition (perpendicular microstructure showing). The STEM lamella was extracted at the tip of a microcrack and the crack can be clearly seen in Figure 9(c). Similar to the CM247LC alloy, the cell structure ranges from ~0.5 to ~1 µm in diameter (Figure 9(a)). A high dislocation density is observed throughout the sample (Figure 9(b)). Precipitates ~60 nm in diameter, rich in Ti /Ta/W/C, and located on the cell boundaries (Figure 9(c)) are presumed to be carbides. Elongated scriptlike carbides were observed on some boundaries (Figure 9(a)). Similarly to the CM247LC samples, X-Ray diffraction (XRD) patterns of a sample produced with Condition 2 (See Supplement Figure 4) did not reveal the presence of superlattice peaks of the γ` phase; however, a SAED pattern (Supplement Figure 11) did reveal 100- and 110-type superlattice reflections of the $L1_2$ (γ`) structure. Similar to the original CM247LC samples, HR-STEM imaging was attempted in order to image the γ` precipitates, but the precipitates could not be imaged, likely due to the small size. Significant micro-segregation was observed; Cr, Ta, Al, and Ti partitioning to the cell boundaries and

W, Co, and Ni partitioning to the cell cores (Figure 9(c)). Zirconium K lines were observed in the STEM-EDX spectra but no partitioning was observed.

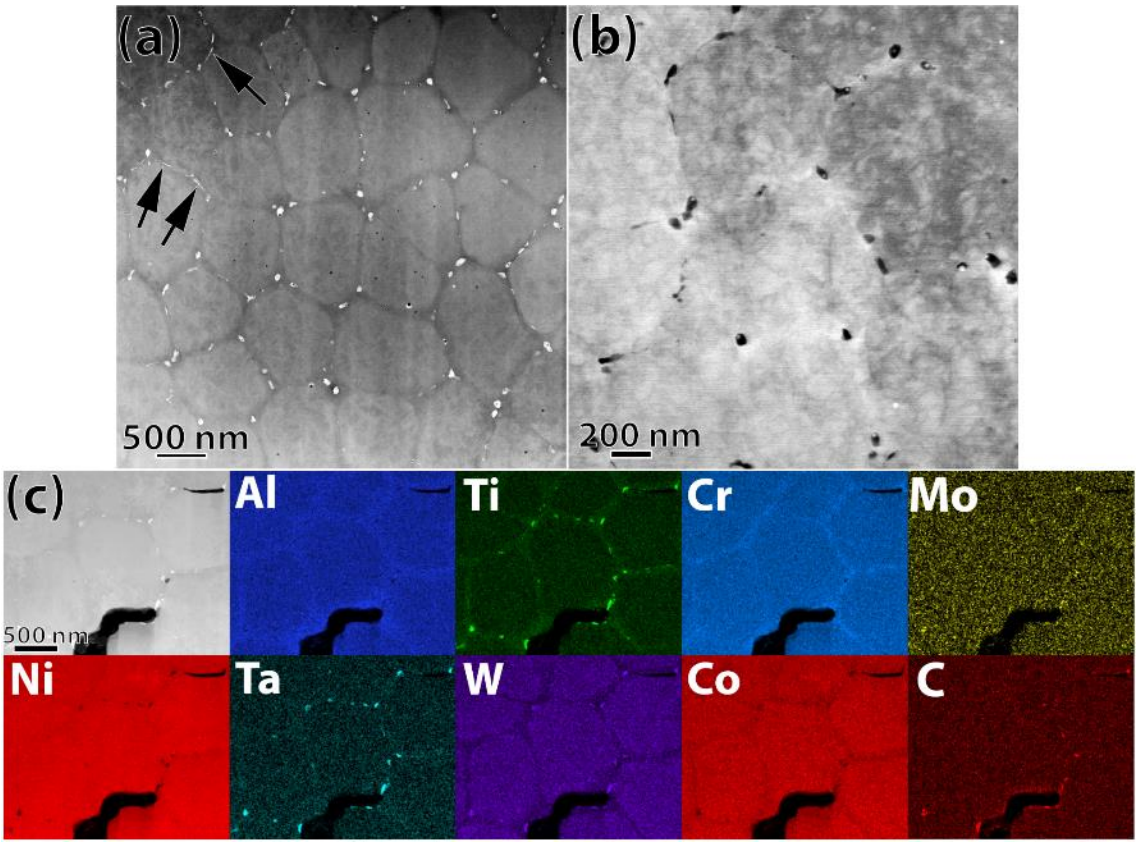

Figure 9: STEM characterization of the as-fabricated microstructure (transverse section) of a CM247LC NHf sample produced using Condition 2. a) ADF-STEM image showing ~0.5-1 µm diameter cells surrounded by grain boundary precipitates, assumed to be carbides. Black arrows point to script like precipitates assumed to be carbides. b) BF-STEM image showing a high dislocation density throughout. c) STEM-EDX map of cell boundaries. The black region is a crack. Precipitates are enriched in Ti /Ta/W and are presumed to be carbides. The chemical analysis is performed with Al-K, Ti-K, Cr-K, Ta-L, W-L, Co-K, Ni-K, Mo-K, Zr-K, and C-K lines.

Micro-cracking was also observed in the CM247LC NHf samples and had similar behavior (perpendicular to beam travel direction) and similar appearance (dendritic appearance on the fracture faces) to the standard alloy described in section 3.3. (Shown in Supplement Figures 12 and 13). The micro-crack density was significantly reduced. This point will be further developed in the next section.

Cracking behavior in the as-fabricated CM247LC NHf samples has also been studied using the same Gleeble test setup as in section 3.3. Analysis was performed to cover the full cross section and no new cracks or areas indicative of grain boundary melting were observed after the Gleeble experiment (Supplement Figure 14).

DSC measurements were performed on as-fabricated CM247LC NHf and CM247LC Condition 2 samples (Figure 10). Each thermogram is characterized by an exothermic reaction $T_{\gamma'}$, corresponding to the γ' dissolution, and two endothermic reactions which mark the carbide dissolution (T_C) and γ matrix melting (in the T_S-T_L range). The onset of melting is not sharply defined, more so in the CM247LC alloy. This phenomenon can be correlated to the dendritic segregation, which leads to incipient melting.

For the CM247LC NHf alloy, the liquidus endset point is measured at 1392 °C and the solidus point is estimated at 1341 °C. The CM247LC sample had a liquidus point of 1384 °C and a solidus of 1282 °C. The γ' solvus temperature of the CM247LC NHf sample was lowered compared to the CM247LC sample, 1226 °C and 1255 °C respectively, which could correlate with a lower equilibrium γ' phase fraction. The CM247LC NHf carbide dissolution temperature increased compared to the CM247LC samples, 1368 °C and 1341°C respectively. The solidification range measured by DSC may understate the solidification interval as the Gleeble experiment on CM247LC performed at 1250 °C showed the presence of grain boundary melting. However, the experimental conditions for the DSC setup may not be optimal for getting a signal from minor grain boundary melting.

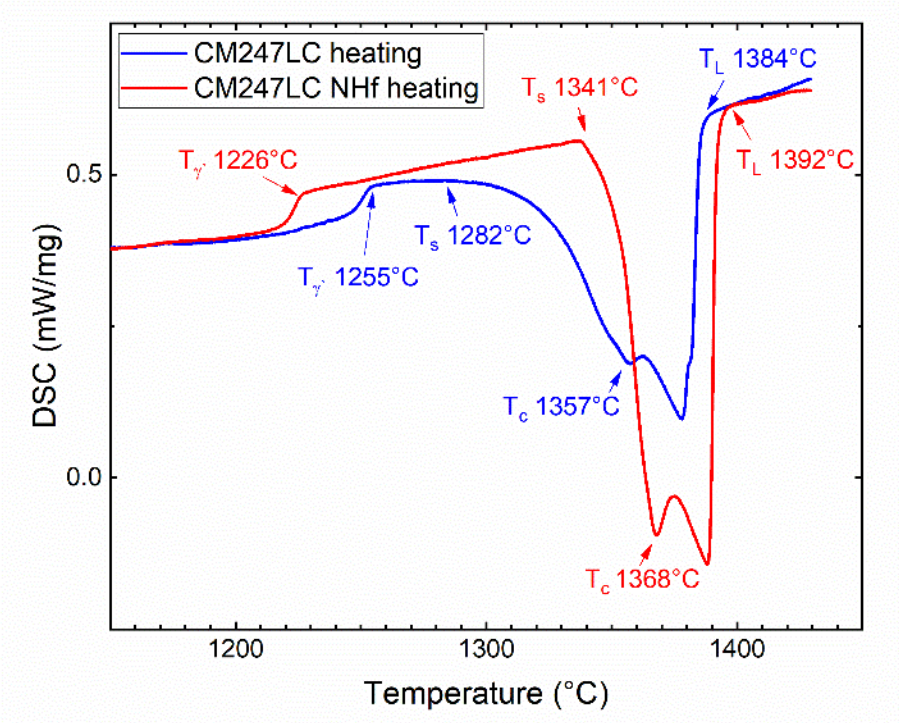

Figure 10: DSC thermograms on heating for both as-fabricated CM247LC and CM247LC NHf samples, built with Condition 2. $T_{\gamma'}$ is the γ`dissolution temperature, T_S is the solidus temperature, T_C is the carbide dissolution temperature, and T_L is the liquidus temperature.

5.2. Micro-Crack Density Comparisons

Optical images of parallel cross sections, showing representative micro-crack density, of as-fabricated CM247LC and CM247LC NHf produced with both Condition 1 and Condition 2 are shown in Figure 11. The results of the micro-crack density analysis are shown in Figure 12(a). Since micro-cracking was observed to be oriented at 0 and 90° to the image frame of the perpendicular cross section (Figure 5), the crack analysis of the parallel cross sections inherently exclude some cracks; however, the values are meant for comparison and the change in scanning direction after each layer ensures some homogeneity. The CM247LC, and CM247LC NHf samples fabricated with Condition 1 had mean crack densities of 1.27 mm/mm^2 and 0.81 mm/mm^2, respectively. The CM247LC, and CM247LC NHf samples fabricated with Condition 2 had mean crack densities of 0.12 and 0.03 mm/mm^2, respectively. A repeat experiment,

to ensure the validity of results, with Condition 2 parameters resulted in micro-crack densities of 0.14 and 0.02 mm/mm^2 for the CM247LC and CM247LC NHf, respectively. A Welch's unequal variances t-test was performed for each study to determine if the mean crack density between the CM247LC and CM247LC NHf were statistically different. The calculated *p* values, shown in Figure 12 (a), are all below 0.05, which is generally regarded as the threshold where one can say the difference in the means are statistically significant. The crack densities on the samples fabricated with Condition 1 were sufficiently high for crack length analysis. Histograms of the individual crack lengths from Condition 1 samples are shown in Figures 12(b) and 12(c). The mean crack length for both the CM247LC and CM247LC NHf samples is ~ 80 μm.

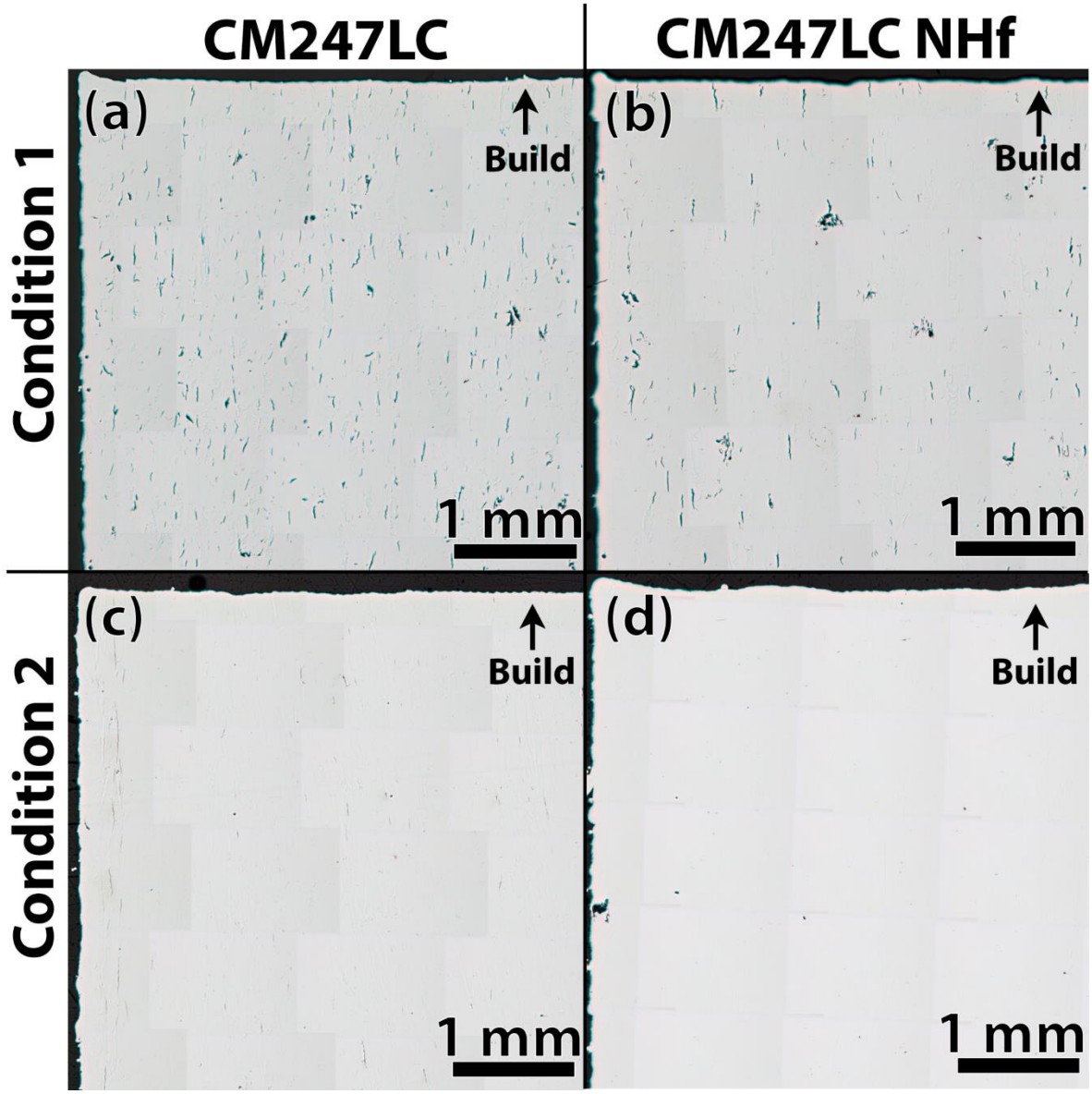

Figure 11: a) Optical image of CM247LC sample fabricated by Condition 1 b) Optical image from CM247LC NHf sample fabricated with Condition 1. c) Optical image of CM247LC fabricated by Condition 2. d) Optical image of the CM247LC NHf fabricated by Condition 2. Images of the entire cubes are shown in Supplement Figure 15.

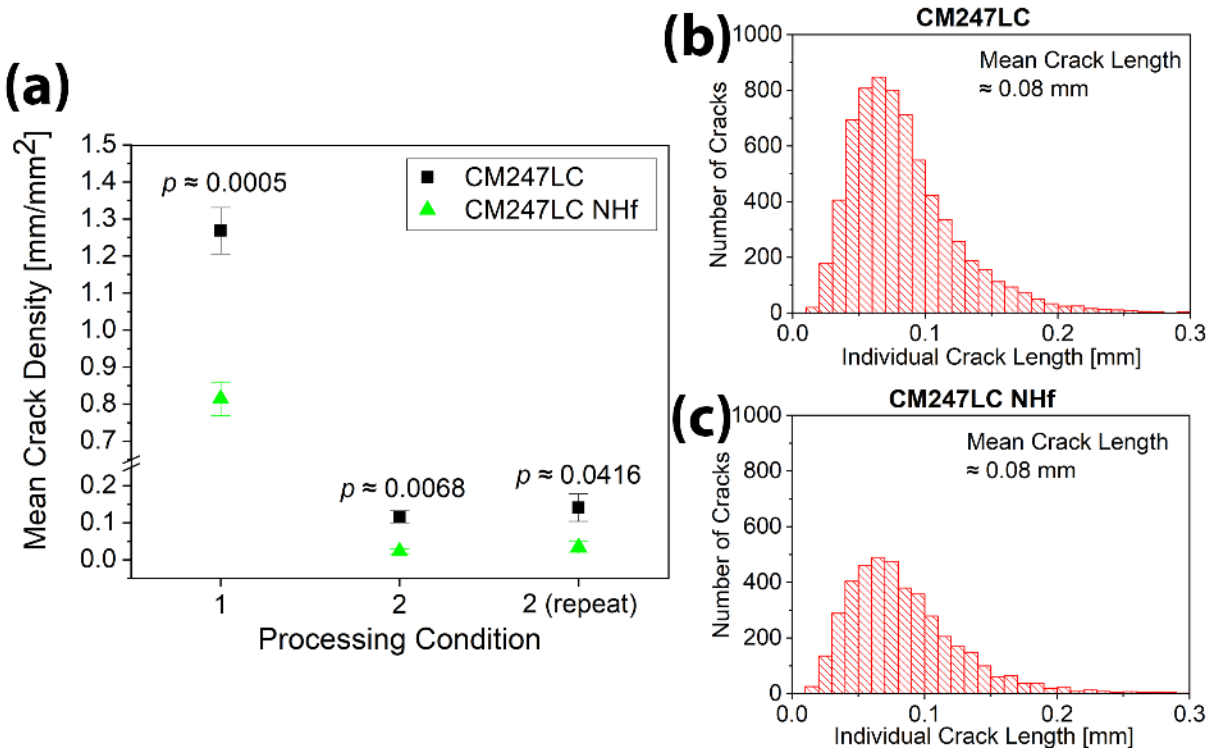

Figure 12: a) Mean micro-crack density. Error bars represent standard error of the mean. b,c) Crack length histogram of cracks observed in a parallel cross section of b) CM247LC and c) CM247LC NHf samples (Condition 1).

5.3. Discussion – reduction of cracking in CM247LC by alloy and process modification

The presented research highlights the importance of both alloy chemistry and processing conditions on micro-crack reduction of L-PBF fabricated γ` hardening Ni-base superalloys.

Samples fabricated with CM247LC NHf, when compared to the CM247LC samples, had a 36 % and 75 % reduction in crack density when fabricated using Condition 1 and Condition 2, respectively. The micro-cracks in the CM247LC NHf have a similar appearance to the micro-cracks in the CM247LC samples suggesting that solidification cracking is present in the modified alloy as well. Micro-crack length also did not change appreciably between the two alloys. Despite the reduction in the freezing range by removal of Hf, the alloy still has other alloying elements (Ti, Ta, Al, etc.) that partition to the liquid and increase the solidification range. The alloy CMSX-4, which is a derivative of CM247LC for single crystal use, does not contain Hf and is still susceptible to solidification cracking [9]. The Hf-free CM247LC alloy used in this study does have significantly higher levels of Zr (180 ppm compared to 60 ppm in the CM247LC alloy) which is known to contribute to hot cracking in these alloys. Reduction in the levels of B and Zr may reduce crack density further, but, again, may alter the creep performance of the alloy. The Gleeble test results show that the liquation cracking susceptibility of CM247LC NHf is lower than the CM247LC. The CM247LC NHf still likely suffers from liquation cracking, but the increased solidus temperature of the boundaries means that less of the HAZ will be affected. The presented results are thus strong evidence that modification of an alloy chemistry can reduce micro-

cracking but, in the case of CM247LC; alone cannot eliminate the cracking. Process optimization will be required in addition to alloy modification to achieve the lowest possible micro-crack densities.

The micro-crack density of samples fabricated with Condition 1 was nearly an order of magnitude higher than samples produced with Condition 2. Micro-cracks were uniformly distributed throughout the cross sections of the Condition 1 sample, but Condition 2 samples did have a higher incidence of micro-cracking near the edges. The contour offset for Condition 2 was 25 μm larger than the hatch distance, and this may have resulted (for reasons not yet known) in increased micro-cracking. Another potential explanation for the increased edge micro-cracking, is the existence of high tensile residual stresses at the part edges. It has been shown that tensile residual stresses are present in the top 1 mm of L-PBF fabricated CM247LC samples [14], and this may result in the opening of cracks more on the edge than the bulk. The two most significant observed differences between Condition 1 and Condition 2 are in the melt pool profiles and the fraction of HAGBs. While the melt pool widths were similar between the two conditions, Condition 1 melt pools were a factor of two deeper. Condition 1 had a depth/width ratio of ~0.6 and condition 2 had a ratio of ~0.3. Condition 1 samples also had a higher incidence of HAGBs compared to the Condition 2 samples. Both melt pool profile and grain boundary misorientation were discussed in section 4 as being factors that influence solidification cracking susceptibility. A narrow and deep melt pool is known to have a higher susceptibility to solidification cracking due to the increased level of restraint that is placed on the final solidification [23]. The melt pool dimensions will also influence the solidification conditions and the direction of columnar grain growth. As the melt pool aspect ratio increases (increasing depth), the misorientation between grains on opposite sides of the melt pool increases, thus leading to an increased amount of solidification cracking [26]. Other variables, such as the stress state, will be different between the two processing conditions, and will influence the solidification susceptibility; however, this was not characterized and the contribution to the overall susceptibility cannot be determined.

Tracking down the laser parameters that are the most responsible for producing a shallow and wide melt pool is challenging due to the large numbers of variables present (laser scan velocity, laser power, spot size, hatch distance, O_2 content, etc.). Simply increasing the laser scan velocity may lower the interaction time enough that the transition from conduction mode to keyhole (or transition mode) is avoided. A decrease of the laser spot radius, r, while keeping laser power, P, constant, will result in a higher laser intensity, which is shown by Eq. 3:

$$I = \frac{P_L}{\pi r^2} \tag{3}$$

that may result in vaporization (keyhole formation) instead of melting. The laser intensity of Condition 1 and Condition 2 is 3.14×10^6 W/cm^2, and 7.35×10^6 W/cm^2 respectively; however, Condition 1, not Condition 2, led to keyhole melting. In order to simplify the comparisons between the two processing

conditions the normalized enthalpies were calculated (Table 2). The normalized enthalpy of Condition 2 (43.15) is higher than Condition 1 (26.34), suggesting that Condition 2 would be more favorable to keyhole formation; however, the opposite behavior is observed. One hypothesis for this behavior is based on the influence of in-process preheating.

There are several differences between the two commercial AM machines used in this study, such as, thermal mass, recoating time, sample size, and construction of machine modifications that would result in drastically different thermal conditions. The Condition 1 fabricated samples were fabricated on a machine with a much larger thermal mass (a larger amount of metallic parts are required to hold and move a 245 × 245 mm build plate) than the Condition 2 fabricated samples. The recoating time (time between laser scans) is generally longer for the Condition 1 samples than the Condition 2 samples, which would provide additional time for heat dissipation. The aluminum support structure used to hold the reduced build platform for the fabrication of Condition 1 samples would further dissipate heat. Lastly, the larger sample sizes of the Condition 1 fabricated samples would increase the thermal mass of the system. Also considering the higher normalized enthalpies of Condition 2, it can be assumed that the Condition 2 fabricated samples had a higher level of preheat than the Condition 1 fabricated samples.

A simple experiment highlighting the influence of preheat on melt pool geometry is shown in Fig. 13. Fig. 13 shows an optical image of an etched Condition 2 fabricated sample (Fig. 13(a)) and an optical image of an etched Condition 2 fabricated sample with a 60 s cooling period added between each layer (Fig. 13(b)). While no quantifiable data was gathered, it is a safe assumption that the 60 s time delay resulted in a lower baseline temperature, in other words, lower preheating, than the standard processing route. Interestingly, the "colder" sample showed extensive signs of keyhole formation (Fig. 13). This behavior is somewhat counter-intuitive as a material with a higher starting temperature will require less absorbed enthalpy for vaporization (keyhole formation). One possible explanation for the keyhole formation in the "colder" sample is related to the thermal diffusivity. Aune et al. [19] reported thermal diffusivities in CMSX-4, a similar Ni-base superalloy, of ~0.025 cm^2/s and ~0.050 cm^2/s at ~300 K and at ~1500 K, respectively. A higher pre-heat in the standard process will result in a higher thermal diffusivity that may inhibit keyhole formation. Indeed, per the normalized enthalpy in Eq. 2 and using the extremes of thermal diffusivities listed above, the normalized enthalpy for the low diffusivity case (~0.025 cm^2/s) is 54.6 and for the high thermal diffusivity case (~0.050 cm^2/s) is 38.6. The higher normalized enthalpy of the "colder" condition may be sufficiently high enough that keyhole formation occurred. King et al. [34] reported the threshold for keyhole formation to be at a normalized enthalpy of 30 ± 4; however, it is plausable that the threshold for the conditions in this study is higher. It is important to note that once the threshold to keyhole mode melting is crossed the absorptivity and therefore the normalized enthalpy will greatly increase.

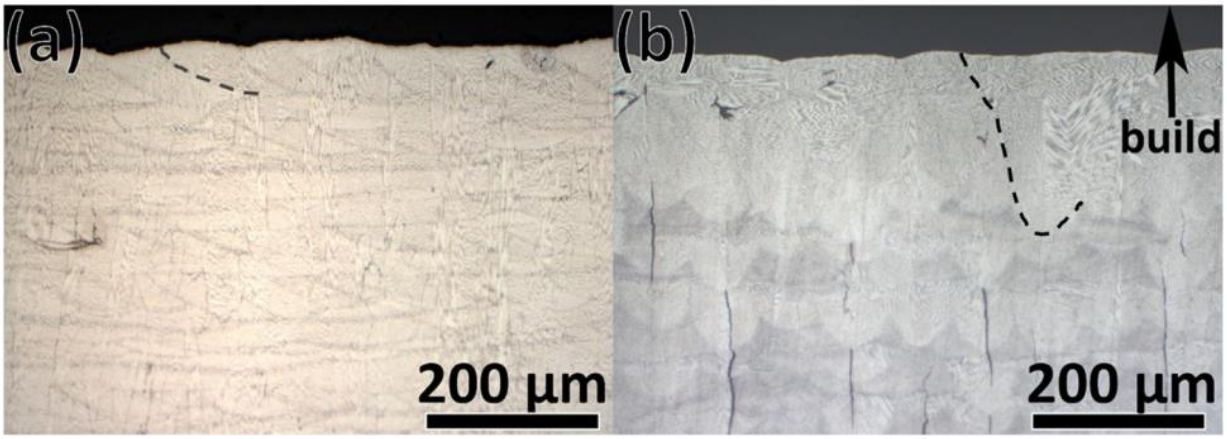

Figure 13. (a) Optical image of an etched Condition 2 fabricated sample (b) Optical image of an etched Condition 2, with 60 s delay, fabricated sample. Dashed lines highlight the melt pools.

It is hypothesized that the combination of the aforementioned factors led to a higher baseline temperature for the Condition 2 fabricated samples that resulted in a higher thermal diffusivity that favored lower crack density conduction mode melts. In addition, an increase in preheat would result in lower thermal residual stress, which may contribute to the lower micro-crack density of the Condition 2 fabricated samples.

Considering the spot size of Condition 2, 55 µm, the melt pool width, 180 µm, appears to be abnormally wide for a conduction mode melt. The reason for this wide and shallow melt pool, in regards to spot size, is likely due to the heat transfer mechanism that is dominant for this material. A useful dimensionless number to look at when considering heat transfer properties of a material is the Prandtl number, Eq. 4:

$$P_r = \frac{C_p \mu}{k} \tag{4}$$

where k is the thermal conductivity, C_p is the specific heat, and µ is the viscosity of the fluid. Using values for liquid Ni-base superalloys at a temperature of 1580 °C (CMSX4: k = 0.328 WK^{-1} cm^{-1}, Cp = 0.70 JK^{-1} g^{-1}, IN738LC: µ = 7.4 mPa s) [19] a Prandtl number of 0.18 was obtained. The higher Prandtl number, the more convection based heat transfer [35]. For instance, the Prandtl number for aluminum is 0.02, which means conduction dominates the heat transfer and the melt pools of Al will be more hemispherical [36]. The Prandtl number for stainless steels is 0.16, meaning that a flatter melt pool will result. Convective flow in a laser melt pool is largerly the result of surface tension driven flow and the extent of this flow will influence the melt pool profile as well. Anderson et al [37] also observed wide and shallow melt pools on electron beam and laser welded CMSX-4 and attributed this behavior to the surface tension driven fluid flow from the center of the weld to the edges.

A high pre-heat temperature can result in the modification of the convective heat transfer in the melt pool. Two dimensionless numbers which can describe melt pool profiles in laser welds are the Peclet and Marangoni numbers [36,38]. The Peclet number is the ratio of heat transfer by convection over conduction and is mathematically given by Eq. 5:

$$P_e = \frac{LV}{\alpha} \tag{5}$$

where L is the characteristic length (radius of melt pool), V is the characteristic velocity (Marangoni flow velocity), and α is the thermal diffusivity. When the Peclet number is much greater than 1, heat transfer via convection dominates, and when it is much less than one, heat transfer via conduction dominates. The Marangoni number is a measure of the amount of surface tension driven flow in the system and is given by Eq. 6 :

$$M_a = \frac{-\frac{\partial y}{\partial T}(\Delta T)L}{\mu\alpha} \tag{6}$$

Where $\frac{\partial y}{\partial T}$ is the temperature dependence of the surface tension, ΔT is the temperature difference from the center to the edge of the melt pool, L is the radius of the melt pool surface, μ is the viscosity, and α is the thermal diffusivity of the liquid [36]. As the Marangoni number is a measure of the amount of surface tension driven flow, it can be related to the characteristic velocity of Eq. 4. The viscosity of liquid CM247LC decreases with an increase in temperature [19]. The higher baseline temperature of the Condition 2 fabricated samples may result in a melt with a lower viscosity that would increase the Marangoni number (assuming $\Delta T$and α in the liquid is unchanged), per Eq. 6, and increase the Peclet number per Eq. 5. A higher Peclet number, due to the increased surface tension driven flow, indicates that convective heat transfer becomes more important, which would result in a wider melt pool. Since the major difference between the Condition 1 and Condition 2 melt pools is the melting mode (conduction vs. keyhole) and not simply a wider conduction mode melt, it is hypothesized that the differences in absorbed enthalpy and not the magnitude of convection are the primary responsible factors.

As previously mentioned, removal of any element will have implications for the alloy`s mechanical behavior and thus will need to be evaluated. Aside from the micro-crack reduction, three differences were observed when comparing the as-fabricated CM247LC and CM247LC NHf: (i) the CM247LC NHf sample had some script-like carbides on the cell boundaries, (ii) the γ`solvus temperature for the CM247LC NHf was reduced by 29 °C, and (iii) a decrease in lattice parameter of the CM247LC NHf sample due to the absence of Hf. Mechanical property tests will be conducted for both alloys in a future study to understand what changes the elimination of Hf causes in CM247LC.

6. Conclusions

A reduction in micro-cracking was observed in the modified CM247LC, CM247LC NHf. The removal of Hf, a melting point depressant, reduces the solidification range of the alloy, and thus mitigates both solidification and liquation cracking of the heat-affected zone during fabrication. Additionally, the use of different machines, translated into differences in process parameters, was shown to be critical on mitigating the micro-cracking. Tight control on chemistry and processing is thus needed to produce defect-free parts. Particularly, the following conclusions were reached:

- The as-fabricated CM247LC samples have a columnar grain microstructure that is oriented parallel to the build direction. The columnar grain are composed of cells ∼1 μm in diameter. The cell boundaries contain precipitates (∼ 55 μm in diameter) that are assumed to be carbides. The cell boundaries also have an increased dislocation density.

- Micro-cracking in CM247LC was attributed to both solidification and liquation cracking. The dendritic appearance of the micro-crack surfaces is indicative of fracture in the liquid phase and thus can be identified as solidification cracking. The Gleeble experiments showed that a liquation cracking mechanism is most likely active in the HAZ.

- Processing Condition 2 resulted in a lower micro-crack density compared to processing Condition 1. The melt pool profile of Condition 2 (shallow and wide) is far less susceptible to solidification cracking due to lower restraint and fewer HAGBs.

- It is hypothesized that the wider and shallower melt pools of Condition 2 are the result of in-process preheating that increased the thermal diffusivity of the sample enough that keyhole formation was avoided.

- A new Hf-Free version of CM247LC, CM247LC NHf, was developed to mitigate micro-cracking of CM247LC via solidification range reduction. Samples fabricated with CM247LC NHf had between 36%–75% reduction in crack density, depending on the condition used, compared to the CM247LC alloy.

Declaration of competing interests

All authors declare that they have no competing interests

Acknowledgements

The authors would like to acknowledge the Competence Center for Materials Science and Technology (CCMX) for financial support, as well as the Swiss industrial consortium associated to the project. The authors would also like to acknowledge Dr. Dieter Sporer and Dr. Thomas Etter for their support during the project. HGT, JJ and REL are thankful for the generous support of PX Group to the LMTM laboratory.

References

[1] D. Thomas, S. Gilbert, Costs and Cost Effectiveness of Additive Manufacturing, (2014),https://doi.org/10.6028/NIST.SP.1176.

[2] M. Donachie Jr., S. Donachie, Superalloys: a Technical Guide, (2002) http://search.ebscohost.com/login.aspx?direct=true&site=edslive&db=edsnop&AN=edsnop.I000004077928.00.

[3] J.N. DuPont, S.D. Kiser, J.C. Lippold, Welding Metallurgy and Weldability of NickelBase Alloys, Wiley,Hoboken,NJ,2009,http://search.ebscohost.com/login.aspx?direct=true&AuthType=ip&db=nlebk&AN=289303&site=ehostlive.

[4] S. Kou Verfasser, Welding Metallurgy, (2003) https://search.ebscohost.com/login.aspx?direct=true&AuthType=ip&db=edsbvb&AN=edsbvb.BV016548906&site=eds-live.

[5] L.N. Carter, C. Martin, P.J. Withers, M.M. Attallah, The influence of the laser scan strategy on grain structure and cracking behaviour in SLM powder-bed fabricated nickel superalloy, J. Alloys. Compd. 615(2014),338–347,https://doi.org/10.1016/j.jallcom.2014.06.172.

[6] X. Wang, L.N. Carter, B. Pang, M.M. Attallah, M.H. Loretto, Microstructure and yield strength of SLM-fabricated CM247LC Ni-Superalloy, Acta Mater. 128 (2017) 87–95,https://doi.org/10.1016/j.actamat.2017.02.007.

[7] V.D. Divya, R. Muñoz-Moreno, O.M.D.M. Messé, J.S. Barnard, S. Baker, T. Illston, H.J. Stone, Microstructure of selective laser melted CM247LC nickel-based superalloy and its evolution through heat treatment, Mater. Charact. 114 (2016) 62–74,https://doi.org/10.1016/j.matchar.2016.02.004.

[8] M. Cloots, P.J. Uggowitzer, K. Wegener, Investigations on the microstructure and crack formation of IN738LC samples processed by selective laser melting using Gaussian and doughnut profiles, Mater. Des. 89(2016)770–784,https://doi.org/10.1016/j.matdes.2015.10.027.

[9] E. Chauvet, P. Kontis, E.A. Jägle, B. Gault, D. Raabe, C. Tassin, J.-J. Blandin, R. Dendievel, B. Vayre, S. Abed, G. Martin, Hot cracking mechanism affecting a nonweldable Ni-based superalloy

produced by selective electron Beam Melting, Acta Mater. 142 (2018) 82–94, https://doi.org/10.1016/j.actamat.2017.09.047.

[10] M. Ramsperger, R.F. Singer, C. Körner, Microstructure of the nickel-base superalloy CMSX-4 fabricated by selective Electron beam melting, Metall. Mater. Trans. A. 47 (2016) 1469–1480, https://doi.org/10.1007/s11661-015-3300-y.

[11] Y.S. Lee, M.M. Kirka, S. Kim, N. Sridharan, A. Okello, R.R. Dehoff, S.S. Babu, Asymmetric cracking in Mar-M247 alloy builds during Electron beam powder bed fusion additive manufacturing, Metall. Mater. Trans.A.49(2018)5065–5079,https://doi.org/10.1007/s11661-018-4788-8.

[12] L.N. Carter, M.M. Attallah, R.C. Reed, Laser powder bed fabrication of nickel-Base superalloys: influence of parameters; Characterisation, quantification and mitigation of cracking, Superalloys 2012, John Wiley & Sons, Inc., 2012, pp. 577–586, https://doi.org/10.1002/9781118516430.ch64.

[13] Y.-C. Hagedorn, J. Risse, W. Meiners, N. Pirch, K. Wissenbach, R. Poprawe, Processing of Nickel Based Superalloy MAR M-247 by Means of High Temperature - Selective Laser Melting (HT - SLM), (2014),pp.291–295,https://www.scopus.com/inward/record.uri?eid=2 s2.084892160456&partnerID=40&md5=62302042d538a33753c4a18268898c63.

[14] N. Kalentics, N. Sohrabi, H.G. Tabasi, S. Griffiths, J. Jhabvala, C. Leinenbach, A. Burn, R.E. Logé, Healing cracks in selective laser melting by 3D laser shock peening, Addit. Manuf. (2019) 100881, , https://doi.org/10.1016/j.addma.2019.100881.

[15] N.J. Harrison, I. Todd, K. Mumtaz, Reduction of micro-cracking in nickel superalloys processed by Selective Laser Melting: a fundamental alloy design approach, Acta Mater. 94 (2015) 59–68, https://doi.org/10.1016/j.actamat.2015.04.035.

[16] R. Engeli, T. Etter, S. Hövel, K. Wegener, Processability of different IN738LC powder batches by selective laser melting, J. Mater. Process. Technol. 229 (2016) 484–491, https://doi.org/10.1016/j.jmatprotec.2015.09.046.

[17] D.B. Hann, J. Iammi, J. Folkes, A simple methodology for predicting laser-weld properties from material and laser parameters, J. Phys. Appl. Phys. 44 (2011) 445401, , https://doi.org/10.1088/0022-3727/44/44/445401.

[18] A.M. Rubenchik, W.E. King, S.S. Wu, Scaling laws for the additive manufacturing, J. Mater. Process. Technol.257(2018)234–243,https://doi.org/10.1016/j.jmatprotec.2018.02.034.

[19] R.E. Aune, L. Battezzati, R. Brooks, I. Egry, H.-J. Fecht, J.-P. Garandet, M. Hayashi, K.C. Mills, A. Passerone, P.N. Quested, E. Ricci, F. Schmidt-Hohagen, S. Seetharaman, B. Vinet, R.K. Wunderlich, Thermophysical properties of IN738lc, MM247lc and CMSX-4 in the liquid and high temperature solid

phase, Superalloys 718 625 706 Deriv. Proc. (2005), pp. 467–476 (Accessed October 14, 2011), http://urn.kb.se/resolve?urn=urn:nbn:se:kth:diva-43342.

[20] R. Przeliorz, J. Piatkowski, Thermophysical properties of nickel-based cast Superalloys, Metalurgija. 54 (2015) 543–546.

[21] C.A. Schneider, W.S. Rasband, K.W. Eliceiri, NIH Image to ImageJ: 25 years of image analysis, Nat. Methods9,(2012) 671.

[22] J. Xu, X. Lin, Y. Zhao, P. Guo, X. Wen, Q. Li, H. Yang, H. Dong, L. Xue, W. Huang, HAZ liquation cracking mechanism of IN-738LC superalloy prepared by laser solid forming, Metall. Mater. Trans. A. 49 (2018),5118–5136,https://doi.org/10.1007/s11661-018-4826-6.

[23] J.C. Lippold, Welding Metallurgy and Weldability, (2015) http://www.books24x7.com/marc.asp?bookid=63808.

[24] G. Matache, D.M. Stefanescu, C. Puscasu, E. Alexandrescu, Dendritic segregation and arm spacing in directionally solidified CMSX-4 superalloy, Int. J. Cast Met. Res. 29 (2016) 303–316, https://doi.org/10.1080/13640461.2016.1166726.

[25] T. Pollock Sammy, Nickel-based superalloys for advanced turbine engines: chemistry, microstructure and properties, J.Propuls. Power.22 (2006) 361–374.

[26] S. Kou, Solidification and liquation cracking issues in welding, JOM 55 (2003) 37–42, https://doi.org/10.1007/s11837-003-0137-4.

[27] J.-W. Park, J.M. Vitek, S.S. Babu, S.A. David, Stray grain formation, thermomechanical stress and solidification cracking in single crystal nickel base superalloy welds, Sci. Technol. Weld. Join. 9 (2004) 472–482, https://doi.org/10.1179/136217104225021841.

[28] B. Hu, I.M. Richardson, Mechanism and possible solution for transverse solidification cracking in laser welding of high strength aluminium alloys, Mater. Sci. Eng. A. 429 (2006) 287–294, https://doi.org/10.1016/j.msea.2006.05.040.

[29] N. Wang, S. Mokadem, M. Rappaz, W. Kurz, Solidification cracking of superalloy single- and bi-crystals, Acta Mater. 52 (2004) 3173–3182, https://doi.org/10.1016/j.actamat.2004.03.047.

[30] J.H. Martin, B.D. Yahata, J.M. Hundley, J.A. Mayer, T.A. Schaedler, T.M. Pollock, 3D printing of high-strength aluminium alloys, Nature 549 (2017) 365–369.

[31] Superalloys : Alloying and Performance, (2010) (Accessed October 7, 2019), http://search.ebscohost.com/login.aspx?direct=true&db=nlebk&AN=395922&site=eds-live.

[32] J. Zhang, R.F. Singer, Effect of grain-boundary characteristics on castability of nickel-base superalloys, Metall. Mater. Trans. A. 35 (2004) 939–946, https://doi.org/10.1007/s11661-004-0018-7.

[33] K. Heck, R. Blackford, R.F. Singer, Castability of directionally solidified nickel base superalloys, Mater. Sci. Technol. 15 (1999) 213–220, https://doi.org/10.1179/026708399101505617.

[34] W.E. King, H.D. Barth, V.M. Castillo, G.F. Gallegos, J.W. Gibbs, D.E. Hahn, C. Kamath, A.M. Rubenchik, Observation of keyhole-mode laser melting in laser powder-bed fusion additive manufacturing, J. Mater. Process. Technol. 214 (2014) 2915–2925, https://doi.org/10.1016/j.jmatprotec.2014.06.005.

[35] J. Mazumder, CHAPTER 3 - laser welding, in: M. BASS (Ed.), Mater. Process. Theory Pract. Elsevier, 1983, pp. 113–200,https://doi.org/10.1016/B978-0-444-86396- 6.50009-X.

[36] C. Limmaneevichitr, S. Kou, Experiments to simulate effect of Marangoni convection on weld pool shape, Weld. J. 79 (2000) 231S–237S.

[37] T.D. Anderson, J.N. DuPont, T. DebRoy, Origin of stray grain formation in singlecrystal superalloy weld pools from heat transfer and fluid flow modeling, Acta Mater. 58 (2010) 1441–1454, https://doi.org/10.1016/j.actamat.2009.10.051.

[38] A. Robert, T. Debroy, Geometry of laser spot welds from dimensionless numbers, Metall. Mater. Trans. B. 32 (2001) 941–947, https://doi.org/10.1007/s11663-001-0080-0.

Supplementary Material

Combining Alloy and Process Modification for Micro-crack Mitigation in an Additively Manufactured Ni-base Superalloy

S. Griffiths[1], H.G. Tabasi[2], T. Ivas[2], A. De Luca[1], K. Zweiacker[1], R. Wrobel[1], J. Jhabvala[2], R.E. Logé[2], C. Leinenbach[1]

1. Empa-Swiss Federal Laboratories for Materials Science and Technology, Laboratory for Advanced Materials Processing, Überlandstrasse 129, 8600 Dübendorf, Switzerland
2. Thermomechanical Metallurgy Laboratory – PX Group Chair, Ecole Polytechnique Federale de Lausanne (EPFL), CH/2002 Neuchatel, Switzerland

The Gleeble 38000 is a thermomechanical simulation system. In this machine, high-speed compressive and tensile tests can be performed. The samples are heated by Joule effect under vacuum and the temperature is screened with thermocouples welded at the surface of the samples. High heating rates can be achieved with the Joule effect heating. Physical simulation is the exact reproduction of the thermal and mechanical processes in the laboratory that a material is subjected to during the manufacturing process or end use. Physical simulation is a valuable tool used to study metallurgical processes, develop new materials and replicate real world conditions in the laboratory. Supplement Figure 1 display the Gleeble machine, test setup, and temperature and cooling rate used in this study.

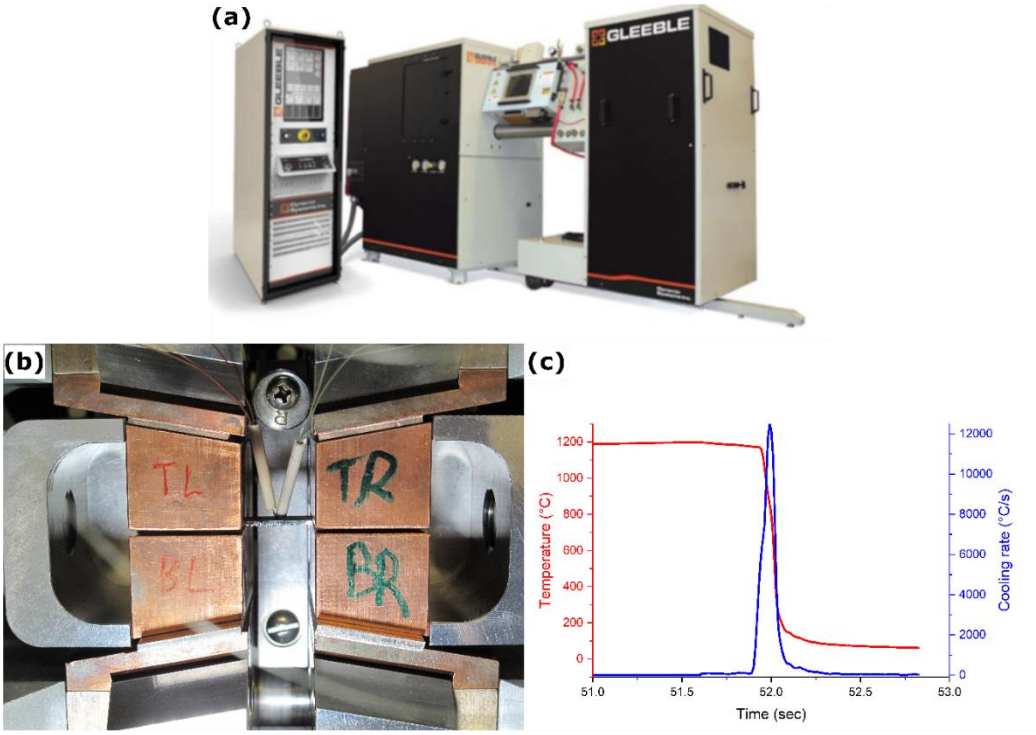

Supplement Figure 1: a) Gleeble 3800 machine, b) physical simulation of the HAZ Test setup of the Gleeble experiments, and c) monitored temperature and cooling rate during the experiments.

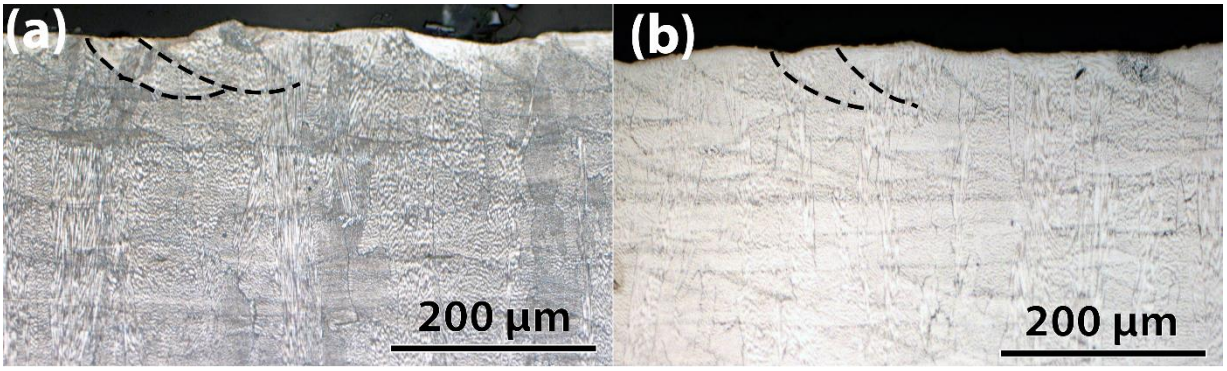

Supplement Figure 2: Optical images, with highlighted melt pools (dashed lines) on etched, as-fabricated CM247LC samples, produced using a) Machine 2 with a 100 mm diameter build plate b) Machine 2 with a 34.5 mm diameter build plate. No significant differences in melt pool dimensions were observed.

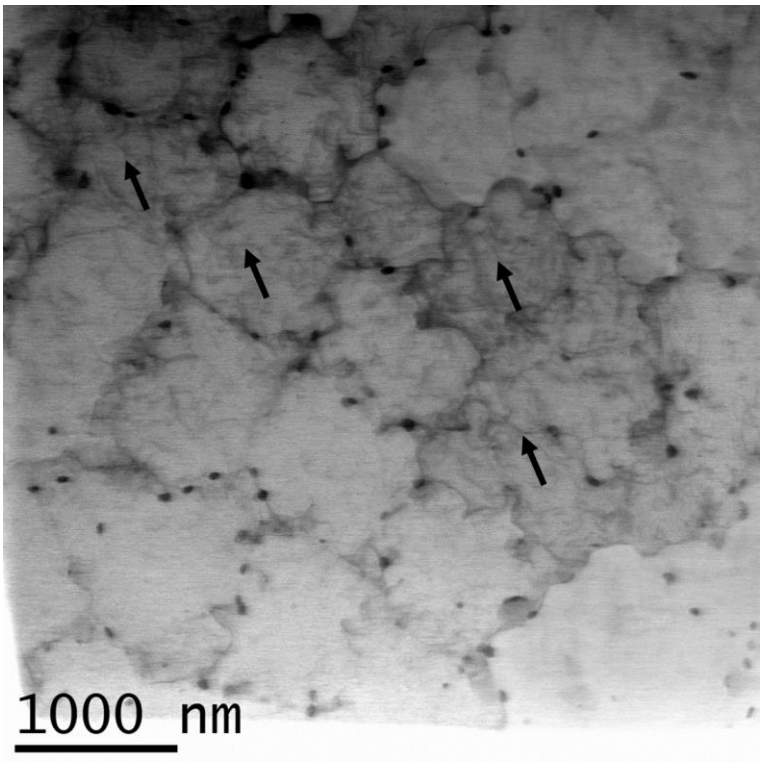

Supplement Figure 3: BF-STEM image of the as-fabricated CM247LC sample showing a high dislocation density over a larger area. Black arrows point to dislocations.

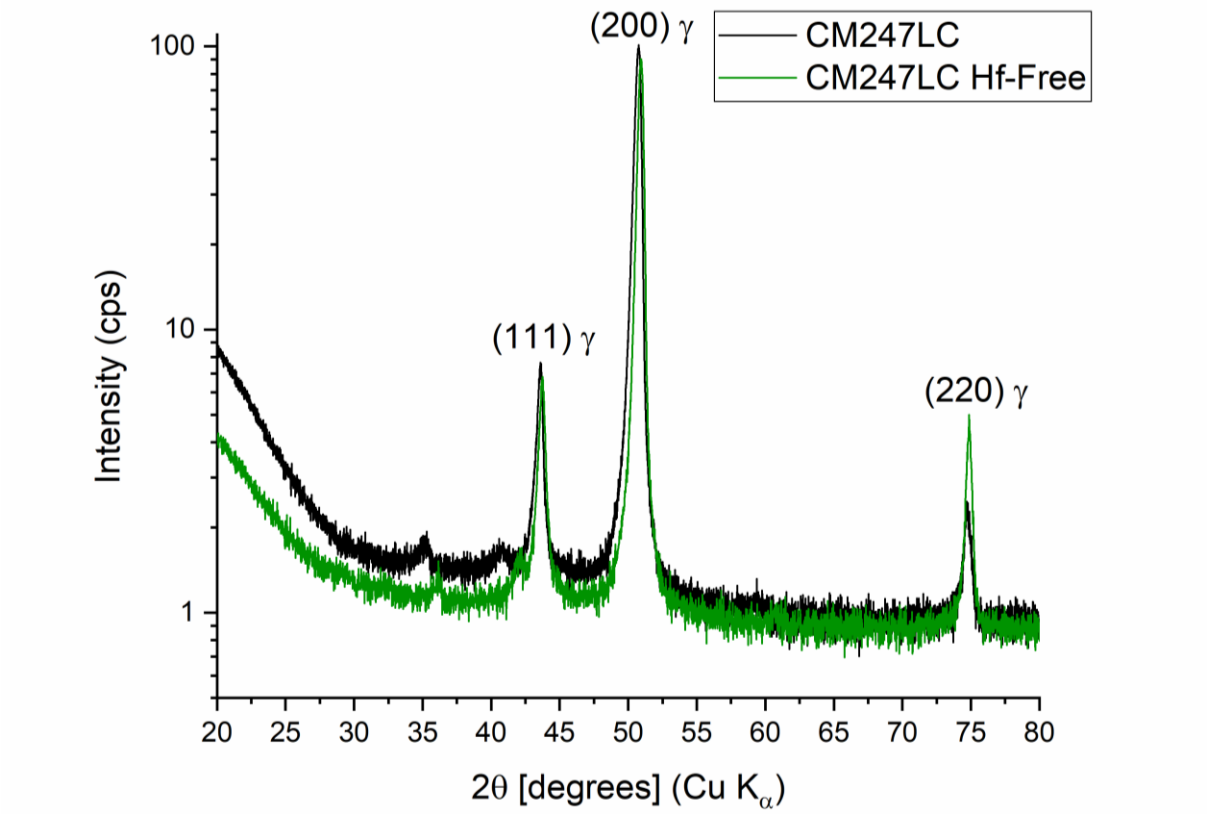

Supplement Figure 4: XRD patterns of as-fabricated CM247LC and CM247LC NHf. Samples were fabricated on Machine 2 with build plate of 100 mm diameter. Small peaks around 35° and 40° may correspond to the carbides. A slight peak shift between the two samples is likely the result of lattice parameter changes caused by the elimination of Hf.

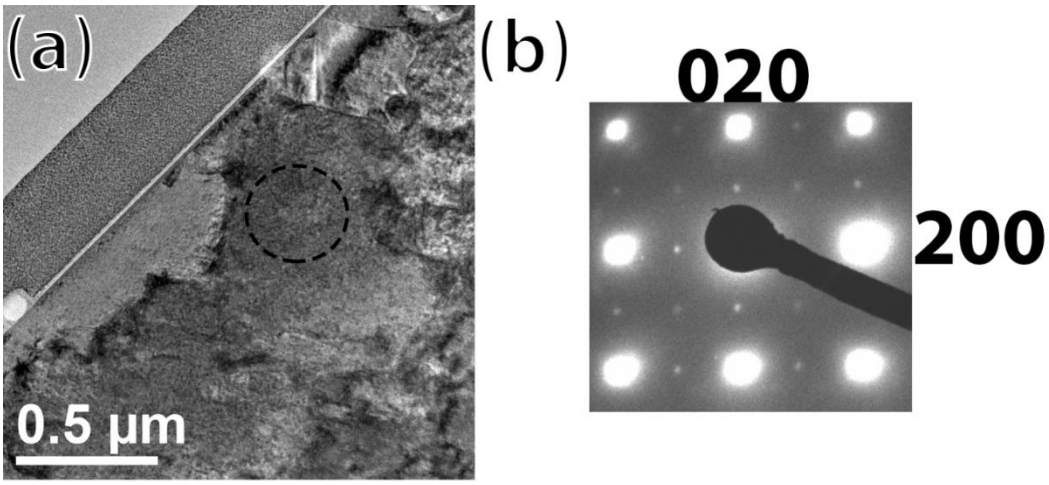

Supplement Figure 5: a) A low magnification BF-TEM image of the as-fabricated CM247LC sample, presented in Figure 2 (Machine 2). (b) Selected area diffraction pattern along a [001] zone axis, acquired from the circled area in a) showing the 100- and 110-type superlattice reflections of the $L1_2$ structure.

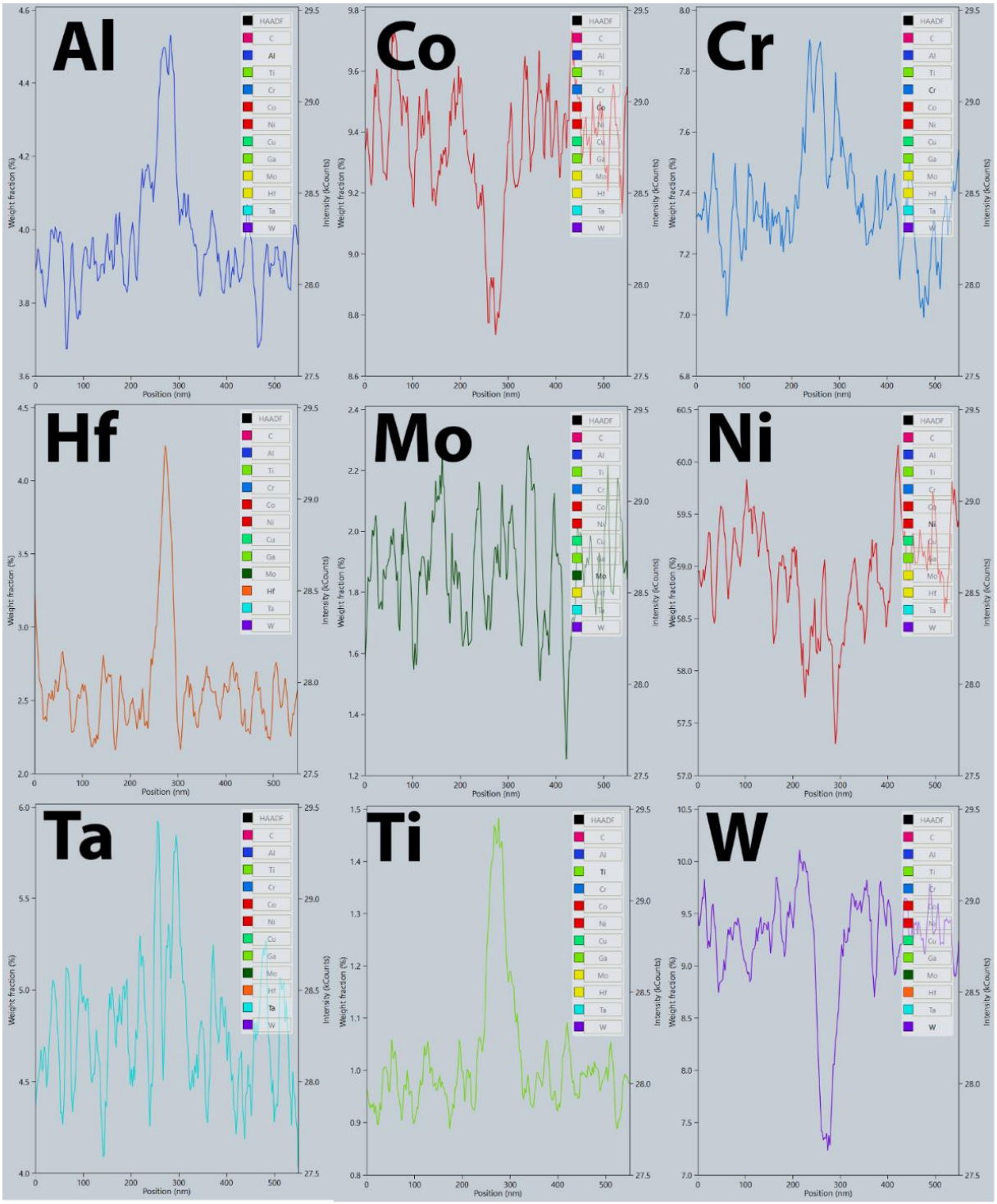

Supplement Figure 6: STEM-EDX line profile (averaged over the line width) quantification data taken from the region highlighted by the white box in Figure 2c. Chemical analysis performed with Al-K, Ti-K, Cr-K, Hf-L, Ta-L, W-L, Co-K, Ni-K, Zr-K, C-K lines

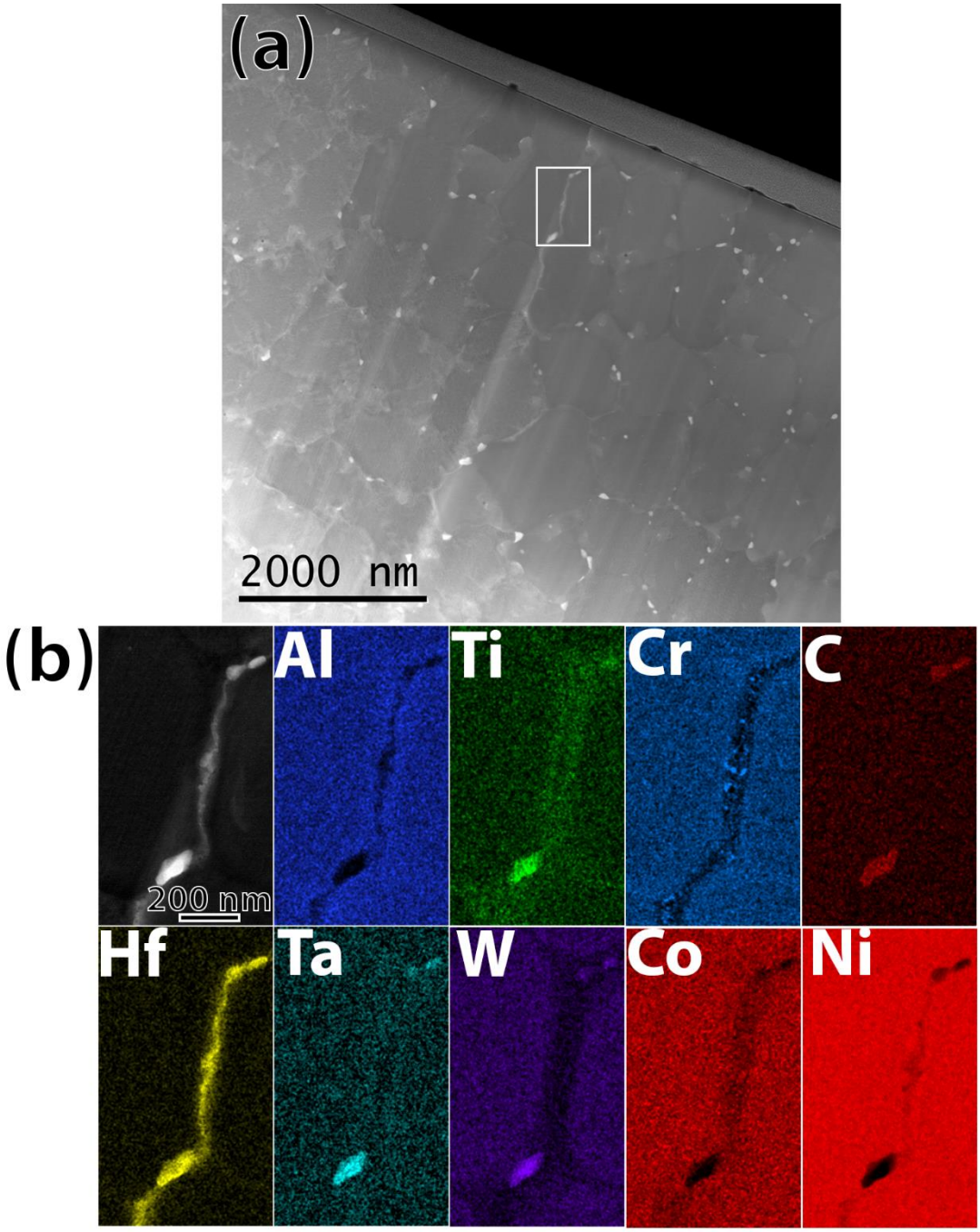

Supplement Figure 7: STEM analysis of the as-fabricated CM247LC microstructure of a transverse section of a Machine 2 (100 mm) fabricated sample. a) ADF-STEM image showing a grain boundary enriched with elevated levels of Hf (white box). b) STEM-EDX map of region highlighted by the white box in a). Chemical analysis performed with Al-K, Ti-K, Cr-K, Hf-L, Ta-L, W-L, Co-K, Ni-K, C-K lines.

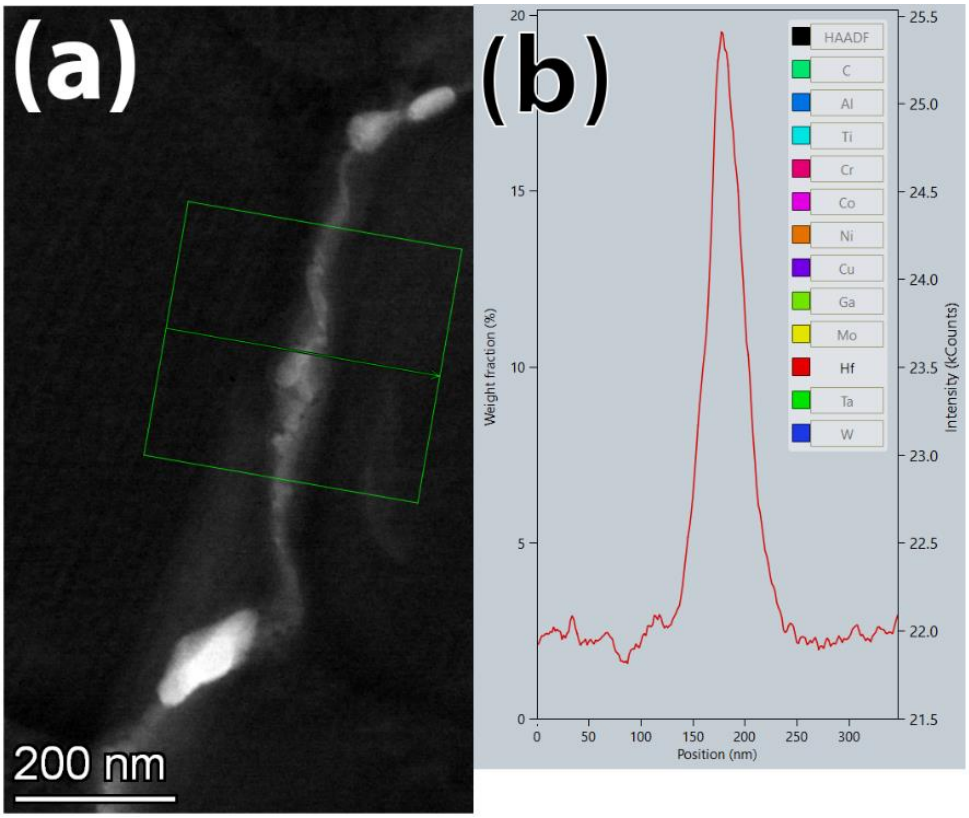

Supplement Figure 8: a) ADF-STEM image of the boundary shown in Supplement Figure 7. The green box highlights the region used for the STEM-EDX line profile. b) STEM-EDX line profile (averaged over the width) of the boundary in a). Hf enrichment on the boundary approaches 20 wt.%. Chemical analysis performed with the Hf-L lines.

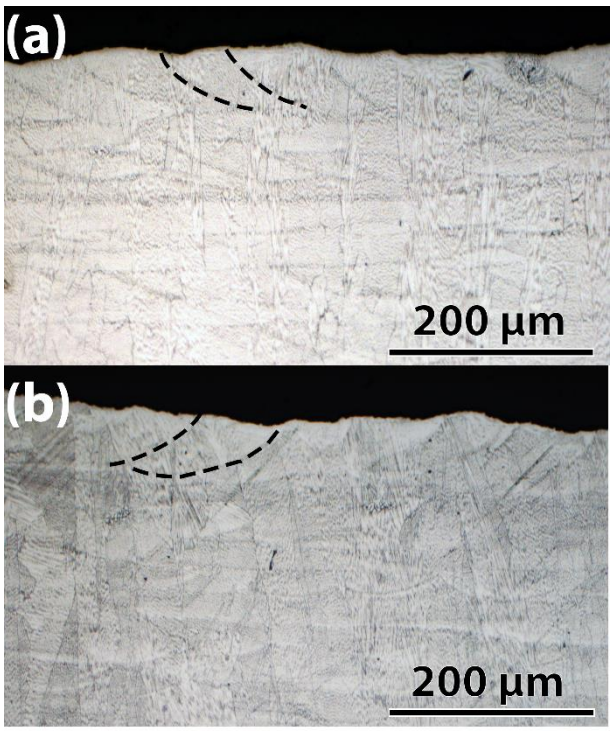

Supplement Figure 9: Condition 2 Samples (a) Optical image of etched CM247LC sample (b) Optical image of etched CM247LC NHf sample.

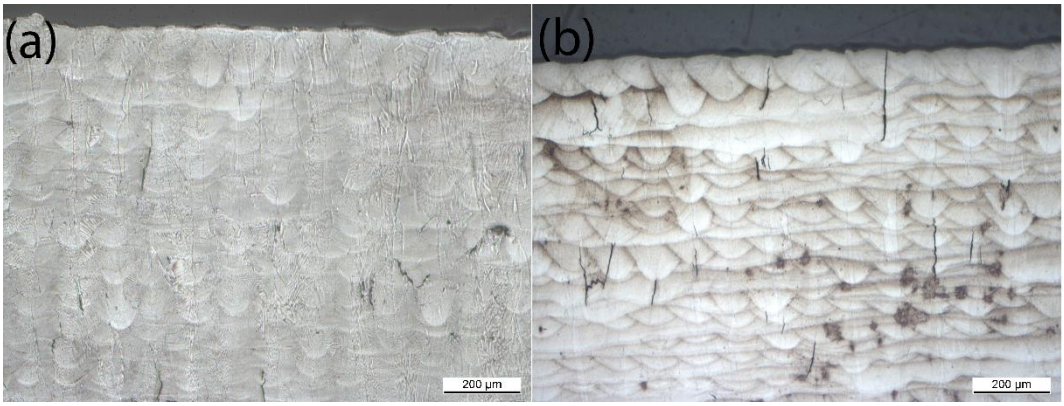

Supplement Figure 10: Condition 1 Samples (a) Optical image of etched CM247LC sample (b) Optical image of etched CM247LC NHf sample.

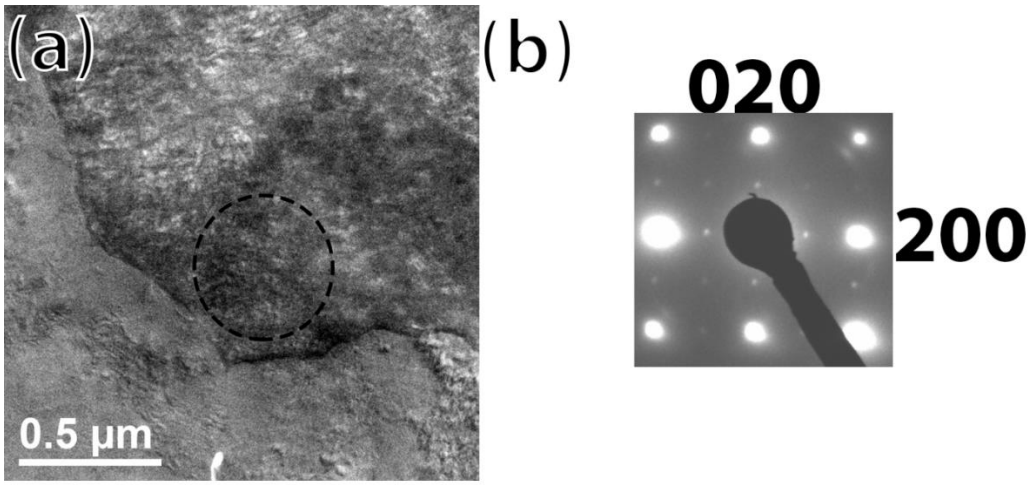

Supplement Figure 11: a) A low magnification BF-TEM image of the as-fabricated CM247LC NHf sample presented in Figure 8 (Machine 2). b) Selected area diffraction pattern along [001] taken from the circled region in a) showing the 100- and 110-type superlattice reflections of the $L1_2$ structure.

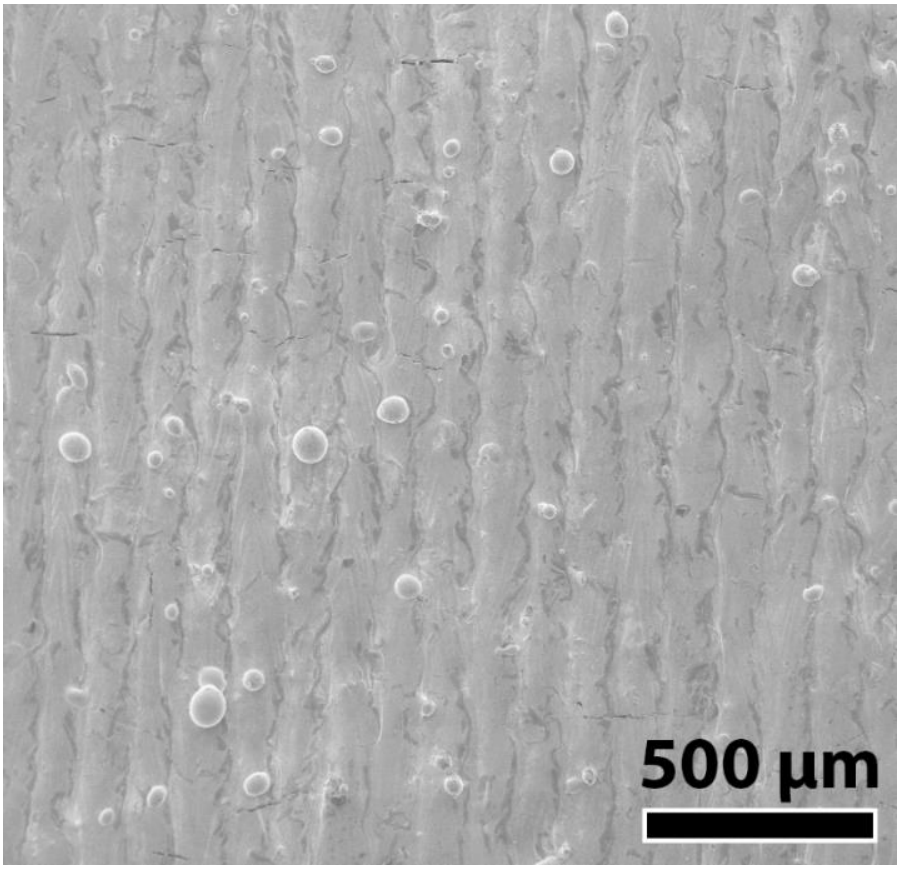

Supplement Figure 12: SE image of the top surface of a CM247LC NHf as-fabricated cube (Condition 1) (unidirectional scanned sample with no change in direction of layers). Cracking is transverse to direction of laser travel.

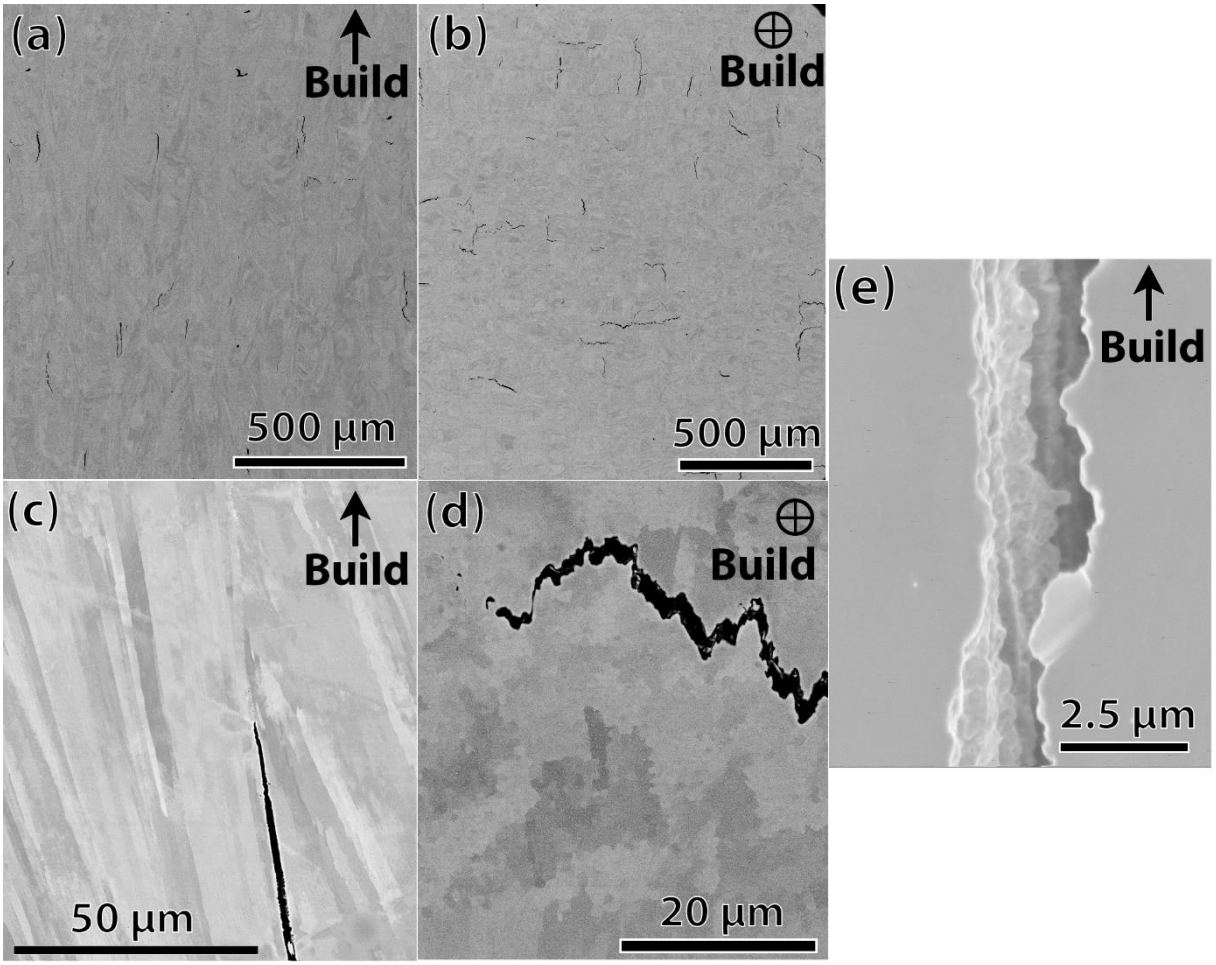

Supplement Figure 13: Electron microscope images taken from CM247LC NHf samples fabricated from Machine 1 and 2. a) BSE Image of a parallel cross section (Machine 1). b) BSE image of perpendicular cross section (Machine 1) c) Higher magnification BSE image of a crack observed in a parallel cross section (Machine 2, 100 mm) d) Higher magnification BSE image of a crack observed in the perpendicular cross section (Machine 2, 34 mm) e) SE image showing the features on the crack faces (Machine 2, 34.5 mm).

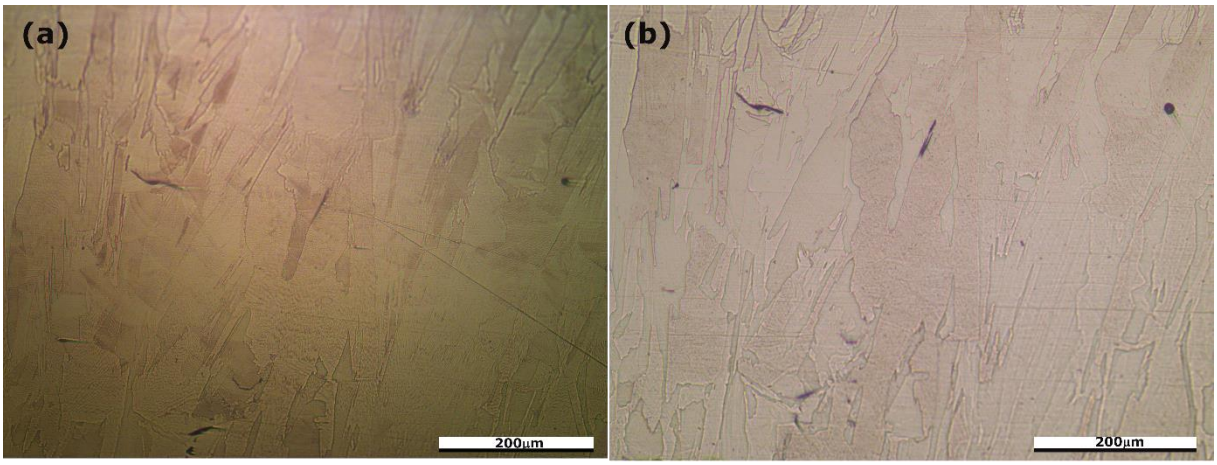

Supplement Figure 14. Optical images of the Hf-free sample microstructure a) before and b) after the Gleeble experiments. No new micro-cracks have appeared.

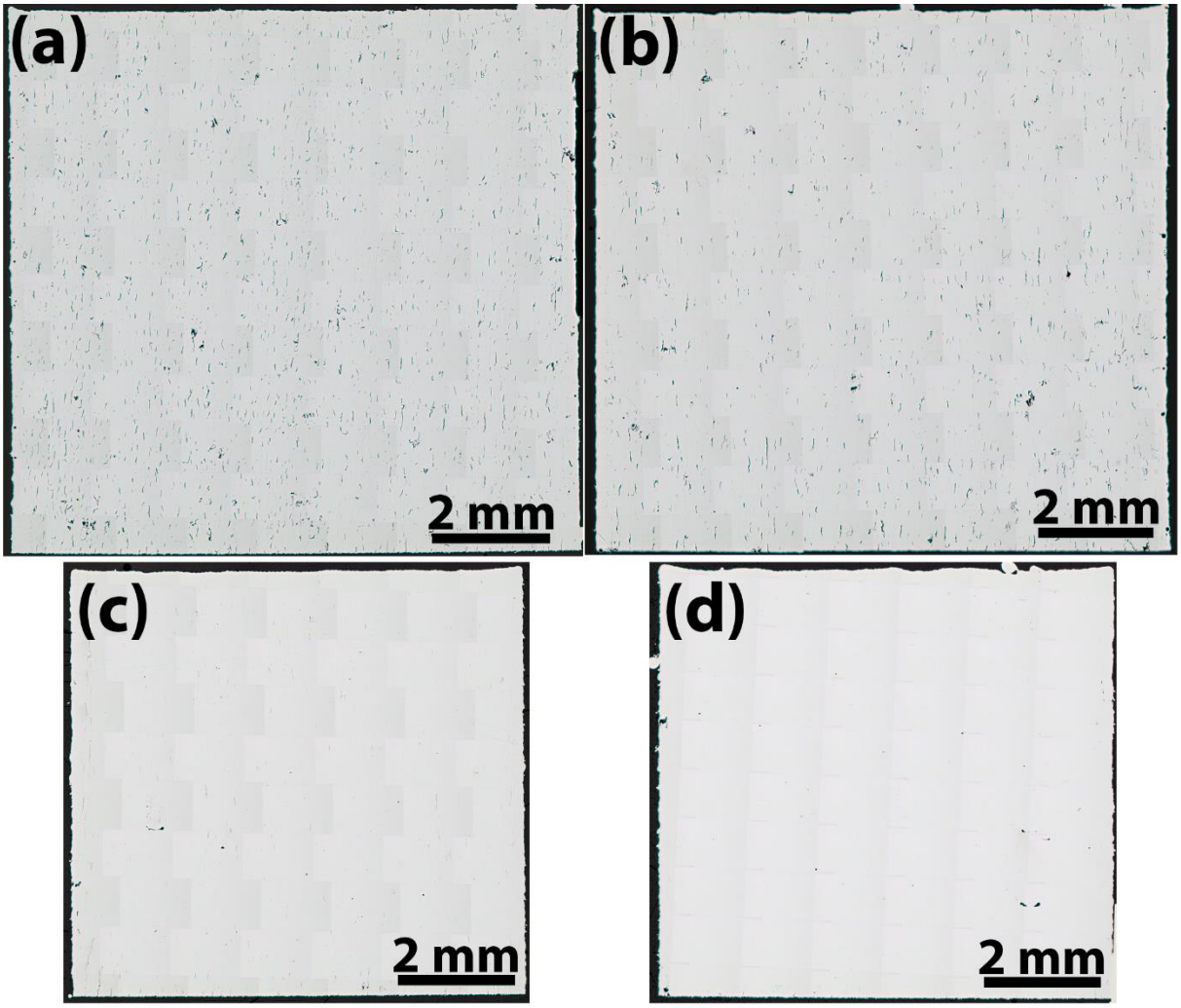

Supplement Figure 15: Full size optical images of the cubes shown in Figure 10. a) Optical micrograph of CM247LC sample from study 1 b) Optical image from CM247LC NHf from study 1. c) Optical image of CM247LC from study 2. d) Optical image of CM247LC NHf from study 2.

Supplement Table 1: Chemical composition of CM247LC used for Thermodynamic calculations

wt. %	Al	B	C	Co	Cr	Hf	Mo	Ni	Ta	Ti	W	Zr
CM247LC	5.6	0.015	0.07	9.2	8.1	1.4	0.5	Bal	3.2	0.7	9.5	0.015

Supplement Table 2: Values used in the normalized enthalpy calculations

Condition	Spot Size: a (μm, $1/e^2$)	Power: P (W)	Scan Speed: u (mm/s)	Absorptivity: A	Thermal Diffusivity at 0.5 T_m : D (cm^2/s)	Density: ρ (Kg/m^3)	Melting Temperature: T_m (K)	Specific Heat Capacity: (C) J/(K Kg)
1	45	200	600	0.3	0.040	8540	1555	580
2	27.5	175	750	0.3	0.040	8540	1555	580
References					[1] CMSX-4			[2] at 1323 K

[1] R.E. Aune, L. Battezzati, R. Brooks, I. Egry, H.-J. Fecht, J.-P. Garandet, M. Hayashi, K.C. Mills, A. Passerone, P.N. Quested, E. Ricci, F. Schmidt-Hohagen, S. Seetharaman, B. Vinet, R.K. Wunderlich, Thermophysical properties of IN738lc, MM247lc and CMSX-4 in the liquid and high temperature solid phase, in: Superalloys 718 625 706 Deriv. Proc., 2005: pp. 467–476. http://urn.kb.se/resolve?urn=urn:nbn:se:kth:diva-43342 (accessed October 14, 2011).

[2] R. Przeliorz, J. Piatkowski, THERMOPHYSICAL PROPERTIES OF NICKEL-BASED CAST SUPERALLOYS, Metalurgija. 54 (2015) 543–546.

Chapter 9 (Supplementary)

Healing cracks in Selective Laser Melting by 3D Laser Shock Peening

Nikola Kalentics[1,*], Navid Sohrabi[1], Hossein Ghasemi Tabasi[1], Seth Griffiths[2], Jamasp Jhabvala[1], Christian Leinenbach[2], Andreas Burn[3], Roland E. Logé[1]

1. Thermomechanical Metallurgy Laboratory – PX Group Chair, Ecole Polytechnique Fédérale de Lausanne (EPFL), CH-2002 Neuchâtel, Switzerland
2. Empa-Swiss Federal Laboratories for Materials Science and Technology, Dübendorf, Switzerland
3. Switzerland Innovation Park Biel/Bienne SIPBB, Swiss Advanced Manufacturing Center SAMC, Aarbergstrasse 46, 2503 Biel/Bienne, Switzerland

N. Kalentics, N. Sohrabi, H.G. Tabasi, S. Griffiths, J. Jhabvala, C. Leinenbach, A. Burn, R.E. Logé, Healing cracks in selective laser melting by 3D laser shock peening, Addit. Manuf. 30 (2019) 100881. doi:10.1016/j.addma.2019.100881.

Contribution:
Hossein Ghasemi Tabasi performed the crack morphology and EDX analysis of the CM247LC samples (as-built samples and 3D LSP samples), and wrote experimental section on the LSP treatment and sample analysis, and crack healing mechanism discussions (3.3).

Abstract

Selective Laser Melting (SLM) of Ni-based superalloys such as CM247LC is prone to weld-cracking. This paper investigates how to suppress cracks by repeatedly applying Laser Shock Peening (LSP) during the building phase of SLM. Samples made of CM247LC were processed with different LSP parameters, and the influence on bulk crack density has been quantified. It was observed that for all chosen conditions, a significant decrease of up to 95% could be achieved, demonstrating the potential of the new hybrid 3D LSP method in improving SLM processability of alloys sensitive to cracking.

Keywords: 3D Laser shock peening; Selective laser melting; Laser shock peening; Crack density; Ni-based superalloy; CM247LC

1. Introduction

Selective Laser Melting (SLM) is a laser based powder bed process considered to be one of the most accurate and widely investigated Additive Manufacturing (AM) processes [1], [2]. AM is known for a number of advantages over conventional manufacturing methods, such as the possibility to build parts with complex geometries, low lead time, mass customization, minimal waste, and the ability to process materials which are difficult or impossible to manufacture with conventional manufacturing methods. SLM is however very sensitive to the accumulation of tensile residual stresses (TRS), which can lead to cracking and warping. If not released after processing, these TRS also usually result in a significant decrease in fatigue life [3]–[5].

Ni-based superalloys have a major importance in industries dealing with high temperature applications, such as gas and jet turbine engines. Among these, CM247LC has demonstrated excellent creep and corrosion resistance at elevated temperatures [6], which places this alloy in an ideal position for production of turbine blades designed for demanding conditions such as high loads and high temperatures [7], [8]. CM247LC is primarily strengthened by a high-amount of γ′ ordered secondary phase [8], and is well-known to be prone to weld-cracking [9], [10]. Both fusion welding and Selective Laser Melting processes therefore lead to the formation of cracks. Four potential mechanisms have been discussed so far in Ni-based superalloys, and could apply to CM247LC:

1) Solidification Cracking (Hot-Tearing) happens where the material is in a partially solid state (solidifying melt pool or mushy zone) as a result of entrapment of liquid remaining in the interdendritic regions [10]. Due to the presence of tensile residual stresses induced by solidification, the entrapped liquid regions can act as crack initiation sites [11], [12].

2) Liquation Cracking mostly occurs in the Heat Affected Zone (HAZ), and some studies have identified it as the main reason of cracking in lower-energy welding conditions [13]. In the HAZ, phases with low melting point, such as γ-γ′ eutectic or zones with chemical segregation, form a liquid film along the grain boundaries. Since the liquid film cannot withstand solidification shrinkage (TRS due to shrinkage), it serves as a crack initiation site.

3) Strain-age cracking (SAC) is correlated with post weld heat treatment (PWHT) of Ni-based superalloys. SAC may occur during reheating of the welded material in the aging region [10]. The mechanism of SAC is explained by two competing actions. First, residual stresses relax slowly during PWHT. One the other hand, γ′ keeps precipitating which makes the alloy less ductile and induces additional residual stresses. If the resulting residual stresses induce strain beyond the ductility limit, cracks form at grain boundaries, usually along carbides. In SLM, reheating repeatedly occurs after deposition of each new layer, but with a different time scale compared to weld reheating [10], [14].

4) Ductility-dip cracking (DDC) is a 'creep-like' mechanism which occurs at elevated temperature, not high enough for dynamic recrystallization, but sufficient for grain boundary sliding [15]. The latter can induce stress concentration at triple grain boundary junctions, and lead to void formation, or cracking.

SLM of Ni-superalloys has been largely studied [9], [16]–[19]. Strategies for reducing crack density include optimizing SLM parameters [9], [18], [19], applying Hot Isostatic Pressing (HIP) [9], and tuning the chemical composition [9], [18]. The HIP process usually leads to grain coarsening [20], [21] which has detrimental consequences on mechanical properties. Carter et al. [9] concluded that the main cracking mechanism in CM247LC is DDC, due to presence of high angle grain boundaries near the cracks. Liquation cracking was also reported in SLM of IN738LC [22] (another γ′-strengthened Ni superalloy). The dendritic structure at the crack surfaces, and the presence of low melting point alloying components are two solid evidences for this cracking mechanism [22].

Although cracking mechanisms in γ′strengthened Ni superalloys are still a matter of debate, all of them require a TRS field which promotes crack nucleation and propagation.

3D Laser Shock Peening (3D LSP) is a hybrid Additive Manufacturing process which repeatedly applies Laser Shock Peening (LSP), a well-known surface treatment [23], [24], during the building phase of SLM. It was developed and patented by the Laboratory of Thermomechanical Metallurgy at EPFL [25]. Initial investigations have shown that LSP can convert the SLM induced TRS into compressive residual stresses (CRS) [26]. When LSP is repeatedly applied every few SLM layers, CRS can accumulate, i.e. both their magnitude and penetration depth from the free surface can increase [27]. Beneficial effects of 3D LSP include improved geometrical accuracy [28], and should result in improved fatigue life. LSP also increases

the stored strain energy in the material, which can help recrystallizing the microstructure during a subsequent heat treatment [29].

γ′ strengthened Ni-based superalloys are susceptible to cracking when subjected to welding or SLM conditions. Cracking is always promoted by TRS, regardless of the particular mechanism involved. From an industrial point of view, any part containing an excessive amount of cracks should be rejected and thus, suppressing cracks is of utmost importance. In this paper, we show for the first time that the 3D LSP approach can significantly reduce the amount of cracks in SLM CM247LC samples. Samples in the AB and 3D LSP treated conditions are compared and the measured cracks density is significantly reduced for all considered 3D LSP processing conditions. The crack healing mechanism is discussed.

2. Experimental setup

2.1 SLM parameters and sample geometry

Two batches of CM247LC with slightly different compositions were used. The first batch was gas atomized by LPW Technology and had a d_{50} of 40.49 µm. The second batch of powder utilized in this study was gas atomized by Oerlikon Metco and had a reported d_{50} of 32.42 µm. The chemical compositions of the two batches are shown in Table 1.

Table 1. Chemical composition of the twoCM247LC powder batches, wt.%

	Cr	Co	Ta	Ti	Al	W	Hf	Mo	C	B	Zr	Ni
B1	8.4	9.4	3.3	0.8	5.6	9.6	1.4	0.5	0.06	0.01	0.009	Bal.
B2	8.6	9.2	3.1	0.7	5.7	9.9	1.4	0.5	0.06	0.017	0.006	Bal

SLM processing of the batch 1 powder was performed on a laboratory machine equipped with an Ytterbium fiber laser operated in continuous mode at a wavelength of 1070 nm and a spot size of 90 microns. The chosen SLM processing parameters were: laser power 200 W, scanning speed 1300 mm/s, hatching distance 0.090 mm, and layer thickness 0.03 mm, with a bi-directional scanning (90° alternating), without baseplate preheating. Processing was done in argon atmosphere and the oxygen content in the SLM chamber was around 0.5%. Twelve samples with dimensions of 10x10x10 mm^3 were manufactured (Figure 1 a,b).

The second powder batch was processed on a ConceptLaser (Concept Laser, Germany) M2 machine, with a 200 W Nd-YAG fiber laser with a 1070 nm wavelength operated in continuous wave mode. Argon shielding gas was used to keep the oxygen content during processing below 1 %. Analysis was done on a sample cube (10x10x10 mm) fabricated with a 200 W laser power, a 600 mm/s laser scanning speed, a 0.105 mm hatch distance, and a 30 µm powder layer, without baseplate preheating. An island scanning strategy, as described by Carter et al.[9] was utilized for the sample cubes.

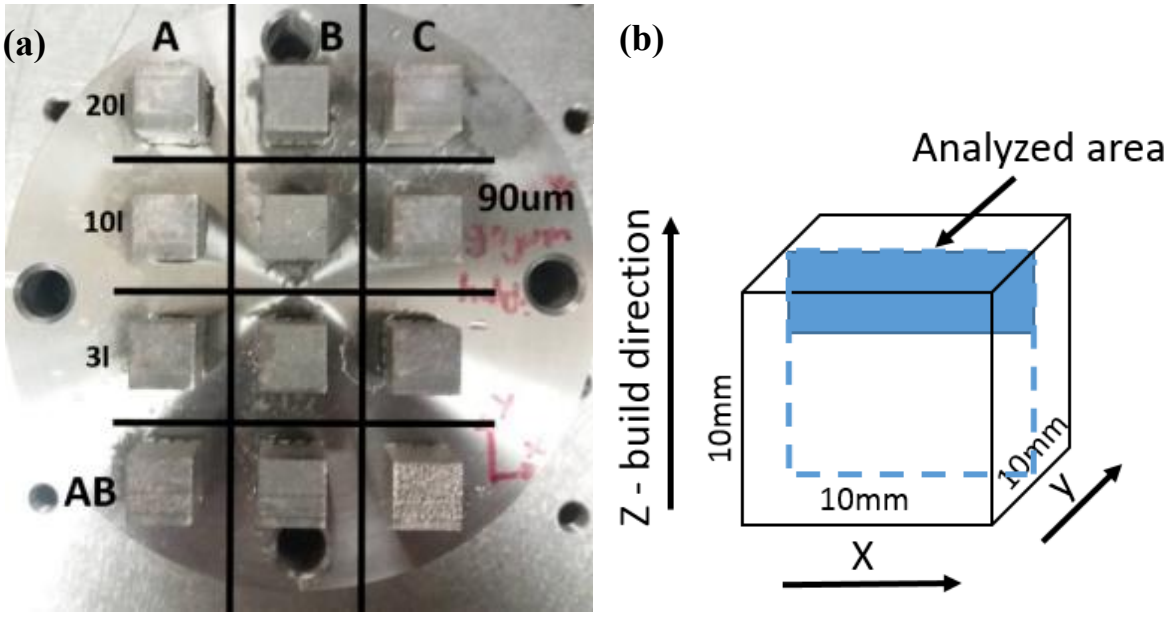

Figure 1. a) Samples attached to the baseplate b) sample geometry with the build direction vertical (Z).

2.2 Laser Shock Peening setup

While still being attached to the baseplate, 9 out of the 12 samples in Figure 1a were treated with different LSP parameters: three samples for each set of parameters A, B and C. The last three samples were left in the as-built (AB) condition. After LSP treatment, samples were brought back to the SLM station and n additional SLM layers were rebuilt (Figure 2). The chosen numbers of layers n were {3, 10, 20}, as shown in Figure 1a.

Similar to previous work [27], the LSP treatment was done with a Nd:YAG SAGA HP laser from Thales company. The LSP process parameters were kept constant with the exception of the overlap rate (Table 2).

The chosen overlap rate was 80% for samples A, 40% for samples B, and two times 80% (two treatments with 80% coverage each) for samples C (Figure 1a). The ratio of number of LSP shots between 80% overlap and 40% overlap is 9. The reader is directed to [26], [27] for more information on the LSP setup.

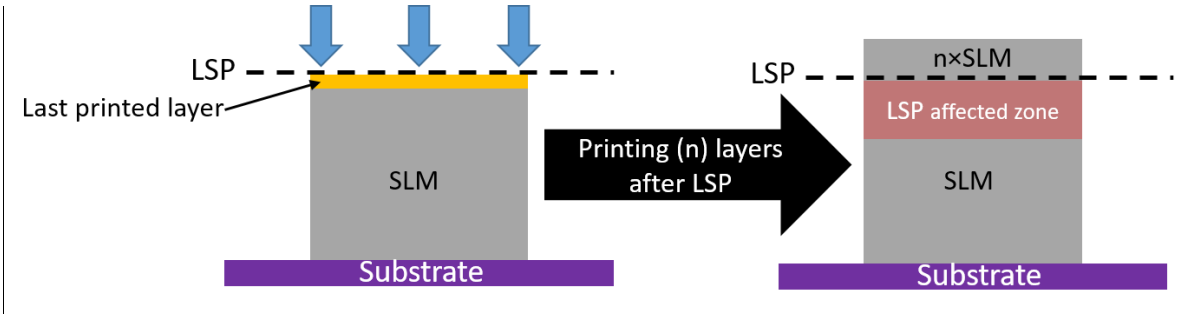

Figure 2. Schematic view of the 3D LSP process with the *n* number of rebuilt SLM layers after the LSP treatment.

Table 2. LSP process parameters

Wavelength	1064nm
Pulse duration	6.3ns
Spot size diameter	1mm
Pulse energy	0.4J
Power density	7.2 GW/cm^2
Frequency	5Hz

2.3 Crack density measurements

Samples were cut according to Figure 1b, ground with sand papers (down to 2500), then polished with suspension of alumina particles until 0.04 µm, and images of the XZ plane were taken on an optical microscope Leica DM6000M with a magnification of 200. Optical micrographs were analyzed with the ImageJ software, and a plugin [30] was used to quantify the crack density values.

2.4 Heat treatment

A stress relieve heat treatment was done on some of the 3D LSP samples in order to assess the influence of residual stresses on the measured crack density. Samples were heat treated at 1250°C in a Borel FP 1400 furnace for 3 hours, and cooled down to room temperature with a flow of compressed argon gas.

2.5 Chemical etching

Chemical etching was done with the Kalling's reagent (2.5 g CuCl2 + 50 mL HCl + 50 mL water). Samples were immersed for 5 seconds in the etching solution. Similarly to the heat treatment, chemical etching was used to evaluate if cracks in the material were barely closed due to the LSP induced CRS and/or smeared due to grinding and polishing, or instead if they were completely removed.

2.6 SEM Analysis

Crack morphology analysis was done with a FEI NanoSEM230 in backscatter and secondary electron mode. Energy-dispersive spectroscopy (EDX) technique was employed using a FEI XL30 scanning electron microscope equipped with an Oxford instrument EDX system operated at 20 kV.

2.7 STEM Analysis

The lamellae for scanning transmission electron microscopy (STEM) analysis was extracted from an as printed cube (batch 2 powder) with a FEI Helios NanoLab 600i focused ion beam (FIB). The lamellae was located nearby a crack tip such that the transverse structure was visible. Since Ga ions were used for extraction and milling of the lamellae, Ga was detected on the grain boundaries during energy dispersive spectroscopy (EDX) analysis. STEM analysis was performed on a FEI Titan Themis microscope operated at 300kV. A probe convergence semiangle of 25mrad was used with an annular dark field detector with a 53mrad inner semiangle and a 200mrad outer semiangle. The STEM EDX was done with the SuperEDX (FEI ChemiSTEM technology utilizing four silicon drift detectors) of the aforementioned micoscope.

2.8 Thermodynamic calculations

Calculations of the equilibrium solidus and liquidus temperatures for different alloy compositions were performed using the Thermocalc software package (version 2018) in combination with the TCNI5 database. The compositions were based on STEM-EDX measurements from one cell boundary (not shown in the presented STEM-EDX map, but with similar segregation). Elemental compositions that were not measured accurately by the STEM-EDX, B and Zr for instance, were taken from the measured powder composition.

3. Results and discussion

Samples were denoted as "AB" in the SLM as - built condition, and 3D LSP "A", "B" or "C" when LSP treated with 80% overlap, 40% or two times 80% respectively. As explained in section 2.2 the number *n* of rebuilt layers after the LSP treatment varied between 3, 10 and 20.

3.1 As – built (AB) state

A large scale and a zoomed view of an AB SLM sample is shown in Figures 3 and 6c. It can be observed that, as reported in [9], [31], there is a significant amount of cracks in these samples. These cracks are mostly oriented along the vertical build direction. No significant difference between samples produced from the two powder batches on the two different machines could be observed. Crack density measurements were made on batch 1 samples in an area of $8.0 \times 0.5\ mm^2$ and at a depth of 600 µm below the top surface (thereby keeping it comparable to the 3D LSP measured area in Figure 6). An average from three measurements gave a crack density of 2.16 $\frac{mm}{mm^2}$, with a relatively small standard deviation of 0.27$\frac{mm}{mm^2}$.

Figure 3. CM247LC sample in the SLM AB condition.

SEM analysis of the microstructure and crack morphology in the AB sample (Batch 2) is shown in Figure 4. The microstructure consists of ~1 µm wide columnar cells mostly oriented in the build direction (Figure 4a). A crack with a jagged appearance is observed on a boundary separating two clusters of cells with different orientations. Similar observations have been made on other SLM studies of CM247LC [31, 32]. SEM analysis utilizing a TLD detector to view the crack faces is shown in Figure 4b. The crack faces have a characteristic dendrite appearance that is indicative of hot cracking.

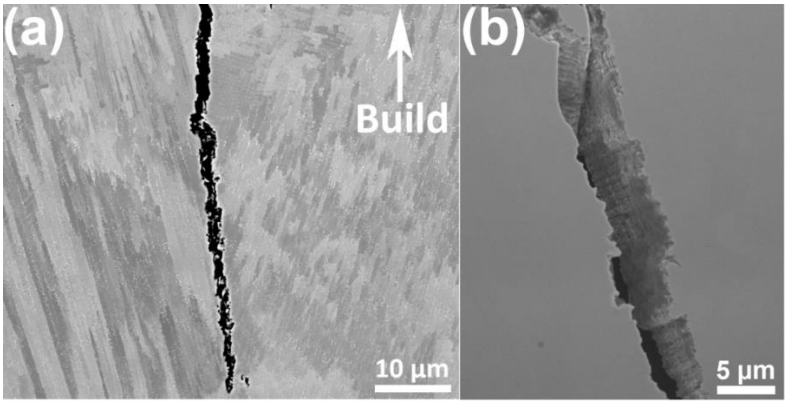

Figure 4. (a) SEM Backscatter electron image showing a fine cellular microstructure and a crack located on what appears to be a grain boundary (b) SEM through the lens detector (TLD) secondary electron (SE) image showing the internal morphology of a different crack. Note the rough appearance indicative of hot cracking.

STEM-EDX chemical mapping of cell boundaries adjacent to a crack is shown in Figure 5. Segregation of Al, Ti, Ta, and Hf to the cell boundaries and W to the cell cores is observed. Numerous carbides enriched in Hf, Ti, Ta, and W are observed on the cell boundaries. The significant segregation measured in these alloys is assumed to result in large freezing ranges which is one of the contributing factors in weld cracking.

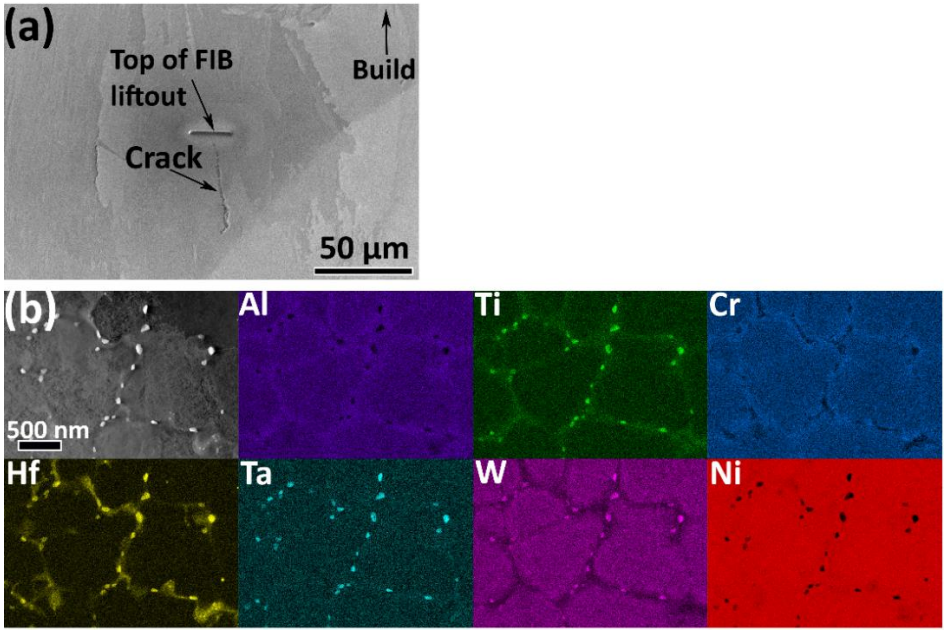

Figure 5. (a) Secondary electron image taking during the the FIB preparation showing where the STEM llamellae was taken with respect to the crack. (b) STEM EDX chemical maps showing numerous boundaries. The following elements are not shown Co (similar behavior to Ni), C (same locations as Ta rich precipitates), Zr (trace amounts with no concentrated areas),Fe (trace amounts) and Mo (a few precipitates on the grain boundaries). Chemical analysis was performed using the Al-K,Ti-K, Cr-K, Hf-L, Ta-L, W-L,Ni-K, Co-K, C-K, Zr-K, Fe-K, and Mo-K lines.

3.2 3D LSP state

As shown in Figure 1a, nine unique 3D LSP conditions were selected, with different overlap rates and numbers of rebuilt layers n={3, 10, 20}. The rebuilding of additional SLM layers used a misalignment step (i.e. the rebuilt SLM layers were offset) so that the zone of the LSP treated layer could be easily observed (Figure 6a). Below the LSP treated layer, an LSP affected zone with a reduced crack density can clearly be distinguished (Figure 6b). The crack density was measured for all samples at different distances below the LSP line. For each measurement, a rectangle was considered, made of the LSP line and a defined distance below it (Figure 6a). Table 3 shows measured crack densities obtained with rectangles extending at 200 microns below the LSP line. Sample A with n = 20 has the lowest crack density (0.12 $\frac{mm}{mm^2}$), which represents

a drastic reduction of almost 95% compared to the AB condition (2.16 $\frac{mm}{mm^2}$). This significant improvement is attributed to the removal of TRS and the introduction of CRS by the 3D LSP treatment. As previously stated [9], [16]–[18] the presence of TRS is the main cause of crack generation in critical areas. 3D LSP does not only remove the detrimental TRS which tend to initiate damage and cracks, but introduces CRS which have the opposite effect.

At increased depth, a gradual change occurs, finally reaching the AB state (Figure 6c). The estimated LSP affected zone extends over 500 microns in depth, while only a marginal improvement of crack density is observed *above* the LSP line. This can be understood from the usual SLM induced (tensile) stresses which, in this case, were generated during the SLM rebuilding step.

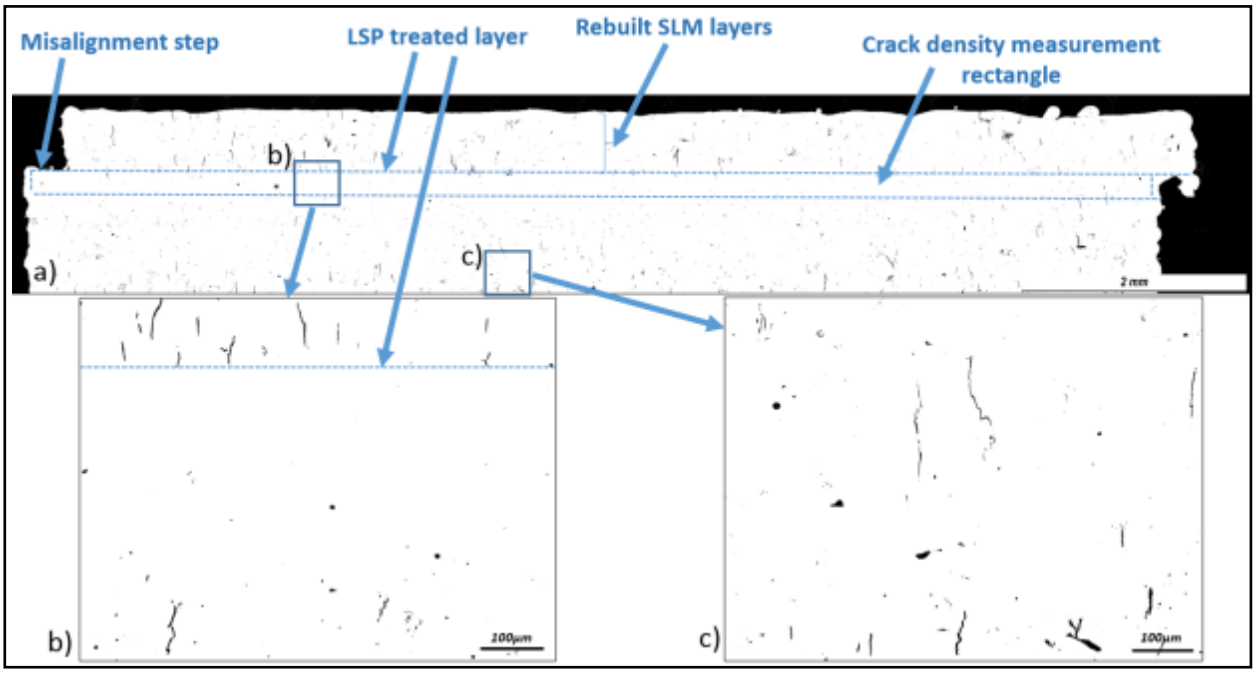

Figure 6. Micrograph of the A1 sample (80% LSP overlap and 20 rebuilt SLM layers) a) illustration of the rebuilding misalignment step, LSP treated layer, rebuilt SLM layers and the crack density measurement rectangle below the LSP treated layer. b) enlarged LSP affected zone, c) enlarged as –built SLM zone.

Table 3. Crack density values in the rectangular area from the LSP line up to 200 microns below

	Crack density ($\frac{mm}{mm^2}$)		
Overlap rate	n = 3	n = 10	n = 20
A = 80%	0.28	0.41	0.12
B= 40%	0.2	0.36	1.39
C= 2x80%	0.23	0.66	0.48
AB	2.16		

From Table 3, it can be observed that except for the B sample with n= 20 (with crack density of 1.39 $\frac{mm}{mm^2}$), all other conditions had a fairly similar crack density, with an average of 0.34 $\frac{mm}{mm^2}$. The particular value of the B 20l sample is difficult to explain, and should probably be related to improper LSP confinement or disturbance in the laser energy. B LSP processing conditions with only 40% overlap are more likely to be sensitive to such variations, due to the lower number of shots per unit area (divided by 9 and 18 compared to A and C respectively). Reversely, B conditions are much more productive compared to A and C.

By changing the vertical size of the rectangle from which the crack density is calculated, the depth of the LSP affected zone can be quantified. Figure 7 shows this analysis for A samples with n = 3 (A3l), 10 (A10l) and 20 (A20l), and the AB state. The performance of the different samples remains in line with the values given in Table 3. A typical LSP affected depth of 500 microns can be concluded for all A conditions (A3l, A10l, A20l). Below this depth, the average crack density starts increasing.

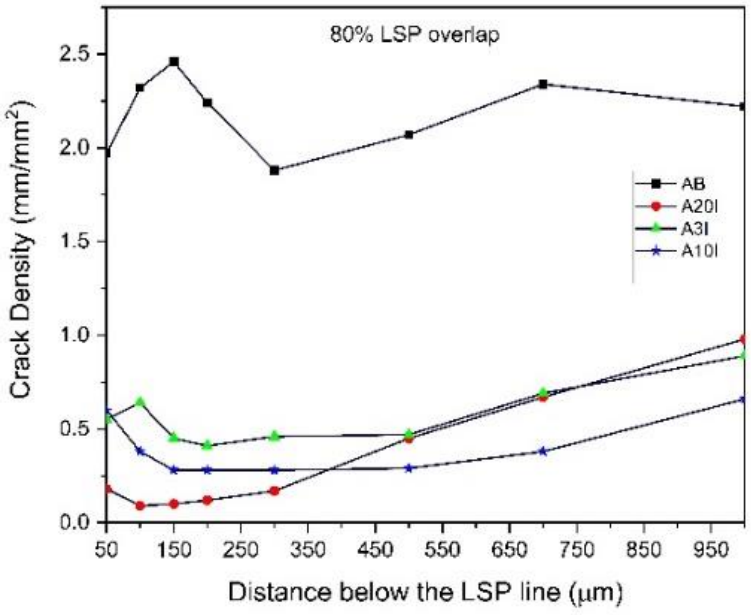

Figure 7. Average crack density values up to 1000 microns below the LSP line for A samples and the as-built (AB) state

Figure 7 and Table 3 also indicate that the most reliable results (for any overlap rate) are achieved with n = 3 (0.2 - 0.28 $\frac{mm}{mm^2}$), i.e. when the least amount of TRS are reintroduced into the sample during the rebuilding phase. These values still represent a significant reduction in crack density of approximately 90% compared to the AB SLM state. An in depth comparison of samples with n = 3 is given in Figure 8. All curves follow a similar trend up to 300 to 500 microns, followed by an increase in crack density. In the B condition, this increase starts earlier, around 300 microns, which is consistent with a decreased LSP affected depth related to the decreased number of LSP shots per surface area [26], [27].

One can conclude from the above that if LSP is applied often enough (e.g. every 3 layers) the effect of the number of shots per unit area becomes low. Although higher overlap rates do increase the magnitude and depth of CRS, this effect is limited (and eventually saturates), and does not strongly influence crack density. In the investigated range of overlap, one can conclude here that lower overlaps can be selected, especially if processing time (productivity) is of concern.

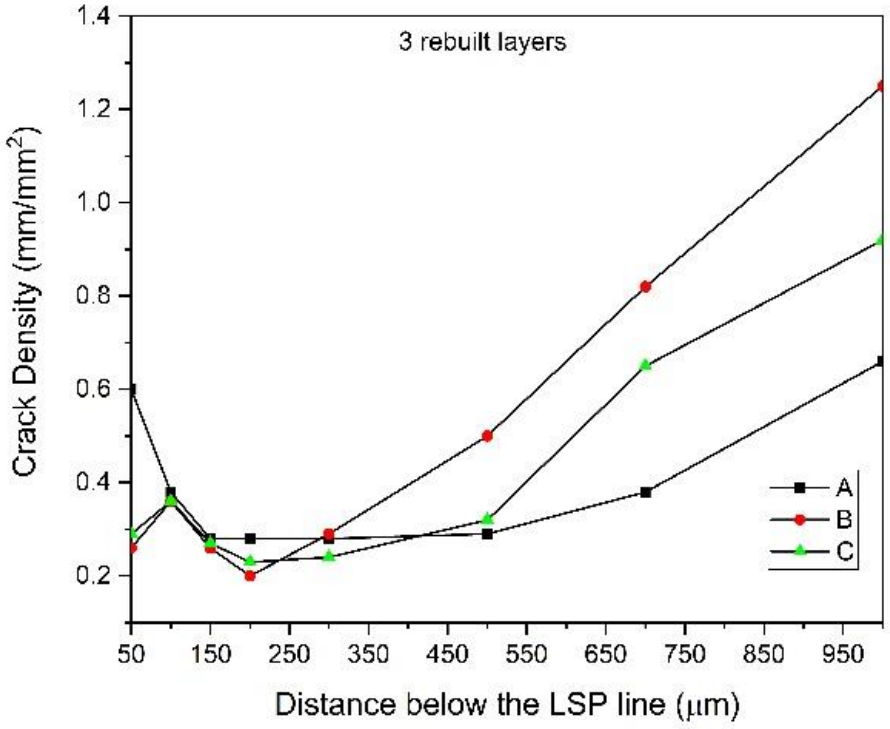

Figure 8. Crack density values up to 1000 microns below the LSP line for A, B and C samples and $n = 3$

3.3 Crack healing mechanism

As compressive residual stresses and/or surface preparation can lead to potential artefacts in the accurate measurement of crack density, both stress relieve heat treatment and chemical etching were performed on some of the samples. The stress relieve heat treatment was meant to remove LSP induced CRS to check if cracks would reopen. Chemical etching was used to better reveal grain boundaries and cracks on the sample surface.

Figure 9 shows optical micrographs of the SLM AB condition, and of the 3D LSP treated case with A condition and $n = 20$. In the latter, heat treatment, chemical etching, and polishing steps were considered. The improvement in crack density previously shown in Figures 6, 7, 8, and Table 3 is confirmed (Figures 9a and 9b), with no significant difference when heat treatment or chemical etching is being used (Figures 9c and 9d). This further strengthens the previously drawn conclusions on the ability of the 3D LSP process to effectively suppress SLM induced cracks.

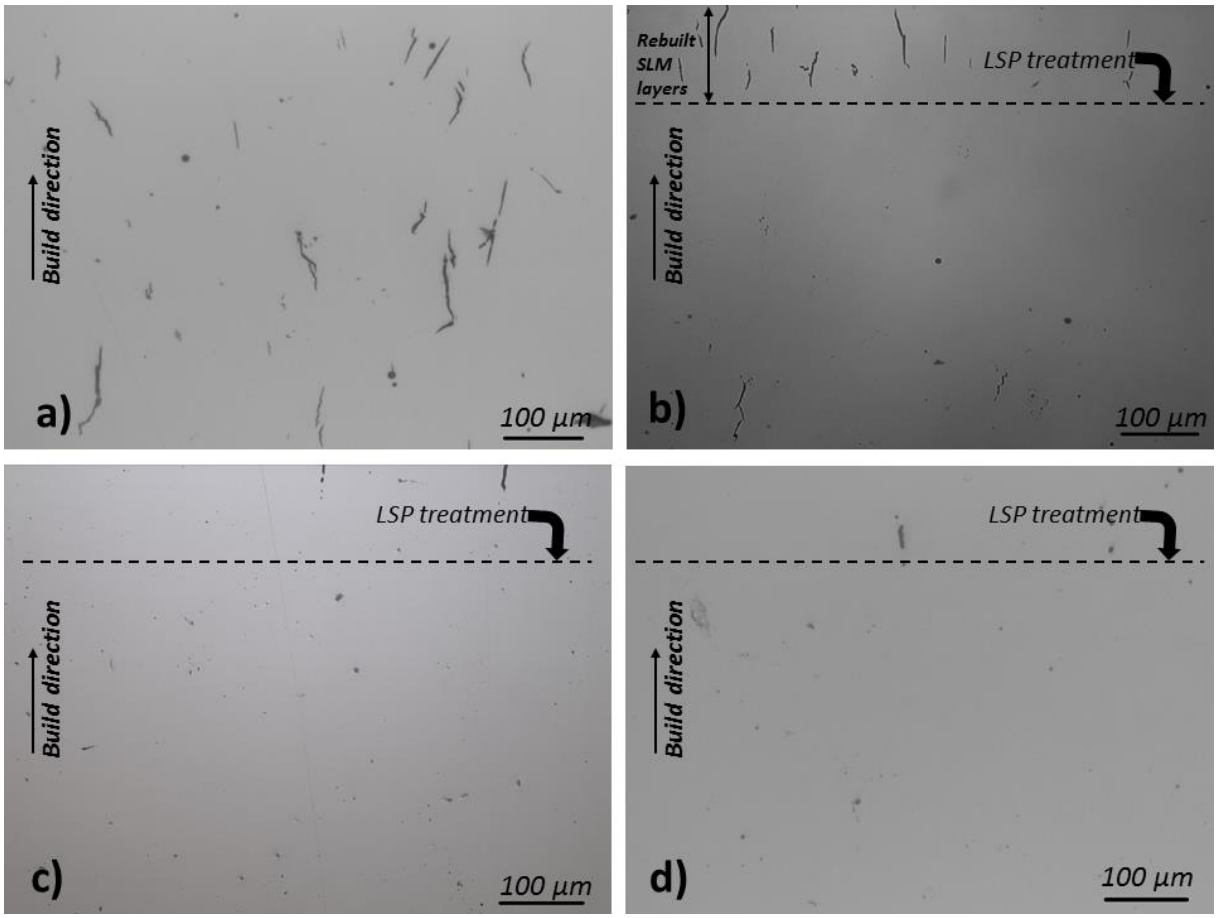

Figure 9. a) micrograph of the polished SLM AB condition; b) polished 3D LSP A sample with $n = 20$; c) 3D LSP A sample with $n = 20$, heat treated and polished; d) 3D LSP A sample with $n = 20$, heat treated, chemically etched and polished

As discussed in the introduction, the cracking mechanism of γ′ strengthened Ni-based superalloys is still a controversial debate; however all proposed cracking mechanisms rely on the presence of tensile residual stresses promoting crack nucleation and/or growth along the build direction. When one considers the dendritic appearance of the crack faces in combination with the significant segregation (especially of Hf) observed in the AB sample, either a solidification or a liquation cracking mechanism is likely dominant. In both of these mechanisms, an increased freezing range due to segregation is needed. Measured cell boundary and cell interior chemistries from the STEM-EDX data were introduced into Thermocalc in order to calculate the equilibrium solidification temperatures (Figure 10). It can be seen that the segregation observed in the AB sample results in a 71˚C decrease in the liquidus temperature from cell interior to cell boundary, and a 78˚C decreases for the solidus temperature. It is important to note that each cell boundary has a different level of measured segregation of Hf, Ti, Al, Ta, and W. For instance Hf segregation ranging from 6 to 10 wt% on the cell boundaries (away from potential Hf enriched carbides) has been observed in in the AB condition, therefore there will be boundaries in the AB condition that have larger and smaller freezing ranges than that shown in Figure 10.

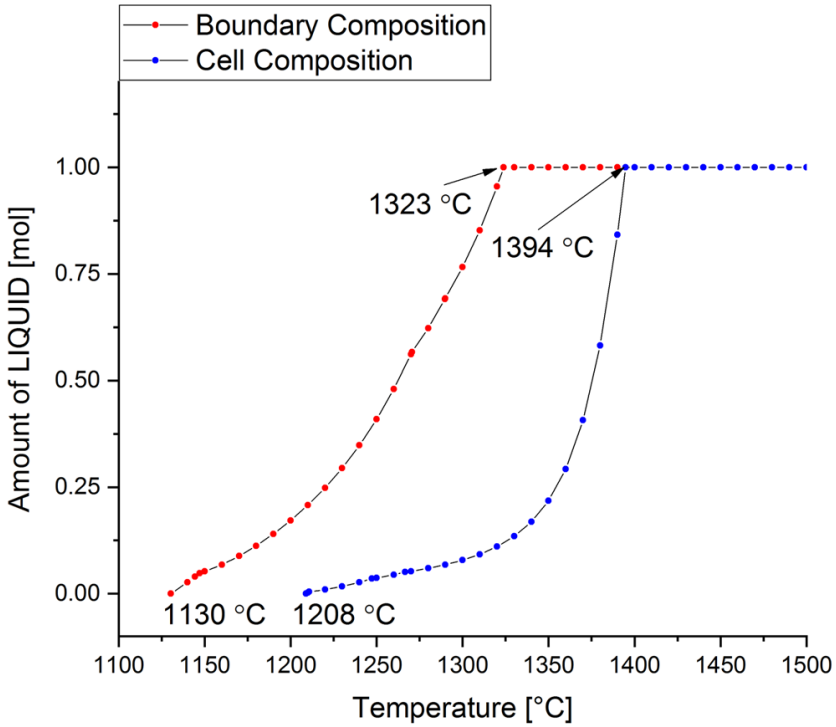

wt. %	Al	B	C	Co	Cr	Hf	Mo	Ni	Ta	Ti	W	Zr
Boundary	4.6	0.017	0.06	7.5	6.0	10	0.54	Bal	3.08	1.5	5.5	0.006
Cell	4.2	0.017	0.06	9.24	8.62	1.37	0.54	Bal	3.08	0.73	9.93	0.006

Figure 10. Calculated amount of liquid as a function of temperature in the melting/solidification range for an alloy composition corresponding to the compositions measured from the interior of the cells and from the cell boundaries, for one particular cell boundary.

The proposed 3D LSP crack closure mechanism (Figure 11) can be attributed to the removal of existing TRS in the AB state (Figure 11a) and the introduction of a compressive stress field in near surface region, after LSP processing (Figure 11b). In the newly introduced CRS zone, vertical cracks are compressed and closed due to the compressive biaxial stress state (Figure 11c). The subsequent SLM rebuilding step melts additional layers on top of the CRS zone (Figure 11d), which introduces heat into the underlying layers and promotes diffusion in the closed cracks, eventually leading to complete healing and bonding. This process produces crack free areas in the 3D LSP affected zone (Figure 6 a,b). As demonstrated in Figure 9, cracks do not reappear upon CRS removal by post heat treatment, or after chemical etching.

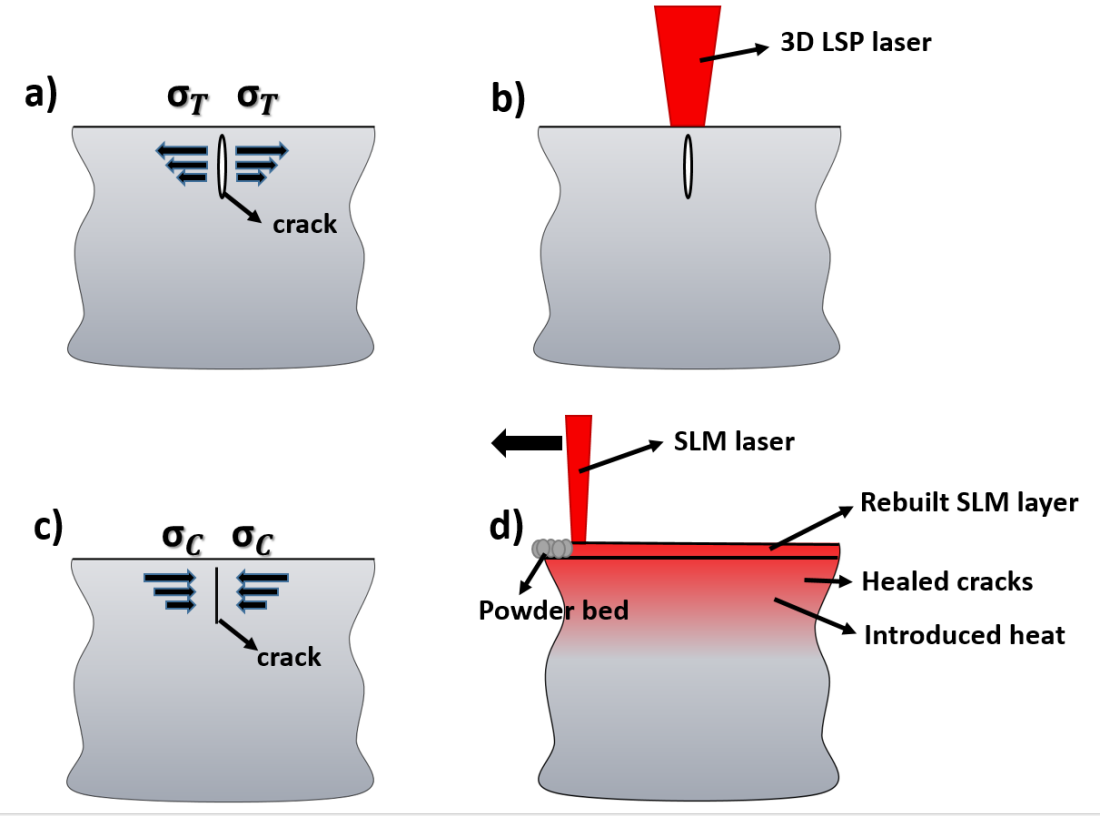

Figure 11. 3D LSP crack healing mechanism a) tensile residual stresses with one crack in the material in the SLM AB state; b) LSP treatment; c) sample after 3D LSP with introduced compressive residual stresses and closed cracks; d) additional SLM layers and crack healing due to the introduced heat.

To confirm the cracking mechanism proposed in Figure 11, lower scale observations were performed within an SEM (Figure 12). In the SLM AB condition, elongated vertically oriented microcracks appear both in the bulk of samples and in the zone close to the top surface, as shown in Figures 12a and 12b, respectively. The opening of these cracks is approximately 3µm. After LSP treatment, cracks in the LSP affected zone are closed due to the introduced CRS. This can be observed in Figures 12c, d and corresponds to Figure 11c in the proposed crack closure mechanism. The crack closure actually leads to a reduction of the apparent crack opening to about 200nm. A fine cell structures with a large number of small W/Mo/Hf/Ta MC carbides typical for this alloy can be noticed [31], [32]. During the subsequent SLM rebuilding step, new layers were added on top of the LSP treated surface (Figure 11d), with associated heat diffusion. Figures 12e and 12f, show healed cracks below the LSP treated line after the SLM rebuilding step was made. The amount of heat appears to be sufficient for inducing localized melting in the vicinity of the crack, reversing somehow the previously described liquation mechanism. The simultaneous presence of a localized liquid film and a

compressive stress field heals the existing cracks in the SLM HAZ, by a mechanism similar to brazing. The actual mechanism could be called “flash brazing” or “flash HIP” due to the very short time scale involved.

Figures 12e and 12f indicate how healed cracks look like in the HAZ, after the SLM rebuilding step. The crack healing mechanism is effective up to 125 µm below the newly deposited layers. At increased depth, the amount of introduced heat and the magnitude of CRS both decrease and become no longer sufficient to create a fully healed material. Discontinuous semi-healed cracks therefore appear in Figures 12g and 12h, 200 µm below the LSP line. Some of the semi-healed or closed cracks may have appeared completely healed when using optical microscopy, which explains the deeper affected zone in Figure 8 compared to the present local SEM measurements. EDX analysis was performed across healed cracks and typically shows significant variations in Ni and Hf content (Figure 13). The significant Hf segregation that was observed in the AB samples may be at the origin of a liquation mechanism. As already suggested above, an “inversed cracking mechanism” following the same principles as those underlying liquation (detailed in the introduction) can explain the reported crack healing by 3D LSP, due to the transformation of TRS into CRS.

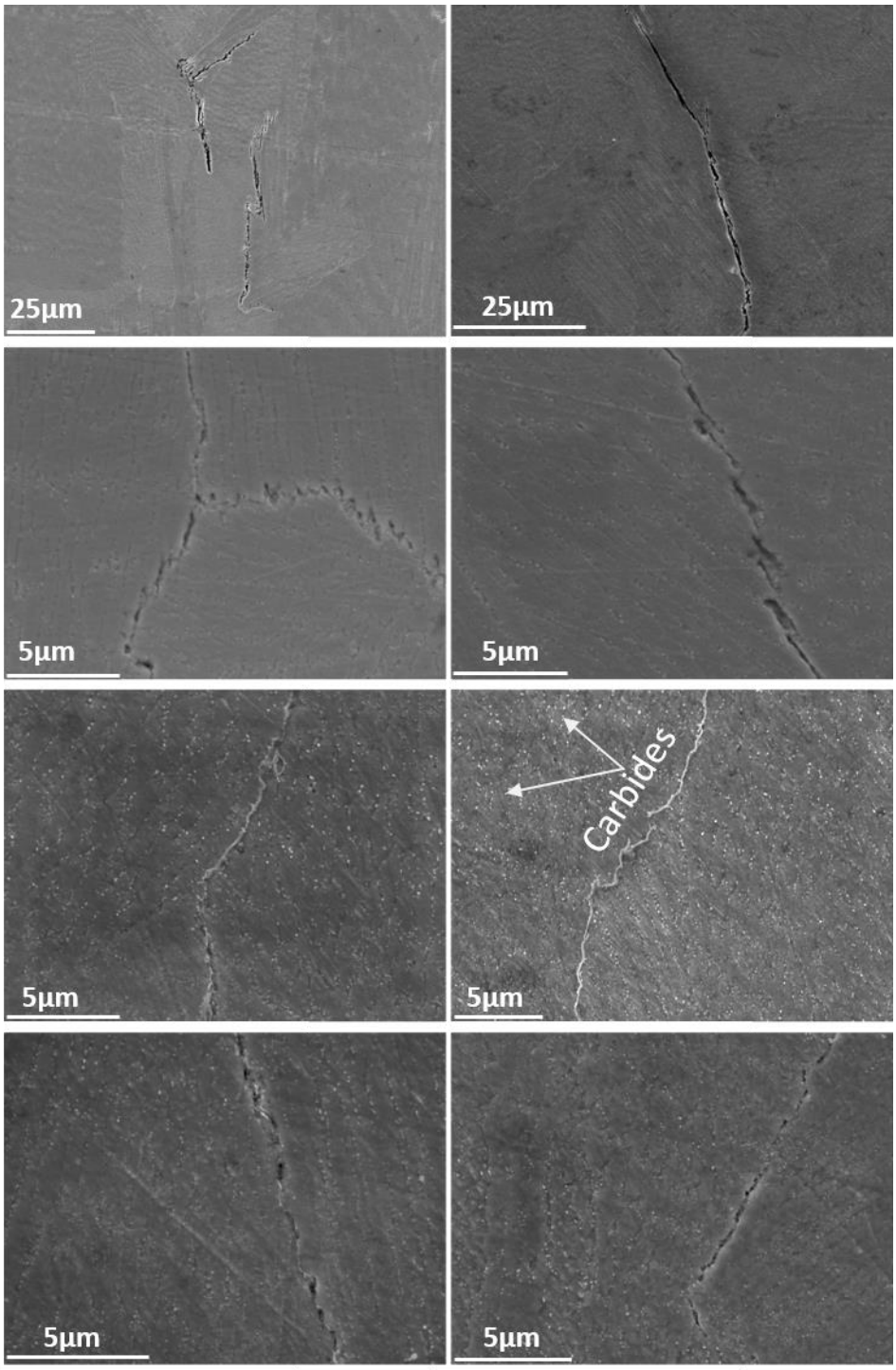

Figure 12. SEM micrograph of sample A with *n*=20 in the X–Z plane showing the cracked regions in: a) the top layers, b) the bulk, c-d) closed cracks after applying LSP, e-f) healed cracks below the LSP treated line after an SLM rebuilding step was made, and g-h) semi-healed cracks 200µm below the LSP line and after the rebuilding step.

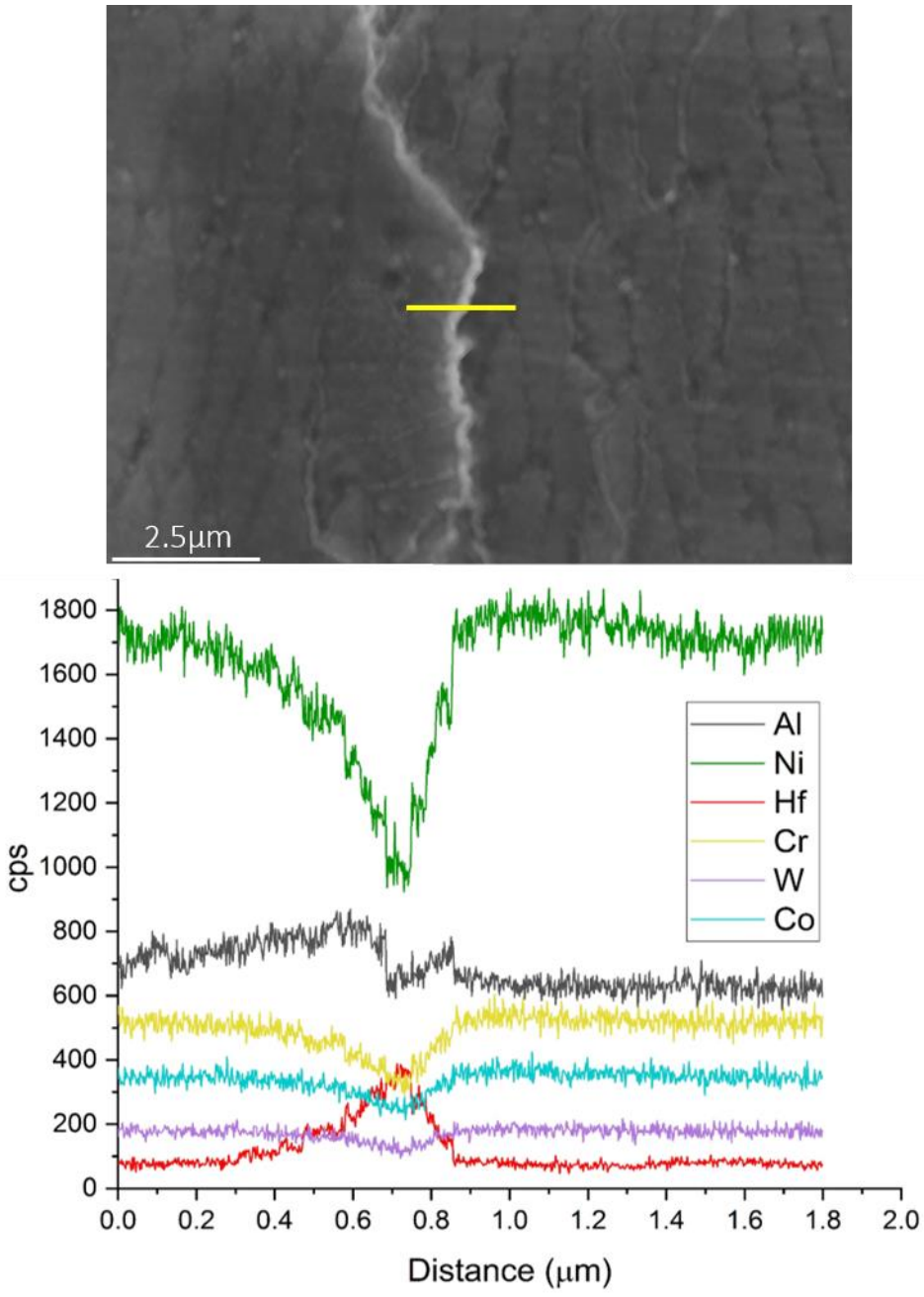

Figure 13. EDX line scan of the sample A with n=20 showing elemental distributions across the healed crack, demonstrating variations of Ni and Hf content

4. Conclusions

Crack density was measured in CM247LC SLM samples, either in the as-built (AB) SLM state or after 3D LSP processing, considering nine different operating conditions. The LSP overlap rate varied between 40%, 80% and 2x80%, and the number of SLM rebuilt layers after LSP treatment was $n = \{3, 10, 20\}$.

The following conclusions can be drawn:

- In the AB state, a substantial and homogeneous crack density of 2.16 $\frac{mm}{mm^2}$ was measured.
- For all nine 3D LSP operating conditions, a significant improvement in crack density was measured.
- The best results were obtained with the 80% LSP overlap rate, where a crack density of 0.12 $\frac{mm}{mm^2}$ up to a depth of 200 microns below the LSP treated line was measured. This represents a decrease of almost 95% compared to the SLM AB state.
- If the LSP treatment is applied often enough (e.g. every 3 layers), there is no significant effect of the overlap rate, and 3D LSP conditions can be chosen with lower overlap and enhanced productivity.
- The proposed crack healing mechanism is inverse to the liquation mechanism leading to crack formation, and can be described as a "flash brazing" or "flash HIP" process, due to the possibility of localized melting in the SLM HAZ and the presence of compressive stresses.

Further investigations and optimization of 3D LSP parameters and their effect on crack density in Ni-based alloys will be performed. Lower LSP overlap rates will be tested, together with increased periodicity (e.g. up to every single SLM layer). Finally, larger samples with more complex geometries will be produced on a hybrid (automated) 3D LSP machine, in order to study the control of cracks in a more systematic way, and for different materials.

Acknowledgments

This work has been supported by the CTI project n°25357.2 PFNM-NM, by the "PREcision Additive Manufacturing of Precious metals Alloys (PREAMPA)"project, and by the "Additive Manufacturing and Metallic Microstructures (AM3)" project. The PREAMPA project is funded by the Swiss ETH domain, within the Strategic Focus Area on Advanced Manufacturing. The AM3 project is funded by the Competence Center for Materials Science and Technology (CCMX) and by an industrial Swiss consortium. The authors thank Marcel Gerstgrasser from IWF, ETHZ for the SLM sample production. The generous support of PX Group to the LMTM laboratory is also highly acknowledged.

References

[1] C. Y. Yap *et al.*, "Review of selective laser melting: Materials and applications," *Appl. Phys. Rev.*, Dec. 2015.

[2] "Wohlers Associates." [Online]. Available: https://wohlersassociates.com/2018report.htm. [Accessed: 07-Jul-2018].

[3] J.-P. Kruth, J. Deckers, E. Yasa, and R. Wauthlé, "Assessing and comparing influencing factors of residual stresses in selective laser melting using a novel analysis method," *Proc. Inst. Mech. Eng. Part B J. Eng. Manuf.*, vol. 226, no. 6, pp. 980–991, 2012.

[4] K. Kempen, B. Vrancken, S. Buls, L. Thijs, J. Van Humbeeck, and J.-P. Kruth, "Selective Laser Melting of Crack-Free High Density M2 High Speed Steel Parts by Baseplate Preheating," *J. Manuf. Sci. Eng.*, vol. 136, no. 6, p. 061026, Oct. 2014.

[5] S. Afazov, W. A. D. Denmark, B. Lazaro Toralles, A. Holloway, and A. Yaghi, "Distortion prediction and compensation in selective laser melting," *Addit. Manuf.*, vol. 17, pp. 15–22, Oct. 2017.

[6] I. Gurrappa, "Hot Corrosion Behavior of CM 247 LC Alloy in Na2SO4 and NaCl Environments," *Oxid. Met.*, vol. 51, no. 5–6, pp. 353–382, Jun. 1999.

[7] K. Harris, G. L. Erickson, and R. E. Schwer, "Mar M 247 Derivations - Cm 247 Lc Ds Alloy Cmsx Single Crystal Alloys Properties & Performance," *Superalloys 1984*, pp. 221–230, 1984.

[8] O. A. Ojo, N. L. Richards, and M. C. Chaturvedi, "Study of the fusion zone and heat-affected zone microstructures in tungsten inert gas-welded INCONEL 738LC superalloy," *Metall. Mater. Trans. Phys. Metall. Mater. Sci.*, vol. 37, no. 2, pp. 421–433, 2006.

[9] L. N. Carter, C. Martin, P. J. Withers, and M. M. Attallah, "The influence of the laser scan strategy on grain structure and cracking behaviour in SLM powder-bed fabricated nickel superalloy," *J. Alloys Compd.*, vol. 615, pp. 338–347, 2014.

[10] M. J. Donachie and S. J. Donachie, *Superalloys A Technical Guide*. 2002.

[11] J. E. Doherty, B. H. Kea, and A. F. Giamei, "On the origin of the ductility enhancement in Hf-doped Mar-M200," *JOM*, vol. 23, no. 11, pp. 59–62, Nov. 1971.

[12] J. Zhang and R. F. Singer, "Effect of Grain-Boundary Characteristics on Castability of Nickel-Base Superalloys," *Metall. Mater. Trans. Phys. Metall. Mater. Sci.*, vol. 35 A, no. 3, pp. 939–946, 2004.

[13] D. Dye, O. Hunziker, and R. C. Reed, "Numerical analysis of the weldability of superalloys," *Acta Mater.*, vol. 49, no. 4, pp. 683–697, 2001.

[14] M. B. Henderson, D. Arrell, R. Larsson, M. Heobel, and G. Marchant, "Nickel based superalloy welding practices for industrial gas turbine applications," *Sci. Technol. Weld. Join.*, vol. 9, no. 1, pp. 13–21, 2004.

[15] A. J. Ramirez and J. C. Lippold, "High temperature behavior of Ni-base weld metal Part II - Insight into the mechanism for ductility dip cracking," *Mater. Sci. Eng. A*, vol. 380, no. 1, pp. 245–258, 2004.

[16] P. Kanagarajah, F. Brenne, T. Niendorf, and H. J. Maier, "Inconel 939 processed by selective laser melting: Effect of microstructure and temperature on the mechanical properties under static and cyclic loading," *Mater. Sci. Eng. A*, vol. 588, pp. 188–195, Dec. 2013.

[17] F. Liu, X. Lin, G. Yang, M. Song, J. Chen, and W. Huang, "Microstructure and residual stress of laser rapid formed Inconel 718 nickel-base superalloy," *Opt. Laser Technol.*, vol. 43, no. 1, pp. 208–213, Feb. 2011.

[18] N. J. Harrison, I. Todd, and K. Mumtaz, "Reduction of micro-cracking in nickel superalloys processed by Selective Laser Melting: A fundamental alloy design approach," *Acta Mater.*, vol. 94, pp. 59–68, Aug. 2015.

[19] S. Catchpole-Smith, N. Aboulkhair, L. Parry, C. Tuck, I. A. Ashcroft, and A. Clare, "Fractal scan strategies for selective laser melting of 'unweldable' nickel superalloys," *Addit. Manuf.*, vol. 15, pp. 113–122, May 2017.

[20] R. W. E. P.W. Davies, "The contribution of voids to the tertiary creep of gold," *Acta Met.*, vol. 13, no. 3, pp. 353–361, 1965.

[21] A. Baldan, "Rejuvenation procedures to recover creep properties of nickel-base superalloys by heat treatment and hot isostatic pressing techniques - A review," *J. Mater. Sci.*, vol. 26, no. 13, pp. 3409–3421, 1991.

[22] M. Cloots, P. J. Uggowitzer, and K. Wegener, "Investigations on the microstructure and crack formation of IN738LC samples processed by selective laser melting using Gaussian and doughnut profiles," *Mater. Des.*, vol. 89, pp. 770–784, 2016.

[23] C. S. Montross, V. Florea, and M. V. Swain, "The influence of coatings on subsurface mechanical properties of laser peened 2011-T3 aluminum," *J. Mater. Sci.*, vol. 36, no. 7, pp. 1801–1807, Apr. 2001.

[24] A. K. Gujba and M. Medraj, "Laser Peening Process and Its Impact on Materials Properties in Comparison with Shot Peening and Ultrasonic Impact Peening," *Materials*, vol. 7, no. 12, pp. 7925–7974, 2014.

[25] N. Kalentics, R. Logé, and E. Boillat, "Method and Device for Implementing Laser Shock Peening or Warm Laser Shock Peening During Selective Laser Melting," US20170087670 A1, 30-Mar-2017.

[26] N. Kalentics, E. Boillat, P. Peyre, S. Ćirić-Kostić, N. Bogojević, and R. E. Logé, "Tailoring residual stress profile of Selective Laser Melted parts by Laser Shock Peening," *Addit. Manuf.*, vol. 16, pp. 90–97, Aug. 2017.

[27] N. Kalentics *et al.*, "3D Laser Shock Peening – A new method for the 3D control of residual stresses in Selective Laser Melting," *Mater. Des.*, vol. 130, pp. 350–356, Sep. 2017.

[28] N. Kalentics, A. Burn, M. Cloots, and R. E. Logé, "3D laser shock peening as a way to improve geometrical accuracy in selective laser melting," *Int. J. Adv. Manuf. Technol.*, Nov. 2018, https://doi.org/10.1007/s00170-018-3033-3.

[29] N. Kalentics, K. Huang, M. O. V. de Seijas, A. Burn, V. Romano, and R. E. Logé, "Laser Shock Peening: a promising tool for tailoring metallic microstructures in Selective Laser Melting," *J. Mater. Process. Technol.*, Nov. 2018, 10.1016/j.jmatprotec.2018.11.024.

[30] R. Engeli, "Selective laser melting & heat treatment of γ´ strengthened Ni-base superalloys for high temperature applications," Doctoral Thesis, ETH Zurich, 2017.

[31] V. D. Divya *et al.*, "Microstructure of selective laser melted CM247LC nickel-based superalloy and its evolution through heat treatment," *Mater. Charact.*, vol. 114, pp. 62–74, 2016.

[32] X. Wang, L. N. Carter, B. Pang, M. M. Attallah, and M. H. Loretto, "Microstructure and yield strength of SLM-fabricated CM247LC Ni-Superalloy," *Acta Mater.*, vol. 128, pp. 87–95, Apr. 2017.

[33] R. P. Turner, C. Panwisawas, Y. Lu, I. Dhiman, H. C. Basoalto, and J. W. Brooks, "Neutron tomography methods applied to a nickel-based superalloy additive manufacture build," *Mater. Lett.*, vol. 230, pp. 109–112, Nov. 2018.

Chapter 10 (Supplementary)

Influence of Hf on the heat treatment response of additively manufactured Ni-base superalloy CM247LC

Seth Griffiths[1], Hossein Ghasemi-Tabasi[2], Anthony De Luca[1], Joanna Pado[1], Shreyas S. Joglekar[1], Jamasp Jhabvala[2], Roland E. Logé[2], Christian Leinenbach[1]

1. Empa - Swiss Federal Laboratories for Materials Science and Technology, Überlandstrasse 129, 8600 Dübendorf, Switzerland
2. Thermomechanical Metallurgy Laboratory, PX Group Chair, Ecole Polytechnique Fédérale de Lausanne (EPFL), 2002 Neuchâtel, Switzerland

S. Griffiths, H. Ghasemi-Tabasi, A. De Luca, J. Pado, S.S. Joglekar, J. Jhabvala, R.E. Logé, C. Leinenbach, Influence of Hf on the heat treatment response of additively manufactured Ni-base superalloy CM247LC, Mater. Charact. 171 (2021) 110815. doi:https://doi.org/10.1016/j.matchar.2020.110815.

Contribution:
Hossein Ghasemi Tabasi performed the high temperature mechanical tests on the printed samples, using the Gleeble machine. He wrote the experimental part on the high temperature test, and discussions on the results (3.4, 3.5).

Abstract

The influence of Hf on the heat treatment response of a Laser Powder Bed Fusion (L-PBF) fabricated Ni-base superalloy was investigated. A Hf-free version of CM247LC, CM247LC NHf, and CM247LC (~1.4 wt% Hf) were subjected to identical thermal treatments and characterized. After solutionizing at 1260 °C for 2 h, both alloys displayed recrystallization and grain growth. The CM247LC NHf had numerous annealing twins suggesting that Hf inhibits twin formation. The CM247LC NHf alloy displayed a lower peak hardness than CM247LC (5000 MPa and 5200 MPa, respectively) and this was attributed to a ~6% point reduction (Calphad calculated) in γ′ phase fraction due to the removal of Hf. Despite the lower hardness values, the CM247LC NHf displayed a higher yield strength than CM247LC at 760 °C (969 MPa and 926 MPa, respectively). Elongation at fracture at 760 °C was similar (~1%) for both CM247LC and CM247LC NHf. The removal of Hf was shown to be effective at mitigating the strain age cracking susceptibility of CM247LC, likely due to the decrease in γ' phase fraction and lattice mismatch.

Keywords : Ni-base superalloys, Additive manufacturing, CM247LC

1. Introduction

Additive Manufacturing (AM), namely Powder Bed Fusion (PBF), of the $L1_2$-Ni_3(Al,Ti, etc.) – also known as γ′ – precipitate strengthened Ni-base superalloys is especially appealing but remains a challenge due micro-cracking. Despite the extensive investigations on the AM of γ′ strengthened Ni-base superalloys, the processing by PBF remains challenging due to the issue of extensive micro-cracking in the fabricated parts [[1], [2], [3], [4], [5], [6], [7], [8], [9]]. Three approaches are typically employed to mitigate the micro-crack issue in PBF fabricated Ni-base superalloys: (i) post-processing (ii) process modification, and (iii) alloy design. Post-processing micro-crack mitigation is, to the authors' knowledge, limited to healing of cracks with exposure to high pressure and high temperature, namely hot isostatic pressing (HIP). Carter et al. [1] demonstrated that post-process HIP is effective at healing internal cracks in a Laser-PBF (L-PBF) fabricated CM247LC. One key disadvantage is that surface exposed micro-cracks are not closed by HIP. Since parts fabricated by AM are intended to be near-net-shape parts, surface exposed cracks would likely exist in the final part rendering the final part unusable.

Micro-crack mitigation by process modification includes preheating, scan strategy modification, melt pool control, and laser shock peening (LSP). Ramsperger et al. [6] reported crack-free CMSX-4 samples fabricated by Electron-PBF (E-PBF) when using high fabrication temperatures (1040 °C and above). Similarly, Hagedorn et al. [10] obtained L-PBF fabricated crack-free CM247LC by preheating the baseplate to 1200 °C. Carter et al. [1] demonstrated that a simple back and forth laser scan strategy, as opposed to

chess scanning, resulted in a homogenous microstructure less susceptible to crack formation. In a prior study [9] we demonstrated that the consolidation in conduction mode, as opposed to keyhole, or transition mode, results in a significant decrease in the micro-crack density. Kalentics et al. [11] demonstrated that 3D LSP applied during the L-PBF fabrication of CM247LC induced compressive residual stress which healed micro-cracks through a reverse brazing mechanism.

Crack mitigation through alloy modification has been demonstrated, but mostly in alloys with no or moderate fractions of γ′ phase. Harrison et al. [12] increased the solid-solution strengthening elements in Hastelloy X to successfully mitigate micro-cracking. Engeli et al. [13] demonstrated that the Si content of IN738LC needed to be lower than 0.02 wt% in order to fabricate crack-free parts. In a previous study [9], we showed that a new Hf-free variant of CM247LC, CM247LC NHf, had lower susceptibility to micro-crack formation due to a reduced freezing interval. However, micro-cracking was still observed and it is clear that a realistic solution to the micro-cracking problem in PBF fabricated Ni-base superalloys will require more than just one of the aforementioned mitigation routes. For example, joint process and alloy modification further improve crack mitigation in Hf-free CM247LC consolidated parts [9].

However, consolidation by AM is only the first step in producing γ′ strengthened Ni-base superalloys parts, the γ′ precipitates need a heat treatment to nucleate and grow to optimal sizes. In conventionally cast superalloys a solutionizing heat treatment and aging treatment are required to obtain the optimal size and volume fraction of γ′. Naturally, this is a next step for AM processed superalloys, which are largely void of γ′ precipitates after printing [9]. Studies on the heat treatment and mechanical properties of PBF fabricated precipitation strengthened Ni-base alloys is somewhat limited, likely due to the aforementioned extensive micro-cracking issue [3,[14], [15], [16]]. Divya et al solutionized a SLM fabricated CM247LC sample at 1230 °C for two hours and observed limited recrystallization and a grain structure similar to that observed in the as-processed condition [3]. The γ′ precipitates in both the recrystallized and unrecrystallized grains (solutionized condition) had a radius of ~100–250 nm, but the γ′ in the unrecystalized grains had a more irregular morphology [3]. Carbides were located on the grain boundaries and were ~200–500 nm in diameter after solutionizing. Dislocation density at cell boundaries was also observed to decrease as to be expected in a solutionized sample [3]. Kunze et al. HIPed (1180 °C 4 h), solutionized (1120 °C 2 h), and aged (850 °C 20 h) a L-PBF fabricated IN738LC [14]. No recrystallization or grain coarsening was observed. The heat treated samples had a duplex γ′ precipitate size distribution of ~50 nm and ~500 nm in radius. Kanagarajah et al. solutionized (1160 °C 4 h) and aged (850 °C 16 h) L-PBF fabricated IN939 [15]. Recrystallization was observed in the heat treated samples. The γ′ precipitate radius was ~30 nm. Boswell et al. investigated the cracking occurring during the post-process thermal treatment of an AM fabricated CM247LC and attributed the cracking to both the ductility-dip and strain age cracking mechanisms [16]. A minimum in

post process thermal treatment crack density was observed for samples undergoing thermal treatment at 850 °C; at this temperature, strain age cracking was identified as the primary cracking mechanism.

Room and elevated temperature mechanical properties have been reported for IN939 [15] and IN738 [14]. Few studies with high γ′ containing alloys, such as CM247LC, exist, likely due to the extensive micro-cracking observed in these alloys. Kanagarajah et al. reported room temperature and 750 °C yield strengths of ~1000 MPa (10–15% elongation) and 800 MPa (~1% elongation), respectively, for L-PBF fabricated IN939 solutionized (1160 °C 4 h) and aged (850 °C 16 h) [15]. Rickenbacker et al. performed room temperature and 850 °C tensile testing on HIPed (not reported), solutionized (1120 °C 2 h), and aged (850 °C 24 h) L-PBF fabricated IN738LC [17]. The yield strength of HIPed, solutionized, and aged IN738 in the transverse direction (gauge section perpendicular to build direction) was reported as 933 ± 8 and 610 ± 1 MPa for the room temperature and 850 °C condition, respectively. Samples parallel to build direction had slightly lower yield strengths of 786 ± 4 and 503 ± 1 MPa for the room temperature and 850 °C condition, respectively. Elongation at fracture was lower in the transverse direction than in the parallel orientation (11.2 ± 1.9% for parallel, and 8.4 ± 4.6% for transverse at room temperature; 14.2 ± 3.9% for parallel, and 8.0 ± 1.2% for transverse at 850 °C). Wang et al. [2] performed tensile testing on L-PBF fabricated CM247LC (tensile bars oriented parallel to the build direction) and observed a 792 MPa yield strength with a 6–8% elongation at fracture. Samples were not HIPed prior to testing. Kunze et al. [14] performed creep tests at 850 °C of both SLM produced samples and traditionally cast samples and found the creep rupture strength to be lower for the SLM fabricated samples. This is not completely unexpected due to the known correlation between grain size and creep properties.

While the influence of post-process heat treatment on a L-PBF fabricated CM247LC has been investigated [3,16], there are currently no studies that address versions of the alloy tailored for micro-crack mitigation, namely CM247LC NHf. Any modification to an existing alloy, even slight composition range changes, could have profound impacts on the microstructural response to heat treatment and the resulting mechanical properties, as for example a loss in ductility [9]. Here, we present an investigation of the micro-structural evolution of both CM247LC and CM247LC NHf during HIPing, solutionizing, and aging. We also present elevated temperature tensile tests of the two alloys in an attempt to address the ductility concerns.

2. Experimental methods

2.1. Materials and additive manufacturing

Oerlikon Metco (Pfaeffikon, Switzerland) produced the inert-gas atomized powders of CM247LC as well as the Hf-free modified version, named herein CM247LC NHf. Both batches of powder had a 15–45 μm

size range and a D_{50} of approximately 32 μm. Chemical composition of the powder was measured by inductively coupled plasma optical emission spectrometry (ICP-OES) and combustion analysis (for carbon), Table 1.

Table 1. Chemical composition of the CM247LC and CM247LC NHf powders. Composition measured with ICP-OES and combustion analysis.

wt. %	**Al**	**B**	**C**	**Co**	**Cr**	**Fe**	**Hf**	**Mo**	**Ni**	**Ta**	**Ti**	**W**	**Zr**
CM247LC	5.71	0.017	0.06	9.24	8.62	0.02	1.37	0.54	Bal	3.08	0.73	9.93	0.006
CM247LC NHf	5.56	0.01	0.07	9.14	8.36	0.07	0.005	0.53	Bal	3.18	0.63	9.48	0.018

The consolidated samples (5 × 5 × 5 mm cubes) for the thermal treatment study and for microstructure characterization were fabricated on a Sisma MySint 100 (Sisma S.p.A., Italy), equipped with a 200 W 1070 nm fiber-laser operating in continuous wave mode with a Gaussian intensity distribution and a 55 μm spot size ($1/e^2$). The samples were built on a 34.5 mm diameter stainless steel build plate with the following parameters: 175 W (7.35×10^6 W/cm^2), 750 mm/s scanning speed, 0.075 mm hatch spacing, and a 30 μm layer thickness. Samples were processed with a bidirectional scan strategy (90 degree rotation between layers) with border contour. Flowing argon shielding gas (99.996% purity) ensured the oxygen content in the build chamber did not exceed 0.1% O_2. Specimen blanks (21 × 21 × 81 mm blocks, build perpendicular to long axis) for the manufacturing of elevated temperature tensile test samples were fabricated from CM247LC and CM247LC NHf with the identical parameters listed above.

2.2. Thermal treatments

Isothermal aging experiments on CM247LC and CM247LC NHf were performed in air at 850 °C on 5 × 5 × 5 mm cubes. The samples were solutionized at 1260 °C for 2 h prior to the aging experiments. All heat treatments were done independently and each stage was followed by air-cooling. Mechanical property test blanks were sent to Deloro Htm GmbH (Biel, Switzerland) for HIPing at 1225 °C and 1000 bar for 5 h. After HIPing, the specimen blanks (and witness coupons ~20 × 21 × 20 mm) were solutionized (1260 °C 2 h) in air followed by air cooling and then aged (850 °C 8 h) in air followed by air cooling.

2.3. Characterization

Cubes and blanks for microstructure and defect characterization were sectioned (parallel to the build direction), cold-mounted in epoxy, ground, polished with monocrystalline diamond suspension and finally

lapped with 50 nm colloidal silica. Samples intended for γ' size analysis were vibro-polished with 50 nm colloidal silica and etched with V2A (200 ml H2O, 200 ml HCL 37%, 20 ml HNO3 65%) for 2 min at a temperature of 50 °C. Scanning Electron Microscope (SEM) analysis was performed with a FEI NanoSEM 230 and FEI Quanta 650 in secondary and backscatter electron imaging mode.

Microhardness measurements were performed with a Fischerscope HM2000 hardness tester with a standard Vickers diamond pyramid intender with a 136° face angle, an automated stage, and microscope. The Vickers microhardness was measured for all samples with a 1800 mN load for 60 s. Between 10 and 20 indentations were made per sample, typically in one line parallel to the build direction. No significant variation of microhardness along the build direction was observed.

Lamellae for scanning transmission electron microscopy (STEM) analysis were prepared from the aforementioned cubes (lamellae is perpendicular to build direction) using an FEI Helios NanoLab 600i focused ion beam (FIB). A FEI Titan Themis microscope, equipped with a probe spherical aberration corrector and a SuperEDX system (ChemiSTEM technology) with four silicon drift detectors for energy-dispersive X-ray (EDX) spectroscopy, was used for STEM analysis. The microscope was operated at 300 kV with a beam convergence semi-angle of 25 mrad. The annular dark field (ADF) detector has a inner and outer collection semi-angles of 66 and 200 mrad, respectively. STEM-EDX spectrum images (with background correction) were pre-filtered.

The average size distribution of the γ′ precipitates after isothermal aging was determined via image analysis of BSE images of the aforementioned cross sections. All micrographs were taken in the center of each cubes. Image analysis was performed with ImageJ [18]. BSE images were filtered with a FFT bandpass filter, and thresholded to highlight the γ′ precipitates. Next, thresholding errors were corrected by a combination of filling holes inside of the precipitates and using a watershed tool to separate conjoined precipitates. The analysis particle feature was used to measure the equivalent γ′ precipitate size (modeled as a circle).

Density analysis of the HIPed mechanical property witness bars were performed via image analysis of 200× BSE SEM images. Carbide size and area fraction anaylsis of the HIPed, solutionized, and aged witness bars were performed via image analysis of 5000× BSE SEM images.

2.4. Thermodynamic simulations

Equilibrium phase fraction calculations of CM247LC and CM247LC NHf were performed with the TCNI5 database in ThermoCalc. The compositions used for the calculations are listed in Supplement Table I.

2.5. Mechanical property testing

Elevated temperature tensile testing was performed on a Gleeble 3800 machine at 760 °C (approximate minimum ductility temperature for superalloys [35]). Tensile dog-bone specimens (3 mm thick) were cut from specimen blanks via milling (profile) and wire Electro-discharge Machining (EDM) with the dimensions shown in Supplement Fig. 1. EDM surfaces were ground with P600 paper to remove the EDM re-cast layer. In the Gleeble machine, the samples are heated by Joule effect to 760 °C at a rate of 1.5 °C/s. The samples were kept at target temperature for 2 min, and then elongated at a constant rate of 3 mm/min. The process temperature is screened with K type thermocouple welded to the surface in the middle of the samples. The testing setup and the temperature during the experiment are shown in Supplement Fig. 2.

3. Results

3.1. As-fabricated samples

Fig. 1 presents BSE images of the as-fabricated samples, CM247LC (Fig. 1a, b) and CM247LC NHf (Fig. 1c, d). In a prior study [9], we reported the density of as-fabricated CM247LC and CM247LC NHf as greater than 99.9% (measured via Archimedes method), and the micro-crack density of the as-fabricated CM247LC and CM247LC NHf samples as 0.12 and 0.03 mm/mm^2, respectively. The as-fabricated microstructures of both alloys display a columnar grain morphology predominately oriented parallel to the build direction. The columnar grains of each alloy are composed of ~1 μm wide cells (low angle grain boundaries). In prior investigations on these alloys by Electron Backscatter Diffraction data (EBSD) [9], it was shown that the grain size (HAGB > 10°) in an as-fabricated CM247LC sample was ~40–80 μm wide and hundreds of μms in length. Both alloys contain carbides, ~55 nm in diameter and rich in Ti/Hf/Ta/W/C, located on the cell boundaries. Qualitatively, no significant difference in the carbide area fraction was observed. In-depth microstructural crystallographic and chemical characterizations of the as-printed condition of the two alloys can be found in our prior publication [9]. The as-fabricated microhardness of CM247LC and CM247LC NHf was 4337 ± 145 MPa and 4226 ± 92 MPa respectively.

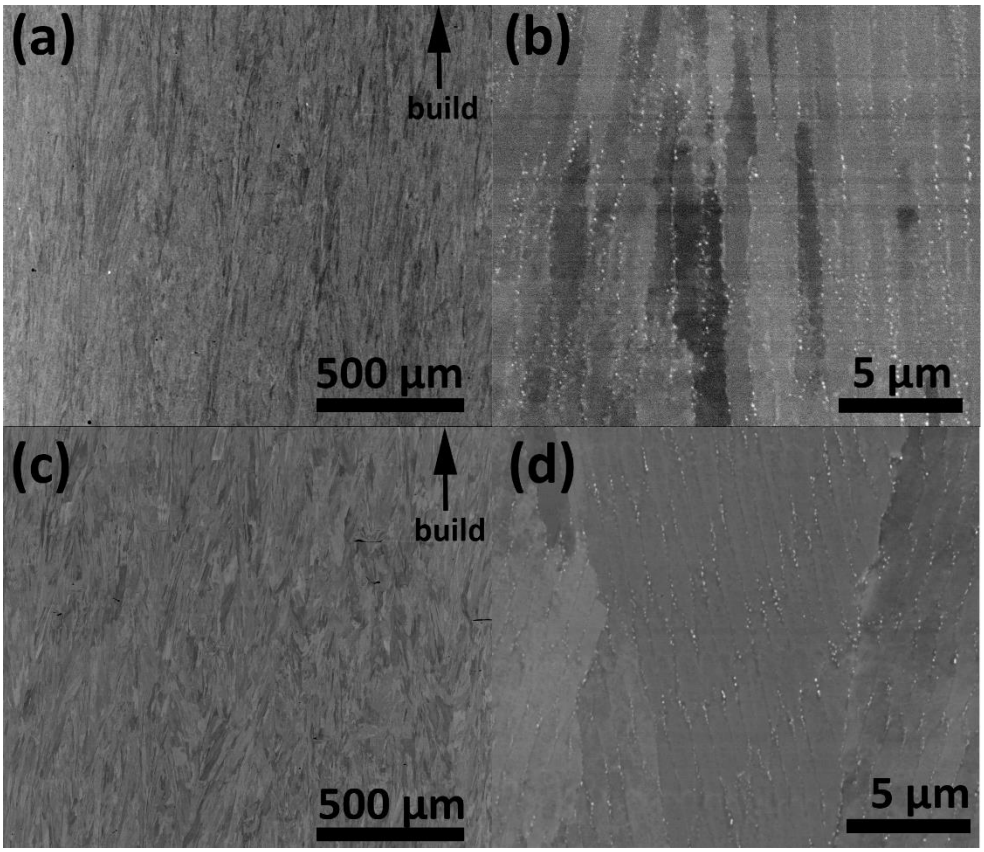

Fig. 1. BSE images of the as-fabricated samples (a,b) CM247LC (c,d) CM247LC NHf

3.2. Solutionized microstructure

Fig. 2 presents the microstructure of the solutionized CM247LC (Fig. 2a, b) and CM247LC NHf (Fig. 2 c, d) samples. The solutionized CM247LC sample is composed of columnar grains primarily oriented parallel to the build direction and ~150–250 µm in width and ~750 µms to mms in length. The solutionized CM247LC carbides are ~300 nm in diameter (Fig. 2b) and are typically found aligned in positions reminiscent of the original grain structure. These "walls" of vertically aligned carbides are efficient at pinning GB, or at least, slowing down the grain growth perpendicular to the build direction, potentially explaining why the columnar grain morphology remains.

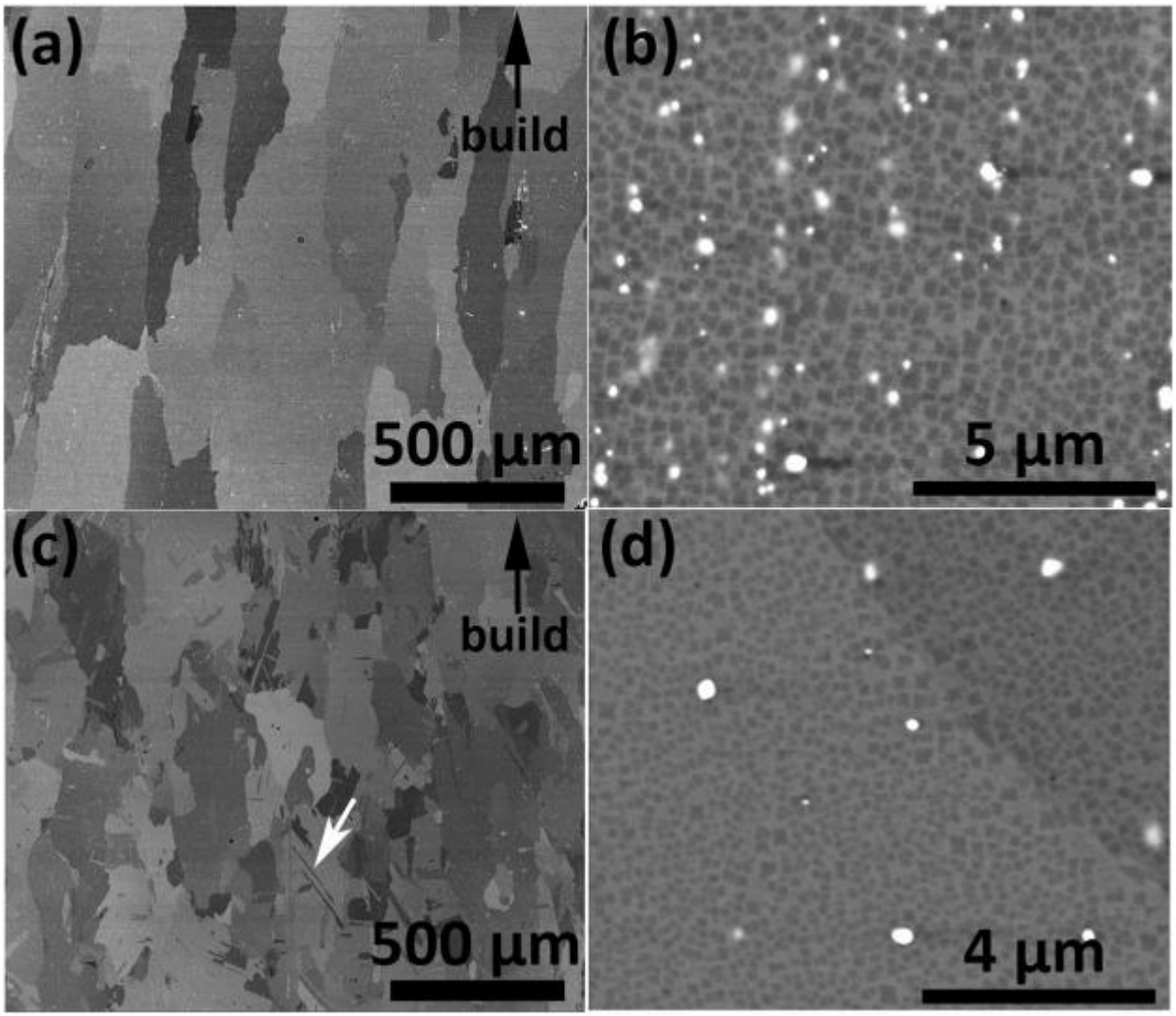

Figure 2. BSE images of the solutionized (1260 °C, 2 h) CM247LC (a, b) and CM247LC NHf (c, d).

In comparison, the grain microstructure of the solutionized CM247LC NHf sample appears finer and more equiaxed compared to the solutionized CM247LC. Also, numerous annealing twins are present (Fig. 2c, white arrow).

Due to the slow air cooling, γ′ precipitates are formed, with mean precipitate radii of 120 and 70 nm for the CM247LC and CM247LC NHf alloys, respectively. As these precipitates are formed during cooling, a large spread in size is observed (±30 nm); the distribution, however, appears mono dispersed.

Fig. 3 presents STEM-EDX maps taken from an as-fabricated CM247LC sample (Sample from prior study [9])(Fig. 3a) and a solutionized CM247LC sample (Fig. 3b). In the as-fabricated state, the CM247LC sample displayed significate levels of micro-segregation; Hf, Al, and Ti partitioning to the cell boundaries and W,

Co, and Ni partitioning to the cell cores, with Ti-W-Ta-Hf-rich carbides detected on cell boundaries. After solutionizing, all traces of the micro-segregation have disappeared and γ/γ′ phase partioning is evident. The γ channels are enriched in Cr, W, and Co and the γ' cuboids are enriched in Ni, Al, Ti, Ta, and Hf. Closer STEM-EDX investigation of some of the larger γ channels show the existence of even smaller γ′, about 25 nm radius (Supplementary Fig. 3). These precipitates represent a small fraction of the total γ′ phase and are expected to have formed in the latest stage of the slow air cooling. The number density of carbides is also strongly reduced, which correlate with their increase in sizes. Their chemistry might have also changed, as they appear to lack W. The homogenization behavior of CM247LC NHf is not anticipated to differ from CM247LC; therefore, the solutionized CM247LC NHf was not investigated.

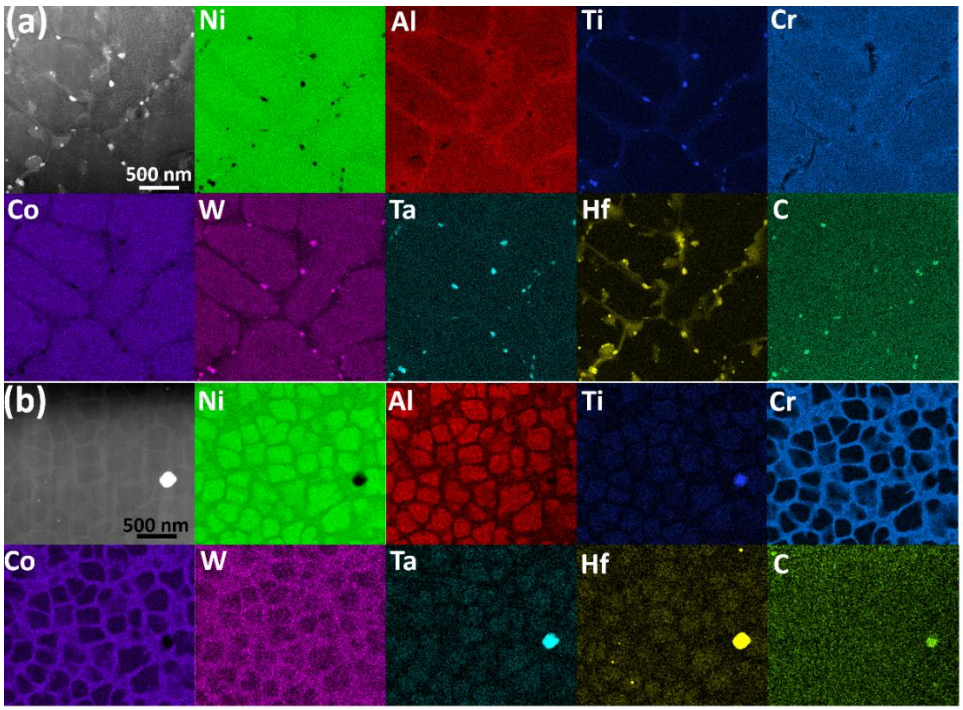

Fig. 3. (a) STEM-EDX map highlighting the micro-segregation of an as-fabricated CM247LC sample. Precipitates are enriched in Ti/Hf/Ta/W/C and are presumed to be carbides. (b) STEM-EDX map highlighting the homogenization (of the solidification segregation) in a solutionized CM247LC sample. The chemical analysis is performed using the Al-K, Ti-K, Cr-K, Hf-L, Ta-L, W-L, Co-K, Ni-K, Mo-K, Zr-K, and C-K lines.

3.3. Isothermal aging at 850 °C

The solutionizing temperature range for the Ni-base superalloys is generally limited at the upper end due to incipient melting concerns (1255 °C to 1282 °C solutionizing range for L-PBF fabricated CM247LC reported in [9]). The solutionizing temperature chosen for this study was 1260 °C, which is the same for solutionizing of conventional directionally solidified (DS) CM247LC [19]. Although removing Hf allows

to significantly open the solutionizing window (1226 °C to 1341 °C), the CM247LC NHf was also solutionized at 1260 °C for comparison purposes. The solutionizing heat treatment duration was kept at 2 h, consistant with literature on DS CM247LC. Aging for DS CM247LC is typically done at 870 °C for 8 h [20]; however, a temperature of 850 °C was utilized for this study due to logistical reasons, with the 20 °C difference not expected to significantly affect precipitation kinetics.

A plot of the microhardness evolution during isothermal aging at 850 °C of CM247LC and CM247LC NHf, for durations up to 44 days, is shown in Fig. 4. The microhardness values in the as-fabricated and solutionized (1260 °C 2 h) states are added for comparison purposes. After solutionizing, the microhardness of CM247LC and CM247LC NHf was 4534 ± 92 MPa and 4575 ± 65 MPa, respectively. Upon heat treatment at 850 °C, the microhardness rapidly increases. CM247LC reaches peak hardness in 8 h, at a value of 5210 ± 104 MPa. The CM247LC NHf appears to reach peak hardness (5000 ± 115 MPa) after 2 h. At 8 h at 850 °C, the CM247LC NHf has a hardness of 4843 ± 111 MPa. For both alloys, the hardness slowly decreases at comparable rates as aging duration increases, reaching down ~4600 MPa and ~4350 MPa for the CM247LC and NHf alloys after 44 days, respectively, falling back to hardness levels comparable to the solutionized states. On average, removing Hf lead to a ~4–5% reduction in microhardness after aging heat treatment.

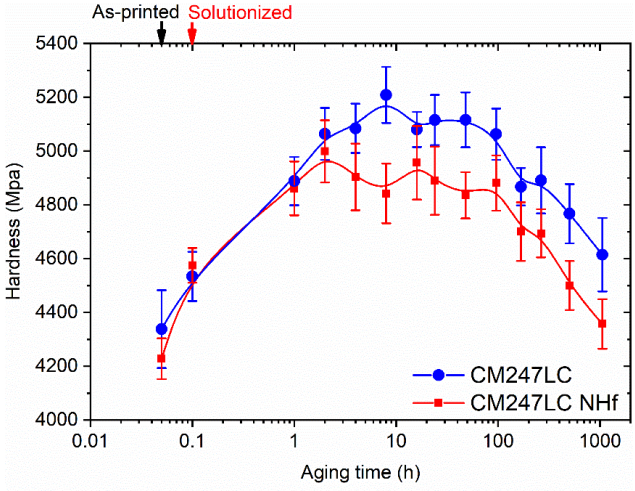

Fig. 4. Plot showing the evolution of microhardness with aging time at a temperature of 850 °C. Note: the change of slope observed at aging durations above 100 h is due to the log scaling.

3.4. Microstructural changes during isothermal aging

In order to link the observed microhardness evolution to microstructural changes, during isothermal aging at 850 °C, the samples were etched to better reveal the γ/γ′ microstructure of the two alloys. The γ′ size evolution was characterized by BSE, with the equivalent radius presented in Fig. 5. Starting from a pre-existing population of γ′ precipitates, which results from the slow air cooling from the solutionizing temperature, it appears that, for the two alloys, the γ′ precipitates are reducing in sizes as the aging duration increases to 8 h, which correspond to peak aging duration. At this time, the γ′ precipitates in CM247LC and CM247LC NHf have equivalent radii of 55 ± 17 and 34 ± 11 nm, respectively. BSE images of the peak aged CM247LC and CM247LC NHf samples is shown in Fig. 6. An inverse coarsening behavior (precipitates getting smaller, possibly due to cuboid splitting) is observed as duration increases to 8 h. For longer durations, the γ′ precipitates coarsen after that, with a slightly higher rate for the Hf-containing alloy. At long aging duration, the precipitates lose their cuboid shape and become initially more rounded, followed by enhanced degeneration and loss of their strength (Supplement Fig. 4 shows BSE images of 48 h aged samples). Closer inspection of the precipitate size distribution revealed that, for CM247LC, the γ′ distribution is bi-modal for durations ranging between 1 and 8 h. A comparison between the aged and solutionized distributions is provided in Supplementary Fig. 5, which allows to tentatively separate the two populations (new small precipitates vs ones formed on solutionizing) by applying a size threshold. Fig. 7a present the size evolution of the two precipitate distributions, during isothermal aging at 850 °C. After 1 h of aging already, a significant fraction of γ′ with radii of ~40 nm are resolved in CM247LC (Fig. 7b). A significant reduction in radii of the large γ′ precipitates in the first 4 h is observed, while the smaller population slowly grows. At durations of 4 h and longer, the two distributions are indistinguishable and can thus be considered as one. Given the overall smaller γ` precipitate radii observed in the CM247LC NHf samples, it is not possible to distinguish by BSE (smallest equivalent radius ~ 25 nm) the formation of an even smaller second population of γ′ precipitates. However, it is very likely that the same inverse coarsening mechanism observed in the CM247LC alloy occurs in the Hf-free version.

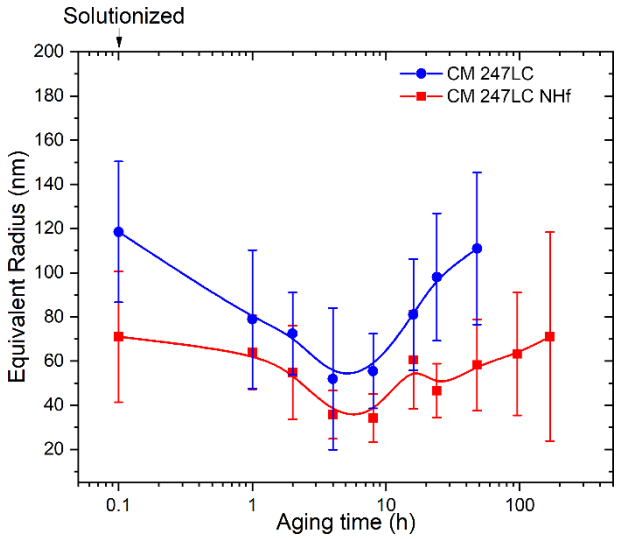

Fig. 5. Equivalent radius of γ′ precipitates at various isothermal aging (850 °C) times. All samples were solutionized (1260 °C, 2 h) prior to aging.

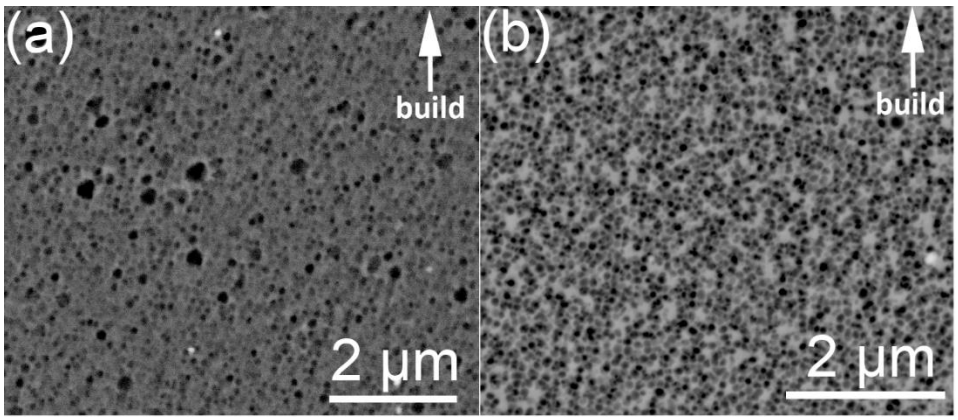

Figure 1. BSE images of (a) CM247LC and (b) CM247LC NHf solutionized(1260°C, 2 hr) and aged (850 C 8hrs). The CM247LC NHf alloy contains a refined population of γ'.

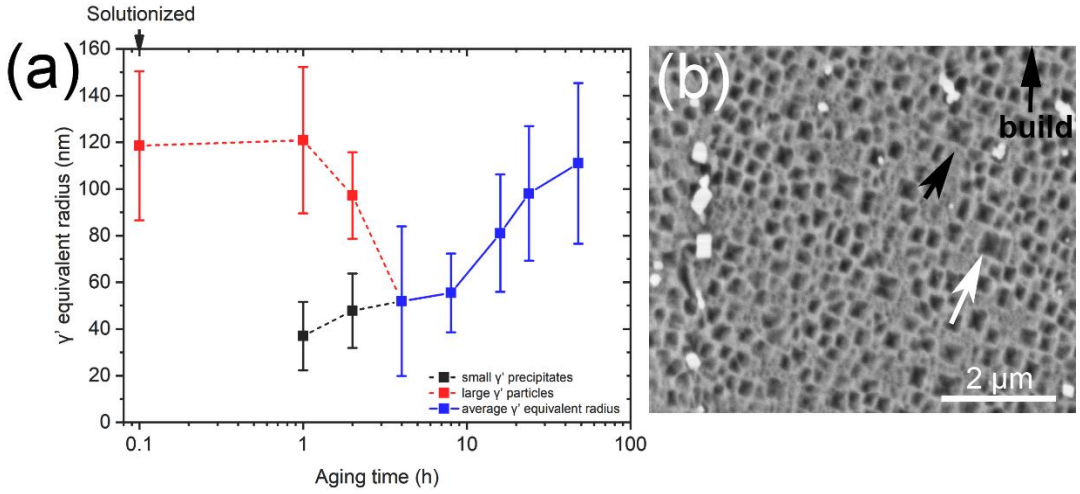

Figure 2. (a) Equivalent radius of γ`precipitates in CM247LC at various isothermal aging (850°C) times. A bi-modal distribution is observed for up to 4 hrs. (b) BSE image of the bi-modal γ`precipitate distribution (1 h). The white arrow point to 120 nm radius precipitates and the black arrow points to 37 nm radius precipitates.

3.5. HIPed specimens for mechanical property testing

The microstructure of HIPed (1225 °C, 5 h, 1000 bar) CM247LC and CM247LC NHf is shown in Fig. 8. No cracking was observed in the HIPed samples (lower magnification images are presented in Supplement Fig. 6). The post HIP densities (measured by image analysis) was greater than 99.9% for both the CM247LC and CM247LC NHf blanks; however, the CM247LC NHf sample did display 0.04% points more voids (highlighted by white arrows in Fig. 8). The voids appear to be unclosed lack of fusion voids. No significant grain microstructure change was observed in the HIPed CM247LC samples, aside from carbide coarsening (~55 nm diameter as-fabricated, ~100–800 nm diameter HIPed). The grain microstructure of HIPed CM247LC NHf samples has recrystallized and numerous annealing twins are observed. Carbide coarsening was also observed in the HIPed CM247LC NHf samples (~60 nm diameter as-fabricated, ~100–900 nm diameter HIPed). Although large γ′ precipitates were observed post HIPing, since the next stage in the thermal processing was solutionizing, their size distribution was not analyzed.

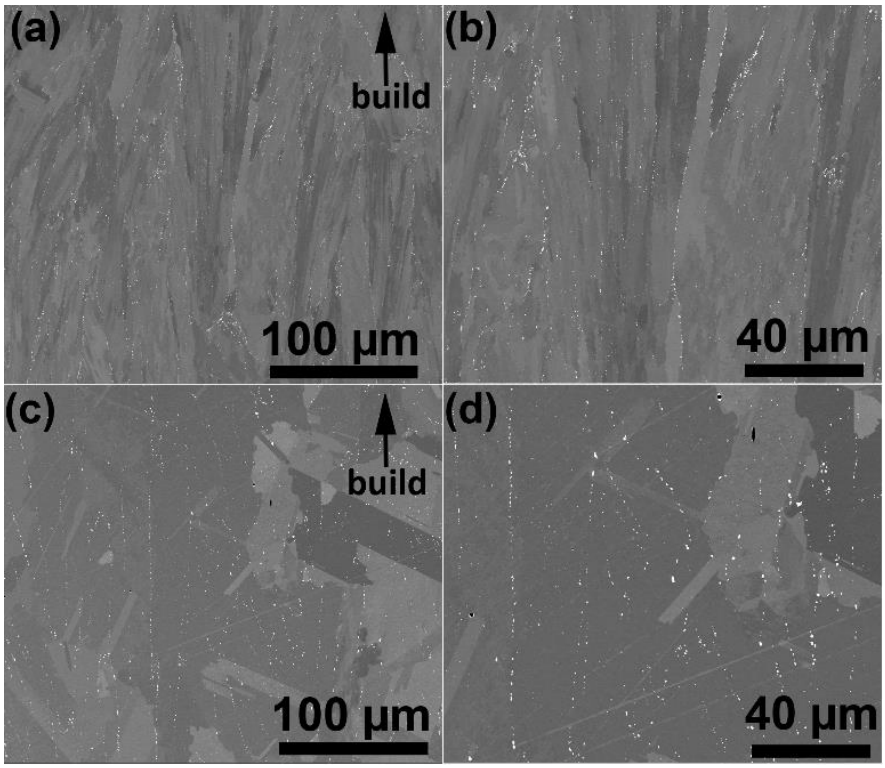

Figure 3. BSE images of HIPed mechanical test bars. Images approximately taken from the center of the 80 mm bar length. (a,b) CM247LC (c,d) CM247LC NHf.

The microstructure of HIPed and solutionized (1260 °C, 2 h) CM247LC and CM247LC NHf witness bars is shown in Fig. 9. Recrystallization and grain growth has occurred for the HIPed and solutionized (1260 °C, 2 h) CM247LC sample (Fig. 9. (a)). No significant difference in grain microstructure was observed between the HIPed and solutionized CM247LC NHf samples and the HIPed only CM247LC NHf samples. Cuboidal γ′ precipitates were observed in HIPed and solutionized CM247LC and CM247LC NHf samples. The γ′ precipitates (in the center of the witness bar) were ~150–200 and ~150–250 nm in radius for the CM247LC and CM247LC NHf samples, respectively; however, a detailed γ′ analysis was not performed. The carbide size (feret size) for the CM247LC and CM247LC NHf HIPed and solutionized samples is 0.44 ± 1.50 µm and 0.35 ± 0.4 µm, respectively. The HIPed and solutionized CM247LC sample appears to have rougher grain boundaries than that of the CM247LC NHf samples, but this was not quantified.

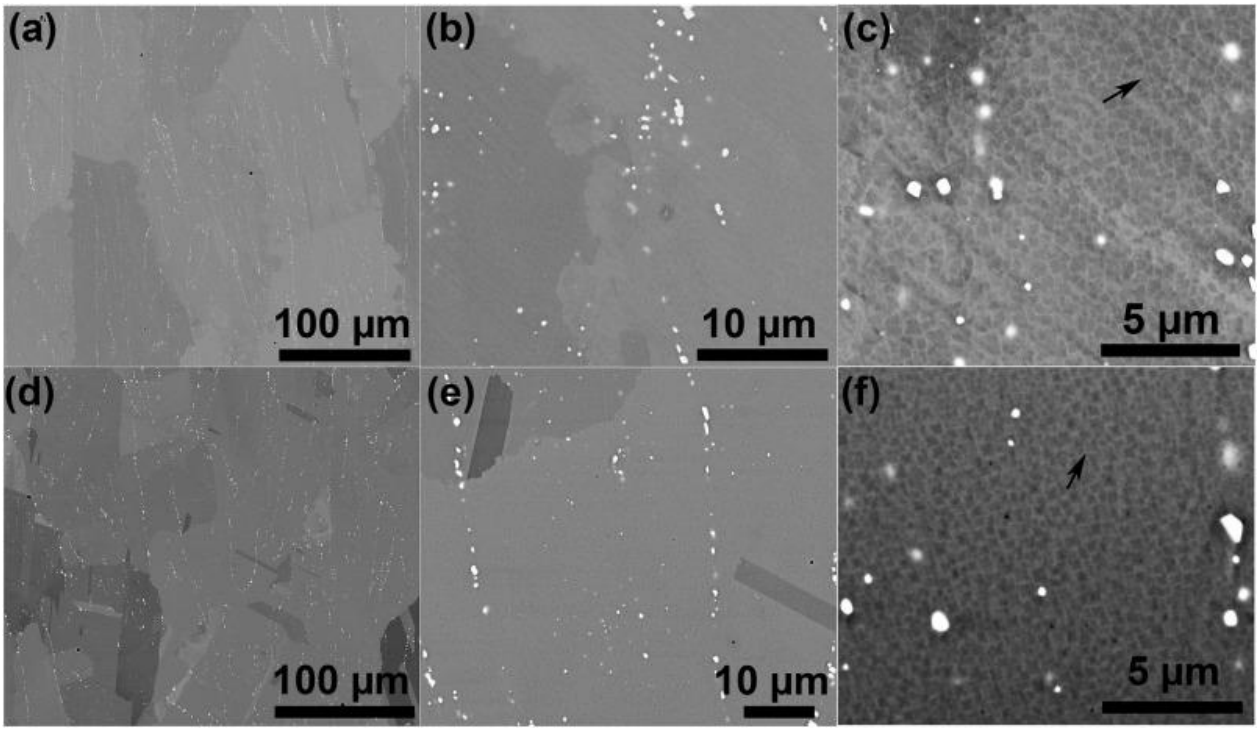

Figure 9. BSE images of HIPed and solutionized witness bars. Images approximately taken from the center of the witness bar. (a, b, c) CM247LC (d, e, f) CM247LC NHf. Black arrows point to the γ′ precipitates.

Macro-cracks(cracks hundreds of µm to mm in length) were observed on the HIPed and solutionized (1260 °C, 2 h) CM247LC witness bars (Fig. 10), but not on the CM247LC NHf witness bars. The cracking appears to be randomly oriented and intergranular (Fig. 10 (a)). The crack faces have a mostly smooth appearance (Fig. 10 (c, d)), with some small topography (small bumps) and bright particles observed (Fig. 10 (c, d)). A higher magnification image of Fig. 10 (c) is shown in Fig. 10 (e). Upon closer examination, there are line-like features (black arrow) on the bump surfaces.

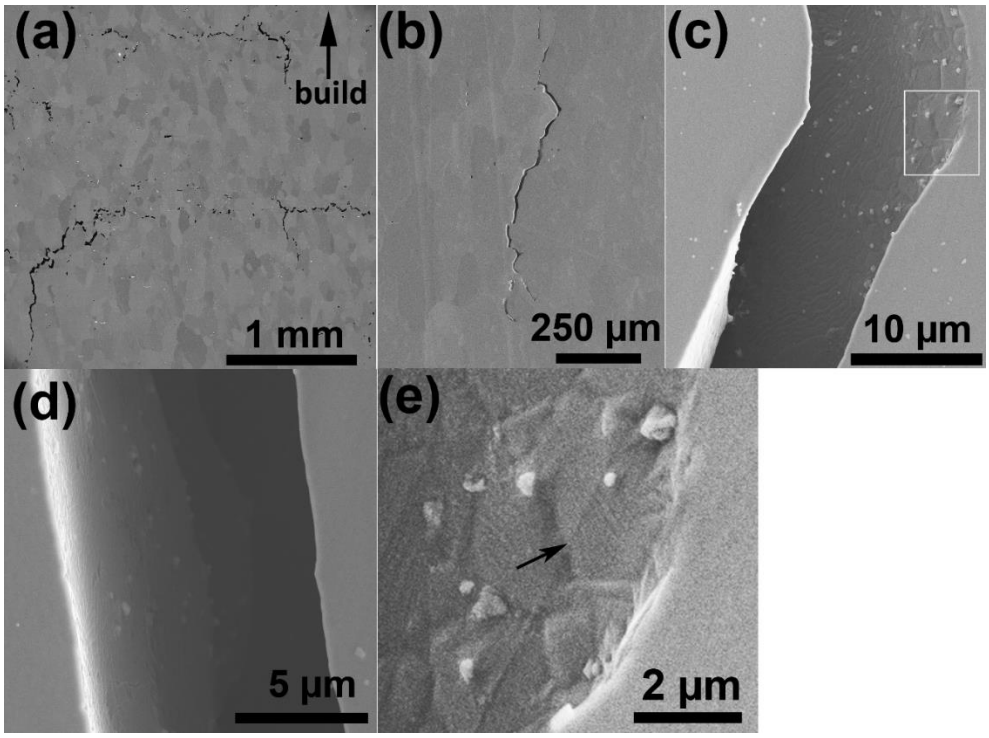

Figure 10. SE images of macro-cracks in the CM247LC witness bar post HIPing and solutionizing. (a, b) overview image of cracks propagating along grain boundaries. (c, d) The crack surfaces appear smooth with small topography and bright particles. (e) higher magnification of the region in c, revealing the presence of line like features (black arrow).

The microstructure of HIPed, solutionized (1260 °C, 2 h), and aged (850 °C, 8 h) CM247LC and CM247LC NHf witness bars is shown in Fig. 11. No significant change in the grain microstructure occurred after aging. Analysis of the γ' precipitates was not performed due to inadequate images and the small γ' size. The carbide sizes (feret size) for the CM247LC and CM247LC NHf HIPed, solutionized, and aged samples are 0.57 ± 0.33 µm and 0.61 ± 0.35 µm, respectively. The carbide area fraction of the CM247LC and CM247LC NHf samples after HIPing, solutionizing and aging were ~1.7% and ~0.9%, respectively. Just like in the HIPed and solutionized CM247LC sample, the HIPed, solutionized, and aged CM247LC sample appears to have rougher grain boundaries than that of the CM247LC NHf samples, but this was not quantified.

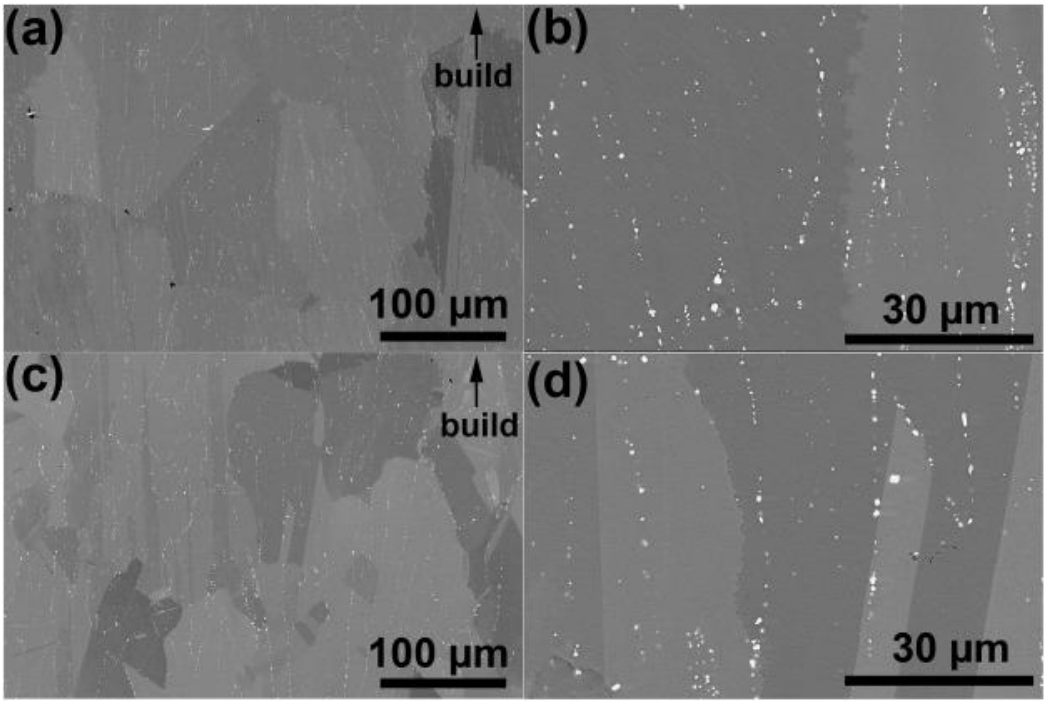

Figure 11. BSE images of HIPed, solutionized, and aged witness bars. Images approximately taken from the center of the witness bar. (a, b) CM247LC (c, d) CM247LC NHf.

3.6. Mechanical properties at 760 °C

While the Hf-free modified CM247LC alloy exhibit a reduced microhardness by ~5%, it is important to investigate other changes in mechanical properties. High temperature tensile tests were thus conducted at 760 °C using a Gleeble machine on consolidated parts from CM247LC and CM247LC NHf. The samples were HIPed, solutionized and then aged at 850 °C for 8 h (peak hardness), with the results presented in Table 2. The presented data is the average of 3 tests per alloy. The CM247LC samples displayed a 0.2% offset yield strength of 926 ± 13.3 MPa and an elongation at fracture of 1.4 ± 0.05% at 760 °C. The CM247LC NHf samples displayed a 0.2% offset yield strength of 969 ± 25.1 MPa and an elongation at fracture of 1.2 ± 0.38% at 760C. A higher degree of elongation data scatter was observed for the CM247LC NHf alloy. One of the CM247LC NHf samples tested fractured prior to 0.2% offset yield and this sample was not included in the averaged data. Overall, the Hf-free alloy is characterized by a ~5% higher tensile strength than the base alloy, despite its lower microhardness. It however could come at the cost of slightly lower ductility, but the difference remains within standard deviation. In comparison, conventionally cast and heat treated polycrystalline CM247LC tensile tested at 760 °C by Huang and Koo [21] displayed a similar yield strength of 990 MPa but a significantly higher elongation at fracture of 7.8%. Tang et al. [22] tensile tested AM fabricated and heat treated CM247LC and obtained a yield strength of ~900 MPa and an

elongation at fracture of 15%. It is important to note that in contrast to the samples tested by Tang et al., our tests were done transverse to the build direction, which is expected to have a lower ductility.

Table 2. Yield strength and elongation at fracture for peak aged CM247LC and CM247LC NHf samples tested at 760C. Error (±) represents the standard deviation.

	~760°C Tensile Tests	
	0.2% Offset Yield [MPa]	**Elongation at Fracture [%]**
Cast Polycrystalline CM247LC [21] Solutionized: 1221°C 2 h Aged: 771°C 20 h Grain size: 150 – 200 µm	990	7.8
AM-fabricated CM247LC [22] Solutionized: 1260°C 2 h Stabilized: 1079°C 2 h Aged: 871°C 20 h	~ 900 (at 800°C)	~15 (at 800°C)
AM-fabricated CM247LC (This study)	926 ± 13	1.4 ± 0.05
AM-fabricated CM247LC NHf (This study)	969 ± 25	1.2 ± 0.38

Fig. 12 displays fractography of a CM247LC sample (911 MPa yield and 1.3% elongation, Fig. 12a, b, c) and a CM247LC NHf sample (988 MPa yield and 0.73% elongation, Fig. 12d, e, f) tested to fracture at 760 °C. All fractures, on both CM247LC and CM247LC NHf samples, intersected at least one thermocouple spot weld. Overall, the CM247LC NHf samples (Fig. 12d) had a flatter, less tortuous, fracture face than the CM247LC (Fig. 12a) samples. This is most certainly related to the very different grain morphology, with CM247LC keeping a columnar grain structure post heat treatment, while grains in CM247LC NHf are more equiaxed. Both samples displayed an intergranular appearance on the fracture faces, but this appeared more pronounced on the CM247NHf samples.

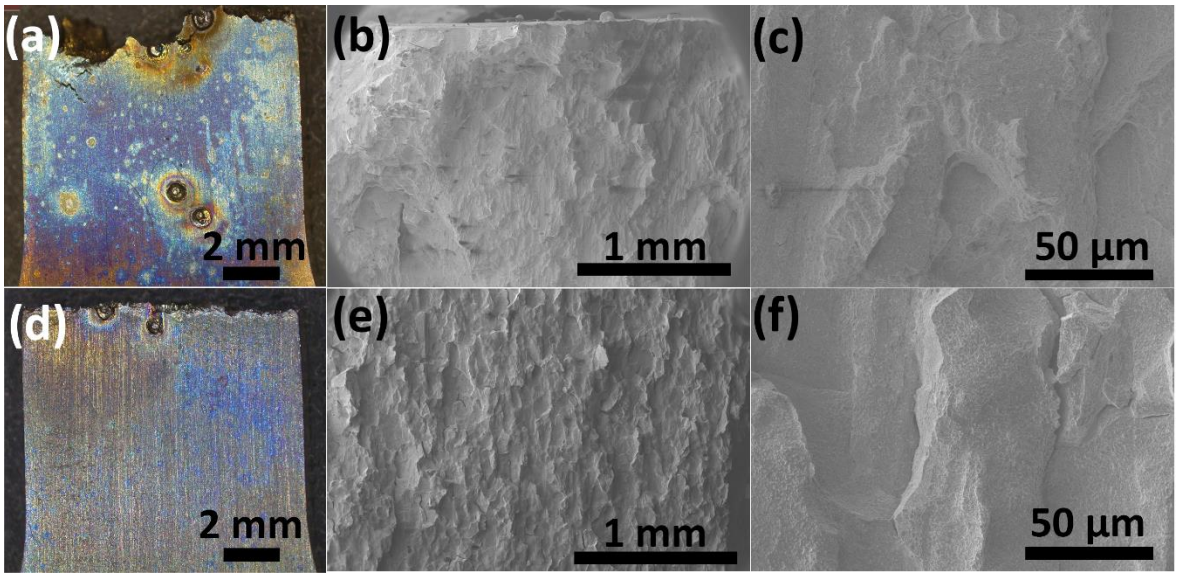

Figure 4. CM247LC samples (a,b,c) and CM247LC NHf samples (d,e,f) tested to fracture at 760 °C

4. Discussion

Significant γ′ phase precipitation was observed in the as-solutionized condition, which is contrary to what is traditionally expected after a solutionizing heat treatment. However, the Ni-base superalloys are typically highly sensitive to cooling rate from solutionizing, with the observation of γ′ phase precipitation after solutionizing being common [23]. Air cooling (no convection) was utilized for all samples, but the cooling rate was not quantified. The peak-aged condition for the isothermally (850 °C) aged CM247LC was obtained at 8 h and 2 h for CM247LC NHf; however, as there is minimal hardness difference between 2 h and 8 h for CM247LC NHf, 8 h was selected for both alloys allowing direct comparison. Inverse coarsening behavior was observed in both alloys during the first few hours of aging. This behavior has been observed in other superalloys and is attributed to elastic stresses (caused by misfits between γ and γ′) resulting in larger precipitates becoming smaller as small precipitates grow larger [24,25]. This effect will not be discussed further and the reader is directed to the references for a more thorough explanation. Most commercial γ′ strengthened superalloy aging treatments will be at a longer duration (20 h at 870 °C for MAR-M-247, similar to CM247LC, [20]) than that observed for peak hardness. Other considerations such as optimal creep rupture strength, creep life, and fatigue life, are considered when designing heat treatments for commercial parts and these factors may necessitate coarser precipitates.

The smooth appearance of the post heat treatment crack faces, their intergranular propagation and the fact that they are observed after solutionizing of the blank samples, strongly suggest strain age cracking is occurring in the CM247LC samples, but not for CM247LC NHf. Strain age cracking susceptibility is quite

high for CM247LC due to the high fractions of γ′ precipitation [26]. Strain age cracking of high γ′-fraction Ni-base alloys typically occurs during the solutionizing stage, when the part's temperature reaches the aging temperature on its way to the set temperature [27]. Once the alloy reaches the aging temperature, the γ′ precipitation begins, which induce corresponding loss of ductility. If the residual stress present within the part is sufficiently high, then cracking occurs. Post-heat treat cracking was not observed on the cuboidal samples produced for the aging study. There are two notable differences between the samples produced for mechanical testing and those for the aging study: the samples for the mechanical property testing were (i) HIPed prior to solutionizing and (ii) of a greater section thickness. The pre-existing population of γ′ after the HIP treatment may have led to a further reduced ductility, which then increased the susceptibility to SAC when solutionizing. In addition, the greater section thickness would have provided more constraint and an increased time in the susceptible region (larger thermal mass takes longer to reach the solutionizing temperature).

Two important observations from the heat treatment study are: (i) CM247LC NHf displays a lower hardness than CM247LC; (ii) CM247LC NHf samples are not prone to strain age cracking during heat treatment. Both of these observations can be explained by the influence of Hf on the γ′ phase. Despite being widely reported as a GB strengthening element, Hf does have solubility in the γ and γ′ phases. Fig. 13(a) shows estimates of the equilibrium phase fraction of γ and γ′ phases as a function of temperature for the two alloys calculated with Thermocalc. At 850 °C, the heat treatment temperature, the equilibrium phase fraction of γ′ is 66% and 61% for the CM247LC and CM247LC NHf respectively. The 5% lower fraction of γ’ explains why the peak hardness of the CM247LC NHf is lower. It also potentially explains why the CM247LC NHf is less prone to strain age cracking, as higher fractions of γ′ phase are correlated with increased SAC susceptibility [26]. Furthermore, the lack of Hf may influence the γ-γ′ mismatch, but this was not investigated.

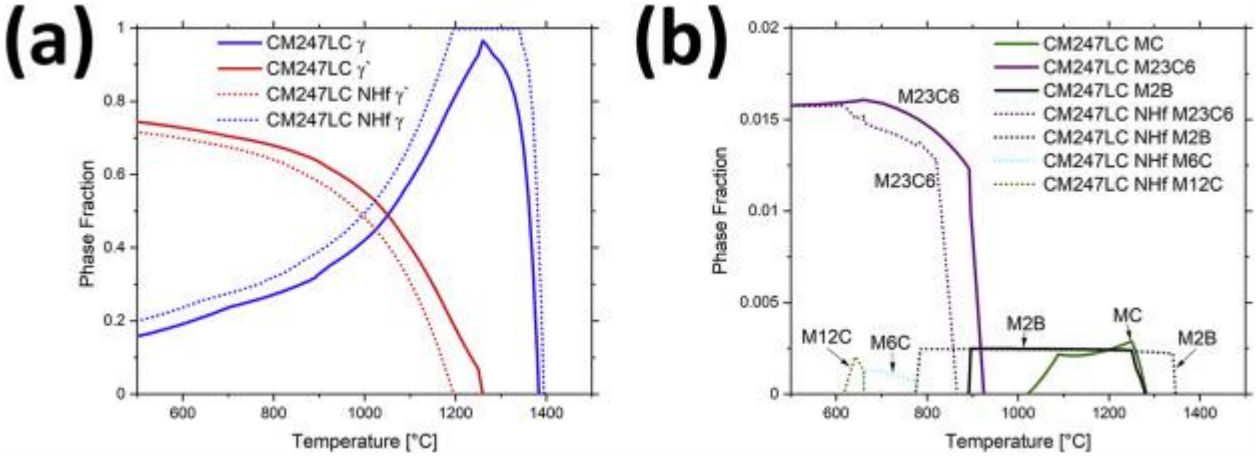

Figure 13. (a) Equilibrium phase fraction of γ (blue) and γ′ (red) phases as a function of temperature for CM247LC (dotted) and CM247LC NHf (dotted). (b) Equilibrium phase fraction of carbide and boride phases as a function of temperature. Calphad calculations were performed with Thermocalc and the TCNI5 database. (For interpretation of the references to colour in this figure legend, the reader is referred to the web version of this article.)

A lower area fraction of carbides was measured in the HIPed, solutionized, and aged CM247LC NHF sample (~0.9%) compared to the HIPed, solutionized, and aged CM247LC sample (~1.7%). In addition, a slight morphological change was observed in our prior study (Hf containing carbides in the as-solidified state are blocky) [9]. Fig. 13(b) shows an estimatation of the equilibrium phase fraction of carbide, and boride phases as a function of temperature for the two alloys. Calphad calculations of the phase fraction of $M_{23}C_6$ at 850 °C for the CM247LC and CM247LC NHf were 1.4% and 0.4%, respectively (Fig. 13b). At ~600 °C, the $M_{23}C_6$ phase fraction is nearly identical in both alloys. It should be noted that there is a slight difference in carbon concentration between the CM247LC NHf in Thermocalc and the actual CM247LC NHf powder, and that may alter the actual phase fractions present. Interestingly, the Calphad calculations resulted in an absence of the MC phase in the CM247LC NHf alloy, but resulted in $M_{12}C$ and M_6C carbides being present at intermediate temperatures, and an extended M_2B temperature stability (Fig. 13b).

One aspect of Ni-base superalloy heat treatment that is only occasionally discussed in the context of AM is homogenization. Homogenization treatments are utilized for many cast alloys in order to remove the solute concentration gradients that occurred due to elemental partitioning during solidification. Micro-segregation in airfoil castings can lead to undesirable consequences such as incipient melting [20]. Directionally solidified cast Ni-base superalloys are prone to significant micro-segregation, which is nearly identical, in terms of partition coefficient, to that observed on the L-PBF fabricated CM247LC [9]. One key difference between a directionally solidified cast part and one that is fabricated via L-PBF, is the cooling rate. The

cooling rate will directly influence the spacing between areas of high and low solute concentration and thereby change the time and temperature required to completely homogenize the alloy. Zhang et al. [28] calculated the relationship between cooling rate and the primary dendrite arm spacing (PDAS) for Ni-base Superalloys and it is given by Eq. (1),

$$PDAS = 134.43\dot{T}^{-0.26} \quad (1)$$

Where $\dot{T}$ is the cooling rate. A rough approximation of the time required to homogenize an alloy can be made with Eqs. (2), (3) :

$$\tau = \frac{l^2}{\pi^2 D} \quad (2)$$

$$D = D_O e^{-Q/RT} \quad (3)$$

where l is half of the PDAS, D is the diffusivity of solute at the temperature of homogenization, τ is the relaxation time, T is the temperature of homogenization, Q is the activation energy, and R is the ideal gas constant [29]. As the cooling rate increases, the PDAS thus decreases, suggesting that the high cooling rate of the L-PBF process will result in small PDAS spacings that would then significantly reduce homogenization times per Eq. (2). Since homogenization can be quickly obtained, incipient melting during solutionizing heat treatment could be mitigated. Evidence for this is shown by the complete homogenization, disappearance of dendritic segregation, of the solutionized sample shown in Fig. 3.

The CM247LC NHf samples displayed a higher mean 0.2% offset yield stress at 760 °C than the CM247LC samples, 969 MPa and 926 MPa, respectively. In contrast, the CM247LC NHf samples displayed a lower microhardness than the CM247LC samples at RT. One potential explanation for this behavior relates to the sampling size of the microhardness measurements. The microhardness indents were ~50 μm in width. While the micro-hardness indents were sufficient to include the contribution of the γ′ to the overall hardness, they were not of sufficient size to sample the microstructural contribution. The CM247LC NHf sample did have a slightly finer grain microstructure and the presence of annealing twins that could have resulted in the higher yield strength. It is currently unclear how Hf influences the occurrence of annealing twins, but it is clear that the absence of Hf increases their occurrence. Pande and Imam studied the influence of B on the annealing twin formation in Ni and found that 200 ppm was sufficient to suppress annealing twin formation

[30]. It was hypothesized that the boron slowed the grain boundary movement thus inhibiting twin nucleation. A similar effect could take place in our system, as Hf is present on the grain boundaries. There are also expected to be differences in grain growth between the two alloys due to the morphological and composition differences of the grain boundary carbides, but this was not investigated.

Polycrystalline Ni-base superalloys show a minimum in tensile ductility between 649 °C and 871 °C and a minimum in stress-rupture ductility at ~760 °C [20]. As discussed in our prior publication [9], Hf was added to the polycrystalline superalloys in order to improve the ductility [31], specifically stress-rupture elongation. One of the potential negative consequences of the removal of Hf could be a loss in ductility. The elongation at fracture was approximately the same for both alloys, but one of the CM247LC NHf samples tested had a low, 0.7%, elongation at fracture. As described in Section 3, all fractures intersected at least one thermocouple spot weld, which are required to control te temperature. It is therefore plausible that the welded thermocouples could have contributed to premature fracture (see Fig. 12). Furthermore, while care was taken to select CM247LC samples with no visible macro-cracks (those believed to be SAC) in the gauge section it is likely that some micro-cracks existed prior to testing. However, no evidence of fracture resulting directly from macro-cracks was observed, and the minimal spread in the data suggests the influence of cracks were minimal.

Further high temperature tensile tests with samples without spot-welded thermocouples and stress-rupture tests are required to determine if the absence of Hf will have a significant impact on the ductility and on creep elongation.

5. Conclusions

The modified alloy without Hf, CM247LC NHf, was discovered to have a few key differences from standard CM247LC in terms of heat treat response after L-PBF.

- The new CM247LC NHf alloy has lower peak hardness than the CM247LC alloy. This was attributed to the lower γ′ volume fraction.
- The new CM247LC NHf alloy appears to be less susceptible to strain age cracking. It was hypothesized that this was due to a lower γ′ volume fraction and reduced lattice misfit from the removal of Hf.
- The finer solidification structure of the L-PBF fabricated alloy will enable homogenization to occur during a standard solutionizing heat treatment.

- Annealing twins were present in CM247LC NHf after thermal treatment, but not in the CM247LC samples suggesting that Hf inhibits annealing twin formation.
- The CM247LC NHf samples displayed a higher mean 0.2% offset yield stress at 760 °C than the CM247LC samples, 969 MPa and 926 MPa, respectively. The mean elongation at fracture for the CM247LC and CM247LC NHf was comparable, ~1%, suggesting that the ductility is not significantly impacted; however, spot-welded thermocouples on the samples might have induced premature failure.

Data availability

The data that support the findings of this study are available from the corresponding author upon reasonable request.

Declaration of Competing Interest

The authors declare that they have no known competing financial interests or personal relationships that could have appeared to influence the work reported in this paper.

Acknowledgments

The authors would like to acknowledge the Competence Center for Materials Science and Technology (CCMX) for financial support, as well as the Swiss Industrial Consortium associated to the project. The authors would also like to acknowledge Dr. Dieter Sporer and Dr. Thomas Etter for their support during the project. HGT, JJ and REL are thankful for the generous support of PX Group to the LMTM laboratory.

References

[1] L.N. Carter, C. Martin, P.J. Withers, M.M. Attallah, The influence of the laser scan strategy on grain structure and cracking behaviour in SLM powder-bed fabricated nickel superalloy, J. Alloys Compd. 615 (2014) 338–347, https://doi.org/10.1016/ j.jallcom.2014.06.172.

[2] X. Wang, L.N. Carter, B. Pang, M.M. Attallah, M.H. Loretto, Microstructure and yield strength of SLM-fabricated CM247LC Ni-Superalloy, Acta Mater. 128 (2017) 87–95, https://doi.org/10.1016/j.actamat.2017.02.007.

[3] V.D. Divya, R. Munoz-Moreno, ˜ O.M.D.M. Mess´e, J.S. Barnard, S. Baker, T. Illston, H.J. Stone, Microstructure of selective laser melted CM247LC nickel-based superalloy and its evolution through heat treatment, Mater. Charact. 114 (2016) 62–74, https://doi.org/10.1016/j.matchar.2016.02.004.

[4] M. Cloots, P.J. Uggowitzer, K. Wegener, Investigations on the microstructure and crack formation of IN738LC samples processed by selective laser melting using Gaussian and doughnut profiles, Mater. Des. 89 (2016) 770–784, https://doi.org/ 10.1016/j.matdes.2015.10.027.

[5] E. Chauvet, P. Kontis, E.A. J¨ agle, B. Gault, D. Raabe, C. Tassin, J.-J. Blandin, R. Dendievel, B. Vayre, S. Abed, G. Martin, Hot cracking mechanism affecting a non-weldable Ni-based superalloy produced by selective electron beam melting, Acta Mater. 142 (2018) 82–94, https://doi.org/10.1016/j.actamat.2017.09.047.

[6] M. Ramsperger, R.F. Singer, C. Korner, ¨ Microstructure of the nickel-base superalloy CMSX-4 fabricated by selective electron beam melting, Metall. Mater. Trans. A 47 (2016) 1469–1480, https://doi.org/10.1007/s11661-015-3300-y.

[7] Y.S. Lee, M.M. Kirka, S. Kim, N. Sridharan, A. Okello, R.R. Dehoff, S.S. Babu, Asymmetric cracking in mar-M247 alloy builds during electron beam powder bed fusion additive manufacturing, Metall. Mater. Trans. A 49 (2018) 5065–5079, https://doi.org/10.1007/s11661-018-4788-8.

[8] L.N. Carter, M.M. Attallah, R.C. Reed, Laser powder bed fabrication of nickel-base superalloys: influence of parameters; characterisation, quantification and mitigation of cracking, in: Superalloys 2012, John Wiley & Sons, Inc., 2012, pp. 577–586, https://doi.org/10.1002/9781118516430.ch64.

[9] S. Griffiths, H. Ghasemi Tabasi, T. Ivas, X. Maeder, A. De Luca, K. Zweiacker, R. Wrobel, ´ J. Jhabvala, R.E. Log´ e, C. Leinenbach, Combining alloy and process modification for micro-crack mitigation in an additively manufactured Ni-base superalloy, Additiv. Manuf. 36 (2020) 101443, https://doi.org/10.1016/j. addma.2020.101443.

[10] Y.-C. Hagedorn, J. Risse, W. Meiners, N. Pirch, K. Wissenbach, R. Poprawe, Processing of Nickel Based Superalloy MAR M-247 by Means of High Temperature - Selective Laser Melting (HT - SLM), 2014, pp. 291–295. https://www.scopus.com/i nward/record.uri?eid=2-s2.0 84892160456&partnerID=40&md5=62302042 d538a33753c4a18268898c63.

[11] N. Kalentics, N. Sohrabi, H.G. Tabasi, S. Griffiths, J. Jhabvala, C. Leinenbach, A. Burn, R.E. Log´e, Healing cracks in selective laser melting by 3D laser shock peening, Additiv. Manuf. 100881 (2019), https://doi.org/10.1016/j. addma.2019.100881.

[12] N.J. Harrison, I. Todd, K. Mumtaz, Reduction of micro-cracking in nickel superalloys processed by selective laser melting: a fundamental alloy design approach, Acta Mater. 94 (2015) 59–68, https://doi.org/10.1016/j. actamat.2015.04.035.

[13] R. Engeli, T. Etter, S. Hovel, ¨ K. Wegener, Processability of different IN738LC powder batches by selective laser melting, J. Mater. Process. Technol. 229 (2016) 484–491, https://doi.org/10.1016/j.jmatprotec.2015.09.046.

[14] K. Kunze, T. Etter, J. Gr¨ asslin, V. Shklover, Texture, anisotropy in microstructure and mechanical properties of IN738LC alloy processed by selective laser melting (SLM), Mater. Sci. Eng. A 620 (2015) 213–222, https://doi.org/10.1016/j. msea.2014.10.003.

[15] P. Kanagarajah, F. Brenne, T. Niendorf, H.J. Maier, Inconel 939 processed by selective laser melting: effect of microstructure and temperature on the mechanical properties under static and cyclic loading, Mater. Sci. Eng. A 588 (2013) 188–195, https://doi.org/10.1016/j.msea.2013.09.025.

[16] J.H. Boswell, D. Clark, W. Li, M.M. Attallah, Cracking during thermal postprocessing of laser powder bed fabricated CM247LC Ni-superalloy, Mater. Des. 174 (2019) 107793, https://doi.org/10.1016/j.matdes.2019.107793.

[17] L. Rickenbacher, T. Etter, S. Hoevel, K. Wegener, High temperature material properties of IN738LC processed by selective laser melting (SLM) technology, Rapid Prototyp. J. 19 (2013) 282–290, https://doi.org/10.1108/ 13552541311323281.

[18] C.A. Schneider, W.S. Rasband, K.W. Eliceiri, NIH image to ImageJ: 25 years of image analysis, Nat. Methods 9 (2012) 671.

[19] G. L. Erickson, K. Harris, R.E. Schwer, Directionally Solidified DS CM 247 LCOptimized Mechanical Properties Resulting From Extensive Gamma Prime Solutioning, (n.d.).

[20] M. Donachie Jr., S. Donachie, Superalloys: A Technical Guide. http://search.ebsco host.com/login.aspx?direct=true&site=eds-live&db=edsnop&AN=edsnop. I000004077928.00, 2002.

[21] H.-E. Huang, C.-H. Koo, Characteristics and mechanical properties of polycrystalline CM 247 LC superalloy casting, Mater. Trans. 45 (2004) 562–568, https://doi.org/10.2320/matertrans.45.562.

[22] Y.T. Tang, C. Panwisawas, J.N. Ghoussoub, Y. Gong, J. Clark, A. N´ emeth, D. G. McCartney, R.C. Reed, Alloys-By-Design: Application to New Superalloys for Additive Manufacturing, Acta Materialia, 2020, https://doi.org/10.1016/j. actamat.2020.09.023.

[23] I. Dempster, R. Wallis, Heat treatment metallurgy of nickel-base alloys, in: G. E. Totten (Ed.), Heat Treating of Nonferrous Alloys, ASM International, 2016, p. 0, https://doi.org/10.31399/asm.hb.v04e.a0006261.

[24] W.C. Johnson, On the elastic stabilization of precipitates against coarsening under applied load, Acta Metall. 32 (1984) 465–475, https://doi.org/10.1016/0001- 6160(84)90120-2.

[25] S. Meher, L.K. Aagesen, L.J. Carroll, M.C. Carroll, T.M. Pollock, Understanding of inverse coarsening of γ′ precipitates in Ni-base superalloys, Microsc. Microanal. 22 (2016) 1258–1259, https://doi.org/10.1017/S1431927616007133.

[26] J.N. DuPont, S.D. Kiser, J.C. Lippold, Welding Metallurgy and Weldability of Nickel-Base Alloys, Wiley, Hoboken, NJ, 2009. http://search.ebscohost.com/login. aspx?direct=true&AuthType=ip&db=nlebk&AN=289303&site=ehost-live.

[27] S. Kou Verfasser, Welding Metallurgy. https://search.ebscohost.com/login.aspx? direct=true&AuthType=ip&db=edsbvb&AN=edsbvb.BV016548906&site=eds -live, 2003.
[28] Y. Zhang, B. Huang, J. Li, Microstructural evolution with a wide range of solidification cooling rates in a Ni-based superalloy, Metall. Mater. Trans. A 44 (2013) 1641–1644, https://doi.org/10.1007/s11661-013-1645-7.

[29] D.A. Porter, K.E. Easterling, Phase Transformations in Metals and Alloys, Second ed., CRC Press, Boca Raton - Fl, 2004 [reprinted].

[30] C.S. Pande, M.A. Imam, Grain growth and twin formation in boron-doped nickel polycrystals, Mater. Sci. Eng. A 512 (2009) 82–86, https://doi.org/10.1016/j. msea.2009.01.030.

[31] B. Geddes, Superalloys: Alloying and Performance, ASM International, 2010.

Supplementary Material

Influence of Hf on the heat treatment response of additively manufactured Ni-base superalloy CM247LC

Seth Griffiths[1], Hossein Ghasemi-Tabasi[2], Anthony De Luca[1], Joanna Pado[1], Shreyas S. Joglekar[1], Jamasp Jhabvala[2], Roland E. Logé[2], Christian. Leinenbach[1]

1. Empa - Swiss Federal Laboratories for Materials Science and Technology, Überlandstrasse 129, 8600 Dübendorf, Switzerland
2. Thermomechanical Metallurgy Laboratory – PX Group Chair, Ecole Polytechnique Fédérale de Lausanne (EPFL), 2002 Neuchâtel, Switzerland

Supplement Table 1. Chemical composition of CM247LC used for Thermodynamic calculations. The Hf free calculations were performed with the same chemistry, minus the Hf.

wt. %	Al	B	C	Co	Cr	Hf	Mo	Ni	Ta	Ti	W	Zr
CM247LC	5.6	0.015	0.07	9.2	8.1	1.4	0.5	Bal	3.2	0.7	9.5	0.015

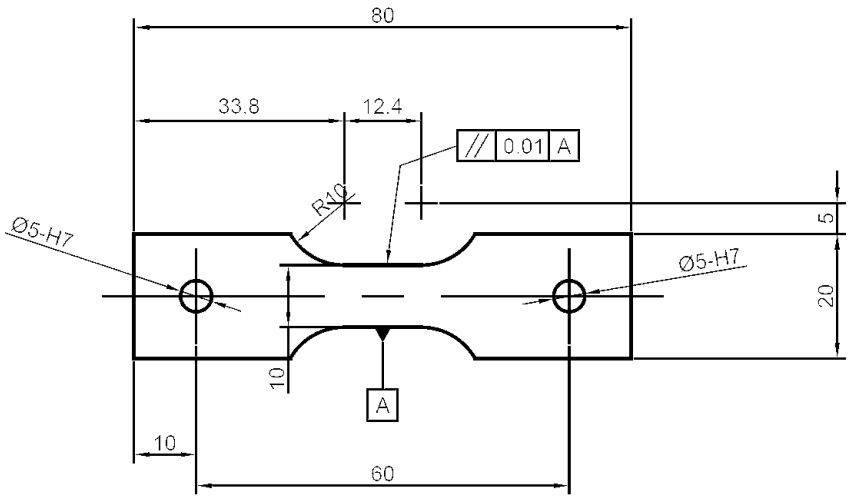

Supplement Figure 5. Dimension of dog bones used for mechanical property testing. Samples were 3 mm thick.

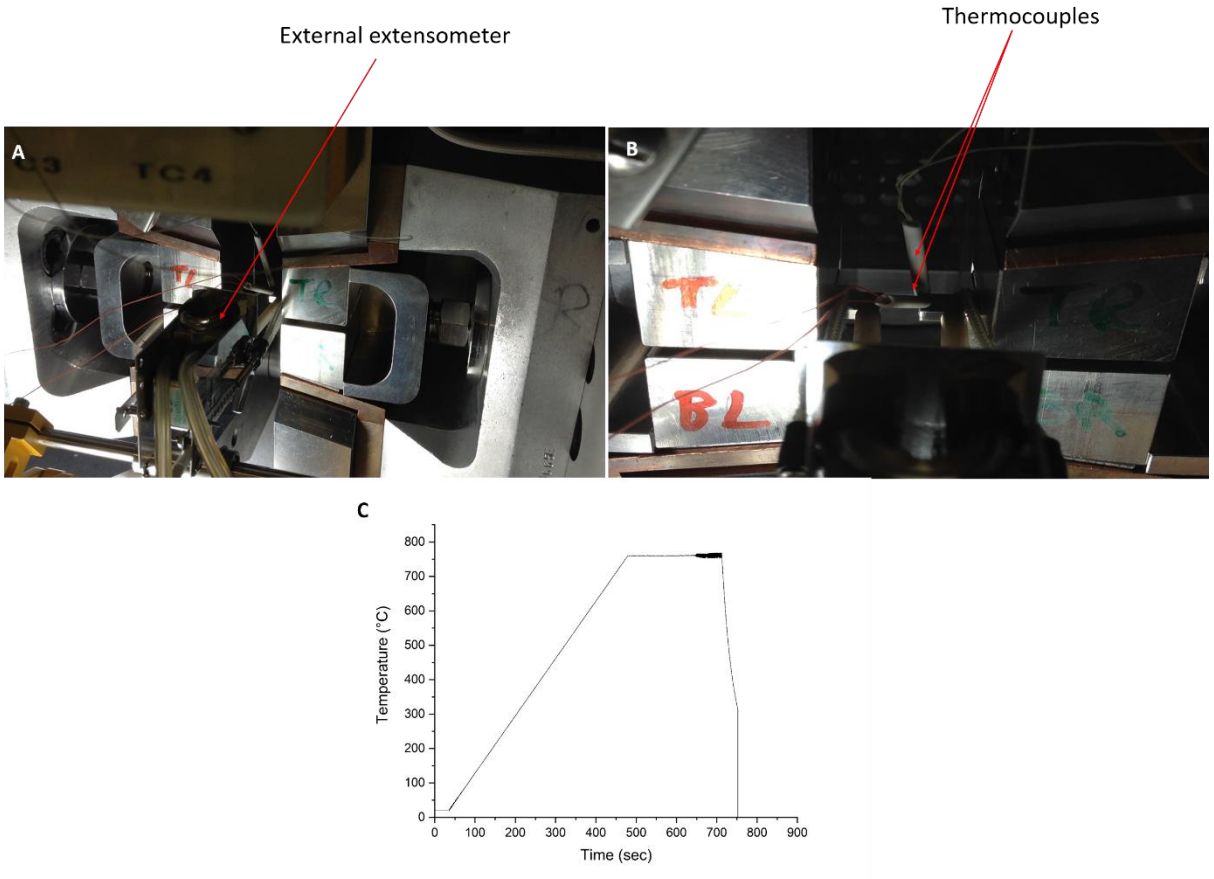

Supplement Figure 2. A) Gleeble testing setup samples in the grips and the external extensometer connected to the sample. B) A failed sample from the gauge zone with the thermocouple welded to the surface. C) Sample temperature is monitored by the thermocouples in middle of the sample. During the tensile test, there is small variation in temperature (± 7 °C) due to the deformation.

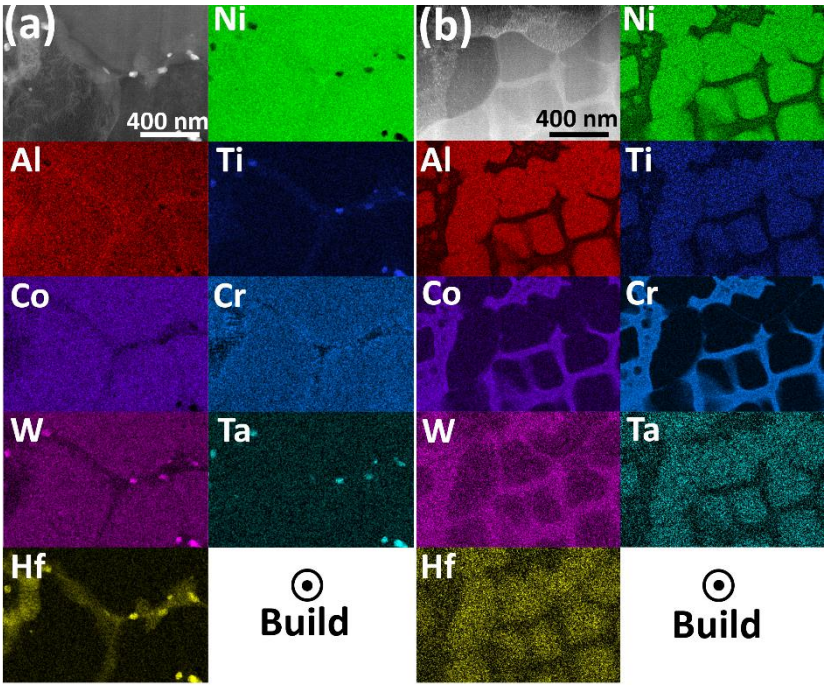

Supplement Figure 3. (a) Higher magnification STEM-EDX map highlighting the micro-segregation of an as-fabricated CM247LC sample. Precipitates are enriched in Ti/Hf/Ta/W/C and are presumed to be carbides. (b)Higher magnification STEM-EDX map highlighting the homogenization (of the solidification segregation) in a solutionized CM247LC sample. The chemical analysis is performed using the Al-K, Ti-K, Cr-K, Hf-L, Ta-L, W-L, Co-K, Ni-K, Mo-K, Zr-K, and C-K lines.

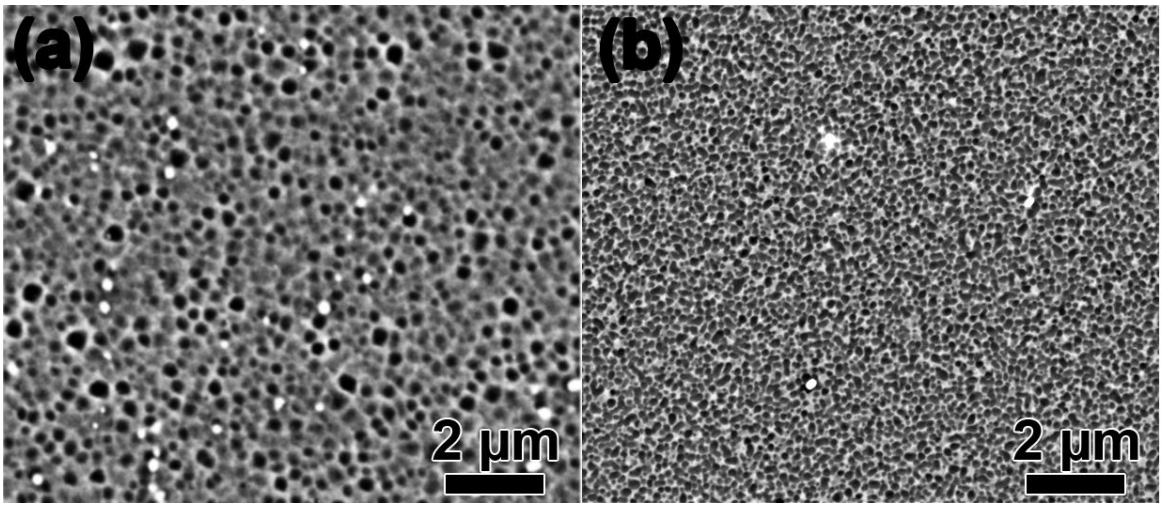

Supplement Figure 4. (a) BSE image showing γ' precipitates in solutionized and aged (850 °C 48 h) CM247LC. (b) BSE image showing γ' precipitates in solutionized and aged (850 °C 48 h) CM247LC NHf.

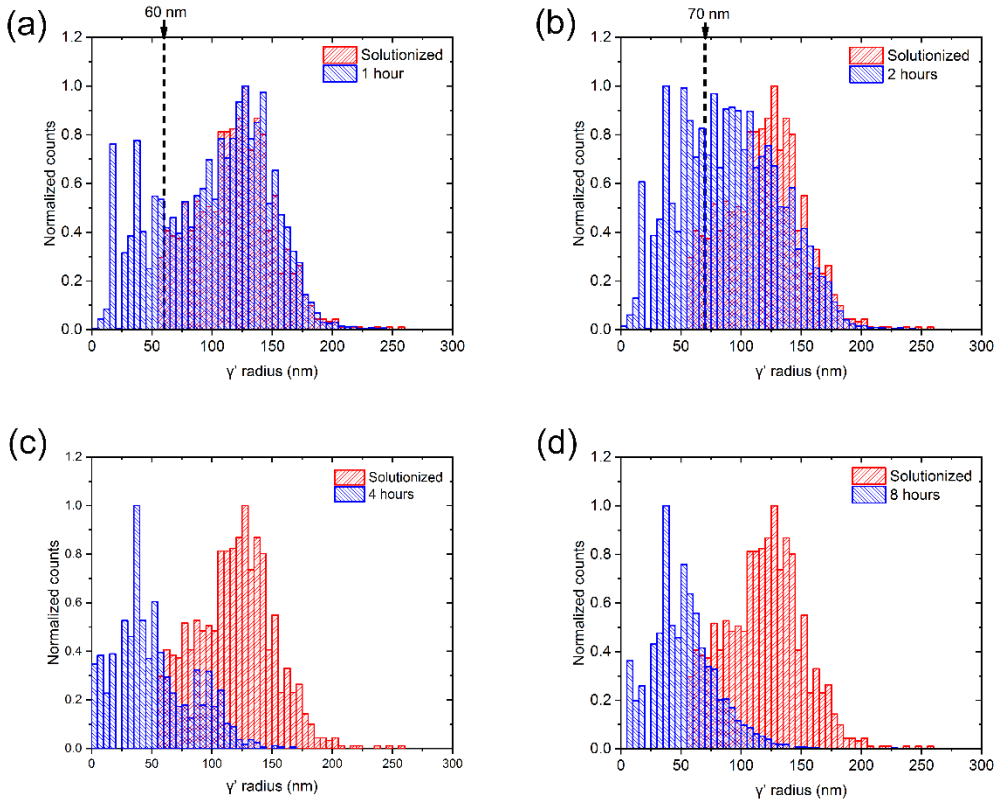

Supplement Figure 5. Comparison of the normalized count of γ' precipitates, in CM247LC, as a function of radius, between solutionized condition (red) and after aging at 850 °C for 1-2-4-8 h. The starting γ' population slowly shift toward smaller sizes as aging duration increases, leading to an overall reduction in γ' average radii.

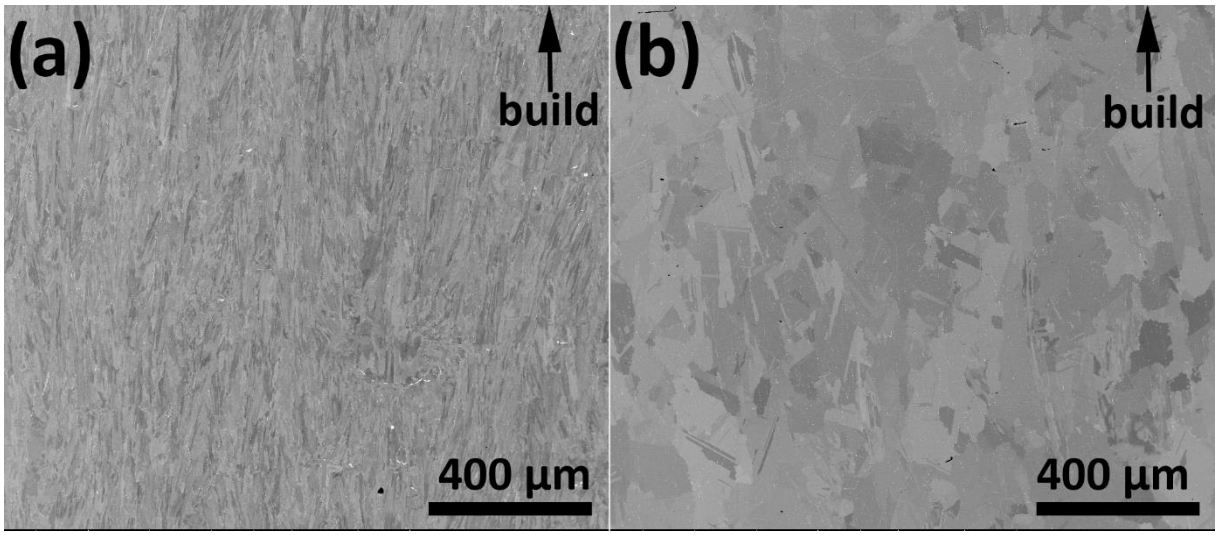

Supplement Figure 6. Low magnification BSE images of HIPed mechanical test bars. Images approximately taken from the center of the 80 mm bar length. (a) CM247LC (b) CM247LC NHf.

Chapter 11

7.1. Conclusions

Throughout the present PhD thesis, different techniques and materials have been used in order to study the L-PBF process at different scales. Studies of laser/matter interactions have been carried out by looking first at bronze and gold; they have been later extended to other materials, such as 316L. Different melt pool regimes have been investigated, with the idea of reaching optimal processing conditions. Different characterization techniques, from 2D optical microscopy to 3D tomography, allowed assessing accurately the defects content in printed samples. Finally, the effect of the process parameters on metallurgical evolutions such as crack formation in the CM247LC Ni-based alloy, and phase transformations in a red-gold alloy, have been related to the corresponding LPBF thermal and stress regimes. The major achievement and results from the presented work are summarized below:

- Laser/matter interactions have been have been analyzed in bronze, red gold and 316L stainless steel. Both simulations and experimental results indicate the importance of the powder absorptivity and light penetration inside the powder bed. Measuring the powder absorptivity at the appropriate laser wavelength and at room temperature, and using the concept of normalized enthalpy, different melt pool regimes have been predicted. Finally, a translation rule has been derived to predict optimal processing conditions in a new material, based on the ones found for a test material. The proposed model is important when dealing with precious materials such as gold, and also for any new material, for which the number of trials and errors should be reduced, for saving time and cost. The generality of the translation rule has been tested on 3 different materials and 2 laser spot sizes. Optimal conditions for different materials lie in a transition zone between keyhole and conduction modes, where the formation of porosities is expected to be the lowest.
- The quality of printed samples has been evaluated by characterizing porosity from mechanically polished cross sections and 3D tomography. Neutron microtomography has been used for the first time as a novel and precise tool to characterize residual porosity in additively manufactured gold alloys, and the results indicate this method is useful for other higher-Z materials where X-Ray analysis is challenging due to the limited penetration depth.
- Laser/matter interaction and process parameters effects on the meltpool formation have been studied by numerical finite element simulations. Detailed thermal histories were used to understand

metallurgical phenomena such as phase transformations in red gold, or cracking in CM247LC. Operando radiography allowed observing crack formation during L-PBF of the CM247LC nickel-based superalloy. In combination with Gleeble experiments and crack surfaces analysis, solidification and liquation cracking mechanisms have been identified, which helped defining approaches to reduce cracking in LPBF.

- In the case of red-gold alloys, variant selection during the disorder-order transformation has been studied by EBSD. The results confirmed the notion of "persistence" of variant selection in printed samples. During the manufacturing process, small f.c.t. domains form in the near surface region under tensile stress conditions. EBSD analysis indicate that despite the change of stress state induced by further LPBF processing, or by Laser Shock Peening (LSP) post-treatment, the variant selection continue to keep the memory of the stress state in the early stages of the transformation. The small amount of f.c.t. phase can however be totally removed with an annealing treatment at 600°C, followed by quenching. This approach then enables subsequent changes in the stress state to trigger new variant selections, and form new textures once the transformation is complete.

A central idea put forward in this thesis is that understanding of laser/matter interaction, melt pool formation and thermal fields under different LPBF parameters can lead to a thorough understanding of microstructure evolution phenomena such as phase transformation, and cracks formation.

7.2. Future Outlook

During the course of this PhD thesis, some topics have been briefly studied and the author believes that they should receive greater attention in the future:

- **Sample size effects:** L-PBF process parameters need to be optimized for different sample sizes and geometries of the same material. Changing the size modifies the laser beam travelling time, and the effective cooling volume of the sample. Therefore, local temperatures near the laser track and average temperatures in the sample both matter, and explain the size effects. An interesting objective would be the development of an extended translation rule considering these size effects.
- **Crack formation in CM247LC:** Crack formation in additively manufactured CM247LC samples has been reduced via process optimization and alloy composition modification. However, cracks remain. Different novel approaches such as using multiple lasers, or beam shaping techniques, could be tested to modify the local thermal histories, and as a result, the susceptibility to cracking.

- **Kinetics of phase transformation in red-gold alloys:** The order-disorder phase transformation has faster kinetics in an as-cast sample compared to an as-built L-PBF sample. There are different features in the L-PBF samples which might affect the kinetics of disorder-order phase transformations, such as residual stresses, grain size, texture, and chemical composition fluctuations due to evaporation phenomena.
- **Operando experiments:** an operando experimental setup has been used in this study to investigate the cracking mechanisms in CM247LC samples. This setup and the acquired data in real process conditions provide a broad range of information on different events occurring during LPBF, such as pore formation, melt pool dynamics, or spatter ejection. These should be further analyzed and compared with previous literature work.

Hossein Ghasemi-Tabasi
Rue des Sablons 43
2000 Neuchâtel
Switzerland

Iranian (Permit B)
Birthday: Jan 3, 1991
hossein.ghasemitabasi@epfl.ch
+41 78 724 85 76
Google Scholar link

Education

2017-Present

Ph.D. in Materials science and engineering, LMTM – PX-Group chair – Thermomechanical Metallurgy Laboratory, **Ecole Polytechnique Fédérale de Lausanne (EPFL)**, Switzerland

Thesis Title: **Understanding Thermomechanical Treatments Induced by the Laser Powder Bed Fusion additive manufacturing process**

2013-2015

M.Sc. in Materials science and engineering, Welding Metallurgy, Sharif University of Technology, Tehran, Iran

2009-2013

B.Sc. in Materials science and engineering, Industrial Metallurgy, Ferdowsi University, Mashhad, Iran

Professional experience

June 2017- Present

EPFL, PhD student in the field of Additive Manufacturing of metallic alloys at the LMTM Laboratory (EPFL)

Research

- Conducting a full study on Laser Powder Bed Fusion (L-PBF) additive manufacturing process at different scales :
    - Macro scale: Metallurgical features (precipitation, crack formation) occur in the heat-affected zone of the L-PBF samples (Materials: CM247LC Ni-based superalloy, and red-gold alloy)
    - Meso scale: Analyze melt pool formation during the printing process and looking at porosities as a general defect in the as-build samples (Materials: CuSn8, CuSn10, red-gold, 316L)
    - Micro scale: Study laser/matter interaction by looking at the optical properties of a material at different states (powder, solid, liquid)
- Devising an effective rule for translating optimal L-PBF processing parameters from one material to another . This approach eventually leads to the highest reported density for an additive manufactured 18-carat gold alloy.
- Developing the translation rule approach by considering the effect of the sample size on the optimal process parameters.
- Identification of the cracking mechanism in Ni-based superalloys during the L-PBF process using operando synchrotron-based X-ray techniques

Teaching and Experiments

- Teaching assistant (TA), Introduction to additive manufacturing for master students at EPFL, Dr. Eric Boillat
- Supervising 6 master semester project students in the field of additive manufacturing of metallic alloys at the LMTM (EPFL)
- Five accepted proposals for beamtime at The Swiss Spallation Neutron Source (SINQ) and Swiss Light Source (SLS) as the principal investigator and proposer.

Sep 2015- Dec 2016

Pasargad Steel Co, as a materials science engineer, I have been involved in designing heat treatment cycles and following uniaxial tensile test experiments to study the effect of the mechanical deformation on the magnetic properties of the austenitic stainless steel.

Skills

Materials characterization:	Tensile test, hardness test, impact test, SEM, XRD, handling with tools and finishing machines
Software:	SolidWorks, Materialise Magics, NETFABB, RayCi (beam profiler), Fusion 360, GIMP, Blender
MS Office:	MS-Project, MS-Excel, MS-Word, MS-PP

Honors

- Best Poster Award in Advanced Manufacturing (EDAM) day – Neuchatel, Switzerland (2019).
- Ranked second among master's students in the Department of Materials Science and Engineering for MS curriculum (welding metallurgy engineering). Iran, (2013-2015).
- Member of the Iran's National Elites Foundation (Ranked 6th among more than 5500 participants in the Nationwide Universities Entrance Exam-2013).
- Ranked first among 20 teams in the Ninth National Heat Treatment Contest. Iran, (2012).
  The subject of the contest was the optimization of mechanical properties of white iron for using in pelletizing industry.

Languages

English (Fluent), French (B1), German (A1), Persian (Mother tongue).

Hobbies

Cycling, Soccer, Music.